MATHEMATICAL MODELLING OF THE ARTERIAL CELLULAR COMMUNICATION

A thesis submitted in partial fulfilment of the requirements for the degree of

Doctor of Philosophy in Mathematics

at the
University of Canterbury

by

Ealasukanthan Thavanayagam

Principle Supervisor: Emeritus Professor David J N Wall
Associate Supervisor: Professor Tim David

School of Mathematics and Statistics
Faculty of Engineering
University of Canterbury
New Zealand

November 2016

Abstract

A study of the arterial cellular communication may be regarded as of greatest importance for understanding cellular physiology and its consequences leading to pathological states of the human arterial diseases. However, it is complex and not an easy task, as biological structures are heterogeneous on many scales such as micro, macro, etc. In particular, a small arterial segment consists of billions of cells among which not only a certain types of cells are connected through cellular gap junctions, but also thousands of nonlinear ion pathways within each cell, which can be regarded to be in nano-scale structures. Mathematical models of these communities of cells typically involve thousands of billions of ordinary differential equations (ODEs), which require simulation on distributed high performance computer. As a result, an attempt to incorporate all of these possible structures leads the mathematical modeler to encounter difficulties due to the computational size of the models. However, multiscale analysis and the theory of mathematical homogenisation provide the mathematical modeler with a way of avoiding vast-scale calculations and are useful in obtaining a small number of partial differential equations for the study of such complex system.

One of the main goals of this project is to further develop the homogenised partial differential equations (HPDEs) derived so far into a more comprehensive and cohesive model, so as to predict communication protocols between cells in the macroscopic arterial domain. In this interest we developed one- and two-dimensional HPDEs for the homocellular (same type of cells) membrane potential of a population of discrete and continuous cells around an arterial ring and along the arterial axis, respectively.

For this, each homogenic cell is treated to be an identical and electrical equivalents of a single FitzHuge-Nagumo (FHN) analogue. Moreover, cells are assumed to as human arterial smooth muscle cells (SMCs). An argument of using FHN equations in the modelling of SMCs is given in relation to the local topological (dynamical) similarities between our FHN equations and the SMC models of koenigsberger et al.. Furthermore, as an application of the homogenised models the effect of macroscopic potential variation coefficient from the microscopic variation was illustrated by constructing numerical examples.

As the next main goal of this project, we carried out a numerical dynamical study for a ring of three discrete cells. As a result we showed the dynamics of the cellular membrane potential of SMCs as oscillations when the system undergoes Hopf bifurcation. In the subsequent numerical simulations a spatial patterning of the membrane potential in one-dimension revealed a propagation of forward and backward plane waves under the application of a stimulus in the form of a second-order spatially-varying spline with respect to the Hopf points identified. Numerical simulations of the HPDEs in two-dimension discovered the membrane potential to be a propagation of curved wave-fronts and -backs, circular wave-fronts (moving in the direction of the outward normal) and -backs (moving opposite to the outward normal) and finally, rigidly rotating spiral waves under a physiological symmetry breaking condition (zero-state depolarization). Dynamics of these membrane potential waves in one and two dimensions were explained in terms of multiple steady states based on new notions, 'moving point of initiation of waves' and interference of waves, and drifts, meanders and wave-breaks, respectively. Finally, mathematical models for the membrane potential heterocellular communication between SMCs and endothelial cells were derived in one and two dimensions. However, the modelling of HPDEs of these models and their related dynamics have been left for future work.

Acknowledgement

This research would not have been possible without guidance and help of several individuals who, in one way or another, contributed and extended their valuable assistance in the preparation and completion of this study.

First and foremost gratitude goes to my principal advisor Emeritus Professor David J N Wall, David has been an excellent mentor for me. I learnt to foster many research questions, during the early stage of my research discussions, from the way David was looking at the problem. His phenomenal expressions are always interesting and helped me sometimes to understand practical insight of some mathematical notions that I have not come across earlier. I would also like to thank David for his encouragement and appreciation, and providing with me a teaching assistantship, during the period of my PhD. David still supervises me even though he is retired. He is simply great.

Secondly, I would like to express my sincere gratitude to my associate advisor Professor Tim David, Tim has been a tremendous advisor and encourager for me. I am very much thankful to Tim as he has provided with me a place in his brain trust research group. This led me to learn further about research in Mathematical Biology. Not only that, but he was also guiding me beside his office table in my intermediate research period. These kinds of opportunities are rare to everyone, and I cannot easily forget them. Further, the knowledge Tim shared with me was absolutely useful for my research in many ways. Both of my supervisor's guidance are invaluable in my research as well as for my future research career.

Beside my advisors, I would like to thank Professor Yuri A Kuznetsov, Department of Mathematics, Utrecht University, for providing a useful research paper about homotopy method, and to Professor Helen Byrne, OCCAM, University of Oxford, for her valuable discussion during her visit to the University of Canterbury. I would also like to thank Paul Brouwers, Steve Gourdie and Angela Armstrong. Paul and Steve were very supportive whenever I knocked on their door for IT support. On the other hand, Angela helped me a lot in organising my research meetings, with my supervisors. Further, I am obliged to Irene David for providing with me a tutorship in Mathematics during the first and second year of my PhD. Also, I would like to thank the Department of Civil and Natural Resources Engineering for an appointment as a Teaching Assistant for a 3 years period. In addition, I am thankful to administrative and other academic staff of the Department of Mathematics as well as my PhD colleagues, for their support in any way.

A special thanks goes to my family. Words cannot express how grateful I am to my father Thavanayagam and mother Mankayatkarasi for all of the sacrifices, unconditional love and care that they have made on my behalf. Their prayers for me were what strengthened me to this extent. The decision made by my mother at the end of my year 13 study in Mathematics brought me to this extent to pursue a doctoral study in Mathematics. I look at my mum as such a brilliant, ever loving, beautiful woman in my life span. I would also like to especially thank all of my beloved brothers; Dr. Gowrikanthan, Dr. Gnanavinthan, Dr. Mathiventhan and my beloved sister Thamillinie, and sister-in-laws, who showed their enthusiasm and gave me a moral support and encouragement during this research period. Further, my beloved wife Kalpana has been my best friend and I thank her for all of her support. Especially, once again, I would like to thank my elder brother Gowri and my wife for their timely support in sharing my hardship period.

I convey my gratefulness to my family friends and other friends for their support, encouragement and an interest in my future aspects through a good friendship during my study period.

The past two years have not been personally an easy ride for me. There was no one to answer my queries in many circumstances, but I thank faithfully the omnipresent and omnipotent power that has been sticking by my side since my childhood for a boundless love and timely guidance.

Dedication

To thousands of people who were lost in Genocides in Sri Lanka

Table of Contents

List of Tables

List of Figures

Glossary

c: Plane wave speed

Ca^{2+}: Calcium ion

DRS: Double real stable leading eigenvalues

DSS: Distance to steady state

EC: Endothelial cell

EDH: Endothelium-derived hyperpolarization

FHN: FitzHuge-Nagumo

HPDE: Homogenised partial differential equation

IP_3: 1,4,5-inositol triphosphate

K^+: Potassium ion

LT: Lasting time

NDSS: New distance to steady state

NPIW: New point of initiation of wave

ODE: Ordinary differential equations

PIW: Point of initiation of wave

PVC: Potential variation coefficient

SMC: Smooth muscle cell

SParam: Stable parameter

UParam: Unstable parameter

$\boldsymbol{w}$: Angular speed

Chapter 1

Introduction

1.1 Biological Background

There are increasing indications that cell-to-cell communication can have an influence not only on cellular growth, migration, differentiation and function [6], but also on an avenue of admitting arterial disease [12]. As an example, signalling between the smooth muscle cells (SMCs) and the endothelial cells (ECs) in the human artery play a major role in a chronic inflammation of large and medium-sized arteries due to an intimal plaque formation (composite of lipids, lipid-laden macrophages, leukocytes, smooth muscle cells and, at later stages, necrotic cores with cholesterol crystals and calcification) and hence occludes blood flow [54]. This is known as stenosis and leads to a pathological state called 'atherosclerosis' [100]. This progressive narrowing and hardening of arteries and the associated complications such as thrombosis, heart attack and stroke are then the leading causes of death in developed and developing countries [63, 84]. Therefore, studying cellular communication in an arterial segment between a population of the same type of cells (homocellular communication) and different types of cells (heterocellular communication) is of vital importance.

Our research is mainly based on a mathematical modelling of the cellular membrane potential as a homocellular and heterocellular communication among and between SMCs and ECs, using FitzHugh-Nagumo (FHN) nonlinear equations, and an attempt to study the similar dynamics of SMCs in $\mathbb{R}$ and $\mathbb{R}^2$ is made in this thesis. For the one-dimensional case, we assumed that the diameter of the artery is small enough for the arterial segment to fix along the real-line $\mathbb{R}$, the x-axis, and hence we avoided modelling the circumferential direction of the artery. Regardless, a cylindrical geometry of the arterial segment in one-dimension was conceptually created by allowing the same electrical signal (this can be considered a current due to the movement of ions) from the last cell to the first cell kept around the arterial circumference.

A higher dimensional problem can be considered in the cylindrical polar coordinates. However, as stated above, we model homocellular signalling between SMCs of a single layer. Therefore, in contrast to a multiple layer problem, the radial direction does not change for the single layer. Thus, the cylindrical polar coordinate system can be approximated by the two-dimensional Cartesian coordinate system when the circumferential direction of the artery is lifted along the Cartesian direction y. Similar argument is suitable for the heterocellular signalling between SMCs and ECs as it can be regarded as a two thin-layer problem where the radial-direction can be again neglected. In addition, the curvature effect on large arteries can be neglected where the wall for large arterial segments can be approximated by Cartesian coordinates. Therefore, we lift the circumferential direction of the artery along the y-direction and hence the higher dimensional cellular problem is considered in a two-dimensional lattice. Under these justifications we follow homogenisation process and multiple-scale

analysis in Chapters 2, 3 and 4, respectively. However, the reader can refer to [73] for a study of generic FHN reaction-diffusion waves on curved two-dimensional surfaces and the effect of curvature on the propagation of waves and nucleation.

In the following sections, we describe the existence of homocellular and heterocellular connections and signalling via such connections among and between the SMCs and ECs. Previous studies are used to justify our results in chapters 5 and 6.

1.1.1 Homocellular and Heterocellular Connections

A longitudinally arranged mono layer of cells along the vessel axis of the lumen region of all blood vessels is known as the endothelium and consists of approximately 1×10^{13} ECs [111] (see Figure 1.1). ECs are estimated to weigh almost 1 kg in an average

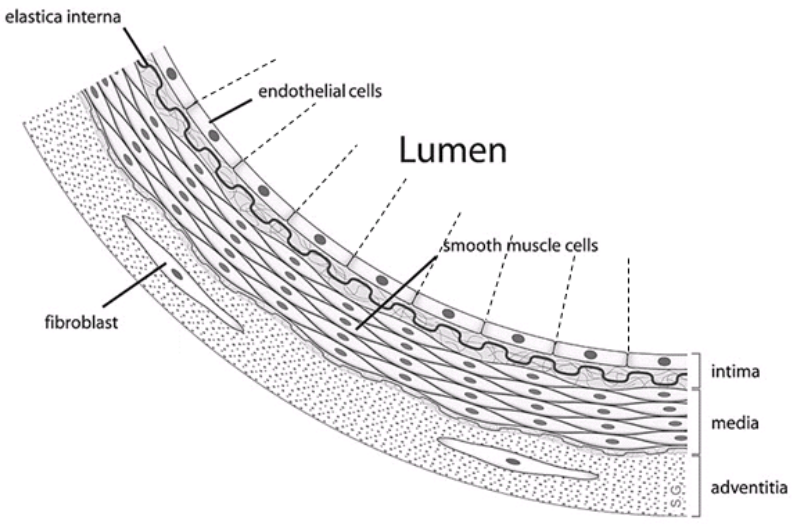

Figure 1.1: ECs along the arterial axis line the inner wall of the arterial vessel. SMCs are aligned perpendicularly to the ECs, around the circumference of the artery. These two cell layers are separated by the layer elastica interna. This Figure is adapted from Wikipedia with a free copyright license and then modified.

human [111]. Direct contact between neighbouring ECs is established via tight gap junctions which have low permeability [27, 50, 89, 120, 122] and allow direct transfer of small molecules such as 1,4,5-inositol triphosphate (IP_3) and calcium ions (Ca^{2+}) between the neighbouring cells via intracellular passage [27, 41]. The endothelium in the artery is surrounded by a layer of SMCs, which are separated by an elastic matrix layer called elastica interna (see Figure 1.1). This layer allows water-soluble molecules to diffuse extracellularly between the endothelium and the smooth muscle by forming a hydrophilic barrier. As for ECs, signalling between SMCs is also known to be via intercellular gap junctions [26, 27, 29, 33]. Therefore, connections between neighbouring ECs and similarly, connections between neighbouring SMCs, are categorized as homocellular connections (gap junctions).

Aside from homocellular gap junctions, heterocellular gap junctions, often called myoendothelial gap junctions, can occur between ECs and SMCs for a heterocellular communication. This heterocellular communication through myoendothelial gap junctions facilitates bidirectional electrical signals in small vessels [18] and allows ions to move between endothelial and smooth muscle cells (for example, movement of Ca^{2+} from smooth muscle to endothelium has been shown in in vitro studies [104]). The existence of myoendothelial gap junctions, mainly in small arteries, were observed via electron microscopy as well as dye and current transfer experiments [27, 101], even though it is technically challenging to identify the occurrence and performance of myoendothelial gap junctions [19]. In the following section, we give a brief review of literature to describe the electrical communication among and between the ECs and SMCs via gap junctions.

1.1.2 Communication Between ECs and SMCs

It is becoming clear that gap-junctional communication may be strongly associated with global vascular physiology or pathophysiology [37]. Morphological studies show a close communication between the EC and SMC membranes without connections, whereas other studies report the presence of heterocellular gap junctions between these cells [31]. Furthermore, in [31] the endothelium-derived hyperpolarization (EDH), a radially transmitted hyperpolarization from the endothelium to smooth muscle cells, is mentioned as one of the factors by which smooth muscle relaxation has been promoted. Moreover, electrical signals initiated by shear stress or by EDH in ECs are believed to be transmitted to the underlying SMCs through myoendothelial gap junctions [19, 31].

EDH and longitudinally propagating responses both in the ECs and SMCs perform a major part in controlling the degree of constriction experienced by a blood vessel relative to its maximally dilated state [19, 31]. In addition, consistent changes of hyperpolarization and depolarization in ECs initiated by SMCs were also documented in [19] and [31]. In particular, in [31], membrane potential has been typically measured in a cell and subsequently propagation of electrical signals between the ECs and SMCs was suggested by recorded synchronized action potential in both cell types. Additionally, [31] tested relaxation and contraction of SMCs promoted by ECs via direct electrical coupling. Therefore, it is clear that myoendothelial gap junctions function as a passage for electrical communication between the ECs and SMCs. As further evidence, variation of lumen (regulation of the arterial diameter) due to hemodynamic forces and a rise in intracellular Ca^{2+} concentration ($[Ca^{2+}]$) in SMCs are

described in [11] and [55], and [62], respectively. In particular, [62] demonstrated the role of pulsatile, oscillatory and unidirectional laminar shear stress in the arterial cellular communication. Good evidence for signal transmission via heterocellular gap junctions from SMCs to ECs can be seen in the work of [78], where experimental observations showed a rise in intracellular $[Ca^{2+}]$ in a part of EC population after a $[Ca^{2+}]$ increase was observed in neighbouring SMCs. Therefore, it is important to model and study the significance of cellular signalling by electrical or other means. In this thesis we have developed models for electrical heterocellular communication between the SMCs and ECs. Apart from all of the above, there is an increasing amount of computational modelling related to myoendothelial communication, which is not limited to literature [24], [68], and [112].

The work of [24] developed a computational model imitating a skeletal muscle resistance artery to promote a quantitative understanding of the vascular electrical cellular communication. As an outcome of this work, homocellular and heterocellular electrical signals were found to spread out distinctively among and between ECs and SMCs. An important notion of homocellular and heterocellular communication among ECs and SMCs is computationally and experimentally studied in [112]. This work explained the importance of threshold excitation of SMCs in transmitting signals from SMCs to ECs and the results are summarized as follows: an insufficient current generated by ions stimulates only a limited number of SMCs, providing only a weak localized membrane potential response. Hence, responses initiated by SMCs are not considerably transmitted to ECs via myoendothelial gap junctions. In addition,

it was suggested that the electrical responses initiated by SMCs are sometimes dissipated due to cellular connectivity properties. Therefore, it is clear that a threshold current needs to be provided by ions to excite a considerable amount of SMCs, by which the electrical signals can only be transmitted to the neighbouring ECs through gap junctions. During our simulation we have taken this notion into consideration and applied a unidirectional and a bi-directional external stimulus respectively in one and two dimensions, with a threshold value for the excitation of a sufficient number of SMCs to produce understandable cellular dynamics.

Another notion in relation to a failure of heterocellular signalling between the ECS and SMCs is also discussed in [78]. That is, a radial response from SMCs to ECs or vice versa lasts for a very short time due to the disappearance or less protein density of myoendothelial gap junctions in large arteries consisting of a thick medial layer. In contrast, in smaller arteries each SMC may communicate with several ECs and vice versa; hence heterocellular coupling is more secure in small arteries than in larger arteries [78]. This is one of the reasons we are motivated to develop one-dimensional models for an arterial segment of very small diameter, which then fit into a real-line $\mathbb{R}$. In the following section we describe our FHN models and their relevance in modelling similar dynamics of the SMCs and ECs.

1.2 FHN Models and Topological Conjugacy

A full dimensionless form of FHN models for the modelling of the membrane potential $\boldsymbol{v}$ and it's recovery potential $\boldsymbol{w}$ of a population of discrete cells can be given by

(derivation of these models are shown in chapter 2):

$$\nu \frac{d\boldsymbol{v}}{dt} = \boldsymbol{g}(\boldsymbol{v}) - GA\boldsymbol{v} - \boldsymbol{w} + \boldsymbol{I}, \tag{1.2.1}$$

$$\frac{d\boldsymbol{w}}{dt} = \boldsymbol{v} - \gamma \boldsymbol{w} - \boldsymbol{p}, \tag{1.2.2}$$

where $\boldsymbol{g}(\boldsymbol{v})$ is a cubic polynomial, G is a coupling coefficient, A is a discrete cellular circulant matrix, $\boldsymbol{I}$ is a varying stimulus and ν, γ and $\boldsymbol{p}$ are parameters. In general, any form of a single unit FHN model is considered to have two variables: the fast variable, v and the slow variable, w. The fast variable v is known as the excitation variable, which has cubic nonlinearity $g(v)$ and shortest relaxation time, allowing regenerative self-excitation via a positive feedback [38, 39, 40, 64]. The slow variable w is referred to as a recovery variable that has linear dynamics, providing a slower negative feedback [38, 39, 40, 64]. The recovery variable w plays an important role in excitation by reacting to the excitation variable. This variable inhibits the excitability of the model after excitation has occurred and brings the system to a recovery stage at the end of the impulse [40]. Moreover, the recovery variable has a relaxation time of an order greater than the order of the excitation variable [40]. Therefore, we use the recovery variable for the modelling of the recovery potential, which may be described in relation to cellular processes such as depolarization, repolarization and hyperpolarization caused by an action of opening and closing of sodium (Na^+) and potassium (K^+) ion channels in the SMCs and ECs.

In addition, we use a cubic nonlinearity in the form of $g(v) = v(1-v)(v-\alpha)$, $0 < \alpha < 1$, as each component of $g(v)$, for modelling the nonlinear time varying ionic currents through the voltage-dependent channels in SMCs and ECs. Regardless, the function $g(v)$ can be modelled by various forms such as the classic cubic polynomial

$g(v) = v - v^3/3$ and McKean piecewise functions: $g(v) = H(v-a) - v$, where H is a Heaviside function and

$$g(v) = \begin{cases} -v, & v < \alpha/2; \\ v - a, & \alpha/2 < v < (1+\alpha)/2; \\ 1 - v, & v > (1+\alpha)/2, \end{cases}$$

(see [70] and the references therein). However, since the dynamics of the SMCs and ECs are more complex, we now seek to discover whether FHN models given by Equations (1.2.1) and (1.2.2) can be used to model signalling among and between SMCs and ECs and if so, whether both the SMCs and ECs can be modelled by similar FHN equations.

To answer the first question, we take advantage of "topological conjugacy" or "equivalent conjugacy" between FHN models given by Equations (1.2.1) and (1.2.2) and more relevant models of the SMCs and ECs. Here, the term "topological conjugacy" has been used to explain the dynamical similarities between two systems in modelling a single dynamical system. Mathematically speaking, topological conjugacy is a notion of possibly constructing a relationship (homeomorphism) between the dynamical states of the first and second system that becomes equivalently conjugate if it preserves the direction of time. However, in this thesis we do not prove mathematically the topological conjugacy or equivalent conjugacy, but instead describe the local dynamical similarities between our FHN models and the models of Koenigsberger et al. as they validated by published in vitro experiments results obtained on rat mesenteric arterial segments. For this, we discuss the dynamical results obtained for the SMCs and ECs in [74], [75], [105] and [106]. We do not provide models and parameter values used in these references, as our aim is to explain only the dynamical behaviour of

the SMCs and ECs those studies report. In [75], the effects of electrical, $[Ca^{2+}]$ and IP_3 on SMC-EC coupling were studied. Results revealed the importance of electrical coupling for the transition of cytosolic $[Ca^{2+}]$ from steady state to an oscillatory state and vice versa in a single SMC, under the action of a receptor ligand agonist. Figure 1.2(a), reproduced from [75], shows an envelope of the oscillatory domain of cytosolic $[Ca^{2+}]$ in the SMC, formed by two Hopf bifurcation points. In addition, the same research showed a similar domain of oscillations for a pair of coupled SMCs as in the case of the single SMC, where Hopf points were observed to move towards each other. The models of Koenigsberger et al. used in [75] are considered physiologically relevant to the dynamics of the SMCs and ECs, as validated by published in vitro experiments results obtained on rat mesenteric arterial segments.

In other research, [74], the authors of [75] studied the role of the endothelium on arterial vasomotion for heterocellular communication between a population of coupled SMCs and ECs by analysing the effects of the SMC vasoconstrictor stimulation on ECs and the feedback of endothelium-derived factors via cytosolic $[Ca^{2+}]$ dynamics. Results of this work showed the existence of oscillatory domain formed by a pair of Hopf points for both homocellular communication between the SMCs and heterocellular communication between a single SMC and an EC. This was based on the decreased $[Ca^{2+}]$ endothelium level in the SMC with respect to the rate of the receptor ligand agonist. Figure 1.2(c), reproduced from [74], shows one of the predicted oscillatory domains between two Hopfs for an SMC coupled heterocellularly to an EC.

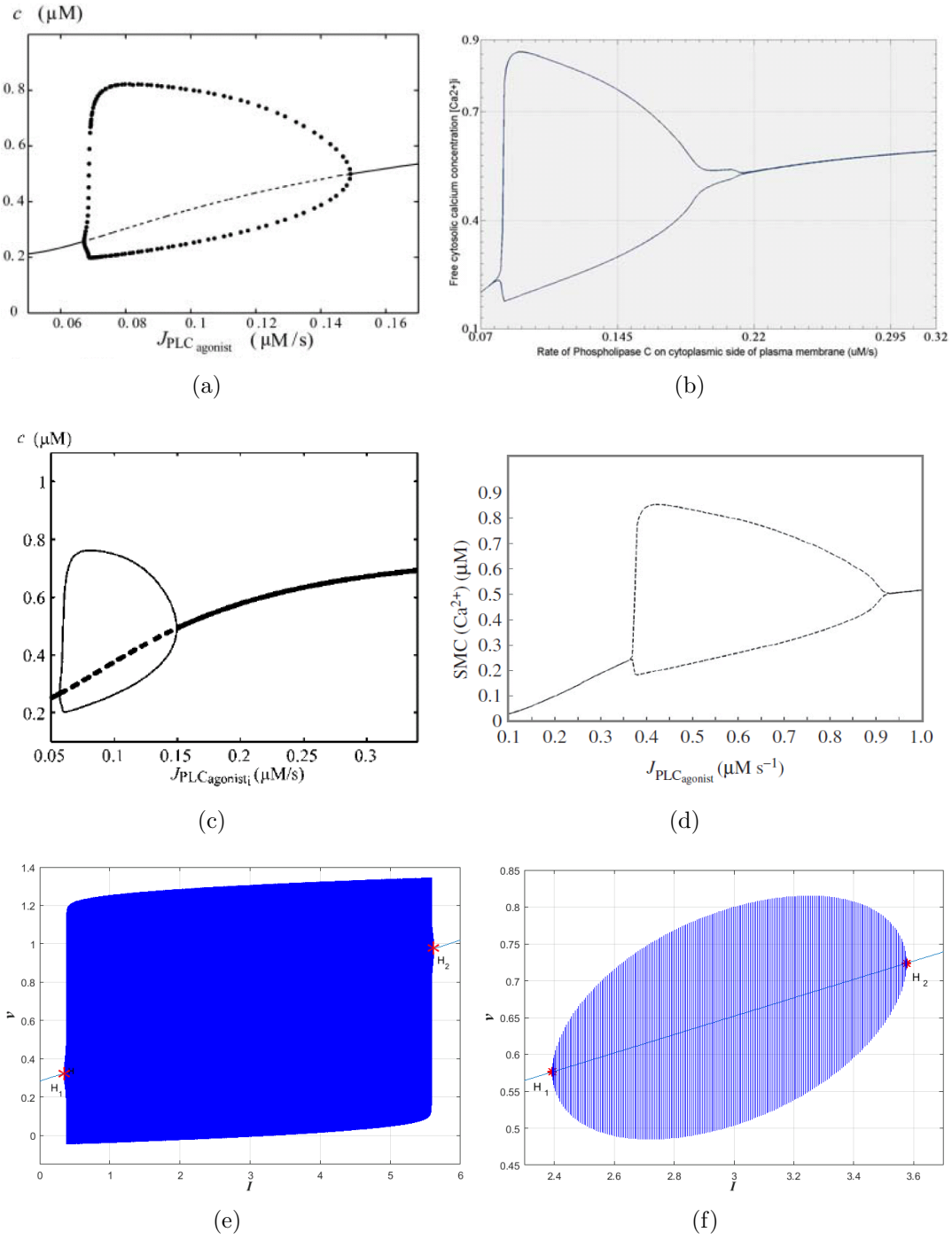

Figure 1.2: Schematic shows oscillatory domains predicted for the cytosolic $[Ca^{2+}]$ in an SMC, respectively in (a) [75] and (b) [105], in an SMC coupled to an EC, respectively in (c) [74] and (d) [106], and for the membrane potential of (e) an SMC and (f) a 3-coupled SMCs, in our modelling using our FHN models

In addition to the above literature, work of [105] and [106] has also shown similar results for the oscillations of cytosolic $[Ca^{2+}]$. Particularly, in [105], the authors used a spatially varying agonist to study computationally the dynamics of a coupled vascular EC-SMC system and illustrated a relationship between increasing agonist concentration and oscillatory frequency of the SMC. Figure 1.2(b), reproduced from [105], shows a domain of oscillations separated from the domain of stable steady states in an SMC. Further, in the same research, propagation of upstream and downstream $[Ca^{2+}]$ waves was also predicted as an effect of high agonist on one cell via electrochemical coupling. In other research, [106], the same authors used hundreds of thousands of identical Koenigsberger et al. ordinary differential equations (ODEs) to mimic an arterial segment of a huge number of cells and solved in a massively parallel Blue Gene computer to address a micro-macro phenomena of the cellular system. Results revealed an oscillatory domain for the cytosolic $[Ca^{2+}]$ in an SMC coupled to an EC, as shown in Figure 1.2(d), obtained from [106]. Furthermore, propagation of $[Ca^{2+}]$ waves from downstream to upstream cells in the axial direction of an arterial segment was also reported for the homocellular coupling between SMCs.

From [74], [75], [105] and [106] the existence of transition dynamics from steady state to an oscillatory state and vice versa in SMCs can be understood as soon as they are stimulated or undergo a physiological process. Notwithstanding the independent variable solved for, our results for the cellular membrane potential of an SMC and coupled SMCs using our FHN models given by Equations (1.2.1) and (1.2.2) show the birth of steady states and an oscillatory state under an action of varying external stimulus. Figure 1.2(e) shows the membrane potential oscillations in an SMC,

whilst an oval-shape oscillatory domain is predicted for a system of three coupled SMCs. Hopf bifurcation points are denoted by red stars. These results are discussed in Chapter 4. Moreover, depletion of the oval-shape oscillatory domain is observed as Hopf points moved towards each other for a set of increasing values of the coupling coefficient. This notion is justified by the similar result of moving Hopfs predicted in [75]. In addition, we have shown in the one- and two-dimensional macroscopic domains respectively the existence of forward and backward plane waves, which are similar to the upstream and downstream waves reported in [105] and [106]. Thus, in spite of the independent variables solved for, we explained the local dynamical similarities between the experimentally validated Koenigsberger et al. models and our FHN models for the modelling of the SMCs. We therefore used FHN models in the interest of simplicity for large-scale cellular nodes.

To answer the second question (whether both the SMCs and ECs can be modelled by similar FHN equations), we describe the suitability of using the same FHN models for the modelling of both SMCs and ECs, as supported by literature: [21], [24], [53], [65], [68], [80], [104] and [120], mainly focused on [24] and [68]. In [24], the authors developed a computational model mimicking a skeletal muscle artery and studied the spread of electrical signals among and between SMCs and ECs under the action of initial stimulus. In that virtual artery, a capacitor and a resistor in parallel were respectively used as electrical equivalents of membrane potential and ionic conductance of each SMC and EC. Moreover, ohmic and stochastic ohmic resistors (in general, let us assume R) were respectively used to represent the homocellular gap junctions among SMCs and ECs and heterocellular (myoendothelial) gap junctions between the

SMCs and ECs. Finally, using the above mentioned electrical equivalents of cellular notions, simulation results of [24] were seen to be in agreement with physiological data obtained from the hamster retractor muscle artery. In addition to [24], with the application of the same analog components, simulation results obtained in [68] were also seen to be consistent with the experimental data for vasoreactivity in rat mesenteric arteries. In both [24] and [68], though similar electrical components were used for the modelling of SMCs and ECs, these cells were physiologically differentiated by assigning different values for the capacitors and ohmic registers.

Authors of [65] and [104] stated a way of determining the properties of ohmic resistor for SMCs and ECs respectively from electrophysiological recordings of hamster cremaster arteriolar SMCs and from rat coronary ECs. Further, determination of properties of SMC-SMC and SMC-EC gap junctional ohmic resisters using voltage claimed neighbouring vascular cells in intact arterioles was discussed in [120]. Similarly, by allowing current through two electrodes in an endothelial monolayer, an estimation of properties of the EC-EC gap junctional ohmic resistor was determined in [80]. These studies clearly show us that SMCs and ECs can be treated as the electrical equivalents of capacitors and ohmic resistors, but an individual component has to be assigned with different values to differentiate one type of cell from the other. A set of physiological values proposed in the above literature are given by $R_{\text{SMC-SMC}} = 90\text{M}\Omega$, $R_{\text{EC-EC}} = 3\text{M}\Omega$ and $R_{\text{SMC-EC}} = 1800\text{M}\Omega$. In addition, the cellular capacitance in [24] was taken as $1\mu\text{Fcm}^{-1}$.

FHN models also use the above mentioned electrical components and are supplemented with two more components: an inductor and a battery (see Figure 1.4). These additional components can be used to further model the physiology of the cellular system. For this reason (in addition to the local dynamical conjugacy ex-

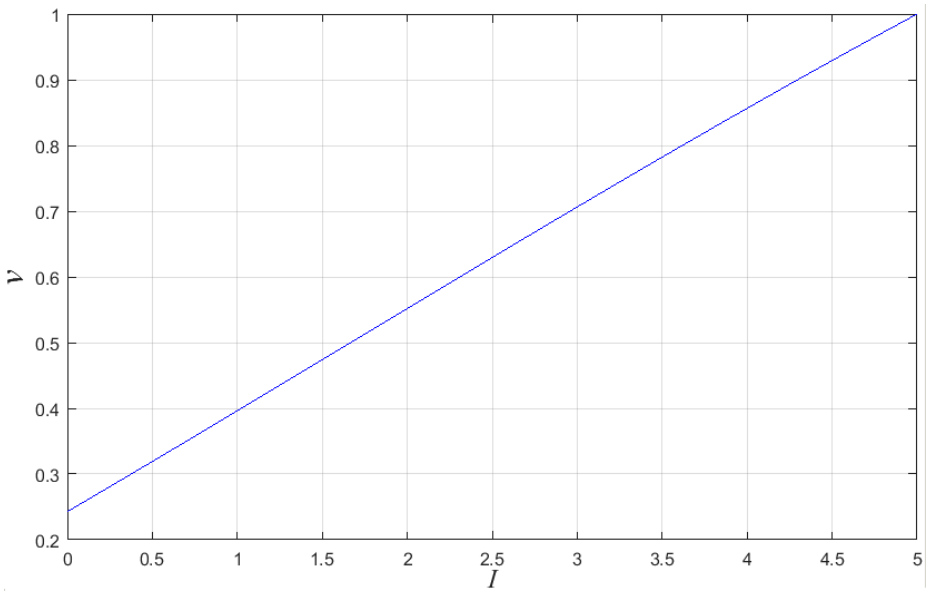

Figure 1.3: Schematic shows the non-oscillatory behavior of a single EC

plained earlier) we were motivated to model both SMCs and ECs using the same FHN equations. As previously mentioned, our intention is also here to use different values for the same parameters appearing in the FHN models given by Equations (1.2.1) and (1.2.2), corresponding to the dynamics of SMCs and ECs. Figure 1.3 illustrates a well-known dynamics that ECs are not exposed to oscillations, in contrast to the oscillatory dynamics of the SMCs. For this simulation, we have used a set of parameter values: $\nu = 0.005, \alpha = 0.5, G = 0, \gamma = 0.15$ and $p = 0.25$, which are different from the values of the same parameters used for the SMC simulation:

$\nu = 0.01, \alpha = 0.95, G = 0, \gamma = 0.12$ and $p = 0.3$. By comparing Figure 1.2(e) and Figure 1.3, we see that while the SMC predicts the oscillatory dynamics, under the application of the same FHN models given by Equations (1.2.1) and (1.2.2) the EC only shows an non-oscillatory behaviour. This shows the fact that both cells can be modelled by FHN equations and more importantly it can be done by assigning a suitable choice of parameters.

We have described the possibility of using FHN models in relation to the dynamics of the SMCs and ECs, as supported by a number of studies and results obtained from our initial simulations. In the following description, we explain the importance of variables and parameters involved in our FHN mathematical models.

1.3 Physiological Meaning of FHN Terms

It is well known that a cell membrane carries a potential across its inner and outer surface, often called as membrane potential. A basic model for a cell is that of a capacitor, C, and a resister, R, in parallel (see Figure 1.4). This model utilizes other additional components: an inductor, L, and a battery, E, in series with R and a nonlinear current source, $F(V_n)$, where n indicates an arbitrary cell. In addition to the standard FHN circuit, we introduce conductors G_n and G_{n+1} (see Figure 1.4). A detail derivation of models given by Equations (1.2.1) and (1.2.2), based on these electrical equivalents as shown in Chapter 2. The physiological meaning of each component above in relation to a possible cellular physiology is described as follows.

The capacitor models the membrane capacitance, which reflects the fact that the

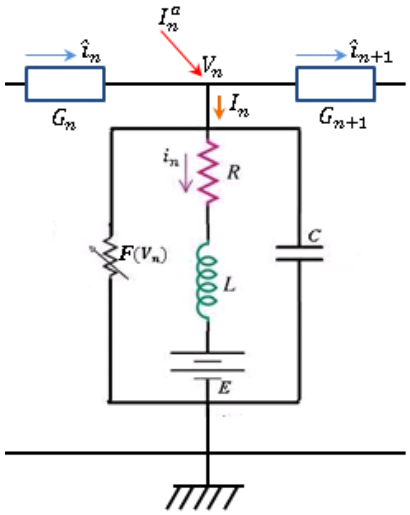

Figure 1.4: Schematic shows the modified FHN circuit for cellular coupling. Here, the subscript n indicates the n^{th} cell, and each neighboring cell is coupled through conductances G_n and G_{n+1}. The bottom end of the circuit is kept at zero potential to model the problem by an averaged unique conductance of gap junction depending on space variable

cellular membranes are good electrical insulators. There is always a current leakage out of the cell [58] and the amount of this leakage depends on the resistivity of the pathway (or ion channels of the cell). Thus, we model the resistivity of the pathway by means of the resister R and the current leakage passing through R by i_n. Moreover, when a cell is at rest in a state of dynamic equilibrium, the leakage of current is balanced by an ionic pump so that the net current in or out of the cell is zero [58]. This ionic pump may be referred to as the Nernst potential by which the potential inside the cell is kept below that of the outside at a normal state. Therefore, the potential gain across the battery E can be used to interpret the notion of the Nernst potential of the cell.

The current flow in or out of the cell is due to the movement of cations (different from the movement of electrons in conductors) and is time dependent. This notion is captured by the nonlinear time varying current source $F(V_n)$ and different forms of $F(V_n)$ are described in the previous section. Further, as previously mentioned, the rate of change of current due to ionic movement during the opening and closing of ion channels induces a recovery potential and is modelled by the inductor, L. Additionally, we introduce conductors G_n and G_{n+1} to interpret gap junctions between neighbouring cells. Therefore, currents $\hat{i}_n$ and $\hat{i}_{n+1}$ respectively model the extracellular current flowing through gap junctions modelled by G_n and G_{n+1}. We also note that an intracellular current I_n is combined as an addition of the following currents: current through the cellular membrane $C\frac{dV_n}{dt}$, the leakage current i_n and the nonlinear current $F(V_n)$. Furthermore, since SMCs are known to be excitable, we apply a current injection (external stimulus) I_n^a for their excitation. Therefore, in the interest of simplicity for a large scale cellular node to utilize FHN analogue (shown in Figure 1.4), we propose modelling the cellular communication among and between SMCs and ECs. As no experimental study for the cellular communication among and between the SMCs and ECs based on a direct application of FHN equations has yet been reported, we respectively name the SMC and EC as 'type A' and 'type B' cells, and will use these terms in the rest of the thesis.

Mathematical models of a population of type A and type B cells typically involve higher number of ODEs. For example, an artery of 1cm characteristic length and 80μm diameter consists of about 10,057 type A cells and 3,868 type B cells, based on a single type A cell's dimension 50μm$\times$5μm and a single type B's dimension

65μm$\times 10\mu$m. Hence, the system consists of a total of 13,925 cells, each of which can be modelled by coupled FHN ODEs, therefore allows 27,850 equations. Moreover, the number of cells increases as the size of the artery increases. Therefore, a system of large numbers of cells requires simulation on a distributed high performance computer to understand the communication among and between type A and type B cells. Another way to approach this problem is to use homogenisation theory to obtain a small number of partial differential equations, which will provide a mathematical understanding of obtaining macro scale behaviour. One of the goals of this project is to further develop the HPDEs derived so far into a more comprehensive and cohesive model, so as to predict the communication protocols likely to be in play between homogenic cells and, in future, between heterogenic cells. In the following section we give in general a brief description of the theory of homogenisation, which will be further followed by a short introduction in Chapter 4.

1.4 Concept of the Theory of Homogenisation

Many physical phenomena such as viscosity, diffusion, conduction, elasticity and porosity are described by different characteristics: homogeneity and heterogeneity of the medium in terms of at least two different scales, for example microscopic and macroscopic scales. The microscopic scale appears due to the occurrence of microscopic-level heterogeneities in the medium [95] and evaluation of the characteristics of the heterogeneous medium at the microscopic level is very difficult. Therefore, it is necessary to apply asymptotic analysis in a particular multiscale heterogeneous media. This immediately leads us to apply the theory of mathematical homogenisation. By applying multiple scales, we look to derive homogenised partial differential

equations (HPDEs), which govern the macroscopic structure and behaviour of the system.

Suppose that the models we are interested in one-dimension are given by a system of partial differential equations:

$$\begin{aligned} \partial_t v + \mathcal{A}v = &\quad f_1(v, w), \\ \partial_t w = &\quad f_2(v, w), \end{aligned} \tag{1.4.1}$$

where $\mathcal{A}$ is a differential operator,

$$\mathcal{A} = -\nabla(G(\boldsymbol{x})\nabla), \quad \boldsymbol{x} \in \Omega, \tag{1.4.2}$$

which describes the domain and $G(\boldsymbol{x})$ is the potential coefficient matrix, a function of spatial variable $\boldsymbol{x}$. Furthermore, $v(\boldsymbol{x}, t)$ and $w(\boldsymbol{x}, t)$ are the fast and slow variables and f_1 and f_2 are nonlinear and linear source terms, respectively, which drive the system. Furthermore, Ω is a heterogeneous domain possesses a macroscopic structure of periodic type with repeating cells of equal lengths $\varepsilon, \varepsilon \ll \ell$, where ℓ is the characteristic length of Ω in each direction. These repeating cells can be accommodated within a region by scaling up with a factor $1/\varepsilon$. This domain is further explained in 2-dimension in Figure 4.1 of Chapter 4. Note that there is no spatial derivative in w-equation of Equation (1.4.1) as w is modelled by an intercellular leakage current and it is used as a recovery potential while v is modelled by the gap-junctional current which varies spatially.

To understand the homogenisation problem let us denote the matrix of potential coefficients and the solution of the problem by G^ε and, v^ε and w^ε, respectively. We

write

$$G^{\varepsilon}(\boldsymbol{x}) = G(\boldsymbol{x}/\varepsilon), \quad \boldsymbol{x} \in \Omega, \tag{1.4.3}$$

for some Λ-periodic matrix $G(\boldsymbol{z})$, where $\boldsymbol{z} = \boldsymbol{x}/\varepsilon$, $\boldsymbol{z} \in \Lambda$ and Λ is the microscopic domain, which describe various local characteristics of the medium.

Now, let us introduce a sequence $\{\varepsilon_n\}, n \in \mathbb{Z}^+$, of positive scales such that $\varepsilon_n \to 0$ as $n \to \infty$, which attains the scale ε for some $n = n_0$. Similarly, we define a sequence $\{G_n^{\varepsilon}\}$ of coefficient matrices such that

$$G_n^{\varepsilon}(\boldsymbol{x}) = G(\boldsymbol{x}/\varepsilon_n), \quad \boldsymbol{x} \in \Omega. \tag{1.4.4}$$

Hence, the problem given by equation (1.4.1)-(1.4.4) can then be written as:

$$\begin{aligned} \partial_t v_n^{\varepsilon} - \nabla(G_n^{\varepsilon}(\boldsymbol{x})\nabla v_n^{\varepsilon}) = &\quad f_1(v_n^{\varepsilon}, w_n^{\varepsilon}), \\ \partial_t w_n^{\varepsilon} = &\quad f_2(v_n^{\varepsilon}, w_n^{\varepsilon}). \end{aligned} \tag{1.4.5}$$

The problem given by equation (1.4.5) attains a sequence $\{v_n^{\varepsilon}, w_n^{\varepsilon}\}$ of unique solutions with respect to appropriate function space such as Sobolev space.

Hence, the homogenization problem shows the possibility of achieving:

$$\begin{aligned} \partial_t v - \nabla(D\nabla v) = &\quad f_1(v, w), \\ \partial_t w = &\quad f_2(v, w), \end{aligned} \tag{1.4.6}$$

such that $G_n^{\varepsilon} \to D$ and $(v_n^{\varepsilon}, w_n^{\varepsilon}) \to (v, w)$ as $n \to \infty$. This kind of convergence is called $G-$ or $H-$convergence (see [13], [94], [95] for methods and applications).

The reaction-diffusion type system given by equation (1.4.6) can be considered for a

traveling wave solution. Many studies (see below) have proven analytically the existence and stability of reaction-diffusion equations. As it is not part of this thesis, we have left theoretical analysis such as convergence and uniqueness of our problem to be considered in future work. However, [4], [82], [103] and [108] offer studies for one-dimensional traveling wave solutions with various forms of diffusion coefficient: [30] for a two-scale convergence for sequences of function in periodic surfaces and [59] for a multiscale convergence and homogenization of parabolic problems.

In the following section we set out the goals and objectives for this study. These goals and objectives are defined based on a modelling of cellular membrane potential as a homocellular and heterocellular communication among and between a population of type A and type B cells using our FHN models, with the goal of studying the dynamics of signalling among type A cells in one and two dimensions.

1.5 Goals and Objectives of the Research

i. To develop a discrete system of ODEs for the cellular membrane potential homocellular communication between type A cells around the circumference of an arterial ring of width equal to the width of a single type A cell and to study the dynamics of that system;

ii. To develop a system of one-dimensional reaction-diffusion type models for a homocellular and heterocellular communication among and between type A and type B cells by homogenising the ring considered in i along the arterial axis;

iii. To develop a system of two-dimensional reaction-diffusion type lattice models for the homocellular and heterocellular communication among and between type

A and type B cells for the membrane potential by lifting the circumference of the arterial ring;

iv. To apply the theory of mathematical homogenisation to the one- and two-dimensional models of the type A system developed in ii and iii and to study the micro-macro phenomena of the arterial segment by deriving comprehensive homogenised partial differential equations (HPDEs) along with an effective potential variation coefficient (PVC);

v. To carry out numerical simulations to obtain spatial patterning of the cellular membrane potential in one- and two-dimensions and to study their related wave dynamics at the macroscopic level using HPDEs derived in iv;

vi. To apply the method of homotopy in MATCONT for the 1- and 2-dimensional HPDEs developed in iv to carry out a qualitative analysis as a justification of the results obtained in v.

1.6 Organisation of the Thesis

The outcomes of the goals and objectives of Section 1.5 are documented and organized in this thesis as follows:

- In Chapter 2, we attained goals i and ii, as stated. We derived a system of discrete ODES for a ring of type A cells and showed a method of developing a one-dimensional reaction-diffusion type system for both homocellular and heterocellular communication among and between type A and type B cells that used discrete cells around the arterial circumference, θ, as well as continuous cells along the arterial axis, x.

- In Chapter 3, we illustrated a step-by-step process for developing a system of both homocellular and heterocellular reaction-diffusion type models in two-dimension by lifting the arterial circumference, θ along the Cartesian direction, y. The models are derived to be continuous in $\mathbb{R}^2$. Goal iii was achieved in this chapter.

- In Chapter 4, based on our goal iv, we studied the micro-macro multiscale structure of the arterial domain by deriving a homogenised version of the homocellular one- and two-dimensional models derived in Chapters 2 and 3, respectively. For deriving HPDEs and an effective PVC, we employed the theory of mathematical homogenisation. Results of the effective potential coefficient were discussed in relation to a number of numerical examples which may be regarded as physiologically relevant models.

- In Chapter 5, we studied the dynamics of the ring of discrete type A cells by applying a continuation technique in MATCONT. One- and two-dimensional HPDEs developed in Chapter 4 for the homocellular membrane potential were also studied in relation to various spatial patterns stipulated by numerical simulations. Corresponding results and discussions about the existence of plan and rigidly rotating spiral waves and their dynamics are detailed. This chapter fulfilled our fifth goal.

- In Chapter 6 a justification for the existence of plane waves in one and two dimensions shown by numerical simulations in Chapter 5 was made by constructing homoclinic orbits. Corresponding results and discussions were also given.

- In the final section we summarized the work and results obtained for this research. This section is followed by a brief proposal for a future work on human arterial heterocellular communication between type A and type B cells, with a proposal for a new direction of research incorporating both cellular communication and cellular level pharmacokinetics.

In this thesis we have developed a reaction-diffusion type system for the cellular membrane potential in one and two dimensions for both homocellular and heterocellular communication among and between type A and type B cells. However, we have only studied the dynamics of the homocellular system and study of the heterocellular system is left as a future work.

Chapter 2

Development and Description of 1-Dimensional Models

2.1 Introduction

In this chapter we will derive one-dimensional models for both homocellular and heterocellular connections among and between a population of type A and type B cells. As described in Chapter 1, type A and type B cells model the smooth muscle cells (SMCs) and the endothelial cells (ECs), respectively.

The Figure 2.1 shows a geometry of an arterial segment consists of type A and type B cells around the circumference and along the axis of the arterial segment. This system resembles the geometry of the SMCs and ECs in the arterial segment. Length, η, of a type A cell is considered as greater than the width, ς, of type B cell. Similarly, the length, ζ, of type B cell is taken as greater than the width, δ, of type A cell. These assumptions are made based on the actual dimension of an SMC and an EC (the diameter of an EC and SMC respectively ranges from $10\mu m - 20\mu m$ and $3\mu m - 10\mu m$, whilst the length of them are respectively notified as $39\mu m - 260\mu m$ and $30\mu m - 200\mu m$ [100]). For example, in [106], diameter and length of the SMC

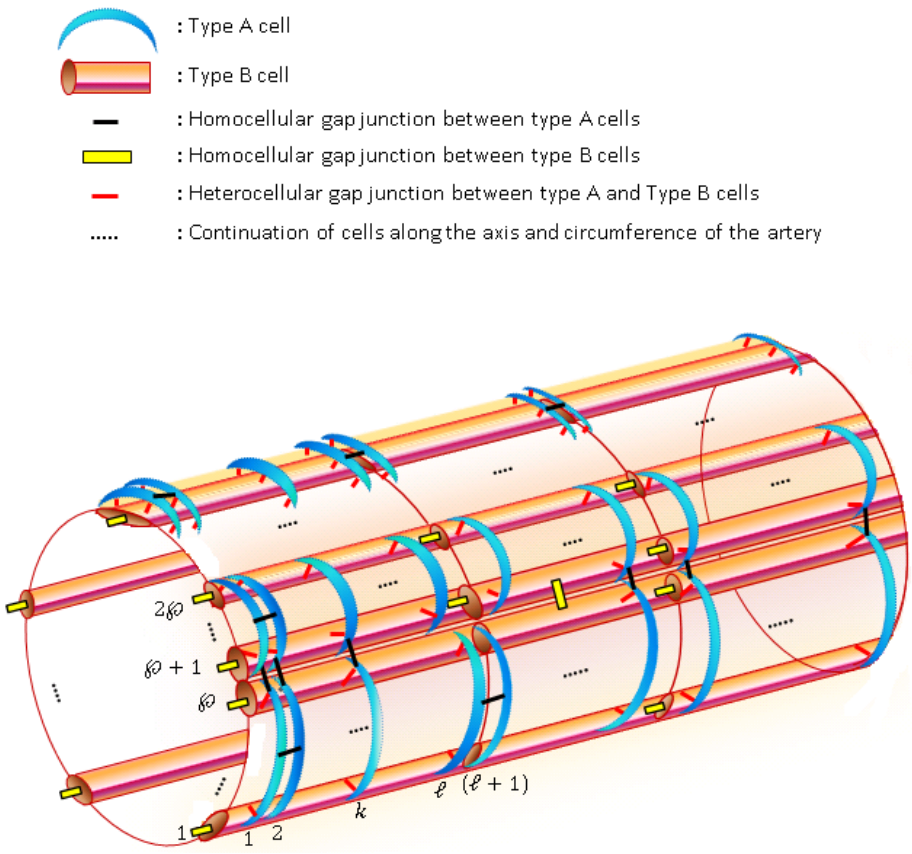

Figure 2.1: Schematic shows an arterial segment consists of type A and type B cells. Each type A cell around the circumference is connected to $\wp$ number of type B cells. Similarly each type B cell along the arterial axis is connected to ℓ number of type A cells.

were respectively chosen as $5\mu m$ and $50\mu m$, and these were $10\mu m$ and $65\mu m$ for the EC. Therefore, each EC was connected to 13 $(= \frac{65}{5} = \frac{\text{length of the EC}}{\text{width of the SMC}})$ SMCs along the arterial axis, and each SMC was connected to 5 $(= \frac{50}{10} = \frac{\text{length of the SMC}}{\text{width of the EC}})$ ECs around the circumference of the arterial segment. However, here we generalise the dimension of type A and type B cells, so that it can be used for any dimension of SMC and EC as the dimension of these cells varies with respect to different location in the human artery. Therefore, we define $\zeta = \ell\delta$ and $\eta = \wp\varsigma$, where ℓ and $\wp$ respectively denote the

number of type A cell connections with a single type B cell located in the direction of the arterial axis, and the number of type B cell connections with a single type A cell kept around the arterial circumference, see Figure 2.1. In other words, length of the type A cell is $\wp$ times greater than the width of a type B cell, and length of the type B cells is ℓ times grater than the width of a type A cell. Later on in this chapter and in the next chapter, we will choose ℓ and $\wp$ to be an odd integer to keep a structural symmetry in both axial and circumferential directions. Note that, a small spatial gap between cells in Figure 2.1 is shown only for a pictorial view. However, cells are assumed as connected via gap junctions that are fully kept within the cellular membranes.

Now, let us assume that there are m number of type A cells around the circumference of the arterial ring, and r number of type B cells along the arterial axis. Therefore, according to our assumptions about number of sharing cells in both directions, the total number of type A cells along the arterial axis is $r\ell$. Similarly, the total number of type B cells around the circumference of the artery is $m\wp$. In section 2.2, firstly we will derive discrete models for the homocellular connections between m number of type A cells of the arterial ring (similar method can be applied for the homocellular connections between $m\wp$ number of type B cells). These models will be then extended to spatial models by incorporating continuous ring of cells along the arterial axis. Similarly, in section 2.3, we will derive models for the heterocellular connections between $m \times r\ell$ number of type A cells and $m\wp \times r$ number of type B cells. Furthermore, these models will be then used to derive heterocellular spatial models of continuous cells along the arterial axis.

2.2 Derivation of Models for Homocellular Communication

This section consists of three subsections. In subsection 2.2.1, we define a set of necessary notations used in Figure 2.3 for the derivation of models. In subsection 2.2.2, as we mentioned before, we derive discrete homocellular mathematical models for the membrane potential of m number of type A cells located in the k^{th} arterial ring, see Figure 2.2, of width equals to the width of a single type A cell.

Models of a ring of finite number of cells to be developed in Section 2.2.2 can be regarded as a simple initial system (for small m, for example $m \leq 5$) to study the gap-junctional effect (coupling effect) on the system dynamics. In addition, the discretized ring of cells may be exposed with different dynamics such as helical waves when the symmetrical character is broken (we do not prove this in this research and it has been left as a future work). Therefore, we are motivated to keep discretized nature of cells around the circumference. To utilize the results of the discretized ring of cells, we consider the arterial segment to be a collection (or series) of 'continuous rings' as shown in Figure 2.2. In addition, as mentioned earlier in Section 1.1, we assume that the arterial characteristic length is much greater than that in the circumferential direction. Due to these reasons, in Section 2.2.3, we homogenise the ring of cells only along the arterial axis while keeping the discretized nature of cells around the circumference. Hence the resultant models become partially homogenised. Indeed, these purposefully designed partially homogenised models are useful for the study of cellular communication as those allow specifically to understand the spatial dynamics of the ring of discrete cells along the arterial axis (see Figure 2.2).

In Chapter 4, we consider partially homogenised one-dimensional models to study multiple scale structure of the artery based on the description and justification explained in this section.

2.2.1 Notations of Type A Cells

m: total number of cells around the circumference of the arterial ring.

n: an arbitrary cell of m cells.

V_n: membrane potential of the n^{th} cell.

G_n: conductance of gap junction connecting $(n-1)^{\text{th}}$ and n^{th} cells.

$\hat{i}_n$: current through gap junction G_n.

I_n^a: stimulus applied to the n^{th} cell.

$\hat{I}_n$: intracellular current in the n^{th} cell.

i_n: leakage current through pathways (channels) in the n^{th} cell.

$F(V_n)$: nonlinear time varying current in the n^{th} cell.

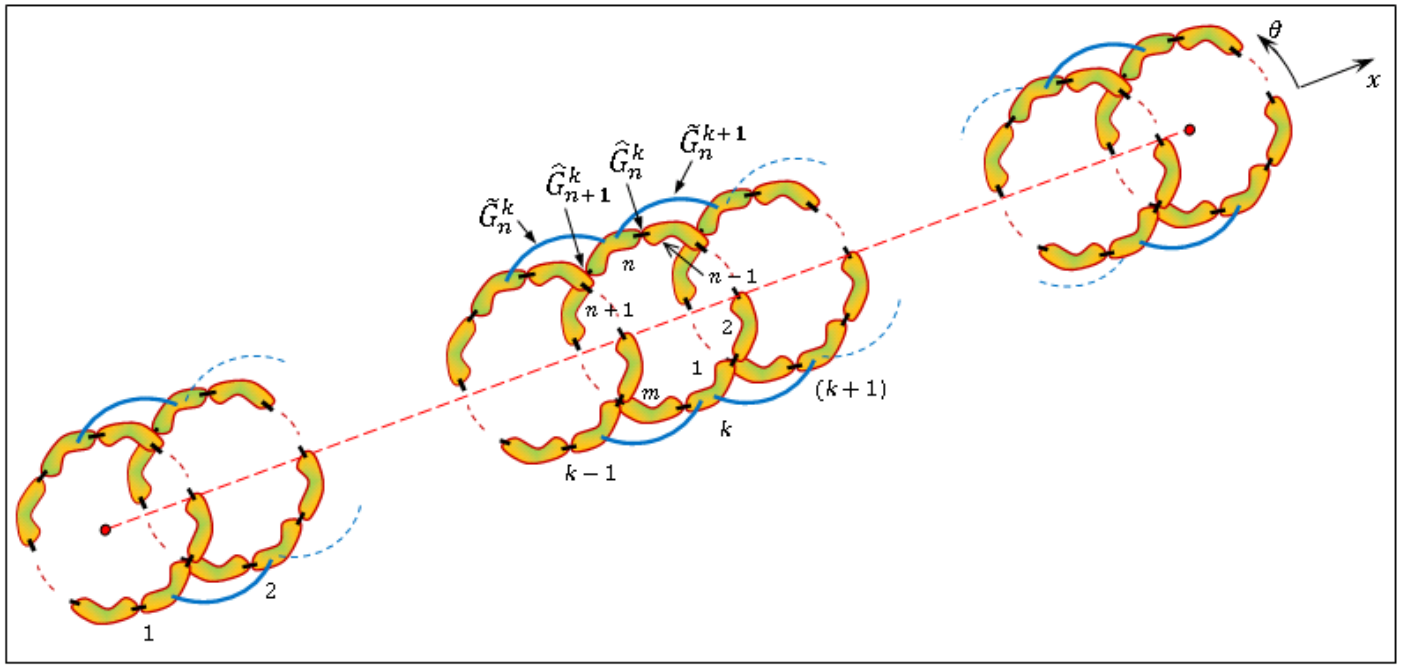

Figure 2.2: Schematic shows a series of rings of type A cells along the arterial axis, x. Indices $1, 2, \cdots, k, \cdots$ indicate the ring number. In each ring there are m number of cells around the circumferential direction, θ, of the ring. The n^{th} cell of the k^{th}-ring is modelled by considering other 2 neighboring cells, $(n-1)$ and $(n+1)$. Each cell is modeled by FHN unit as illustrated in Figure 2.3. Conductance $\widehat{G}_n^k$ and $\widehat{G}_{n+1}^k$ respectively indicate the coupling of n^{th} cell with neighbouring $(n-1)^{\text{th}}$ and $(n+1)^{\text{th}}$ cells around the circumference of the arterial ring. Similarly, the n^{th} cell of the k^{th} ring is coupled with neighboring n^{th} cell of the $(k-1)^{\text{th}}$ and $(k+1)^{th}$ cells using conductance $\widetilde{G}_n^k$ and $\widetilde{G}_n^{k+1}$, along the arterial axis

2.2.2 Derivation of Discrete Models

Modelling of the n^{th} cell of m cells in an arbitrary ring, see Figure 2.2, is shown in Figure 2.3. For this, the n^{th} cell is coupled with it's neighbouring cells, $(n-1)$ and $(n+1)$. These cells are modelled by identical FHN nonlinear oscillators.

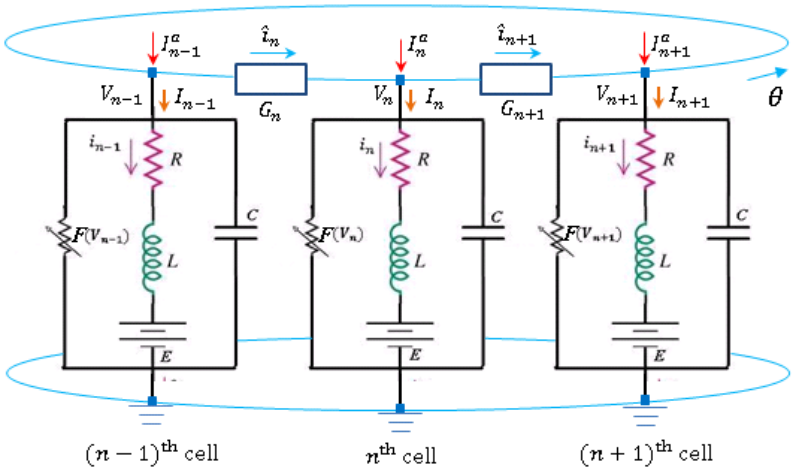

Figure 2.3: Schematic shows a horizontally placed arbitrary ring of cells, that is modelled by FHN nonlinear oscillators, where 3 arbitrary consecutive cells; $n, (n-1)$ and $(n+1)$, of ms are shown. Notations in this figure are described in section 2.2.1

By respectively applying Kirchhoff's and Ohm's laws to the n^{th} cell we have

$$\hat{i}_n - \hat{i}_{n+1} - I_n + I^a_n = 0, \tag{2.2.1}$$

$$\hat{i}_n = G_n(V_{n-1} - V_n), \quad \hat{i}_{n+1} = G_{n+1}(V_n - V_{n+1}), \tag{2.2.2}$$

Furthermore, we write for the n^{th} cell the circuit relations;

$$C\frac{dV_n}{d\tau} + i_n + F(V_n) = I_n, \tag{2.2.3}$$

$$L\frac{di_n}{d\tau} + Ri_n = V_n - E, \tag{2.2.4}$$

where τ is dimensional time, and $F(V_i) = V_i(V_i - \alpha)(1 - V_i), i = 1, \cdots, m, 0 < \alpha < 1$, interprets a nonlinear time varying current.

Now, let us assume a homogeneous coupling between the cells around the circumference of the arterial ring. Then, we set

$$G_n = G_{n+1} = \widehat{G}. \tag{2.2.5}$$

By substituting equations (2.2.2)-(2.2.5) into equation (2.2.1) we have

$$\widehat{G}(V_{n-1} - 2V_n + V_{n+1}) - \left[C\frac{dV_n}{d\tau} + i_n + F(V_n)\right] + I_n^a = 0, \tag{2.2.6}$$

$$L\frac{di_n}{d\tau} + Ri_n = V_n - E, \tag{2.2.7}$$

If we write a similar set of models given by equation (2.2.6) and (2.2.7), for the other (m-1) cells around the circumference of the arterial ring, then we have, for

$$\left.\begin{aligned}
n = 1; \quad & \widehat{G}(V_0 - 2V_1 + V_2) - \left[C\frac{dV_1}{d\tau} + i_1 + F(V_1)\right] + I_1^a = 0, \\
& L\frac{di_1}{d\tau} + Ri_1 = V_1 - E, \\
n = 2; \quad & \widehat{G}(V_1 - 2V_2 + V_3) - \left[C\frac{dV_2}{d\tau} + i_2 + F(V_2)\right] + I_2^a = 0, \\
& L\frac{di_2}{d\tau} + Ri_2 = V_2 - E, \\
\vdots & \qquad\qquad \vdots \\
n = m; \quad & \widehat{G}(V_{m-1} - 2V_m + V_{m+1}) - \left[C\frac{dV_m}{d\tau} + i_m + F(V_m)\right] + I_m^a = 0, \\
& L\frac{di_m}{d\tau} + Ri_m = V_m - E,
\end{aligned}\right\} \tag{2.2.8}$$

By applying periodic boundary conditions: $V_0 = V_m$ and $V_{m+1} = V_1$, around the circumference of the ring, equation (2.2.8) can be written as

$$C\frac{d\boldsymbol{V}}{d\tau} + \boldsymbol{i} + \boldsymbol{F}(\boldsymbol{V}) + \widehat{G}A\boldsymbol{V} = \boldsymbol{I}^a, \tag{2.2.9}$$

$$L\frac{d\boldsymbol{i}}{d\tau} + R\boldsymbol{i} = \boldsymbol{V} - \boldsymbol{E}, \tag{2.2.10}$$

where

$$A = \begin{pmatrix} 2 & -1 & 0 & \dots & 0 & -1 \\ -1 & 2 & -1 & \dots & 0 & 0 \\ \vdots & \vdots & \vdots & \dots & \vdots & \vdots \\ -1 & 0 & 0 & \dots & -1 & 2 \end{pmatrix}_{m\times m} \tag{2.2.11}$$

is a circulant matrix (a special case of Toeplitz matrix) which gives a discrete formulation of cells around the circumference, $\boldsymbol{E}$ is a constant vector, and

$$\boldsymbol{V} = [V_1 \quad V_2 \dots V_m]^T, \quad \boldsymbol{i} = [i_1 \quad i_2 \dots i_m]^T, \quad \boldsymbol{I}^a = [I_1^a \quad I_2^a \dots I_m^a]^T.$$

Now, we transform equations (2.2.9) and (2.2.10) into it's dimensionless form. Let us define

$$\begin{aligned} &\hat{V} = \max\{\hat{V}_1, \hat{V}_2, \dots, \hat{V}_m\}, \quad \hat{R} = \min\{\hat{R}_1, \hat{R}_2, \dots, \hat{R}_m\}, \\ &\boldsymbol{V} = \hat{V}\boldsymbol{v}, \qquad\qquad\qquad\qquad t = \hat{R}\tau/L, \end{aligned} \tag{2.2.12}$$

where, for all $i = 1, \dots m$, $\hat{V}_i$ is the highest stable solution of the differential equation: $\frac{dV_i}{d\tau} = -F(V_i)$, and $\hat{R}_i$ is defined by $\hat{R}_i = 1/F'(V_i)|_{V_i=0}$, see [70] for a definition of $\hat{V}$ and $\hat{R}$, for a single model. A detail description of choosing $\hat{V}$ and $\hat{R}$ is given in section 2.3.4.

By multiplying equation (2.2.9) by $\hat{R}/\hat{V}$, and by substituting equation (2.2.12) into

equations (2.2.9) and (2.2.10) we have

$$\nu \frac{d\boldsymbol{v}}{dt} = \boldsymbol{g}(\boldsymbol{v}) - GA\boldsymbol{v} - \boldsymbol{w} + \boldsymbol{I}, \tag{2.2.13}$$

$$\frac{d\boldsymbol{w}}{dt} = -\gamma \boldsymbol{w} + \boldsymbol{v} - \boldsymbol{p}, \tag{2.2.14}$$

where

$$\begin{aligned} &\boldsymbol{w} = \hat{R}\boldsymbol{i}/\hat{V}, \quad G = \hat{R}\widehat{G}, \qquad \gamma = R/\hat{R}, \quad \boldsymbol{p} = \boldsymbol{E}/\hat{V}, \\ &\boldsymbol{I} = \hat{R}\boldsymbol{I}^a/\hat{V}, \quad \nu = C\hat{R}^2/L, \quad \boldsymbol{g}(\boldsymbol{v}) = -\hat{R}\boldsymbol{F}(\boldsymbol{V})/\hat{V}, \end{aligned} \tag{2.2.15}$$

and $\boldsymbol{v}$ and $\boldsymbol{w}$ are respectively the fast (excitation) and slow (recovery) variables. Moreover, ν, G, and γ are parameters, and $\boldsymbol{p}$ is a constant vector.

From equation (2.2.13), we note the standard FHN equations are modified by an additional term, $GA\boldsymbol{v}$, that interprets homocellular coupling between discrete type A cells around the circumference of the arterial ring.

In the following section we will incorporate a spatial term with the model given by equation (2.2.13), for studying the spatial variation of the cellular membrane potential along the arterial axis. Hence, our resultant model will be a reaction-diffusion type of equation of an arterial ring consist of discrete cells around the circumference. In other words, we will have a system of equations, that will model continuous cells along the arterial axis as well as discrete cells around the circumference.

2.2.3 Derivation of Reaction-Diffusion Type Equations

As we have shown in the preceding section, each arterial ring of type A cells can be modeled by equations (2.2.13) and (2.2.14). To study the spatial variation of the membrane potential we now couple such an arterial ring with it's neighboring rings,

along the arterial axis, by connecting them using 'averaged' conductors. Therefore, these conductors model the gap junctions between cells. Note that here we emphasize the term 'average' as there are thousands of gap junctions between cells, and we model all of them by an averaged nonlinear conductor.

In Figure 2.4, three arbitrary consecutive rings, $(k-1)$, k and $(k+1)$, of ℓ number of arterial rings along the arterial axis are considered. As mentioned above, each arterial ring is spatially coupled with neighboring arterial rings, such as $\widetilde{G}_n^k$. Coupling between arterial rings is considered with respect to coupling between cells kept at the same array position in each ring, along the arterial axis, see Figure 2.4. For example, the 1^{st} cell of the k^{th} ring is coupled with the 1^{st} cell of the $(k-1)^{\text{th}}$ and $(k+1)^{\text{th}}$ rings. Similarly, the 2^{nd} cell of the k^{th} ring is coupled with the 2^{nd} cell of the $(k-1)^{\text{th}}$ and $(k+1)^{\text{th}}$ rings, and so on. Therefore, for deriving spatial models, we have considered connections between the n^{th} cells of each ring. This is done by $\widetilde{G}_n^k$, $\widetilde{G}_n^{k+1}$ and $\widetilde{G}_n^{k+1}$, which are shown by rectangular blue blocks. Similarly, discrete coupling between cells around the circumference, θ-direction, of the arterial rings are shown by rectangular purple blocks, $\widehat{G}_n^k$, etc. Other notations used in Figure 2.4 are as described below. FHN_n^k models the n^{th} cell of the k^{th} ring, and it's components:

- V_n^k: membrane potential of the n^{th} cell of the k^{th} ring,
- I_n^k: intracellular current in the n^{th} cell of the k^{th} ring,
- $I_n^{k^a}$: external stimulus applied to the n^{th} cell of the k^{th} ring,
- i_n^k: leakage current through pathways (channels) in the n^{th} cell of the k^{th} ring,
- $F(V_n^k)$: nonlinear time varying current in the n^{th} cell of the k^{th} ring.

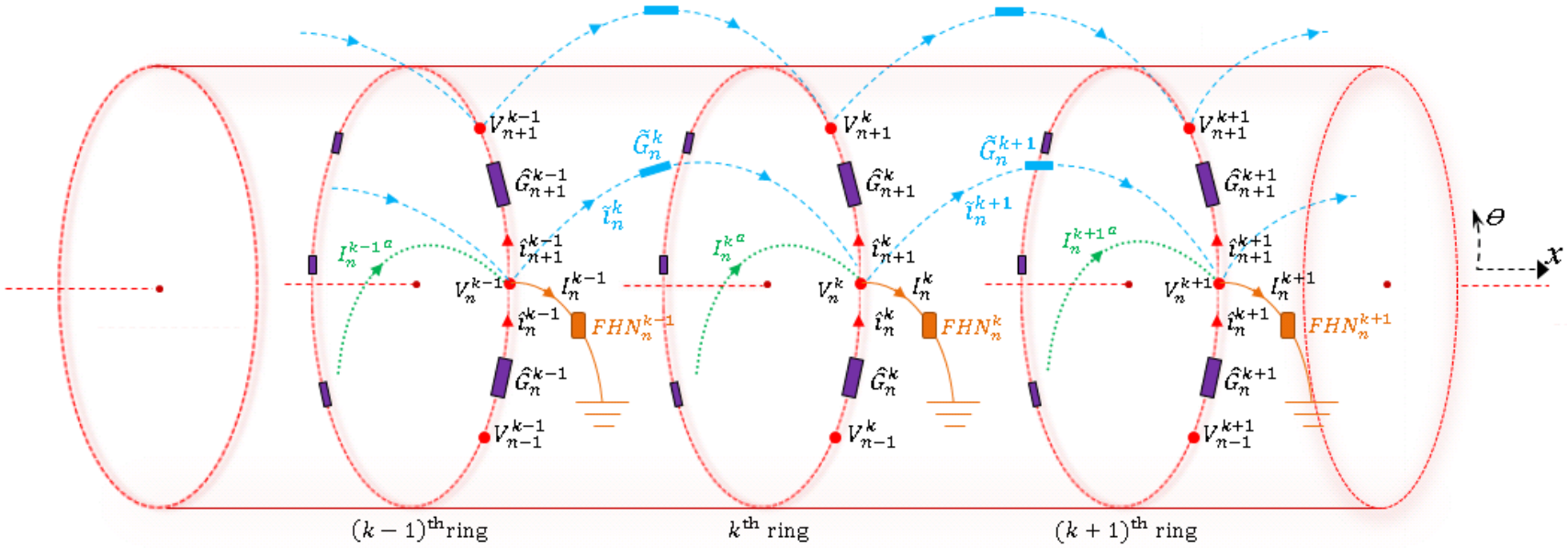

Figure 2.4: Three arbitrary rings, $(k-1)$, k and $(k+1)$, of ℓ number of type A rings are considered along the axial direction. In each ring the n^{th} cell in the θ-direction is considered for modelling. FHN blocks in orange colour are identical FHN circuits, each of them models a single cell, see Figure 2.3 for an expanded view of FHN circuit. Applied stimulus are shown by green color dotted lines. Blue and purple rectangular blocks are used to model gap junction between cells along the arterial axis and around the circumference, respectively.

Symbols for circumferential direction are assigned with the *hat*, $\widehat{*}$, sign:

- $\widehat{G}_n^k$: conductance of gap junction connecting $(n-1)^{\text{th}}$ and n^{th} cells of the k^{th} ring.
- $\hat{i}_n^k$: current through gap junction $\widehat{G}_n^k$.

Symbols for axial direction are assigned with the *tilde*, $\widetilde{*}$, sign:

- $\widetilde{G}_n^k$: conductance of gap junction connecting n^{th} cell of the $(k-1)^{\text{th}}$ and k^{th} rings.
- $\tilde{i}_n^k$: current through gap junction $\widetilde{G}_n^k$.

In Figure 2.4, by applying Kirchhoff's and Ohm's laws to the n^{th}-cell of the k^{th}-ring, we write the following relations:

$$\tilde{i}_n^{k+1} - \tilde{i}_n^k = \hat{i}_n^k - \hat{i}_{n+1}^k - I_n^k + I_n^{k^a} \tag{2.2.16}$$

$$\tilde{i}_n^k = \widetilde{G}_n^k(V_n^{k-1} - V_n^k), \quad \tilde{i}_n^{k+1} = \widetilde{G}_n^{k+1}(V_n^k - V_n^{k+1}) \tag{2.2.17}$$

$$\hat{i}_n^k = \widehat{G}_n^k(V_{n-1}^k - V_n^k), \quad \hat{i}_{n+1}^k = \widehat{G}_{n+1}^k(V_n^k - V_{n+1}^k). \tag{2.2.18}$$

As we mentioned in the previous section, let us assume that coupling between discrete cells around the circumference of the arterial ring is homogeneous. Hence, we have

$$\widehat{G}_n^k = \widehat{G}_{n+1}^k = \widehat{G}. \tag{2.2.19}$$

By substituting equation (2.2.19) into equation (2.2.18) we have

$$\hat{i}_n^k - \hat{i}_{n+1}^k = \widehat{G}(V_{n-1}^k - 2V_n^k + V_{n+1}^k). \tag{2.2.20}$$

Further, by adding the superscript k in models given by equations (5.2.1) and (2.2.4) (as the cell is now being modelled in the k^{th}-ring), we write relations for the FHN_n^k

block (see Figure 2.4),

$$C\frac{dV_n^k}{d\tau} + i_n^k + F(V_n^k) = I_n^k, \tag{2.2.21}$$

$$L\frac{di_n^k}{d\tau} + Ri_n^k = V_n^k - E. \tag{2.2.22}$$

Let $x_k = k\delta$, where k is the index of the arterial ring as mentioned before, and δ is the width of a single type A cell, be spatial points along the arterial axis.

By applying Taylor Series expansions for $\widetilde{G}_n^{k+1}, V_n^{k-1}$ and V_n^{k+1}, for the membrane potential variation in the spatial direction, we have

$$\widetilde{G}_n^{k+1}(x) = \widetilde{G}_n^k(x) + \delta\partial_x\widetilde{G}_n^k(x) + \frac{\delta^2}{2}\,\partial_x^2\widetilde{G}_n^k(x) + \cdots, \tag{2.2.23}$$

$$V_n^{k-1}(x,t) = V_n^k(x,t) - \delta\partial_x V_n^k(x,t) + \frac{\delta^2}{2}\,\partial_x^2 V_n^k(x,t) + \cdots, \tag{2.2.24}$$

$$V_n^{k+1}(x,t) = V_n^k(x,t) + \delta\partial_x V_n^k(x,t) + \frac{\delta^2}{2}\,\partial_x^2 V_n^k(x,t) + \cdots. \tag{2.2.25}$$

Now, by substituting equations (2.2.23)-(2.2.25) into equation (2.2.17) we have

$$\tilde{i}_n^k - \tilde{i}_n^{k+1} = \delta^2\widetilde{G}_n^k\partial_x^2 V_n^k + \delta^2\partial_x\widetilde{G}_n^k\partial_x V_n^k = \delta^2\frac{\partial}{\partial x}\left(\widetilde{G}_n^k(x)\,\frac{\partial V_n^k}{\partial x}\right). \tag{2.2.26}$$

By substituting equations (2.2.20)-(2.2.22) and (2.2.26) into equation (2.2.16) we have

$$\begin{aligned} C\frac{\partial V_n^k}{\partial\tau} + i_n^k + F(V_n^k) &- \widehat{G}(V_{n-1}^k - 2V_n^k + V_{n+1}^k) - I_n^{k^a} \\ &= \delta^2\frac{\partial}{\partial x}\left(\widetilde{G}_n^k(x)\,\frac{\partial V_n^k}{\partial x}\right), \end{aligned} \tag{2.2.27}$$

$$L\frac{\partial i_n^k}{d\tau} + Ri_n^k = V_n^k - E. \tag{2.2.28}$$

Since models given by equations (2.2.27) and (2.2.28) are continuous along the arterial axis, the index k is not further needed. Therefore, we will drop the spatial index k in the following derivation.

Moreover, by writing a system of similar equations for other discrete cells around the circumference of the ring, we have, for

$$\left.\begin{aligned}
n=1; \qquad C\frac{\partial V_1}{\partial \tau} + i_1 + F(V_1) - \widehat{G}(V_0 - 2V_1 + V_2) - I_1^a \\
= \delta^2 \frac{\partial}{\partial x}\left(\widetilde{G}_1(x)\ \frac{\partial V_1}{\partial x}\right), \\
L\frac{\partial i_1}{\partial \tau} + Ri_1 = V_1 - E, \\
\\
n=2; \qquad C\frac{\partial V_2}{\partial \tau} + i_2 + F(V_2) - \widehat{G}(V_1 - 2V_2 + V_3) - I_2^a \\
= \delta^2 \frac{\partial}{\partial x}\left(\widetilde{G}_2(x)\ \frac{\partial V_2}{\partial x}\right), \\
L\frac{\partial i_2}{\partial \tau} + Ri_2 = V_2 - E, \\
\vdots \qquad\qquad\qquad \vdots \\
n=m; \quad C\frac{\partial V_m}{\partial \tau} + i_m + F(V_m) - \widehat{G}(V_{m-1} - 2V_m + V_{m+1}) - I_m^a \\
= \delta^2 \frac{\partial}{\partial x}\left(\widetilde{G}_m(x)\ \frac{\partial V_m}{\partial x}\right), \\
L\frac{\partial i_m}{\partial \tau} + Ri_m = V_m - E.
\end{aligned}\right\} \tag{2.2.29}$$

By applying periodic boundary conditions: $V_0 = V_m$ and $V_{m+1} = V_1$, around the circumference, equation (2.2.29) can be written as

$$C\frac{\partial \boldsymbol{V}}{\partial \tau} + \boldsymbol{i} + \boldsymbol{F}(\boldsymbol{V}) + \widehat{G}A\,\boldsymbol{V} = \delta^2 \frac{\partial}{\partial x}\left(\widetilde{G}(x)\ \frac{\partial \boldsymbol{V}}{\partial x}\right) + \boldsymbol{I}^a, \tag{2.2.30}$$

$$L\frac{\partial \boldsymbol{i}}{\partial \tau} + R\boldsymbol{i} = \boldsymbol{V} - \boldsymbol{E}, \tag{2.2.31}$$

where $\widetilde{G}(x)$ and A are respectively given by the tensor diagonal matrix,

$$\widetilde{G}(x) = \begin{pmatrix} \widetilde{G}_1(x) & 0 & \cdots & 0 \\ 0 & \widetilde{G}_2(x) & \cdots & 0 \\ \vdots & \vdots & \ddots & \vdots \\ 0 & 0 & \cdots & \widetilde{G}_m(x) \end{pmatrix}_{m\times m}, \tag{2.2.32}$$

and by equation (2.2.11), and

$$\boldsymbol{V} = [V_1 \;\; V_2 \ldots V_m]^T, \quad \boldsymbol{i} = [i_1 \;\; i_2 \ldots i_m]^T, \;\text{ and }\; \boldsymbol{I}^a = [I_1^a \;\; I_2^a \ldots I_m^a]^T.$$

By following the same non-dimensionalization technique prescribed in the previous section, with definitions defined by equation (2.2.12), and by defining a new dimensionless form for the spatial variable; $x = lx'$, where l is the characteristic length of the arterial segment, equations (2.2.30) and (2.2.31) can be written as

$$\nu\frac{\partial \boldsymbol{v}}{\partial t} - \boldsymbol{g}(\boldsymbol{v}) + \boldsymbol{w} + GA\boldsymbol{v} = \frac{\partial}{\partial x}\left(D(x)\frac{\partial \boldsymbol{v}}{\partial x}\right) + \boldsymbol{I}, \tag{2.2.33}$$

$$\frac{\partial \boldsymbol{w}}{\partial t} + \gamma \boldsymbol{w} = \boldsymbol{v} - \boldsymbol{p}, \tag{2.2.34}$$

where $D(x)$ is a $m \times m$ diagonal tensor matrix with diagonal elements defined by dimensionless 'potential variation coefficients' (PVC); $D_i(x) = \delta^2 \hat{R}\widetilde{G}_i(x)/l^2$, $i = 1, \ldots, m$, and other parameters in equation (2.2.33) and (2.2.34) are as defined in equation (2.2.15). Note that, for keeping a usual notation, the dimensionless variable x' is again replaced by x, and therefore x is now dimensionless in equation (2.2.33).

Equation (2.2.33) is a reaction-diffusion type of equation for the membrane potential, which models the homocellular communication between both m number of of discrete cells around the circumference of the arterial ring, and an infinite number of continuous cells along the arterial axis.

Remark 2.2.1 Since the membrane potential is not physiologically diffusing, we call $D(x)$ as PVC (potential variation coefficient) instead of diffusion coefficient, that interprets the variation of the membrane potential gradient between the neighboring cells.

Remark 2.2.2 Let $D(x) = 0$. Then, the system of models given by equations (2.2.33) and (2.2.34) can be deduced to the single-ring models of type A cells, given by equations (2.2.13) and (2.2.14).

2.3 Derivation of Models for Heterocellular Communication

As mentioned in section 2.1, this section is devoted to derive models for the membrane potential of type A and type B cells coupled through heterocellular connections, see Figure 2.1. For this, we differentiate type A and type B cells using non-identical FHN models by assigning different circuit components for cells. These non-identical components allow us to define different parameters for type A and type B cells. However, connection between homocellular cells are modelled by identical electrical components as taken in section 2.2.

2.3.1 Notations and Domain Description

In this section we describe necessary notations for deriving models for type A-type B heterocellular communication. In Figure 2.5, an arbitrary $(\imath, \jmath)^{\text{th}},\ \imath = 1, \cdots, m\wp,\ \jmath = 1, \cdots, r$, type B cell in the arterial domain is regarded to get connected with an arbitrary $(n, k)^{\text{th}},\ n = 1, \cdots, m,\ k = 1, \cdots, r\ell$, type A cell, see the list of notations described in this section. Therefore, heterocellular connections between $(n, k)^{\text{th}}$ type

A cell and $(\imath, \jmath)^{\text{th}}$ type B cell are established based on the geometry illustrated in Figure 2.1. Hence, it requires further number of type A and type B cells as described in section 2.1. These connections are shown by red arrows in Figure 2.5.

As described before, since each type A cell is connected to $\wp$ number of consecutive type B cells around, the circumference the upper portion of red colour connections of gap junctional currents is kept to vary from $(n-1)\wp+1$ to $n\wp$, see Figure 2.5(a). Similarly, since each type B cell is connected to ℓ number of consecutive type A cells in the axial direction, the lower portion of red colour connections of gap junctional currents in Figure 2.5(b) is set to vary from $(\jmath-1)\ell+1$ to $\jmath\ell$. Furthermore, arrow in subscripts denotes the location of type B cell from which signals are passed through gap junctions to type A cells, see the list of notations for further meaning of sub and superscripts. Moreover, connections in green and blue colours respectively in Figure 2.5(a) and Figure 2.5(b) denote homocellular links among type A cells and among type B cells, respectively. Figure 2.5(c) shows a simplified version of heterocellular connections between type A and type B cells illustrated in Figure 2.5(a) and Figure 2.5(b). All symbols used in Figure 2.5 are defined in the following list of notations.

Cell indices:

- r: total number of type B cells along the arterial axis,
- $\jmath$: an arbitrary type B cell among r. Thus, $\jmath = 1, \ldots, r$,
- ℓ: number of type A cells coupled with a single type B cell along the axis,

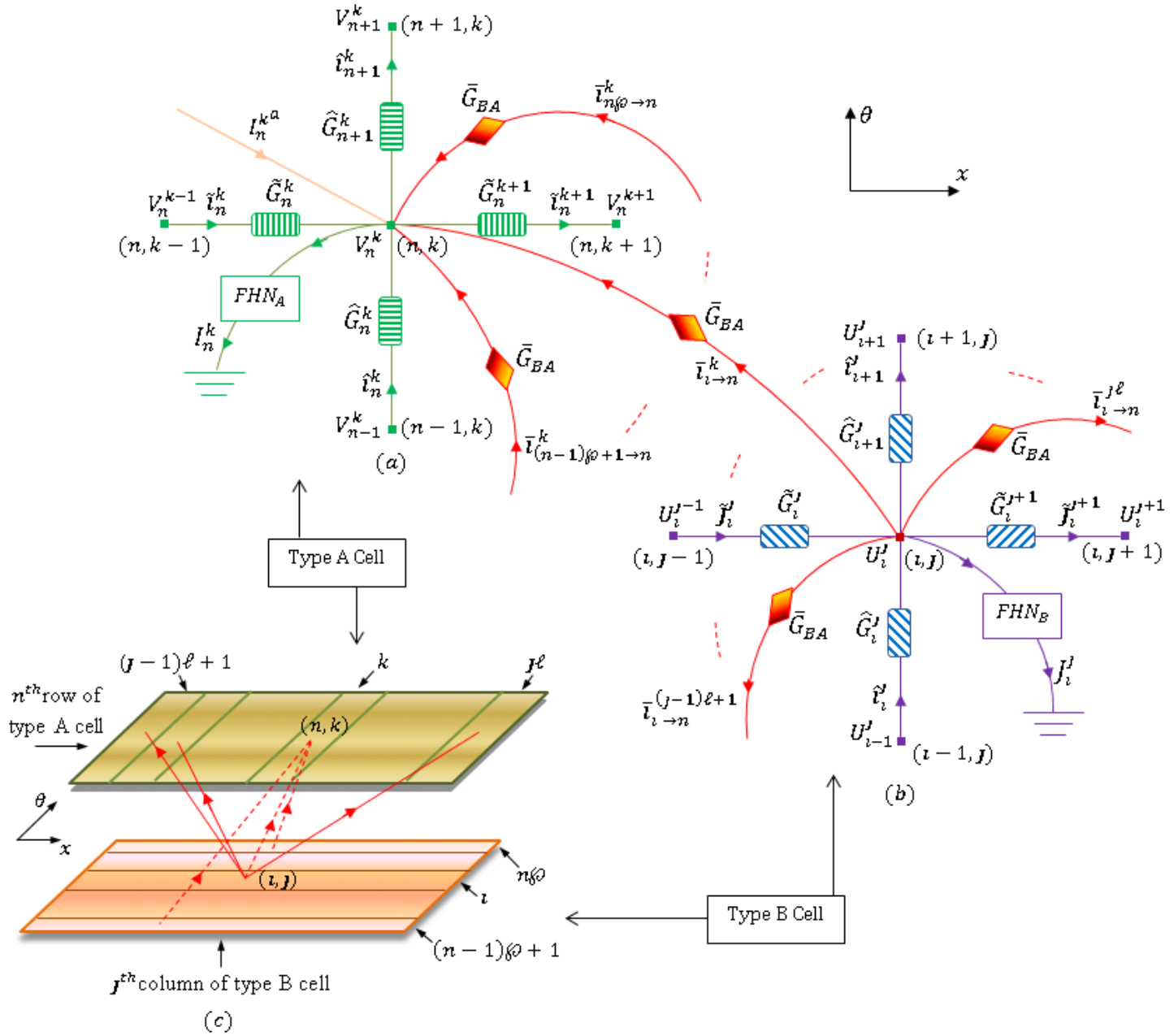

Figure 2.5: Schematic shows heterocellular connections (red in colour) between type A and type B cells in an arterial segment. An arbitrary $(n,k)^{\text{th}}$ type A cell and $(\imath,\jmath)^{\text{th}}$ type B cell in Figure (c) are respectively modelled in Figure 2.5(a) and Figure 2.5(b)

- k: an arbitrary type A cell in the axial direction. Hence, $k = 1, \ldots, r\ell$,
- m: total number of type A cells around the circumference,
- n: an arbitrary type A cell among m. Hence, $n = 1, \ldots, m$,
- $\wp$: number of type B cells coupled with a single type A cell around the circumference of the artery,
- $\imath$: an arbitrary type B cell considered around the circumferential direction. Therefore, $\imath = 1, \ldots, m\wp$.

FHN (FHN_A, FHN_B) components:

- V_n^k: membrane potential of the $(n,k)^{\text{th}}$ type A cell,
- $U_\imath^\jmath$: membrane potential of the $(\imath,\jmath)^{\text{th}}$ type B cell,
- I_n^k: intracellular current flowing in the $(n,k)^{\text{th}}$ type A cell,
- $J_\imath^\jmath$: intracellular current flowing in the $(\imath,\jmath)^{th}$ type B cell,
- $I_n^{k^a}$: external stimulus applied to the $(n,k)^{\text{th}}$ type A cell,
- $J_\imath^{\jmath^a}$: external stimulus applied to the $(\imath,\jmath)^{th}$ type B cell.

Symbols for circumferential direction are assigned with the *hat*, $\widehat{*}$, sign:

- $\widehat{G}_n^k$: nonlinear homocellular conductance of gap junction connecting $(n-1,k)^{\text{th}}$ and $(n,k)^{\text{th}}$ type A cell around the circumference,
- $\widehat{G}_\imath^\jmath$: nonlinear homocellular conductance of gap junction connecting $(\imath-1,\jmath)^{\text{th}}$ and $(\imath,\jmath)^{\text{th}}$ type B cell around the circumference,
- $\hat{\imath}_n^k$: current passing through the homocellular gap junction $\widehat{G}_n^k$,
- $\hat{\jmath}_\imath^\jmath$: current passing through the homocellular gap junction $\widehat{G}_\imath^\jmath$,

Symbols for axial direction are assigned with the *tilde*, $\widetilde{*}$, sign:

- $\widetilde{G}_n^k$: nonlinear homocellular conductance of gap junction connecting $(n, k-1)^{\text{th}}$ and $(n, k)^{\text{th}}$ type A cell along the arterial axis,
- $\widetilde{G}_\imath^\jmath$: nonlinear homocellular conductance of gap junction connecting $(\imath, \jmath-1)^{\text{th}}$ and $(\imath, \jmath)^{\text{th}}$ type B cell along the arterial axis,
- $\tilde{i}_n^k$: current passing through the homocellular gap junction $\widetilde{G}_n^k$,
- $\tilde{j}_\imath^\jmath$: current passing through the homocellular gap junction $\widetilde{G}_\imath^\jmath$,

Symbols for heterocellular connections are assigned with the *bar*, $\overline{*}$, sign:

- $\overline{G}_{BA}$: nonlinear heterocellular conductance of gap junction connecting type A and type B cells, and is assumed to be homogeneous everywhere,
- $\bar{i}_{\imath\to n}^k$: current passing through the heterocellular gap junction $\overline{G}_{BA}$, from $(\imath, \jmath)^{\text{th}}$ type B cell to $(n, k)^{\text{th}}$ type A cell.

2.3.2 Derivation of Discrete Heterocellular Models

With an understanding of notations described in section 2.3.1, and with a help of Figure 2.5, here we develop discrete models for heterocellular communication between type A and type B cells.

For this, we consider an arbitrary Type B cell in the axial direction. According to the geometry, see Figure 2.1, each type B cell in the axial direction forms an arterial ring consists of additional ($m_\wp$-1) number of discretely connected same type cells around the circumference. Hence, the total number of type B cells in a single type B ring is $m_\wp \times 1$. Since the domain has r number of type B cells along the arterial axis the total number of type B cells in the domain is $m_\wp \times r$. Each of r number of type B cells passes signals to ℓ number of type A cells, see Figure 2.5(c), along the arterial axis, and there are m number of type A cells around the circumference.

Therefore, the total number of type A cells in the domain is $m \times r\ell$. In other words, we will develop discrete models for a system of $m \times r\ell$ number of type A cells coupled with $m\wp \times r$ number of type B cells. Moreover, each of m number of type A cells is connected to $\wp$ number of type B cells around the circumference, see Figure 2.1, in their respective order. Here the respective order means that the very first p number of type B cells are coupled with the very first type A cell. Similarly, the next p number of type B cells are coupled with the second type A cell, and so on. Therefore, in general, by counting this way the n^{th} type A cell will be coupled with type B cells from $(n-1)p+1$ to np. These cells are connected via gap junctions allowing currents from $\bar{i}^k_{(n-1)\wp+1\to n}$ to $\bar{i}^k_{n\wp\to n}$ in Figure 2.5, and are taken into account for the summation appeared in equation (2.3.1) below.

2.3.2.1 Models of Type A Cells

By applying Kirchhoff's law to the $(n,k)^{th}$ type A cell in Figure 2.5, we have

$$\hat{i}^k_n - \hat{i}^k_{n+1} + \tilde{i}^k_n - \tilde{i}^{k+1}_n = I^k_n - I^{k^a}_n - \sum_{\imath=(n-1)\wp+1}^{n\wp} \bar{i}^k_{\imath\to n}, \tag{2.3.1}$$

where $n = 1, \ldots, m$, for every $k = 1, \ldots, \ell$.

By Using Ohm's law we have

$$\left.\begin{aligned} \hat{i}^k_n &= \widehat{G}^k_n(V^k_{n-1} - V^k_n), \quad \hat{i}^k_{n+1} = \widehat{G}^k_{n+1}(V^k_n - V^k_{n+1}), \\ \tilde{i}^k_n &= \widetilde{G}^k_n(V^{k-1}_n - V^k_n), \quad \tilde{i}^{k+1}_n = \widetilde{G}^{k+1}_n(V^k_n - V^{k+1}_n), \\ \bar{i}^k_{\imath\to n} &= \overline{G}_{BA}(U^j_\imath - V^k_n). \end{aligned}\right\} \tag{2.3.2}$$

Let us assume (for deriving discrete models) the coupling around the circumference as homogeneous, then we have

$$\widehat{G}^k_n = \widehat{G}^k_{n+1} = \widehat{G}_A, \quad \widetilde{G}^k_n = \widetilde{G}^{k+1}_n = \widetilde{G}_A. \tag{2.3.3}$$

where $\widehat{G}_A$ and $\widetilde{G}_A$ are now respectively the homogenous conductance of gap junctions of type A cells around the circumferential and along the axial direction of the artery.

By substituting equations (2.3.2) and (2.3.3) into equation (2.3.1) we have

$$\widehat{G}_A(V_{n-1}^k - 2V_n^k + V_{n+1}^k) + \widetilde{G}_A(V_n^{k-1} - 2V_n^k + V_n^{k+1}) + \overline{G}_{BA}\left(\sum_{\imath=(n-1)\wp+1}^{n\wp} U_\imath^\jmath - \wp V_n^k\right) = I_n^k - I_n^{k^a}. \tag{2.3.4}$$

Now, from equations (2.2.21) and (2.2.22) we have

$$C_A\frac{dV_n^k}{d\tau} + i_n^k + F_A(V_n^k) = I_n^k, \tag{2.3.5}$$

$$L_A\frac{di_n^k}{d\tau} + R_A i_n^k = V_n^k - E_A. \tag{2.3.6}$$

By comparing equations (2.3.4), (2.3.5) and (2.3.6) we have

$$\begin{aligned} C_A\frac{dV_n^k}{d\tau} + i_n^k + F_A(V_n^k) - \widehat{G}_A(V_{n-1}^k - 2V_n^k + V_{n+1}^k) & \\ -\widetilde{G}_A(V_n^{k-1} - 2V_n^k + V_n^{k+1}) + \overline{G}_{BA}\left(\wp V_n^k - \sum_{\imath=(n-1)\wp+1}^{n\wp} U_\imath^\jmath\right) &= I_n^{k^a}, \end{aligned} \tag{2.3.7}$$

$$L_A\frac{di_n^k}{d\tau} + R_A i_n^k = V_n^k - E_A. \tag{2.3.8}$$

Equations (2.3.7) and (2.3.8) represent heterocellular connection of a single type A cell (n^{th}-cell in the k^{th} ring) with $\wp$ number of type B cells (given by summation term in equation (2.3.7)) around the circumference of the arterial ring, and homocellular communication with it's neighboring type A cells around the circumferential (2^{nd} term on the left hand side of equation (2.3.7)) and along the arterial axis (3^{rd} term on the left hand side of equation (2.3.7)) directions. However, according to the geometry, there are $r\ell$ number of type A cells coupled with r number of type B cell along the axis, and there are m number of type A cells coupled with $m\wp$ number of type B cells around the circumference. Hence, we can write a set of similar equations for the rest of the (m-1)×($r\ell$-1) number of type A cells coupled with type B cells by

applying appropriate boundary conditions.

For a 1-dimensional torus, we set up periodic boundary conditions respectively along the arterial axis and around the circumference of the artery as follows:

$$V_n^0 = V_n^{r\ell}, \quad V_n^{r\ell+1} = V_n^1, \quad \forall n = 1, 2, \ldots, m, \tag{2.3.9}$$

$$V_0^k = V_m^k, \quad V_{m+1}^k = V_1^k, \quad \forall k = 1, 2, \ldots, r\ell. \tag{2.3.10}$$

Now, let us define a column vector consists of membrane potential of each cell in the domain, as follows:

$$\boldsymbol{V} = \Big(\underbrace{V_1^1\ V_1^2 \ldots V_1^{r\ell}}_{\text{for } n=1}\ \underbrace{V_2^1\ V_2^2 \ldots V_2^{r\ell}}_{\text{for } n=2}\ \ldots\ldots\ \underbrace{V_m^1\ V_m^2 \ldots V_m^{r\ell}}_{\text{for } n=m} \Big)^T_{1\times mr\ell}, \tag{2.3.11}$$

where note that the potential components are arranged by collecting terms along the arterial axis, for every type A cell in the circumferential direction. That is, for the 1^{st} type A cell in the circumferential direction the system is allowed to vary from 1 to $r\ell$ since there are $r\ell$ number of type A cells along the arterial axis. This is denoted by the 1^{st} underbrace in equation (2.3.11). Similarly, the 2^{nd} underbrace in equation (2.3.11) again denotes $r\ell$ number of cells for the 2^{nd} cell around the circumference, and so on.

For writing vector equations for the full system ($n = 1, \ldots, m$), we firstly deal with the 2^{nd} and 3^{rd} terms of the equation (2.3.7).

Hence, for $n = 1$, by applying the periodic boundary conditions given by Equations (2.3.9) and (2.3.10), to the Equation (2.3.7), we have

$$- \widehat{G}_A(V_{n-1}^k - 2V_n^k + V_{n+1}^k) - \widetilde{G}_A(V_n^{k-1} - 2V_n^k + V_n^{k+1})$$

$$= \begin{cases} 2(\widehat{G}_A + \widetilde{G}_A)V_1^1 - \widetilde{G}_A V_1^2 - \widetilde{G}_A V_1^{r\ell} - \widehat{G}_A V_2^1 - \widehat{G}_A V_m^1, & k = 1; \\ -\widetilde{G}_A V_1^1 + 2(\widehat{G}_A + \widetilde{G}_A)V_1^2 - \widetilde{G}_A V_1^3 - \widehat{G}_A V_2^2 - \widehat{G}_A V_m^2, & k = 2; \\ \vdots \qquad\qquad\qquad\qquad \vdots \qquad\qquad\qquad\qquad \vdots & \\ -\widetilde{G}_A V_1^1 - \widetilde{G}_A V_1^{r\ell-1} + 2(\widehat{G}_A + \widetilde{G}_A)V_1^{r\ell} - \widehat{G}_A V_2^{r\ell} - \widehat{G}_A V_m^{r\ell}, & k = r\ell; \end{cases}$$

$$= (\,[T_A] \quad [H_A] \quad [0] \cdots [0] \quad [H_A]\,)\,\boldsymbol{V} \tag{2.3.12}$$

where block matrices are given by

$$\left.\begin{aligned} [T_A] &= \begin{pmatrix} 2(\widehat{G}_A + \widetilde{G}_A) & -\widetilde{G}_A & 0 & \cdots & 0 & -\widetilde{G}_A \\ -\widetilde{G}_A & 2(\widehat{G}_A + \widetilde{G}_A) & -\widetilde{G}_A & \cdots & 0 & 0 \\ \vdots & \vdots & \vdots & \ddots & \vdots & \vdots \\ -\widetilde{G}_A & 0 & 0 & \cdots & -\widetilde{G}_A & 2(\widehat{G}_A + \widetilde{G}_A) \end{pmatrix}_{r\ell \times r\ell}, \\ [H_A] &= \begin{pmatrix} -\widehat{G}_A & 0 & \cdots & 0 \\ 0 & -\widehat{G}_A & \cdots & 0 \\ \vdots & \vdots & \ddots & \vdots \\ 0 & 0 & \cdots & -\widehat{G}_A \end{pmatrix}_{r\ell \times r\ell}, \quad [0_A] = \begin{pmatrix} 0 & 0 & \cdots & 0 \\ 0 & 0 & \cdots & 0 \\ \vdots & \vdots & \ddots & \vdots \\ 0 & 0 & \cdots & 0 \end{pmatrix}_{r\ell \times r\ell}. \end{aligned}\right\} \tag{2.3.13}$$

Similarly, for other ns, $n = 2, 3, \ldots, m$, by following the same way, one can be shown that block matrices in equation (2.3.12) to be circulated among them.

Hence, we have

$$- \widehat{G}_A(V_{n-1}^k - 2V_n^k + V_{n+1}^k) - \widetilde{G}_A(V_n^{k-1} - 2V_n^k + V_n^{k+1}) \tag{2.3.14}$$

$$= \begin{cases} (\,[T_A] \quad [H_A] \quad [0_A] \cdots [0_A] \quad [H_A]\,)\,\boldsymbol{V}, & n = 1; \\ (\,[H_A] \quad [T_A] \quad [H_A] \cdots [0_A] \quad [0_A]\,)\,\boldsymbol{V}, & n = 2; \\ (\,[0_A] \quad [H_A] \quad [T_A] \cdots [0_A] \quad [0_A]\,)\,\boldsymbol{V}, & n = 3; \\ \vdots \qquad\qquad\qquad\qquad \vdots \qquad\qquad\qquad\quad \vdots & \\ (\,[H_A] \quad [0_A] \quad [0_A] \cdots [H_A] \quad [T_A]\,)\,\boldsymbol{V}, & n = m. \end{cases} \tag{2.3.15}$$

$$= [P_A]\,\boldsymbol{V}, \tag{2.3.16}$$

where

$$[P_A] = \begin{pmatrix} [T_A] & [H_A] & [0_A] & \cdots & [0_A] & [H_A] \\ [H_A] & [T_A] & [H_A] & \cdots & [0_A] & [0_A] \\ \vdots & \vdots & \vdots & \ddots & \vdots & \vdots \\ [H_A] & [0_A] & [0_A] & \cdots & [T_A] & [H_A] \end{pmatrix}_{mr\ell \times mr\ell} . \tag{2.3.17}$$

Now, we will find the summing term in equation (2.3.7).

For this, let $\boldsymbol{U}$ be the vector of the form:

$$\boldsymbol{U} = \Big(\underbrace{U_1^1\ U_1^2 \ldots U_1^r}_{\text{for the } 1^{\text{st}} \text{ cell}} \ \underbrace{U_2^1\ U_2^2 \ldots U_2^r}_{\text{for the } 2^{\text{nd}} \text{ cell}} \ \ldots\ldots \ \underbrace{U_{m\wp}^1\ U_{m\wp}^2 \ldots U_{m\wp}^r}_{\text{for the } m\wp^{\text{th}} \text{ cell}} \Big)_{1 \times m\wp r}^T , \tag{2.3.18}$$

where the first underbrace denotes r number of membrane potential since there are r number of type B cells along the arterial axis, with respect to the 1^{st} type B cell around the circumference. Similarly, according to the last position of type B cell around the circumference (the $m\wp^{\text{th}}$ one) there are r number of potential components along the arterial axis, which are denoted by the last underbrace.

Therefore, for n=1, we have

$$\sum_{\imath=(n-1)\wp+1}^{n\wp} U_\imath^\jmath = \sum_{\imath=1}^{\wp} U_\imath^\jmath$$

$$= \begin{cases} (\,U_1^1 + U_2^1 + \ldots + U_\wp^1\,), & k = 1, \jmath = 1; \\ (\,U_1^1 + U_2^1 + \ldots + U_\wp^1\,), & k = 2; \\ \qquad\vdots & \qquad\vdots \\ (\,U_1^1 + U_2^1 + \ldots + U_\wp^1\,), & k = \ell; \\ \hline (\,U_1^2 + U_2^2 + \ldots + U_\wp^2\,), & k = \ell+1, \jmath = 2; \\ (\,U_1^2 + U_2^2 + \ldots + U_\wp^2\,), & k = \ell+2; \\ \qquad\vdots & \qquad\vdots \\ (\,U_1^2 + U_2^2 + \ldots + U_\wp^2\,), & k = 2\ell; \\ \hline \qquad\vdots & \qquad\vdots \\ \hline (\,U_1^r + U_2^r + \ldots + U_\wp^r\,), & k = (r-1)\ell+1, \jmath = r; \\ (\,U_1^r + U_2^r + \ldots + U_\wp^r\,), & k = (r-1)\ell+2; \\ \qquad\vdots & \qquad\vdots \\ (\,U_1^r + U_2^r + \ldots + U_\wp^r\,), & k = r\ell, \end{cases}$$

$$= \begin{cases} (\,[C1] \quad [C1]\cdots[C1] \quad [\hat{0}] \quad [\hat{0}]\cdots[\hat{0}]\cdots[\hat{0}] \quad [\hat{0}]\cdots[\hat{0}]\,)\,\boldsymbol{U}, & \jmath = 1; \\ (\,[C2] \quad [C2]\cdots[C2] \quad [\hat{0}] \quad [\hat{0}]\cdots[\hat{0}]\cdots[\hat{0}] \quad [\hat{0}]\cdots[\hat{0}]\,)\,\boldsymbol{U}, & \jmath = 2; \\ \qquad\vdots \qquad\qquad\vdots \qquad\qquad\qquad\qquad\qquad\vdots \\ (\underbrace{[Cr] \quad [Cr]\cdots[Cr]}_{\text{cells: } 1\to\wp} \quad \underbrace{[\hat{0}] \quad [\hat{0}]\cdots[\hat{0}]}_{\text{cells: } \wp+1\to 2\wp} \cdots \underbrace{[\hat{0}] \quad [\hat{0}]\cdots[\hat{0}]}_{(m-1)\wp+1\to m\wp}\,)\,\boldsymbol{U}, & \jmath = r, \end{cases} \tag{2.3.19}$$

where note that $U_\imath^\jmath$s, $\jmath = 1, \ldots, r$, vary only for every ℓ number of k values as each type B cell is coupled with ℓ number of type A cells along the arterial axis, and

$$[C\vartheta] = \begin{pmatrix} 0 & \cdots & 0 & \underset{\substack{\uparrow \\ \vartheta^{\text{th}} \\ position}}{1} & 0 & \cdots 0 \\ 0 & \cdots & 0 & 1 & 0 & \cdots 0 \\ \vdots & \cdots & \vdots & \vdots & \vdots & \cdots 0 \\ 0 & \cdots & 0 & 1 & 0 & \cdots 0 \end{pmatrix}_{\ell \times r}, \quad [\hat{0}] = \begin{pmatrix} 0 & 0 & \cdots & 0 \\ 0 & 0 & \cdots & 0 \\ \vdots & \vdots & \ddots & \vdots \\ 0 & 0 & \cdots & 0 \end{pmatrix}_{\ell \times r}. \quad (2.3.20)$$

Therefore, equation (2.3.19) can be written in the form of

$$\sum_{\imath=(n-1)\wp+1}^{n\wp} U_\imath^\jmath = (\,[1] \quad [0] \cdots [0]\,)\,\boldsymbol{U}, \quad n = 1, \quad (2.3.21)$$

where

$$[1] = \begin{pmatrix} [C1] & [C1] & \cdots & [C1] \\ [C2] & [C2] & \cdots & [C2] \\ \vdots & \vdots & \ddots & \vdots \\ [Cr] & [Cr] & \cdots & [Cr] \end{pmatrix}_{r\ell \times \wp r}, \quad [0] = \begin{pmatrix} [\hat{0}] & [\hat{0}] & \cdots & [\hat{0}] \\ [\hat{0}] & [\hat{0}] & \cdots & [\hat{0}] \\ \vdots & \vdots & \ddots & \vdots \\ [\hat{0}] & [\hat{0}] & \cdots & [\hat{0}] \end{pmatrix}_{r\ell \times \wp r}. \quad (2.3.22)$$

By following similar derivation, one can be shown that, for other ns, $n = 2, \ldots, m$, block matrices on the right hand side of the equation (2.3.21) to be circulated among them.

Thus, we have

$$\sum_{\imath=(n-1)\wp+1}^{n\wp} U_\imath^\jmath = \begin{cases} (\,[1] & [0] \cdots [0] & [0]\,)\,\boldsymbol{U}, & n = 1; \\ (\,[0] & [1] \cdots [0] & [0]\,)\,\boldsymbol{U}, & n = 2; \\ & \vdots & & \vdots \\ (\,[0] & [0] \cdots [0] & [1]\,)\,\boldsymbol{U}, & n = m; \end{cases}$$

$$= [Q_A]\,\boldsymbol{U}, \quad (2.3.23)$$

where

$$[Q_A] = \begin{pmatrix} [1] & [0] & \cdots & [0] & [0] \\ [0] & [1] & \cdots & [0] & [0] \\ \vdots & \vdots & \ddots & \vdots & \vdots \\ [0] & [0] & \cdots & [0] & [1] \end{pmatrix}_{mr\ell \times m\wp r} \tag{2.3.24}$$

Therefore, once we write for other cells, $n = 2, \ldots, m$, a set of similar equations given by (2.3.7) and (2.3.8), and by substituting equations (2.3.16) and (2.3.23) into the resultant system, we have

$$C_A \frac{d\boldsymbol{V}}{d\tau} + \boldsymbol{i} + \boldsymbol{F}_A(\boldsymbol{V}) + [P_A]\,\boldsymbol{V} + \overline{G}_{BA}(\wp \boldsymbol{V} - [Q_A]\,\boldsymbol{U}) = \boldsymbol{I}^a, \tag{2.3.25}$$

$$L_A \frac{d\boldsymbol{i}}{d\tau} + R_A \boldsymbol{i} = \boldsymbol{V} - \boldsymbol{E}_A, \tag{2.3.26}$$

where

$$\left.\begin{aligned} \boldsymbol{i} &= \Big(\underbrace{i_1^1\ i_1^2 \ldots i_1^{r\ell}}_{\text{for } n=1} \ \ldots\ldots\ \underbrace{i_m^1\ \ i_m^2 \ldots i_m^{r\ell}}_{\text{for } n=m} \Big)^T_{1\times mr\ell}, \\ \boldsymbol{I}^a &= \Big(\underbrace{I_1^{1^a}\ I_1^{2^a} \ldots I_1^{r\ell^a}}_{\text{for } n=1} \ \ldots\ldots\ \underbrace{I_m^{1^a}\ \ I_m^{2^a} \ldots I_m^{r\ell^a}}_{\text{for } n=1} \Big)^T_{1\times mr\ell}, \\ \boldsymbol{F(V)} &= \Big(\underbrace{F(V_1^1)\ F(V_1^2) \ldots F(V_1^{r\ell})}_{\text{for } n=1} \ \ldots\ \underbrace{F(V_m^1)\ \ F(V_m^2) \ldots F(V_m^{r\ell})}_{\text{for } n=m} \Big)^T_{1\times mr\ell}, \\ F(V_n^k) &= V_n^k(V_n^k - \alpha_A)(1 - V_n^k), \quad 0 < \alpha_A < 1, \quad \forall n, k, \end{aligned}\right\} \tag{2.3.27}$$

and $\boldsymbol{V}$, $[P_A]$, $\boldsymbol{U}$ and $[Q_A]$ are respectively given by equations (2.3.11), (2.3.17), (2.3.18) and (2.3.24).

Equations (2.3.25) and (2.3.26) are the heterocellular discrete models for the membrane potential of type A cells of dimension $m \times r\ell$, in which heterocellular connections between type A and type B cells are kept by modelling heterocellular gap junctions.

Conductance of such gap junctions is modeled by $\overline{G}_{BA}$, and connections are made by the term $\overline{G}_{BA}(\wp \boldsymbol{V} - [Q_A]\,\boldsymbol{U})$ in equation (2.3.25).

However, to have a complete system of models we are now required to construct another system of similar equations for type B cells since models given by equation (2.3.25) are coupled with the membrane potential of type B cells of dimension $m_\wp \times r$. This is done in the following section.

2.3.2.2 Models of Type B Cells

Here, we derive models for discrete heterocellular connections of type B cells coupled with type A cells.

By applying Kirchhoff's law to the $(\imath, \jmath)^{\text{th}}$ type B cell in Figure 2.5, we have

$$\hat{j}_i^{\jmath} - \hat{j}_{i+1}^{\jmath} + \tilde{j}_i^{\jmath} - \tilde{j}_i^{\jmath+1} = \sum_{k=(\jmath-1)\ell+1}^{\jmath\ell} \bar{\imath}_{i\to n}^{k} + J_i^{\jmath} - J_i^{\jmath^a}. \tag{2.3.28}$$

Here note that the summation in equation (2.3.28) is varied from $(\jmath-1)\ell+1$ to $\jmath\ell$ as each type B cell in the axial direction is coupled with an ℓ number of type A cells in their respective order. That is, the very first type B cell is coupled with the very first ℓ number of type A cells, and similarly, the second type B cell is coupled with the following ℓ number of type A cells, and so on. Hence, in general, the $\jmath^{\text{th}}$ type B cell along the arterial axis will be coupled with type A cells from $(\jmath-1)\ell+1$ to $\jmath\ell$.

Now, by Using Ohm's law we have

$$\left.\begin{aligned} \hat{j}_i^{\jmath} &= \widehat{G}_i^{\jmath}(U_{i-1}^{\jmath} - U_i^{\jmath}), \quad \hat{j}_{i+1}^{\jmath} = \widehat{G}_{i+1}^{\jmath}(U_i^{\jmath} - U_{i+1}^{\jmath}), \\ \tilde{j}_i^{\jmath} &= \widetilde{G}_i^{\jmath}(U_i^{\jmath-1} - U_i^{\jmath}), \quad \tilde{j}_i^{\jmath+1} = \widetilde{G}_i^{\jmath+1}(U_i^{\jmath} - U_i^{\jmath+1}), \\ \bar{\imath}_{i\to n}^{k} &= \overline{G}_{BA}(U_i^{\jmath} - V_n^{k}), \end{aligned}\right\} \tag{2.3.29}$$

where $\overline{G}_{BA}$ is the heterocellular conductance of nonlinear gap junction between type A and type B cells.

Further, for deriving discrete models, let us assume for homogeneous coupling the followings:

$$\begin{aligned} \widehat{G}_{\imath}^{\jmath} &= \widehat{G}_{\imath+1}^{\jmath} = \widehat{G}_B, \\ \widetilde{G}_{\imath}^{\jmath} &= \widetilde{G}_{\imath}^{\jmath+1} = \widetilde{G}_B, \end{aligned} \tag{2.3.30}$$

where $\widehat{G}_B$ and $\widetilde{G}_B$ are now respectively the homocellular conductance of gap junctions between type B cells in the direction of the arterial circumference and arterial axis.

By substituting equations (2.3.29) and (2.3.30) into equation (2.3.28) we have

$$\begin{aligned} \widehat{G}_B(U_{\imath-1}^{\jmath} - 2U_{\imath}^{\jmath} + U_{\imath+1}^{\jmath}) + \widetilde{G}_B(U_{\imath}^{\jmath-1} - 2U_{\imath}^{\jmath} + U_{\imath}^{\jmath+1}) \\ + \overline{G}_{BA}\left(\sum_{k=(\jmath-1)\ell+1}^{\jmath\ell} V_n^k - \ell U_{\imath}^{\jmath}\right) = J_{\imath}^{\jmath}. \end{aligned} \tag{2.3.31}$$

Note that in equation (2.3.31), n varies only for every $\wp$ number of $\imath$ values since a single type A cell is coupled with $\wp$ number of type B cells around the circumference. That is: for $\imath = 1, \ldots, \wp$, $n = 1$; for $\imath = \wp, \ldots, 2\wp$, $n = 2$; and so on. Therefore, while $\imath$ varies from 1 to $m\wp$, n will vary from 1 to m. Hence, the system models m and $m\wp$ number of type A and type B cells around the circumference of the artery, respectively.

Now, as we mentioned before, we will use for type B cells an identical set of FHN circuit models, but they differ from type A cells FHN models.

Hence, by writing for type B cells similar models given by equations (2.3.5) and (2.3.6) we have

$$C_B\frac{dU_{\imath}^{\jmath}}{d\tau} + j_{\imath}^{\jmath} + F_B(U_{\imath}^{\jmath}) = J_{\imath}^{\jmath}, \tag{2.3.32}$$

$$L_B\frac{dj_{\imath}^{\jmath}}{d\tau} + R_B j_{\imath}^{\jmath} = U_{\imath}^{\jmath} - E_B, \tag{2.3.33}$$

where note that the components C_B, L_B and E_B of type B cells are distinguished from the components C_A, L_A and E_A of type A cells. These distinguished components

separate the dynamics of type B from type A cells.

Now, by comparing equations (2.3.31), (2.3.32) and (2.3.33) we have

$$C_B\frac{dU_\imath^\jmath}{d\tau} + j_\imath^\jmath + F_B(U_\imath^\jmath) - \widehat{G}_B(U_{\imath-1}^\jmath - 2U_\imath^\jmath + U_{\imath+1}^\jmath)$$

$$-\widetilde{G}_B(U_\imath^{\jmath-1} - 2U_\imath^\jmath + U_\imath^{\jmath+1}) + \overline{G}_{BA}\left(\ell U_\imath^\jmath - \sum_{k=(\jmath-1)\ell+1}^{\jmath\ell} V_n^k\right) = J_\imath^{\jmath^a}, \qquad (2.3.34)$$

$$L_B\frac{dj_\imath^\jmath}{d\tau} + R_B j_\imath^\jmath - U_\imath^\jmath + E_B = 0. \qquad (2.3.35)$$

The system of equations (2.3.34) and (2.3.35) models heterocellular communication of a single type B cell, the $(\imath,\jmath)^{\text{th}}$ cell, with ℓ number of type A cells along the arterial axis. This is indicated by the 4^{th} term on the left hand side of equation (2.3.34). Moreover, 2^{nd} and 3^{rd} terms on the left hand side of equation (2.3.34) model homocellular communication between $(\imath,\jmath)^{\text{th}}$ cell with it's neighboring cells in both directions.

Since there are respectively $m_\wp$ and r number of type B cells around the circumference and along the axis of the artery, we will have $m_\wp \times r$ total number of similar models given by equation (2.3.34), that are coupled with a system of $m_\wp \times r$ slow variables given by equation (2.3.35). For this, we set up periodic boundary conditions along the arterial axis and around the circumferential, which are given by

$$U_\imath^0 = U_\imath^r, \qquad U_\imath^{r+1} = U_\imath^1, \quad \forall \imath = 1,2,\ldots,m_\wp, \qquad (2.3.36)$$

$$U_0^\jmath = U_{m_\wp}^\jmath, \quad U_{m_\wp+1}^\jmath = U_1^\jmath, \quad \forall \jmath = 1,2,\ldots,r. \qquad (2.3.37)$$

Now, to write models for the full system ($\imath = 1,2,\ldots,m_\wp$), as we have derived in section 2.3.2.1 we will separately find for $\imath = 1,2,\ldots,m_\wp$ the second and third, and the summing terms of equation (2.3.34). Thus, firstly for $\imath = 1$, by applying periodic boundary conditions given by (2.3.36) and (2.3.37), we have

$$- \widehat{G}_B(U_{i-1}^{\jmath} - 2U_i^{\jmath} + U_{i+1}^{\jmath}) - \widetilde{G}_B(U_i^{\jmath-1} - 2U_i^{\jmath} + U_i^{\jmath+1})$$

$$= \begin{cases} 2(\widehat{G}_B + \widetilde{G}_B)U_1^1 - \widetilde{G}_B U_1^2 - \widetilde{G}_B U_1^r - \widehat{G}_B U_2^1 - \widehat{G}_B U_{m\wp}^1, & \jmath = 1; \\ -\widetilde{G}_B U_1^1 + 2(\widehat{G}_B + \widetilde{G}_B)U_1^2 - \widetilde{G}_B U_1^3 - \widehat{G}_B U_2^2 - \widehat{G}_B U_{m\wp}^2, & \jmath = 2; \\ \vdots \qquad\qquad\qquad \vdots \qquad\qquad\qquad \vdots \\ -\widetilde{G}_B U_1^1 - \widetilde{G}_B U_1^{r-1} + 2(\widehat{G}_B + \widetilde{G}_B)U_1^r - \widehat{G}_B U_2^r - \widehat{G}_B U_{m\wp}^r, & \jmath = r; \end{cases}$$

$$= (\,[T_B] \quad [H_B] \quad [0_B] \cdots [0_B] \quad [H_B]\,)\,\boldsymbol{U}, \tag{2.3.38}$$

where $\boldsymbol{U}$ is given by equation (2.3.18), and

$$\left.\begin{aligned} [T_B] &= \begin{pmatrix} 2(\widehat{G}_B + \widetilde{G}_B) & -\widetilde{G}_B & 0 & \cdots & 0 & -\widetilde{G}_B \\ -\widetilde{G}_B & 2(\widehat{G}_B + \widetilde{G}_B) & -\widetilde{G}_B & \cdots & 0 & 0 \\ \vdots & \vdots & \vdots & \ddots & \vdots & \vdots \\ -\widetilde{G_B} & 0 & 0 & \cdots & -\widetilde{G}_B & 2(\widehat{G}_B + \widetilde{G}_B) \end{pmatrix}_{r\times r}, \\ [H_B] &= \begin{pmatrix} -\widehat{G}_B & 0 & \cdots & 0 \\ 0 & -\widehat{G}_B & \cdots & 0 \\ \vdots & \vdots & \ddots & \vdots \\ 0 & 0 & \cdots & -\widehat{G}_B \end{pmatrix}_{r\times r}, \quad [0_B] = \begin{pmatrix} 0 & 0 & \cdots & 0 \\ 0 & 0 & \cdots & 0 \\ \vdots & \vdots & \ddots & \vdots \\ 0 & 0 & \cdots & 0 \end{pmatrix}_{r\times r}, \end{aligned}\right\} \tag{2.3.39}$$

Note that matrices in equations (2.3.13) and (2.3.39) differ only by their dimension. In the first case the dimension of matrices was $r\ell$, and it is r in this latter case, since there are respectively $r\ell$ number of type A and r number of type B cells exist along the arterial axis.

If we write for other $(m\wp - 1)$ type B cells; that is, $\imath = 2, \ldots, m\wp$, around the

circumference similar models of type given by equation (2.3.38), then we have

$$
\begin{aligned}
&- \widehat{G}_A(V_{n-1}^k - 2V_n^k + V_{n+1}^k) - \widetilde{G}_A(V_n^{k-1} - 2V_n^k + V_n^{k+1}) \\
&= \begin{cases}
([T_B] \quad [H_B] \quad [0_B] \cdots [0_B] \quad [H_B])\,\boldsymbol{U}, & \imath = 1; \\
([H_B] \quad [T_B] \quad [H_B] \cdots [0_B] \quad [0_B])\,\boldsymbol{U}, & \imath = 2; \\
([0_B] \quad [H_B] \quad [T_B] \cdots [0_B] \quad [0_B])\,\boldsymbol{U}, & \imath = 3; \\
\quad \vdots \qquad\qquad\qquad \vdots \qquad\qquad\quad \vdots & \\
([H_B] \quad [0_B] \quad [0_A] \cdots [H_B] \quad [T_B])\,\boldsymbol{U}, & \imath = m\wp.
\end{cases} \\
&= [P_B]\,\boldsymbol{U}, \qquad (2.3.40)
\end{aligned}
$$

where

$$
[P_B] = \begin{pmatrix}
[T_B] & [H_B] & [0] & \cdots & [0] & [H_B] \\
[H_B] & [T_B] & [H_B] & \cdots & [0] & [0] \\
\vdots & \vdots & \vdots & \ddots & \vdots & \vdots \\
[H_B] & [0] & [0] & \cdots & [H_B] & [T_B]
\end{pmatrix}_{m\wp r \times m\wp r} . \qquad (2.3.41)
$$

Now, we will find a relation for the summing term of equation (2.3.34). Note that for every $\imath = 1, 2, \ldots, m\wp$ around the circumference, $\jmath$ takes values from 1 to r along the arterial axis.

Thus; for $\imath = 1$, $n = 1$, we have

$$
\sum_{k=(\jmath-1)\ell+1}^{\jmath\ell} V_n^k = \begin{cases}
V_1^1 + V_1^2 + \ldots + V_1^\ell, & \jmath = 1; \\
V_1^{\ell+1} + V_2^{\ell+2} + \ldots + V_1^{2\ell}, & \jmath = 2; \\
\qquad \vdots & \qquad \vdots \\
V_1^{(r-1)\ell+1} + V_1^{(r-1)\ell+2} + \ldots + V_1^{r\ell}, & \jmath = r;
\end{cases}
$$

$$
= ([L] \quad [0] \cdots [0])_{r \times mr\ell}\,\boldsymbol{V} \qquad (2.3.42)
$$

where $\boldsymbol{V}$ is given by equation (2.3.11), and

$$[L] = \begin{pmatrix} \underbrace{1\ 1\ldots1}_{\ell \text{ times}} & \underbrace{0\ 0\ldots0}_{\ell \text{ times}} & \cdots & \underbrace{0\ 0\ldots0}_{\ell \text{ times}} \\ \underbrace{0\ 0\ldots0}_{\ell \text{ times}} & \underbrace{1\ 1\ldots1}_{\ell \text{ times}} & \cdots & \underbrace{0\ 0\ldots0}_{\ell \text{ times}} \\ \vdots & \vdots & \ddots & \vdots \\ \underbrace{0\ 0\ldots0}_{\ell \text{ times}} & \underbrace{0\ 0\ldots0}_{\ell \text{ times}} & \cdots & \underbrace{1\ 1\ldots1}_{\ell \text{ times}} \end{pmatrix}_{r\times r\ell}, \tag{2.3.43}$$

and $[0]$ is a matrix of the same dimension of $[L]$, $r \times r\ell$, with all elements zero.

Note that we have fixed $n = 1$ as it changes only for every $\wp$ values of $\imath$ since a single type A cell is coupled with $\wp$ number of type B cells around the circumference. Therefore, the summation does not change until $\imath = \wp + 1$ for which $n = 2$, and hence we will have exactly the same relation for all $\imath = 1, \ldots, \wp$, given by equation (2.3.42).

Therefore, from equation (2.3.42), we have

$$\sum_{k=(\jmath-1)\ell+1}^{\jmath\ell} V_n^k = [I1]\,\boldsymbol{V}, \quad \imath = 1, \ldots, \wp, \tag{2.3.44}$$

where

$$[I1] = \begin{pmatrix} [L] & [0] & \cdots & [0] \\ [L] & [0] & \cdots & [0] \\ \vdots & \vdots & \ddots & \vdots \\ [L] & [0] & \cdots & [0] \end{pmatrix}_{\wp r\times mr\ell}. \tag{2.3.45}$$

Similarly for the next set of $\imath$ values, that is, $\imath = \wp + 1, \ldots, 2\wp$ and $n = 2$, we observe that $[L]$ matrices in equation (2.3.45) to be moved to the second column (and hence, we name that matrix as $[I2]$), and so on for other set of $\wp$ values of $\imath$.

Therefore, for $\imath = 1, \ldots, m\wp$, we have

$$\sum_{k=(\jmath-1)\ell+1}^{\jmath\ell} V_n^k = \begin{cases} [I1]\,\boldsymbol{V}, & \imath = 1, \ldots, \wp; \\ [I2]\,\boldsymbol{V}, & \imath = \wp+1, \ldots, 2\wp; \\ \vdots & \vdots \\ [Im]\,\boldsymbol{V}, & \imath = (m-1)\wp+1, \ldots, m\wp. \end{cases}$$

$$= [Q_B]\,\boldsymbol{U}, \tag{2.3.46}$$

where

$$[Q_B] = \begin{pmatrix} [I1] \\ [I2] \\ \vdots \\ [Im] \end{pmatrix}_{mpr\times mr\ell}, \quad [I\Theta] = \begin{pmatrix} 0 & \cdots & 0 & [L] & 0 & \cdots 0 \\ 0 & \cdots & 0 & [L] & 0 & \cdots 0 \\ \vdots & \cdots & \vdots & \vdots & \vdots & \cdots 0 \\ 0 & \cdots & 0 & [L] & 0 & \cdots 0 \end{pmatrix}_{pr\times mr\ell}. \tag{2.3.47}$$

$$\uparrow$$
$$\Theta^{\text{th}}$$
$$position$$

and $\Theta = 1, 2, \ldots, m$.

Thus, by writing for all $m\wp$ number of type B cells around the circumference a set of similar models given by equations (2.3.34) and (2.3.35), and by substituting equations (2.3.40) and (2.3.46) into the resultant set of equations, we have

$$C_B\frac{d\,\boldsymbol{U}}{d\tau} + \boldsymbol{j} + \boldsymbol{F}_B(\,\boldsymbol{U}) + [P_B]\,\boldsymbol{U} + \overline{G}_{BA}(\ell\,\boldsymbol{U} - [Q_B]\,\boldsymbol{V}) \;\; = \boldsymbol{J}^a, \tag{2.3.48}$$

$$L_B\frac{d\boldsymbol{j}}{d\tau} + R_B\boldsymbol{j} - \boldsymbol{U} + \boldsymbol{E}_B \;\; = 0, \tag{2.3.49}$$

where $\boldsymbol{V}, \boldsymbol{U}, [P_B]$ and $[Q_B]$ are respectively given by equations (2.3.11), (2.3.18), (2.3.41) and (2.3.47), and

$$
\left.
\begin{aligned}
\boldsymbol{j} &= [\underbrace{j_1^1 \;\; j_1^2 \cdots j_1^r}_{1^{\text{st}}\text{ type B cell}}, \cdots\cdots, \underbrace{j_{m\wp}^1 \;\; j_{m\wp}^2 \cdots j_{m\wp}^r}_{m\wp^{\text{th}}\text{ type B cell}}]_{1\times m\wp r}^T, \\
\boldsymbol{J}^a &= [\underbrace{J_1^{1^a} \;\; J_1^{2^a} \cdots J_1^{r_a}}_{1^{\text{st}}\text{ type B cell}}, \cdots\cdots, \underbrace{J_{m\wp}^{1^a} \;\; J_{m\wp}^{2^a} \cdots J_{m\wp}^{r^a}}_{m\wp^{\text{th}}\text{ type B cell}}]_{1\times m\wp r}^T, \\
\boldsymbol{F}_B(\boldsymbol{U}) &= [\underbrace{F(U_1^1) \;\; F(U_1^2) \cdots F(U_1^r)}_{1^{\text{st}}\text{ type B cell}}, \cdots\cdots, \underbrace{F(U_{m\wp}^1) \;\; F(U_{m\wp}^2) \cdots F(U_{m\wp}^r)}_{m\wp^{\text{th}}\text{ type B cell}}]_{1\times m\wp r}^T, \\
F(U_i^\jmath) &= U_i^\jmath(U_i^\jmath - \alpha_B)(1 - U_i^\jmath), \quad 0 < \alpha_B < 1, \ \forall \imath, \jmath.
\end{aligned}
\right\} \tag{2.3.50}
$$

Hence, from equations (2.3.25), (2.3.26), (2.3.48) and (2.3.49), we have the following system of coupled discrete models for the heterocellular communication between type A and type B cells:

$$C_A \frac{d\boldsymbol{V}}{d\tau} + \boldsymbol{i} + \boldsymbol{F}_A(\boldsymbol{V}) + [P_A]\boldsymbol{V} + \overline{G}_{BA}(\wp \boldsymbol{V} - [Q_A]\boldsymbol{U}) - \boldsymbol{I}^a = 0, \tag{2.3.51}$$

$$C_B \frac{d\boldsymbol{U}}{d\tau} + \boldsymbol{j} + \boldsymbol{F}_B(\boldsymbol{U}) + [P_B]\boldsymbol{U} + \overline{G}_{BA}(\ell \boldsymbol{U} - [Q_B]\boldsymbol{V}) - \boldsymbol{J}^a = 0, \tag{2.3.52}$$

$$L_A \frac{d\boldsymbol{i}}{d\tau} + R_A \boldsymbol{i} - \boldsymbol{V} + \boldsymbol{E}_A = 0, \tag{2.3.53}$$

$$L_B \frac{d\boldsymbol{j}}{d\tau} + R_B \boldsymbol{j} - \boldsymbol{U} + \boldsymbol{E}_B = 0. \tag{2.3.54}$$

Note that heterocellular coupling between type A and B cells in equations (2.3.51) and (2.3.52) is represented by terms $\overline{G}_{BA}(\wp \boldsymbol{V} - [Q_A]\boldsymbol{U})$ and $\overline{G}_{BA}(\ell \boldsymbol{U} - [Q_B]\boldsymbol{V})$, where $\overline{G}_{BA}$ is the heterocellular coupling coefficient that models the heterocellular gap junctions between type A and type B cells.

The above heterocellular system can be deduced to the ones of homocellular system and a single ring model in their respective domain. These are summarized in the following remarks.

Remark 2.3.1. Let $\overline{G}_{BA} = 0$. Then, models given by equations (2.3.51) and (2.3.53) can be deduced to models of a system of homocellular discrete type A cells of dimension $m \times r\ell$. Thus, we have

$$C_A \frac{d\boldsymbol{V}}{d\tau} + \boldsymbol{i} + \boldsymbol{F}_A(\boldsymbol{V}) + [P_A]\boldsymbol{V} = \boldsymbol{I}^a, \tag{2.3.55}$$

$$L_A \frac{d\boldsymbol{i}}{d\tau} + R_A \boldsymbol{i} = \boldsymbol{V} - \boldsymbol{E}_A. \tag{2.3.56}$$

where $[P_A]$ is a matrix of dimension $mr\ell \times mr\ell$, given by equation (2.3.17) which models homocellular connections between $mr\ell$ number of type A cells. Indeed, models given by equations (2.3.55) and (2.3.56) are an extension of the single ring homocellular models given by equations (2.2.9) and (2.2.10). To show this, we check these models with models given by equations (2.2.9) and (2.2.10), for their consistency. This is done in the following remark.

Similarly, models of a system of homocellular discrete type B cells of dimension $m\wp \times r$ can be obtained by setting again the heterocellular coupling coefficient $\overline{G}_{BA} = 0$, in equation (2.3.52). Hence, from equations (2.3.52) and (2.3.54), we have

$$C_B \frac{d\boldsymbol{U}}{d\tau} + \boldsymbol{j} + \boldsymbol{F}_B(\boldsymbol{U}) + [P_B]\boldsymbol{U} = \boldsymbol{J}^a, \tag{2.3.57}$$

$$L_B \frac{d\boldsymbol{j}}{d\tau} + R_B \boldsymbol{j} = \boldsymbol{U} - \boldsymbol{E}_B, \tag{2.3.58}$$

where $[P_B]$ is a matrix of dimension $m\wp r \times m\wp r$, and is given by equation (2.3.41).

Remark 2.3.2. To get for type A cells the single ring models given by equations (2.2.9) and (2.2.10) from equations (2.3.55) and (2.3.56), set the coupling coefficient between the cells along the arterial axis to be $\widetilde{G}_A = 0$, and the number of cells along the arterial axis as $r\ell = 1$.

Then, the matrices $[T_A], [H_A]$ and $[0_A]$ given by equation (2.3.13) can be written as follows:

$$[T_A] = \begin{pmatrix} 2(\widehat{G}_A + \widetilde{G}_A) & -\widetilde{G}_A & 0 & \cdots & 0 & -\widetilde{G}_A \\ -\widetilde{G}_A & 2(\widehat{G}_A + \widetilde{G}_A) & -\widetilde{G}_A & \cdots & 0 & 0 \\ \vdots & \vdots & \vdots & \ddots & \vdots & \vdots \\ -\widetilde{G}_A & 0 & 0 & \cdots & -\widetilde{G}_A & 2(\widehat{G}_A + \widetilde{G}_A) \end{pmatrix}_{r\ell \times r\ell}$$

$$\to [2(\widehat{G}_A + \widetilde{G}_A)]_{1\times 1}$$

$$= 2\widehat{G}_A, \tag{2.3.59}$$

and

$$[H_A] = \begin{pmatrix} -\widehat{G}_A & 0 & \cdots & 0 \\ 0 & -\widehat{G}_A & \cdots & 0 \\ \vdots & \vdots & \ddots & \vdots \\ 0 & 0 & \cdots & -\widehat{G}_A \end{pmatrix}_{r\ell \times r\ell}, \qquad [0_A] = \begin{pmatrix} 0 & 0 & \cdots & 0 \\ 0 & 0 & \cdots & 0 \\ \vdots & \vdots & \ddots & \vdots \\ 0 & 0 & \cdots & 0 \end{pmatrix}_{r\ell \times r\ell}$$

$$\to [-\widehat{G}_A]_{1\times 1} \qquad \to [0]_{1\times 1}$$

$$= -\widehat{G}_A, \qquad = 0. \tag{2.3.60}$$

By substituting equations (2.3.56) and (2.3.60) into equation (2.3.17) we have

$$[P_A] = \begin{pmatrix} [T_A] & [H_A] & [0_A] & \cdots & [0_A] & [H_A] \\ [H_A] & [T_A] & [H_A] & \cdots & [0_A] & [0_A] \\ \vdots & \vdots & \vdots & \ddots & \vdots & \vdots \\ [H_A] & [0_A] & [0_A] & \cdots & [H_A] & [T_A] \end{pmatrix}_{mr\ell \times mr\ell}$$

$$\to \widehat{G}_A \begin{pmatrix} 2 & -1 & 0 & \cdots & 0 & -1 \\ -1 & 2 & -1 & \cdots & 0 & 0 \\ \vdots & \vdots & \vdots & \ddots & \vdots & \vdots \\ -1 & 0 & 0 & \cdots & 1 & 2 \end{pmatrix}_{m\times m} = G[A], \tag{2.3.61}$$

where $[A]$ is given by equation (2.2.11).

Thus, we have deduced homocellular coupling matrix $[P_A]$ of dimension $mr\ell \times mr\ell$ to homocellular matrix $[A]$ of dimension of $m \times m$, the matrix for the single ring. This proves the result. A similar proof can be shown for type B cells.

From *Remark 2.3.1* and *Remark 2.3.2* we have shown the deduction of heterocellular discrete system into homocellular discrete system, and is followed by the single ring model of circumferentially coupled discrete cells. These confirm the consistency of our models that can be applied at any situation based on the geometry.

Remark 2.3.3 Non-dimensional form of the system given by equations (2.3.51)-(2.3.54) can be shown by following the detail method of non-dimensionalization described in section 2.3.4, as follows:

$$\nu_A \frac{d\boldsymbol{v}}{dt} + \boldsymbol{w} - \boldsymbol{g}_A(\boldsymbol{v}) + [\mathbb{P}_A]\boldsymbol{v} + G_{BA}(\wp \boldsymbol{v} - [Q_A]\boldsymbol{u}) = \boldsymbol{I}, \tag{2.3.62}$$

$$\nu_B \frac{d\boldsymbol{u}}{dt} + \boldsymbol{z} - \boldsymbol{g}_B(\boldsymbol{u}) + [\mathbb{P}_B]\boldsymbol{u} + G_{BA}(\ell \boldsymbol{u} - [Q_B]\boldsymbol{v}) = \boldsymbol{J}, \tag{2.3.63}$$

$$\frac{d\boldsymbol{w}}{dt} + \gamma_A \boldsymbol{w} = \boldsymbol{v} - \boldsymbol{p}_A, \tag{2.3.64}$$

$$\frac{d\boldsymbol{z}}{dt} + \gamma_B \boldsymbol{z} = \boldsymbol{u} - \boldsymbol{p}_B, \tag{2.3.65}$$

where $[\mathbb{P}_A] = \tilde{R}[P_A]$ and $[\mathbb{P}_B] = \tilde{R}[P_B]$, see section 2.3.4 for definitions of all non-dimensional variables and parameters, and for the method of non-dimensionalization.

In the following section we will drive a system of reaction-diffusion type of equations for heterocellular connections between type A and type B cells, by using equations (2.3.62)-(2.3.65).

2.3.3 Derivation of Reaction-Diffusion Type Equations

In this section, we will introduce a spatial variable in the direction of the arterial axis whilst the discrete behaviour around the circumference of the artery has been kept unchanged. In other words, cells around the circumference are discrete as well as

they are continuous in the axial direction. This will reduce the order of complexity of the system given by equations (2.3.62)-(2.3.65) by a considerable amount while it will capture the same dynamics of the original system. Hence, we treat the resultant system as a 1-dimensional one as it is modelled with a unique spatial variable, and simultaneously, it captures a cylindrical geometry as cells are discrete around the circumference and are assigned with the period boundary conditions:

$$V_0^k = V_m^k, \qquad V_{m+1}^k = V_1^k, \quad \forall k = 1, \ldots, r\ell; \tag{2.3.66}$$

$$U_0^\jmath = V_{m\wp}^\jmath, \quad U_{m\wp+1}^\jmath = U_1^k, \quad \forall \jmath = 1, \ldots, r, \tag{2.3.67}$$

Hence, for this, we respectively treat the coupling coefficients in the circumferential and axial direction as homogenous and inhomogeneous. Thus, from equations (2.3.3) and (2.3.30), for homogeneity, we have

$$\widehat{G}_n^k = \widehat{G}_{n+1}^k = \widehat{G}_A, \tag{2.3.68}$$

$$\widehat{G}_\imath^\jmath = \widehat{G}_{\imath+1}^\jmath = \widehat{G}_B. \tag{2.3.69}$$

Further, since the coupling coefficients of type A and type B cells along the arterial axis are inhomogeneous (due to the assumption), by applying Taylor's series expansion we have

$$\widetilde{G}_n^{k+1}(x') = \widetilde{G}_n^k + \delta \partial_{x'} \widetilde{G}_n^k + \frac{\delta^2}{2} \partial_{x'}^2 \widetilde{G}_n^k + \cdots, \tag{2.3.70}$$

$$\widetilde{G}_\imath^{\jmath+1}(x'') = \widetilde{G}_\imath^\jmath + \zeta \partial_{x''} \widetilde{G}_\imath^\jmath + \frac{\zeta^2}{2} \partial_{x''}^2 \widetilde{G}_\imath^\jmath + \cdots, \tag{2.3.71}$$

where δ and ζ are respectively width of type A cell and length of type B cell. Further, each spatial point in the type A and type B cell's domain is respectively defined by

$$x' = h\delta, \quad x'' = h\zeta, \quad h = 1, 2, \ldots. \tag{2.3.72}$$

Note that we will write different length scales x' and x'' into a unique length scale x later in this derivation.

Since the membrane potential varies in the spacial direction, again by using Taylor series, we have

$$\left.\begin{aligned} V_n^{k-(\frac{\ell-1}{2})}(x',t) &= V_n^k - \left(\frac{\ell-1}{2}\right)\delta\partial_{x'}V_n^k + \left(\frac{\ell-1}{2}\right)^2\frac{\delta^2}{2}\,\partial_{x'}^2V_n^k - \cdots, \\ &\vdots \\ V_n^{k-1}(x',t) &= V_n^k - \delta\partial_{x'}V_n^k + \frac{\delta^2}{2}\,\partial_{x'}^2V_n^k - \cdots, \\ V_n^{k+1}(x',t) &= V_n^k + \delta\partial_{x'}V_n^k + \frac{\delta^2}{2}\,\partial_{x'}^2V_n^k + \cdots, \\ &\vdots \\ V_n^{k+(\frac{\ell-1}{2})}(x',t) &= V_n^k + \left(\frac{\ell-1}{2}\right)\delta\partial_{x'}V_n^k + \left(\frac{\ell-1}{2}\right)^2\frac{\delta^2}{2}\,\partial_{x'}^2V_n^k + \cdots, \end{aligned}\right\} \tag{2.3.73}$$

and

$$\begin{aligned} U_i^{\jmath-1}(x'',t) &= U_i^\jmath - \zeta\partial_{x''}U_i^\jmath + \frac{\zeta^2}{2}\,\partial_{x''}^2U_i^\jmath - \cdots, \\ U_i^{\jmath+1}(x'',t) &= U_i^\jmath + \zeta\partial_{x''}U_i^\jmath + \frac{\zeta^2}{2}\,\partial_{x''}^2U_i^\jmath + \cdots, \end{aligned} \tag{2.3.74}$$

where ℓ is assumed as an odd number, and hence there are $(\ell-1)/2$ number of terms exist on both side of V_n^k. Note that we needed expansion for the membrane potential of $(\ell-1)$ terms as ℓ number of type A cells along the spatial direction are coupled to a single type B cell.

Since we allow spatial variation only in the direction of the arterial axis, we will find only the spatial terms $(\tilde{i}_n^k - \tilde{i}_n^{k+1})$ and $(\tilde{j}_i^\jmath - \tilde{j}_i^{\jmath+1})$ respectively appeared in equations (2.3.1) and (2.3.28) as they model currents through gap junctions in the axial direction. Therefore, we will replace the corresponding term $\widetilde{G}_A(V_n^{k-1} - 2V_n^k + V_n^{k+1})$ in equation (2.3.7) and $\widetilde{G}_B(U_i^{\jmath-1} - 2U_i^\jmath + U_i^{\jmath+1})$ in equation (2.3.34) by spatial terms, and we will leave rest of the terms unchanged.

For this, we have

$$\tilde{i}_n^k - \tilde{i}_n^{k+1} = \widetilde{G}_n^k(V_n^{k-1} - V_n^k) - \widetilde{G}_n^{k+1}(V_n^k - V_n^{k+1}), \tag{2.3.75}$$

$$\tilde{j}_\imath^\jmath - \tilde{j}_\imath^{\jmath+1} = \widetilde{G}_\imath^\jmath(U_\imath^{\jmath-1} - U_\imath^\jmath) - \widetilde{G}_\imath^{\jmath+1}(U_\imath^\jmath - U_\imath^{\jmath+1}), \tag{2.3.76}$$

Now, by comparing equations (2.3.70)-(2.3.76) we have

$$\tilde{i}_n^k - \tilde{i}_n^{k+1} = \delta^2 \frac{\partial}{\partial x'}\left(G_n^k(x')\frac{\partial V_n^k}{\partial x'}\right), \tag{2.3.77}$$

$$\tilde{j}_\imath^\jmath - \tilde{j}_\imath^{\jmath+1} = \zeta^2 \frac{\partial}{\partial x''}\left(G_\imath^\jmath(x'')\frac{\partial U_\imath^\jmath}{\partial x''}\right). \tag{2.3.78}$$

Thus, as mentioned above, by substituting equations (2.3.77) and (2.3.78) for terms $\widetilde{G}_A(V_n^{k-1} - 2V_n^k + V_n^{k+1})$ and $\widetilde{G}_B(U_\imath^{\jmath-1} - 2U_\imath^\jmath + U_\imath^{\jmath+1})$ respectively in equation (2.3.7) and equation (2.3.34) we have

$$\begin{aligned} C_A\frac{\partial V_n^k}{\partial \tau} + i_n^k + F_A(V_n^k) - \widehat{G}_A(V_{n-1}^k - 2V_n^k + V_{n+1}^k) &+ \overline{G}_{BA}\left(\wp V_n^k - \sum_{\imath=(n-1)\wp+1}^{n\wp} U_\imath^\jmath\right) \\ &= \delta^2\frac{\partial}{\partial x'}\left(G_n^k(x')\frac{\partial V_n^k}{\partial x'}\right) + I_n^{k^a}, \end{aligned} \tag{2.3.79}$$

$$L_A\frac{\partial i_n^k}{\partial \tau} + R_A i_n^k - V_n^k + E_A = 0, \tag{2.3.80}$$

$$\begin{aligned} C_B\frac{\partial U_\imath^\jmath}{\partial \tau} + j_\imath^\jmath + F_B(U_\imath^\jmath) - \widehat{G}_B(U_{\imath-1}^\jmath - 2U_\imath^\jmath + U_{\imath+1}^\jmath) &+ \overline{G}_{BA}\left(\ell U_\imath^\jmath - \sum_{k=(\jmath-1)\ell+1}^{\jmath\ell} V_n^k\right) \\ &= \zeta^2\frac{\partial}{\partial x''}\left(G_\imath^\jmath(x'')\frac{\partial U_\imath^\jmath}{\partial x''}\right) + J_\imath^{\jmath^a}, \end{aligned} \tag{2.3.81}$$

$$L_B\frac{\partial j_\imath^\jmath}{\partial \tau} + R_B j_\imath^\jmath - U_\imath^\jmath + E_B = 0. \tag{2.3.82}$$

Since equations (2.3.79) and (2.3.81) are modelled with continuous terms, we do not further require the spatial index k of type A cell and $\jmath$ of type B cell. However, the summation in equation (2.3.81) for type A cellular membrane potential varies in the

spatial direction, and for any $\jmath$, it is just an addition of ℓ number of terms.

Therefore, by using equation (2.3.73), we find for any $\jmath$ the summing term in terms of V_n^k as follows :

$$\begin{aligned}
\sum_{k=(\jmath-1)\ell+1}^{\jmath\ell} V_n^k &= \sum_{a=k-(\frac{\ell-1}{2})}^{k+(\frac{\ell-1}{2})} V_n^a \\
&= V_n^{k-(\frac{\ell-1}{2})} + \cdots + V_n^{k-1} + V_n^k + V_n^{k+1} \cdots + V_n^{k+(\frac{\ell-1}{2})} \\
&= \ell V_n^k + \delta^2 \left(1^2 + 2^2 + 3^2 + \cdots + \left(\frac{\ell-1}{2}\right)^2\right) \frac{\partial^2 V_n^k}{\partial x'^2} \\
&= \ell V_n^k + \frac{\ell(\ell^2-1)\delta^2}{24} \frac{\partial^2 V_n^k}{\partial x'^2}. \qquad (2.3.83)
\end{aligned}$$

Now, by comparing equations (2.3.79)-(2.3.83) and omitting the spatial indices; k and $\jmath$, finally we have

$$\begin{aligned}
C_A \frac{\partial V_n}{\partial \tau} + i_n + F_A(V_n) - \widehat{G}_A(V_{n-1} - 2V_n + V_{n+1}) &+ \overline{G}_{BA}\left(\wp V_n - \sum_{\imath=(n-1)\wp+1}^{n\wp} U_\imath\right) \\
&= \delta^2 \frac{\partial}{\partial x'}\left(G_n(x') \frac{\partial V_n}{\partial x'}\right) + I_n^a, \qquad (2.3.84) \\
L_A \frac{\partial i_n}{\partial \tau} + R_A i_n &= V_n - E_A, \qquad (2.3.85)
\end{aligned}$$

$$\begin{aligned}
C_B \frac{\partial U_\imath}{\partial \tau} + j_\imath + F_B(U_\imath) - \widehat{G}_B(U_{\imath-1} - 2U_\imath + U_{\imath+1}) &+ \ell\, \overline{G}_{BA}(U_\imath - V_n) \\
&= \xi^2 \frac{\partial^2 V_n}{\partial x'^2} + \zeta^2 \frac{\partial}{\partial x''}\left(G_\imath(x'') \frac{\partial U_\imath^\jmath}{\partial x''}\right), \\
&\quad + J_\imath^a \qquad (2.3.86) \\
L_B \frac{\partial j_\imath}{\partial \tau} + R_B j_\imath &= U_\imath - E_B, \qquad (2.3.87)
\end{aligned}$$

where n in equation (2.3.86) changes for every $\wp$ values of $\imath$, and

$$\xi = \delta\sqrt{\frac{\ell(\ell^2-1)\overline{G}_{BA}}{24}}. \tag{2.3.88}$$

As mentioned before, the 2 different length scales, x' and x'', can be transformed into a single length scale x. It will be done at a later stage of this derivation. Hence, as we expected at the beginning of modelling of heterocellular connection, the first term on the right hand side of the equation (2.3.86) interprets a resultant spatial effect of ℓ number of type A cells on a single type B cell, along the direction of the arterial axis.

Since there are respectively m and $m\wp$ number of type A and type B cells in the arterial ring, we will write a similar system of equations satisfying the membrane potential of such number of cells around the circumference of the artery. That is, the resultant system of equations will interpret variation of membrane potential of a ring of discrete cells coupled via heterocellular connections along the arterial axis.

Now, for $\imath = 1, \ldots, m\wp$, the membrane potential V_n in equation (2.3.86) can be written as,

$$V_n = \begin{cases} V_1, & \imath = 1; \\ \vdots & \\ V_1, & \imath = \wp; \\ V_2, & \imath = \wp + 1; \\ \vdots & \\ V_2, & \imath = 2\wp; \\ \vdots & \\ \vdots & \\ V_m, & \imath = (m-1)\wp + 1; \\ \vdots & \\ V_m, & \imath = m\wp; \end{cases} = [1]\,\boldsymbol{V}, \tag{2.3.89}$$

where

$$\boldsymbol{V} = \Big(\; V_1 \;\; V_2 \ldots V_m \; \Big)^T_{1\times m}, \tag{2.3.90}$$

and

$$[1] = \begin{pmatrix} [C1] \\ [C2] \\ \vdots \\ [Cm] \end{pmatrix}_{m\wp\times m}, \; [C\vartheta] = \begin{pmatrix} 0 & \cdots & 0 & \underset{\substack{\uparrow \\ \vartheta^{\text{th}} \\ position}}{1} & 0 & \cdots 0 \\ 0 & \cdots & 0 & 1 & 0 & \cdots 0 \\ \vdots & \cdots & \vdots & \vdots & \vdots & \cdots 0 \\ 0 & \cdots & 0 & 1 & 0 & \cdots 0 \end{pmatrix}_{\wp\times m}. \tag{2.3.91}$$

where $\vartheta = 1, \ldots, m$.

Let us define

$$\boldsymbol{U} = \Big(\; U_1 \;\; U_2 \ldots U_\wp \;\; U_{\wp+1} \ldots U_{2\wp} \;\; \ldots\ldots U_{(m-1)\wp+1} \ldots U_{m\wp} \; \Big)^T_{1\times m\wp}. \tag{2.3.92}$$

Then, for $n = 1, \ldots, m$, we have

$$\begin{aligned} \sum_{\imath=(n-1)\wp+1}^{n\wp} U_\imath &= \begin{cases} U_1 + U_2 + \cdots + U_\wp, & n = 1; \\ U_{\wp+1} + U_{\wp+2} + \cdots + U_{2\wp}, & n = 2; \\ \quad \vdots & \quad \vdots \\ U_{(m-1)\wp+1} + U_{(m-1)\wp+2} + \cdots + U_{m\wp}, & n = m; \end{cases} \\ &= [L]\,\boldsymbol{U}, \end{aligned} \tag{2.3.93}$$

where

$$[L] = \begin{pmatrix} \underbrace{1\;1\ldots1}_{\wp \text{ times}} & \underbrace{0\;0\ldots0}_{\wp \text{ times}} & \cdots & \underbrace{0\;0\ldots0}_{\wp \text{ times}} \\ \underbrace{0\;0\ldots0}_{\wp \text{ times}} & \underbrace{1\;1\ldots1}_{\wp \text{ times}} & \cdots & \underbrace{0\;0\ldots0}_{\wp \text{ times}} \\ \vdots & \vdots & \ddots & \vdots \\ \underbrace{0\;0\ldots0}_{\wp \text{ times}} & \underbrace{0\;0\ldots0}_{\wp \text{ times}} & \cdots & \underbrace{1\;1\ldots1}_{\wp \text{ times}} \end{pmatrix}_{m\times m\wp}. \tag{2.3.94}$$

Now, for the full system, $n = 1, \ldots, m$ and $\imath = 1, \ldots, m_{\wp}$, we write a system of similar models of type given by equations (2.3.84)-(2.3.87). By substituting equations (2.3.89) and (2.3.93) into the resultant equations, and by applying periodic boundary conditions given by equations (2.3.66) and (2.3.67), we have

$$\begin{aligned} C_A \frac{\partial \boldsymbol{V}}{\partial \tau} + \boldsymbol{i} + \boldsymbol{F}_A(\boldsymbol{V}) + \widehat{G}_A[A_m]\,\boldsymbol{V} &+ \overline{G}_{BA}(\wp\,\boldsymbol{V} - [L]\,\boldsymbol{U}) \\ &= \delta^2 \frac{\partial}{\partial x'}\left(G_A(x')\frac{\partial \boldsymbol{V}}{\partial x'}\right) + \boldsymbol{I}^a, \qquad (2.3.95) \\ L_A \frac{\partial \boldsymbol{i}}{\partial \tau} + R_A \boldsymbol{i} &= \boldsymbol{V} - \boldsymbol{E}_A, \qquad (2.3.96) \end{aligned}$$

$$\begin{aligned} C_B \frac{\partial \boldsymbol{U}}{\partial \tau} + \boldsymbol{j} + \boldsymbol{F}_B(\boldsymbol{U}) + \widehat{G}_B[A_{m\wp}]\,\boldsymbol{U} &+ \ell\,\overline{G}_{BA}(\boldsymbol{U} - [1]\,\boldsymbol{V}) \\ &= \xi^2[1]\frac{\partial^2 \boldsymbol{V}}{\partial x'^2} + \zeta^2 \frac{\partial}{\partial x''}\left(G_B(x'')\frac{\partial \boldsymbol{U}}{\partial x''}\right), \\ &\quad + \boldsymbol{J}^a \qquad (2.3.97) \\ L_B \frac{\partial \boldsymbol{j}}{\partial \tau} + R_B \boldsymbol{j} &= \boldsymbol{U} - \boldsymbol{E}_B, \qquad (2.3.98) \end{aligned}$$

where

$$\left.\begin{array}{ll} \boldsymbol{V} = [V_1 \;\; V_2 \ldots V_m]^T, & \boldsymbol{U} = [U_1 \;\; U_2 \ldots U_{m_{\wp}}]^T, \\ \boldsymbol{i} = [i_1 \;\; i_2 \ldots i_m]^T, & \boldsymbol{j} = [j_1 \;\; j_2 \ldots j_{m_{\wp}}]^T, \\ \boldsymbol{I}^a = [I_1^a \;\; I_2^a \ldots I_m^a]^T, & \boldsymbol{J} = [J_1^a \;\; J_2^a \ldots J_{m_{\wp}}^a]^T, \\ \boldsymbol{F}(\boldsymbol{V}) = [F(V_1) \;\; F(V_2) \cdots F(V_m)]^T, & \boldsymbol{F}(\boldsymbol{U}) = [F(U_1) \;\; F(U_2) \cdots F(U_{m_{\wp}})]^T, \\ F(V_n) = V_n(V_n - \alpha_A)(1 - V_n), & F(U_\imath) = U_\imath(U_\imath - \alpha_B)(1 - U_\imath), \end{array}\right\} \qquad (2.3.99)$$

$$[A_e] = \begin{pmatrix} 2 & -1 & 0 & \ldots & 0 & -1 \\ -1 & 2 & -1 & \ldots & 0 & 0 \\ \vdots & \vdots & \ddots & \ldots & \vdots & \vdots \\ -1 & 0 & 0 & \ldots & -1 & 2 \end{pmatrix}_{e \times e}, \qquad (2.3.100)$$

with $e = m, m\wp$, and

$$G(\hat{x}) = \begin{pmatrix} G_1(\hat{x}) & 0 & \cdots & 0 \\ 0 & G_2(\hat{x}) & \cdots & 0 \\ \vdots & \vdots & \ddots & \vdots \\ 0 & 0 & \cdots & G_e(\hat{x}) \end{pmatrix}_{e\times e}, \quad \hat{x} = \begin{cases} x', \text{ for } e = m, \\ x'', \text{ for } e = m\wp. \end{cases} \tag{2.3.101}$$

Now, from equation (2.3.72), each spatial point in type A and type B cell domain is respectively defined by $x' = h\delta$ and $x'' = h\zeta, h = 1, 2, \ldots$. Thus,

$$x'' = \ell x', \quad \ell = \zeta/\delta. \tag{2.3.102}$$

Hence, each spatial point in the type B cell domain can be modelled to be ℓ multiple of the corresponding point in the type A cell domain. This is true under the assumption that there is no spatial gaps between type A cells, and gap junctions between them are fully opened through cellular membranes.

Let us define $x' = \tilde{x}$. Then, we have $x'' = \ell\tilde{x}$. Therefore, with the help of change of variables, equations (2.3.95)-(2.3.98) can be written as follows:

$$\begin{aligned} C_A\frac{\partial \boldsymbol{V}}{\partial \tau} + \boldsymbol{i} + \boldsymbol{F}_A(\boldsymbol{V}) + \widehat{G}_A[A_m]\,\boldsymbol{V} &+ \overline{G}_{BA}(\wp\,\boldsymbol{V} - [L]\,\boldsymbol{U}) \\ &= \delta^2\frac{\partial}{\partial\tilde{x}}\left(G_A(\tilde{x})\frac{\partial \boldsymbol{V}}{\partial\tilde{x}}\right) + \boldsymbol{I}^a, \qquad (2.3.103) \\ L_A\frac{\partial \boldsymbol{i}}{\partial\tau} + R_A\boldsymbol{i} &= \boldsymbol{V} - \boldsymbol{E}_A, \qquad (2.3.104) \end{aligned}$$

$$\begin{aligned} C_B\frac{\partial \boldsymbol{U}}{\partial \tau} + \boldsymbol{j} + \boldsymbol{F}_B(\boldsymbol{U}) + \widehat{G}_B[A_{m\wp}]\,\boldsymbol{U} &+ \ell\,\overline{G}_{BA}(\boldsymbol{U} - [1]\,\boldsymbol{V}) \\ &= \xi^2[1]\frac{\partial^2 \boldsymbol{V}}{\partial\tilde{x}^2} + \delta^2\frac{\partial}{\partial\tilde{x}}\left(G_B(\ell\tilde{x})\frac{\partial \boldsymbol{U}}{\partial\tilde{x}}\right), \\ &\quad + \boldsymbol{J}^a \qquad (2.3.105) \\ L_B\frac{\partial \boldsymbol{j}}{\partial\tau} + R_B\boldsymbol{j} &= \boldsymbol{U} - \boldsymbol{E}_B. \qquad (2.3.106) \end{aligned}$$

Hence, the resultant system is derived in a unique length-scale (domain with spatial variable $\tilde{x}$) even though they are originally itself defined in 2 different length-scales (domains with spatial variable x' and x''). Further, from equations (2.3.97) and (2.3.105), we note that in the unique length scale domain, the membrane potential variation coefficient (PVC) of type B cell as ℓ multiple of it's PVC in the original domain. Therefore, the original PVC in the domain of type B cells can be found by finding PVC in the unique length-scale domain via scaling by $1/\ell$. Equations (2.3.103)-(2.3.106) model the heterocellular connections between m number of type A and $m\wp$ number of type B discrete cells around the circumference of the arterial ring, as well as the heterocellular connections of continuous cells along the arterial axis.

2.3.4 Non-dimensionalisation of Heterocellular Models

In this section, we will transform the system given by equations (2.3.103)-(2.3.106) into a non-dimensional form by defining number of variables and parameters.

Firstly, we define

$$\tilde{W} = \max\{\hat{V}, \hat{U}\}, \tag{2.3.107}$$

where, as define in equation (2.2.12),

$$\hat{V} = \max\{\hat{V}_1, \hat{V}_2, \ldots, \hat{V}_m\},$$

and $\hat{V}_i,\ i = 1, \ldots, m$, is the highest stable solution of the corresponding differential equation: $\frac{dV_i}{d\tau} = -F_A(V_i)$, with $F_A(V_i) = V_i(1 - V_i)(V_i - \alpha_A)$. Similarly,

$$\hat{U} = \max\{\hat{U}_1, \hat{U}_2, \ldots, \hat{U}_{m\wp}\},$$

and $\hat{U}_j,\ j = 1, \ldots, m\wp$, is the highest stable solution of the corresponding differential equation: $\frac{dU_j}{d\tau} = -F_B(U_j)$, with $F_B(U_j) = U_j(1 - U_j)(U_j - \alpha_B)$, see [70] for non-dimensionalisation of a single FHN system. Note that $F_A(V_i)$ and $F_B(U_j)$ are differentiated by parameters α_A and α_B.

Secondly, to keep for both type A and type B cellular domains a common unique time scale, we define the followings:

$$\tilde{L} = \max\{L_A, L_B\}, \quad \tilde{R} = \min\{\hat{R}_A, \hat{R}_B\}, \tag{2.3.108}$$

where, again as define in equation (2.2.12),

$$\hat{R}_A = \min\{\bar{R}_1, \bar{R}_2, \ldots, \bar{R}_m\}, \quad \hat{R}_B = \min\{\breve{R}_1, \breve{R}_2, \ldots, \breve{R}_{m\wp}\},$$

and $\bar{R}_i$ and $\breve{R}_j$ are passive resistance of nonlinear time varying components $F_A(V_i)$ and $F_B(U_j)$, respectively, and are defined by

$$\bar{R}_i = \left.\frac{1}{F'_A(V_i)}\right|_{V_i=0}, \quad \breve{R}_j = \left.\frac{1}{F'_B(U_j)}\right|_{U_j=0},$$

see [70] for non-dimensionalisation of a single FHN system.

Remark 2.3.4 We have chosen $\hat{V}$ and $\hat{U}$ so that the maximum of $\hat{V}_i$s and $\hat{U}_j$s, respectively, where $i = 1, \ldots, m$ and $j = 1, \ldots, m\wp$, as the highest stable solution of the membrane potential of each cell not to become simultaneously zero. Hence, $\tilde{W}$ can not be a zero potential that allows us to have a well defined system as dimensionless models will be derived by scaling equations (2.3.110) and (2.3.112) using the factor $\tilde{R}/\hat{W}$.

Remark 2.3.5 The variation of membrane potential can be studied with respect to a small time scale as the dynamics of the cell system changes more rapidly with time. Therefore, to have a small dimensionless time scale t defined by equation (2.3.109), $\tilde{R}$ and $\tilde{L}$ are respectively chosen as a minimum and maximum of their corresponding terms, $\hat{R}$s and Ls, in equation (2.3.108). Hence, the resultant system is modelled with the small dimensionless time scale corresponding to a fixed dimensional time τ.

By using equations (2.3.107) and (2.3.108) we write

$$\boldsymbol{V} = \tilde{W}\boldsymbol{v}, \quad \boldsymbol{U} = \tilde{W}\boldsymbol{u}, \quad \tau = \frac{\tilde{L}}{\tilde{R}}\,t, \quad \tilde{x} = lx, \tag{2.3.109}$$

where l is the characteristic length of the arterial segment. Hence, variables $\boldsymbol{v}, \boldsymbol{u}, t$ and x are now dimensionless.

Now by multiplying equations (2.3.103) and (2.3.105) by $\tilde{R}/\tilde{W}$, and by substituting equation (2.3.109) into equations (2.3.103)-(2.3.106) we have

$$\begin{aligned}
\frac{\tilde{R}^2 C_A}{\tilde{L}}\frac{\partial \boldsymbol{v}}{\partial t} + \frac{\tilde{R}}{\tilde{W}}\boldsymbol{i} + \frac{\tilde{R}}{\tilde{W}}\boldsymbol{F}_A(\tilde{W}\boldsymbol{v}) &+ \tilde{R}\widehat{G}_A[A_m]\boldsymbol{v} + \tilde{R}\overline{G}_{BA}(\wp\boldsymbol{v} - [L]\boldsymbol{u}) \\
&= \frac{\tilde{R}\delta^2}{l^2}\frac{\partial}{\partial x}\left(G_A(lx)\frac{\partial \boldsymbol{v}}{\partial x}\right) + \frac{\tilde{R}}{\tilde{W}}\boldsymbol{I}^a, \qquad (2.3.110) \\
\frac{L_A\tilde{R}}{\tilde{L}}\frac{\partial \boldsymbol{i}}{\partial t} + R_A\boldsymbol{i} &= \tilde{W}\boldsymbol{v} - \boldsymbol{E}_A, \qquad (2.3.111)
\end{aligned}$$

$$\begin{aligned}
\frac{\tilde{R}^2 C_B}{\tilde{L}}\frac{\partial \boldsymbol{u}}{\partial t} + \frac{\tilde{R}}{\tilde{W}}\boldsymbol{j} + \frac{\tilde{R}}{\tilde{W}}\boldsymbol{F}_B(\tilde{W}\boldsymbol{u}) &+ \tilde{R}\widehat{G}_B[A_{m\wp}]\boldsymbol{u} + \ell\tilde{R}\,\overline{G}_{BA}(\boldsymbol{u} - [1]\boldsymbol{v}) \\
&= \frac{\tilde{R}\xi^2}{l^2}[1]\frac{\partial^2 \boldsymbol{v}}{\partial x^2} + \frac{\tilde{R}\rho^2}{l^2}\frac{\partial}{\partial x}\left(G_B(l\ell x)\frac{\partial \boldsymbol{u}}{\partial x}\right), \\
&\quad + \frac{\tilde{R}}{\tilde{W}}\boldsymbol{J}^a \qquad (2.3.112) \\
\frac{L_B\tilde{R}}{\tilde{L}}\frac{\partial \boldsymbol{j}}{\partial t} + R_B\boldsymbol{j} &= \tilde{W}\boldsymbol{u} - \boldsymbol{E}_B. \qquad (2.3.113)
\end{aligned}$$

Now, let us define the followings;

$$\left.\begin{array}{lll}
\nu_A = \dfrac{\tilde{R}^2 C_A}{\tilde{L}}, & \boldsymbol{w} = \dfrac{\tilde{R}}{\tilde{W}}\,\boldsymbol{i}, & \boldsymbol{g}_A(\boldsymbol{v}) = -\dfrac{\tilde{R}}{\tilde{W}}\boldsymbol{F}_A(\tilde{W}\boldsymbol{v}), \\
G_A = \tilde{R}\widehat{G}_A, & G_{BA} = \tilde{R}\overline{G}_{BA}, & D_A(x) = \dfrac{\delta^2}{l^2}\,\tilde{R}G_A(lx), \\
\beta_A = \dfrac{L_A}{\tilde{L}}, & \gamma_A = \dfrac{R_A}{\tilde{R}}, & \boldsymbol{p}_A = \dfrac{\boldsymbol{E}_A}{\tilde{W}}, \quad \boldsymbol{I} = \dfrac{\tilde{R}}{\tilde{W}}\boldsymbol{I}^a,
\end{array}\right\} \qquad (2.3.114)$$

and

$$\left.\begin{array}{lll} \nu_B = \dfrac{\tilde{R}^2 C_B}{\tilde{L}}, & \boldsymbol{z} = \dfrac{\tilde{R}}{\tilde{W}}\boldsymbol{j}, & \boldsymbol{g}_B(\boldsymbol{u}) = -\dfrac{\tilde{R}}{\tilde{W}}\boldsymbol{F}_B(\tilde{W}\boldsymbol{u}), \\ G_B = \tilde{R}\widehat{G}_B, & D_{AB} = \dfrac{\tilde{R}\xi^2}{l^2}, & D_B(x) = \dfrac{\tilde{R}\rho^2}{l^2}\, G_B(l\ell x), \\ \beta_B = \dfrac{L_B}{\tilde{L}}, & \gamma_B = \dfrac{R_B}{\tilde{R}}, & \boldsymbol{p}_B = \dfrac{\boldsymbol{E}_B}{\tilde{W}}, \quad \boldsymbol{J} = \dfrac{\tilde{R}}{\tilde{W}}\boldsymbol{J}^a. \end{array}\right\} \tag{2.3.115}$$

By comparing equations (2.3.110)-(2.3.115), we have

$$\begin{aligned} \nu_A \frac{\partial \boldsymbol{v}}{\partial t} + \boldsymbol{w} - \boldsymbol{g}_A(\boldsymbol{v}) + G_A[A_m]\boldsymbol{v} &+ G_{BA}(\wp \boldsymbol{v} - [L]\boldsymbol{u}) \\ &= \frac{\partial}{\partial x}\left(D_A(x)\frac{\partial \boldsymbol{v}}{\partial x}\right) + \boldsymbol{I}, \end{aligned} \tag{2.3.116}$$

$$\beta_A \frac{\partial \boldsymbol{w}}{\partial t} + \gamma_A \boldsymbol{w} = \boldsymbol{v} - \boldsymbol{p}_A, \tag{2.3.117}$$

$$\begin{aligned} \nu_B \frac{\partial \boldsymbol{u}}{\partial t} + \boldsymbol{z} - \boldsymbol{g}_B(\boldsymbol{u}) + G_B[A_{m\wp}]\boldsymbol{u} &+ \ell G_{BA}(\boldsymbol{u} - [1]\boldsymbol{v}) \\ &= D_{AB}[1]\frac{\partial^2 \boldsymbol{v}}{\partial x^2} + \frac{\partial}{\partial x}\left(D_B(x)\frac{\partial \boldsymbol{u}}{\partial x}\right) + \boldsymbol{J}, \end{aligned} \tag{2.3.118}$$

$$\beta_B \frac{\partial \boldsymbol{z}}{\partial t} + \gamma_B \boldsymbol{z} = \boldsymbol{u} - \boldsymbol{p}_B. \tag{2.3.119}$$

Equations (2.3.116)-(2.3.119) interpret the non-dimensional form of equations (2.3.103)-(2.3.106).

Remark 2.3.6 The heterocellular coupling coefficient D_{AB} in equation (2.3.115) can be shown as dimensionless, using equation (2.3.88), as follows:

$$D_{AB} = \frac{\tilde{R}\xi^2}{l^2} = \frac{\ell(\ell^2 - 1)\delta^2 \tilde{R}\overline{G}_{BA}}{24 l^2} = \frac{\ell(\ell^2 - 1)\delta^2 G_{BA}}{24 l^2}. \tag{2.3.120}$$

Remark 2.3.7 As stated in *Remark 2.3.3*, dimensionless form of the discrete heterocellular models, equations (2.3.51)-(2.3.54), can be shown as equations (2.3.62)-(2.3.65) by applying the same technique and, definitions of variables and parameters as described here in this section, with $r = 1$ (indicates only a single type B cell along the arterial axis) and $D_A = D_B = D_{AB} = 0$.

2.4 Summary

This chapter has described in detail a comprehensive mathematical modelling techniques of both homocellular and heterocellular communication between 2 different types of human cells (type A resembles smooth muscle cells, and type B resembles endothelial cells), in terms of their cellular membrane potential.

Firstly, we have derived a system of discrete models for homocellular connections between type A cells around the circumference of an arterial ring. The ring shape was conceptually crated by allowing the same cellular current between the first and last cells around the circumference. Discrete models of the ring of cells were then extended to a system of reaction-diffusion type of equations in 1-dimension, by homogenising the ring along the arterial axis. Hence, the resultant system of equations modelled both a finite number of discrete cells around the circumference and an infinite number of cells (continuous cells) along the axis of the artery. Then, we coupled both type A and type B cells and derived initially a system of complete discrete models for heterocellular communication. Moreover, a system of reaction-diffusion type of equations were also derived for heterocellular signalling between type A and type B cells. In addition, the non-dimensionalisation technique of a single FHN system described in [70] was extended for the non-dimensionalisation of our multi-dimensional homocellular and heterocellular FHN models.

The system of models we have derived here is a multidimensional one and, hence,

the complexity of the problem is substantially high when the number discrete cells around the circumference increases. In other words, we have thousands of reaction-diffusion type of equations, even though they have continuous characteristic along the arterial axis. Therefore, solving such massive number of equations is analytically impossible, and it is cost in computational time even under an application of a numerical techniques. This is one of the reasons we are motivated to construct a few number of continuous models instead of using large number of discrete models. In the next chapter, we have achieved this by developing fully continuous lattice models in 2-dimension.

Chapter 3

Development and Description of 2-Dimensional Lattice Models

3.1 Introduction

To describe the importance of two-dimensional lattice models we recall Equations (2.2.30) and (2.2.31):

$$C\frac{\partial \boldsymbol{V}}{\partial \tau} + \boldsymbol{i} + \boldsymbol{F}(\boldsymbol{V}) + \widehat{G}A\boldsymbol{V} = \delta^2 \frac{\partial}{\partial x}\left(\widetilde{G}(x)\ \frac{\partial \boldsymbol{V}}{\partial x}\right) + \boldsymbol{I}^a, \tag{3.1.1}$$

$$L\frac{\partial \boldsymbol{i}}{\partial \tau} + R\boldsymbol{i} = \boldsymbol{V} - \boldsymbol{E}. \tag{3.1.2}$$

In Equation (3.1.1) the term $\widehat{G}A\boldsymbol{V}$ modelled the coupling between m number of discrete type A cells around the circumference, θ, of an arterial ring, under the assumption that the cells in the θ-direction are homogeneous. In this direction the conductance of gap junctions, $\widehat{G}$, between type A cells was taken to be homogeneous (refer to Equation (2.2.19) in Section 2.2.3). Similarly, models of the heterocellular communication between type A and type B cells (see Equations (2.3.103)-(2.3.106)) were also derived based on the same assumption. However, this assumption models thousands of equations of types (3.1.1) and (3.1.2) for a large m due to the real world situation of the existence of thousands of cells around the arterial circumference. Moreover, the number of equations in the case of heterocellular communication is double that of the number of equations of the homocellular communication. As

mentioned in Section 2.4, the order of complexity of the problem increases as number of cells around the circumference increases. Therefore, in this chapter we lift the θ-direction of the cylindrical geometry (see Figure 2.1) along the spatial direction y of the Cartesian coordinates to form a two-dimensional lattice, which considerably reduces the number of equations.

In Sections 4.2 and 3.3 we will derive lattice models in two-space dimensions for the homocellular and heterocellular signalling among and between type A and type B cells, respectively.

3.2 2-D lattice models for homocellular communication

Figure 3.1 shows a lifted cylindrical domain in the form of a lattice in two-dimension. By applying Kirchhoff's and Ohm's laws to the $(n,k)^{\text{th}}$ center cell in Figure 3.1, respectively, we have

$$\tilde{i}_n^{k+1} - \tilde{i}_n^k = \hat{i}_n^k - \hat{i}_{n+1}^k - I_n^k + I_n^{k^a} \tag{3.2.1}$$

$$\tilde{i}_n^k = \widetilde{G}_n^k(V_n^{k-1} - V_n^k), \quad \tilde{i}_n^{k+1} = \widetilde{G}_n^{k+1}(V_n^k - V_n^{k+1}) \tag{3.2.2}$$

$$\hat{i}_n^k = \widehat{G}_n^k(V_{n-1}^k - V_n^k), \quad \hat{i}_{n+1}^k = \widehat{G}_{n+1}^k(V_n^k - V_{n+1}^k), \tag{3.2.3}$$

where notations in Equations (3.2.1)-(3.2.3) are defined in Section 2.2.3.

Let us assume the domain in Figure 3.1 is nonhomogeneous. Then, we have $\widehat{G}_n^k \neq \widehat{G}_{n+1}^k$ and $\widetilde{G}_n^{k+1} \neq \widetilde{G}_n^k$. Assume a conductance $G_n^k(x,y)$ to be exist at the center node (n,k). This assumption allows to model conductance ($\widehat{G}$s and $\widetilde{G}$s) around the $(n,k)^{\text{th}}$ cell in terms of the unique conductance $G_n^k(x,y)$, Hence the distance between $G_n^k(x,y)$ and, $\widehat{G}_k^n$ and $\widehat{G}_{n+1}^k$ would be a half of the cell length, η, in the y-direction. Similarly, $\widetilde{G}_k^n$ and $\widetilde{G}_{n+1}^k$ along the x-direction can be separated by the half of the cell width, δ, from $G_n^k(x,y)$. We apply this assumption on the modelling Equation (3.2.4).

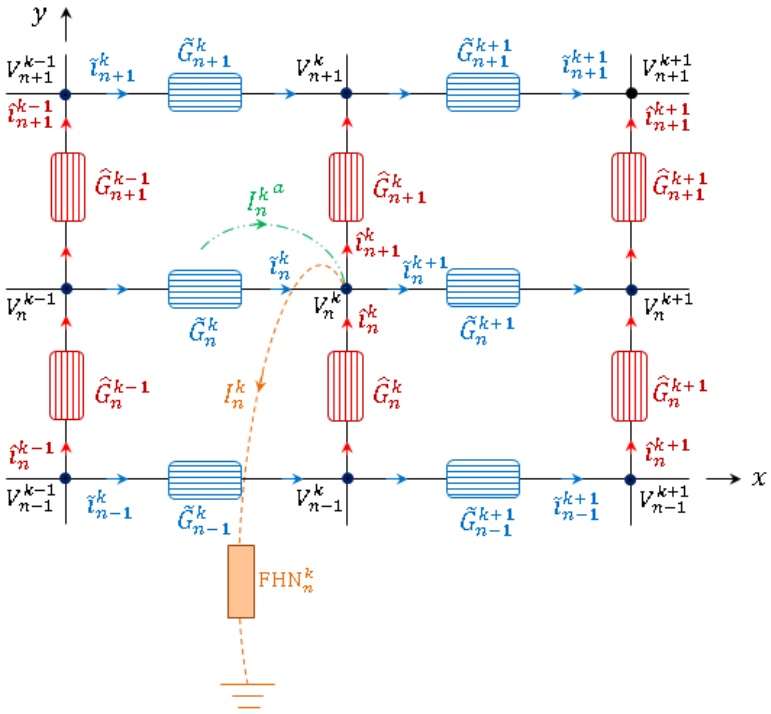

Figure 3.1: Schematic shows the lifted cylindrical geometry ($\theta \to y$) of Figure 2.4. All notations are used in Figure 2.4 and in Section 2.2.3. The $(n,k)^{\text{th}}$ type A cell has been modelled by an FHN analogue. Homocellular gap junctions between cells along the x and y axes are denoted by blue and red blocks, respectively.

By applying Taylors Series expansion for both membrane potential and conductance we have

$$\left.\begin{aligned}
\widetilde{G}_n^{k+1}(x,y) &= G_n^k(x,y) + \left(\frac{\delta}{2}\right)\partial_x G_n^k(x,y) + \frac{1}{2}\left(\frac{\delta}{2}\right)^2 \partial_x^2 G_n^k(x,y) + \cdots, \\
\widetilde{G}_n^{k}(x,y) &= G_n^k(x,y) - \left(\frac{\delta}{2}\right)\partial_x G_n^k(x,y) + \frac{1}{2}\left(\frac{\delta}{2}\right)^2 \partial_x^2 G_n^k(x,y) + \cdots, \\
\widehat{G}_{n+1}^{k}(x,y) &= G_n^k(x,y) + \left(\frac{\eta}{2}\right)\partial_y G_n^k(x,y) + \frac{1}{2}\left(\frac{\eta}{2}\right)^2 \partial_y^2 G_n^k(x,y) + \cdots, \\
\widehat{G}_{n}^{k}(x,y) &= G_n^k(x,y) - \left(\frac{\eta}{2}\right)\partial_y G_n^k(x,y) + \frac{1}{2}\left(\frac{\eta}{2}\right)^2 \partial_y^2 G_n^k(x,y) + \cdots,
\end{aligned}\right\} \tag{3.2.4}$$

and

$$\left.\begin{aligned} V_n^{k-1}(x,y,t) &= V_n^k(x,y,t) - \delta\partial_x V_n^k(x,y,t) + \frac{1}{2}\delta^2\partial_x^2 V_n^k(x,y,t) + \cdots, \\ V_n^{k+1}(x,y,t) &= V_n^k(x,y,t) + \delta\partial_x V_n^k(x,y,t) + \frac{1}{2}\delta^2\partial_x^2 V_n^k(x,y,t) + \cdots, \\ V_{n-1}^k(x,y,t) &= V_n^k(x,y,t) - \eta\partial_y V_n^k(x,y,t) + \frac{1}{2}\eta^2\partial_y^2 V_n^k(x,y,t) + \cdots, \\ V_{n+1}^k(x,y,t) &= V_n^k(x,y,t) + \eta\partial_y V_n^k(x,y,t) + \frac{1}{2}\eta^2\partial_y^2 V_n^k(x,y,t) + \cdots, \end{aligned}\right\} \tag{3.2.5}$$

where δ and η are respectively the width and length of a single type A cell.

By substituting Equations (3.2.4) and (3.2.5) into Equation (3.2.2) we have

$$\begin{aligned} \tilde{i}_n^k - \tilde{i}_n^{k+1} &= \widetilde{G}_n^k(V_n^{k-1} - V_n^k) - \widetilde{G}_n^{k+1}(V_n^k - V_n^{k+1}) \\ &= \delta^2 G_n^k \partial_x^2 V_n^k + \delta^2 \partial_x G_n^k \partial_x V_n^k \\ &= \delta^2 \frac{\partial}{\partial x}\left(G_n^k \frac{\partial V_n^k}{\partial x}\right). \end{aligned} \tag{3.2.6}$$

Similarly, by substituting Equations (3.2.4) and (3.2.5) into Equation (3.2.3) we have

$$\hat{i}_n^k - \hat{i}_n^{k+1} = \eta^2 \frac{\partial}{\partial y}\left(G_n^k \frac{\partial V_n^k}{\partial y}\right). \tag{3.2.7}$$

From equations (2.2.21) and (2.2.22) we have

$$C\frac{dV_n^k}{d\tau} + i_n^k + F(V_n^k) = I_n^k, \tag{3.2.8}$$

$$L\frac{di_n^k}{d\tau} + Ri_n^k = V_n^k - E. \tag{3.2.9}$$

By comparing Equations (3.2.1) and (3.2.6)-(3.2.9) we have

$$C\frac{\partial V_n^k}{\partial \tau} + i_n^k + F(V_n^k) - I_n^{k^a} = \delta^2 \frac{\partial}{\partial x}\left(G_n^k \frac{\partial V_n^k}{\partial x}\right) + \eta^2 \frac{\partial}{\partial y}\left(G_n^k \frac{\partial V_n^k}{\partial y}\right), \tag{3.2.10}$$

$$L\frac{di_n^k}{d\tau} + Ri_n^k = V_n^k - E. \tag{3.2.11}$$

As membrane potential in the domain is modelled at an arbitrary $(n,k)^{\text{th}}$ cell, we do not need further the indices n and k and hence we rewrite Equations (3.2.10) and (3.2.11) in the form:

$$C\frac{\partial V}{\partial \tau} + i + F(V) - I^a = \delta^2 \frac{\partial}{\partial x}\left(G(x,y)\frac{\partial V}{\partial x}\right) + \eta^2 \frac{\partial}{\partial y}\left(G(x,y)\frac{\partial V}{\partial y}\right), \tag{3.2.12}$$

$$L\frac{\partial i}{\partial \tau} + Ri = V - E. \tag{3.2.13}$$

Equations (3.2.12) and (3.2.13) model the membrane potential of continuous type A cells in both x and y directions. In the following section we will transform these models to their non-dimensional forms.

3.2.1 Non-dimensionalisation of 2-D homocellular models

We apply the same method in Section 2.2.2 for a non-dimensionalisation of models given by Equations (3.2.12) and (3.2.13). For this, let us define

$$\begin{aligned} V &= \hat{V}v, \quad t = \hat{R}\tau/L, \\ x &= \delta x', \quad y = \eta y'. \end{aligned} \tag{3.2.14}$$

where $\hat{V}$ is the highest stable solution of the differential equation: $\frac{dV}{d\tau} = -F(V)$ and $\hat{R}$ is defined by $\hat{R} = 1/F'(V)|_{V=0}$ (see [70]).

By multiplying Equation (3.2.12) by $\hat{R}/\hat{V}$ and substituting Equation (3.2.14) into Equations (3.2.12) and (3.2.13) we have

$$\begin{aligned} \frac{C\hat{R}^2}{L}\frac{\partial v}{\partial t} + \frac{\hat{R}}{\hat{V}}i + \frac{\hat{R}}{\hat{V}}F(\hat{V}v) - \frac{\hat{R}}{\hat{V}}I^a &= \hat{R}\frac{\partial}{\partial x'}\left(G(x,y)\frac{\partial v}{\partial x'}\right) \\ &\quad + \hat{R}\frac{\partial}{\partial y'}\left(G(x,y)\frac{\partial v}{\partial y'}\right), \end{aligned} \tag{3.2.15}$$

$$\hat{R}\frac{\partial i}{\partial t} + Ri = \hat{V}v - E. \tag{3.2.16}$$

Equations (3.2.15) and (3.2.16) can be written in the following non-dimensional form:

$$\nu\frac{\partial v}{\partial t} - g(v) + w - I = \frac{\partial}{\partial x}\left(D(x,y)\frac{\partial v}{\partial x}\right) + \frac{\partial}{\partial y}\left(D(x,y)\frac{\partial v}{\partial y}\right), \quad (3.2.17)$$

$$\frac{\partial w}{\partial t} + \gamma w = v - p, \quad (3.2.18)$$

where the non-dimensional variables x' and y' are again replaced by x and y in equation (3.2.17) for a conventional writing and

$$\left.\begin{array}{llll} \nu = \dfrac{C\hat{R}^2}{\hat{L}}, & g(v) = -\dfrac{\hat{R}}{\hat{V}}F(\hat{V}v), & w = \dfrac{\hat{R}}{\hat{V}}\,i, & D(x,y) = \hat{R}G(x,y), \\ I = \dfrac{\hat{R}}{\hat{V}}I^a, & \gamma = \dfrac{R}{\hat{R}}, & p = \dfrac{E}{\hat{V}}. & \end{array}\right\} \quad (3.2.19)$$

Remark 3.1 For $D = 0$, models of Equations (3.2.17) and (3.2.18) can be deduced to a single cell FHN models.

Remark 3.2 For $D =$ constant $\neq 0$, the right hand side of the equation (3.2.17) can be deduced to $D\nabla^2 v$, where ∇ is the 2-dimensional Laplace operator.

Remark 3.2 One can observe from the term GAv in Equation (2.2.33), describing coupling between discrete cells around the circumference of the artery has been modelled by the term; $\frac{\partial}{\partial y}(D\frac{\partial v}{\partial y})$ in Equation (3.2.17) of continuous cells.

3.3 2-D lattice models for heterocellular communication

Let (x', y') and (x'', y'') be the spatial coordinates of the domain of type A cells and type B cells, respectively, for the derivation of two-dimensional lattice models for heterocellular communication between type A and type B cells.

By recalling models of Equations (2.3.1) and (2.3.28) we have for type A and type B

cells, respectively:

$$\hat{i}_n^k - \hat{i}_{n+1}^k + \tilde{i}_n^k - \tilde{i}_n^{k+1} = I_n^k - I_n^{k^a} - \sum_{\imath=(n-1)\wp+1}^{n\wp} \bar{i}_{\imath\to n}^k, \tag{3.3.1}$$

$$\hat{j}_\imath^\jmath - \hat{j}_{\imath+1}^\jmath + \tilde{j}_\imath^\jmath - \tilde{j}_\imath^{\jmath+1} = J_\imath^\jmath + \sum_{k=(\jmath-1)\ell+1}^{\jmath\ell} \bar{i}_{\imath\to n}^k. \tag{3.3.2}$$

For type A cells, we obtain from Equations (3.2.6) and (3.2.7):

$$\tilde{i}_n^k - \tilde{i}_n^{k+1} + \hat{i}_n^k - \hat{i}_{n+1}^k = \delta^2 \frac{\partial}{\partial x'}\left(G_n^k(x',y')\frac{\partial V_n^k}{\partial x'}\right) + \eta^2 \frac{\partial}{\partial y'}\left(G_n^k(x',y')\frac{\partial V_n^k}{\partial y'}\right), \tag{3.3.3}$$

We can write similar equation of type (3.3.3) for type B cells by following the same method of derivation in Section 4.2 hence we have

$$\tilde{j}_\imath^\jmath - \tilde{j}_\imath^{\jmath+1} + \hat{j}_\imath^\jmath - \hat{j}_{\imath+1}^\jmath = \zeta^2 \frac{\partial}{\partial x''}\left(G_\imath^\jmath(x'',y'')\frac{\partial U_\imath^\jmath}{\partial x''}\right) + \varsigma^2 \frac{\partial}{\partial y''}\left(G_\imath^\jmath(x'',y'')\frac{\partial U_\imath^\jmath}{\partial y''}\right), \tag{3.3.4}$$

where ζ and ς are length and width of a single type B cell, respectively.

Now, from the last model of Equation (2.3.29), we have

$$\sum_{k=(\jmath-1)\ell+1}^{\jmath\ell} \bar{i}_{\imath\to n}^k = \sum_{k=(\jmath-1)\ell+1}^{\jmath\ell} \overline{G}_{BA}(U_\imath^\jmath - V_n^k) = \overline{G}_{BA}\left(\ell U_\imath^\jmath - \sum_{k=(\jmath-1)\ell+1}^{\jmath\ell} V_n^k\right), \tag{3.3.5}$$

$$\sum_{\imath=(n-1)\wp+1}^{n\wp} \bar{i}_{\imath\to n}^k = \sum_{\imath=(n-1)\wp+1}^{n\wp} \overline{G}_{BA}(U_\imath^\jmath - V_n^k) = \overline{G}_{BA}\left(\sum_{\imath=(n-1)\wp+1}^{n\wp} U_\imath^\jmath - \wp V_n^k\right). \tag{3.3.6}$$

From equation (2.3.83), we have

$$\sum_{k=(\jmath-1)\ell+1}^{\jmath\ell} V_n^k = \ell V_n^k + \frac{\ell(\ell^2-1)\delta^2}{24}\frac{\partial^2 V_n^k}{\partial x'^2}. \tag{3.3.7}$$

By comparing Equations (3.3.5) and (3.3.7) we have

$$\begin{aligned}\sum_{k=(\jmath-1)\ell+1}^{\jmath\ell} \bar{i}^{k}_{\imath\to n} &= \ell\overline{G}_{BA}(U^{\jmath}_{i} - V^{k}_{n}) - \frac{\ell(\ell^2-1)\delta^2\overline{G}_{BA}}{24}\frac{\partial^2 V^{k}_{n}}{\partial x'^2} \\ &= \ell\overline{G}_{BA}(U^{\jmath}_{i} - V^{k}_{n}) - \xi^2\frac{\partial^2 V^{k}_{n}}{\partial x'^2}, \end{aligned} \tag{3.3.8}$$

where

$$\xi = \sqrt{\frac{\ell(\ell^2-1)\delta^2\overline{G}_{BA}}{24}}. \tag{3.3.9}$$

Now, we will find a relation for the summation on the righthand side of the Equation (3.3.6). Consider the $(n,k)^{\text{th}}$ type A cell, coupling with $\wp$ number of type B cells (from cell $(n-1)\wp+1$ to $n\wp$) along the y-direction (see Figure 2.5(c)). Therefore, one can observe a $(\wp-1)/2$ type B cells to be exists on both side of the $(\imath,\jmath)^{\text{th}}$ type B cell in the y-direction, where $\wp$ is assumed to be an odd number. Hence, we need terms from $U^{\jmath}_{\imath-(\frac{\wp-1}{2})}$ to $U^{\jmath}_{\imath+(\frac{\wp-1}{2})}$ and the summation is just an addition of $\wp$ number of terms for any j.

By applying Taylor Series expansion we have

$$\left.\begin{aligned} U^{\jmath}_{\imath-(\frac{\wp-1}{2})}(x'',y'',t) &= U^{\jmath}_{i} - \left(\frac{\wp-1}{2}\right)\varsigma\partial_{y''}U^{\jmath}_{i} + \left(\frac{\wp-1}{2}\right)^2\frac{\varsigma^2}{2}\partial^2_{y''}U^{\jmath}_{i} - \cdots, \\ &\vdots \\ U^{\jmath}_{\imath-1}(x'',y'',t) &= U^{\jmath}_{i} - \varsigma\partial_{y''}U^{\jmath}_{i} + \frac{\varsigma^2}{2}\partial^2_{y''}U^{\jmath}_{i} - \cdots, \\ U^{\jmath}_{\imath+1}(x'',y'',t) &= U^{\jmath}_{i} + \varsigma\partial_{y''}U^{\jmath}_{i} + \frac{\varsigma^2}{2}\partial^2_{y''}U^{\jmath}_{i} + \cdots, \\ &\vdots \\ U^{\jmath}_{\imath+(\frac{\wp-1}{2})}(x'',y'',t) &= U^{\jmath}_{i} + \left(\frac{\wp-1}{2}\right)\varsigma\partial_{y''}U^{\jmath}_{i} + \left(\frac{\wp-1}{2}\right)^2\frac{\varsigma^2}{2}\partial^2_{y''}U^{\jmath}_{i} + \cdots. \end{aligned}\right\} \tag{3.3.10}$$

From Equation (3.3.10) the summation on the righthand side of the Equation (3.3.6)

can be written as:

$$\begin{aligned}\sum_{\imath=(n-1)\wp+1}^{n\wp} U_\imath^\jmath &= \sum_{a=\imath-(\frac{\wp-1}{2})}^{\imath+(\frac{\wp-1}{2})} U_a^\jmath \\ &= U_{\imath-(\frac{\wp-1}{2})}^\jmath + \cdots + U_{\imath-1}^\jmath + U_\imath^\jmath + U_{\imath+1}^\jmath \cdots + U_{\imath+(\frac{\wp-1}{2})}^\jmath \\ &= \wp U_\imath^\jmath + \varsigma^2\left(1^2+2^2+3^2+\cdots+\left(\frac{\wp-1}{2}\right)^2\right)\frac{\partial^2 U_\imath^\jmath}{\partial y''^2} \\ &= \wp U_\imath^\jmath + \frac{\wp(\wp^2-1)\varsigma^2}{24}\frac{\partial^2 U_\imath^\jmath}{\partial y''^2}. \end{aligned} \tag{3.3.11}$$

By comparing Equations (3.3.6) and (3.3.11) we have

$$\begin{aligned}\sum_{\imath=(n-1)\wp+1}^{n\wp} \bar{\imath}_{\imath\to n}^k &= \wp\overline{G}_{BA}(U_\imath^\jmath - V_n^k) + \frac{\wp(\wp^2-1)\varsigma^2\overline{G}_{BA}}{24}\frac{\partial^2 U_\imath^\jmath}{\partial y''^2} \\ &= \wp\overline{G}_{BA}(U_\imath^\jmath - V_n^k) + \rho^2\frac{\partial^2 U_\imath^\jmath}{\partial y''^2}, \end{aligned} \tag{3.3.12}$$

where

$$\rho = \sqrt{\frac{\wp(\wp^2-1)\varsigma^2\overline{G}_{BA}}{24}}. \tag{3.3.13}$$

Now, from Equations (2.3.5), (2.3.6), (2.3.32) and (2.3.33) we have

$$C_A\frac{dV_n^k}{d\tau} + \imath_n^k + F_A(V_n^k) = I_n^k, \tag{3.3.14}$$

$$C_B\frac{dU_\imath^\jmath}{d\tau} + \jmath_\imath^\jmath + F_B(U_\imath^\jmath) = J_\imath^\jmath, \tag{3.3.15}$$

$$L_A\frac{d\imath_n^k}{d\tau} + R_A\imath_n^k = V_n^k - E_A, \tag{3.3.16}$$

$$L_B\frac{d\jmath_\imath^\jmath}{d\tau} + R_B\jmath_\imath^\jmath = U_\imath^\jmath - E_B. \tag{3.3.17}$$

By substituting Equations (3.3.3), (3.3.12) and (3.3.14) into Equation (3.3.1) we have

$$\begin{aligned} C_A\frac{\partial V_n^k}{\partial\tau} + i_n^k &+ F_A(V_n^k) + \wp\,\overline{G}_{BA}(V_n^k - U_\imath^\jmath) - I_n^{k^a} \\ &= \delta^2\frac{\partial}{\partial x'}\left(G_n^k(x',y')\frac{\partial V_n^k}{\partial x'}\right) + \eta^2\frac{\partial}{\partial y'}\left(G_n^k(x',y')\frac{\partial V_n^k}{\partial y'}\right) + \rho^2\,\frac{\partial^2 U_\imath^\jmath}{\partial y''^2}. \end{aligned} \tag{3.3.18}$$

Similarly, for type B cells, by substituting Equations (3.3.4), (3.3.8) and (3.3.15) into equation (3.3.2) we have

$$\begin{aligned} C_B\frac{\partial U_i^{\jmath}}{\partial \tau}+j_i^{\jmath} &+ F_B(U_i^{\jmath})+\ell\,\overline{G}_{BA}(U_i^{\jmath}-V_n^k)-J_i^{\jmath^a} \\ &= \zeta^2\frac{\partial}{\partial x''}\left(G_i^{\jmath}(x'',y'')\frac{\partial U_i^{\jmath}}{\partial x''}\right)+\varsigma^2\frac{\partial}{\partial y''}\left(G_i^{\jmath}(x'',y'')\frac{\partial U_i^{\jmath}}{\partial y''}\right)+\xi^2\frac{\partial^2 V_n^k}{\partial x'^2}. \end{aligned} \tag{3.3.19}$$

Since Equations (3.3.16)-(3.3.19) model an arbitrary type A and an arbitrary type B cell we avoid writing of corresponding spatial indices. Hence, we have

$$\begin{aligned} C_A\frac{\partial V}{\partial \tau}+i &+ F_A(V)+\wp\,\overline{G}_{BA}(V-U)-I^a \\ &= \delta^2\frac{\partial}{\partial x'}\left(G_A(x',y')\frac{\partial V}{\partial x'}\right)+\eta^2\frac{\partial}{\partial y'}\left(G_A(x',y')\frac{\partial V}{\partial y'}\right)+\rho^2\,\frac{\partial^2 U_i^{\jmath}}{\partial y''^2}, \end{aligned} \tag{3.3.20}$$

$$\begin{aligned} C_B\frac{\partial U}{\partial \tau}+j &+ F_B(U)+\ell\,\overline{G}_{BA}(U-V)-J^a \\ &= \zeta^2\frac{\partial}{\partial x''}\left(G_B(x'',y'')\frac{\partial U}{\partial x''}\right)+\varsigma^2\frac{\partial}{\partial y''}\left(G_B(x'',y'')\frac{\partial U}{\partial y''}\right)+\xi^2\frac{\partial^2 V}{\partial x'^2}, \end{aligned} \tag{3.3.21}$$

$$L_A\frac{\partial i}{\partial \tau}+R_A i = V-E_A, \tag{3.3.22}$$

$$L_B\frac{\partial j}{\partial \tau}+R_B j = U-E_B. \tag{3.3.23}$$

From Equations (3.3.20) and (3.3.21) we see that type A and type B cells have been modelled with their corresponding length-scales: (x',y') and (x'',y''), respectively. We transform the domain of type A and type B cells into a domain of unique length-scale, $(\tilde{x},\tilde{y})$, to avoid using different length-scales.

As defined in Equation (2.3.102), spatial points of type A and type B cells with respect to the corresponding domain can be defined, respectively:

$$(x',y')=(h_1\delta,h_2\eta),\quad (x'',y'')=(h_1\zeta,h_2\varsigma),\quad h_1,h_2=1,2,\ldots. \tag{3.3.24}$$

Since $\eta = \wp\varsigma$ and $\zeta = \ell\delta$, from Equation (3.3.24), we have

$$\begin{aligned} x'' &= \quad \ell x', \quad \ell = \zeta/\delta, \\ y' &= \wp y'', \quad \wp = \eta/\varsigma. \end{aligned} \tag{3.3.25}$$

Let us assume $x' = \tilde{x}$ and $y'' = \tilde{y}$. Then Equation (3.3.25) can be written as

$$\begin{aligned} x'' &= \quad \ell\tilde{x}, \quad \ell = \zeta/\delta, \\ y' &= \wp\tilde{y}, \quad \wp = \eta/\varsigma. \end{aligned} \tag{3.3.26}$$

From Equation (3.3.26) we have

$$(x', y') = (\tilde{x}, \wp\tilde{y}), \quad (x'', y'') = (\ell\tilde{x}, \tilde{y}). \tag{3.3.27}$$

By applying Equation (3.3.26) and transformations in Equation (3.3.27) to the spatial operators in Equations (3.3.20) and (3.3.21), we have

$$\begin{aligned} C_A\frac{\partial V}{\partial \tau} + i &+ F_A(V) + \wp\,\overline{G}_{BA}(V-U) - I^a \\ &= \delta^2\frac{\partial}{\partial\tilde{x}}\left(G_A(\tilde{x},\wp\tilde{y})\frac{\partial V}{\partial\tilde{x}}\right) + \varsigma^2\frac{\partial}{\partial\tilde{y}}\left(G_A(\tilde{x},\wp\tilde{y})\frac{\partial V}{\partial\tilde{y}}\right) + \rho^2\frac{\partial^2 U}{\partial\tilde{y}^2}, \end{aligned} \tag{3.3.28}$$

$$\begin{aligned} C_B\frac{\partial U}{\partial \tau} + j &+ F_B(U) + \ell\,\overline{G}_{BA}(U-V) - J^a \\ &= \delta^2\frac{\partial}{\partial\tilde{x}}\left(G_B(\ell\tilde{x},\tilde{y})\frac{\partial U}{\partial\tilde{x}}\right) + \varsigma^2\frac{\partial}{\partial\tilde{y}}\left(G_B(\ell\tilde{x},\tilde{y})\frac{\partial U}{\partial\tilde{y}}\right) + \xi^2\frac{\partial^2 V}{\partial\tilde{x}^2}, \end{aligned} \tag{3.3.29}$$

$$L_A\frac{\partial i}{\partial\tau} + R_A i = V - E_A, \tag{3.3.30}$$

$$L_B\frac{\partial j}{\partial\tau} + R_B j = U - E_B, \tag{3.3.31}$$

Equations (3.3.28) and (3.3.29) show modelling of type A and type B cells in the domain of unique length-scale, $(\tilde{x}, \tilde{y})$. One can also observe that the potential variation coefficients (PVCs): $G_A(\tilde{x}, \wp\tilde{y})$ and $G_B(\ell\tilde{x}, \tilde{y})$ of type A and type B cells in the new domain to be a uni-directional multiple of PVCs of cells in their original domain. Here the scaling of G_A and G_B by $\wp$ and ℓ, respectively, only in a single direction is meant

by the term 'uni-directional multiple'. Moreover, the last term on the right hand side of Equations (3.3.28) and (3.3.29) respectively models the spatial effect on one type cell by the other only in one-direction due to the heterocellular communication between them, as mentioned above.

3.3.1 Non-dimensionalization of 2-D heterocellular models

For the non-dimensionalisation of heterocellular models of Equations (3.3.28)-(3.3.31), first we define

$$\hat{W} = \max\{\hat{V}, \hat{U}\}, \tag{3.3.32}$$

where, as define in Equation (3.2.14), $\hat{V}$ is the highest stable solution of the differential equation: $\frac{dV}{d\tau} = -F_A(V)$ with $F_A(V) = V(1-V)(V-\alpha_A)$ for type A cell. Similarly, $\hat{U}$ is the highest stable solution of the differential equation: $\frac{dU}{d\tau} = -F_B(U)$ with $F_B(U) = U(1-U)(U-\alpha_B)$ for type B cell (see [70]). Note that $F_A(V)$ and $F_B(U)$ are differentiated by parameters α_A and α_B.

Second we define the following parameters to have a unique time scale t for both type A and type B cells:

$$\hat{L} = \max\{L_A, L_B\}, \quad \hat{R} = \min\{\hat{R}_A, \hat{R}_B\}, \tag{3.3.33}$$

where $\hat{R}_A$ is a passive resistance of nonlinear time varying components $F_A(V)$ and is defined by $\hat{R}_A = 1/F'_A(V)|_{V=0}$, see [70]. Similarly, $\hat{R}_B$ is a passive resistance of nonlinear time varying components $F_B(U)$ and is defined by $\hat{R}_B = 1/F'_B(U)|_{U=0}$.

By using Equations (3.3.32) and (3.3.33) we define

$$V = \hat{W}v, \quad U = \hat{W}\boldsymbol{u}, \quad \tau = \frac{\hat{L}}{\hat{R}}\,t, \quad \tilde{x} = \delta x, \quad \tilde{y} = \varsigma y. \tag{3.3.34}$$

Hence, variables v, u, t, x and y in Equation (3.3.34) are now dimensionless.

By multiplying Equations (3.3.28) and (3.3.29) by $\frac{\hat{R}}{\hat{W}}$ and by comparing with Equations (3.3.26) and (3.3.34) we have

$$\begin{aligned}\frac{C_A\hat{R}^2}{\hat{L}}\frac{\partial v}{\partial t}+\frac{\hat{R}}{\hat{W}}\,i &+ \frac{\hat{R}}{\hat{W}}F_A(\hat{V}v)+\wp\hat{R}\,\overline{G}_{BA}(v-u)-\frac{\hat{R}}{\hat{W}}I^a\\ &= \hat{R}\frac{\partial}{\partial x}\left(G_A\frac{\partial v}{\partial x}\right)+\hat{R}\frac{\partial}{\partial y}\left(G_A\frac{\partial v}{\partial y}\right)+\frac{\hat{R}\rho^2}{\varsigma^2}\,\frac{\partial^2 u}{\partial y^2},\end{aligned} \tag{3.3.35}$$

$$\begin{aligned}\frac{C_B\hat{R}^2}{\hat{L}}\frac{\partial u}{\partial t}+\frac{\hat{R}}{\hat{W}}\,j &+ \frac{\hat{R}}{\hat{W}}\,F_B(\hat{U}u)+\hat{R}\ell\,\overline{G}_{BA}(u-v)-\frac{\hat{R}}{\hat{W}}J^a\\ &= \hat{R}\frac{\partial}{\partial x}\left(G_B\frac{\partial u}{\partial x}\right)+\hat{R}\frac{\partial}{\partial y}\left(G_B\frac{\partial u}{\partial y}\right)+\frac{\hat{R}\xi^2}{\delta^2}\frac{\partial^2 V}{\partial\tilde{x}^2},\end{aligned} \tag{3.3.36}$$

$$\frac{\hat{R}L_A}{\hat{L}}\frac{\partial i}{\partial t}+R_A i = \hat{W}v-E_A, \tag{3.3.37}$$

$$\frac{\hat{R}L_B}{\hat{L}}\frac{\partial j}{\partial t}+R_B j = \hat{W}u-E_B. \tag{3.3.38}$$

The models of Equations (3.3.35)-(3.3.38) can be written as:

$$\begin{aligned}\nu_A\frac{\partial v}{\partial t}+w &- g_A(v)+\wp\,G_{BA}(v-u)-I\\ &= \frac{\partial}{\partial x}\left(D_A\frac{\partial v}{\partial x}\right)+\frac{\partial}{\partial y}\left(D_A\frac{\partial v}{\partial y}\right)+D_{ABA}\frac{\partial^2 u}{\partial y^2},\end{aligned} \tag{3.3.39}$$

$$\begin{aligned}\nu_B\frac{\partial u}{\partial t}+z &- g_B(u)+\ell G_{BA}(u-v)-J\\ &= \frac{\partial}{\partial x}\left(D_B\frac{\partial u}{\partial x}\right)+\frac{\partial}{\partial y}\left(D_B\frac{\partial u}{\partial y}\right)+D_{ABB}\frac{\partial^2 v}{\partial x^2},\end{aligned} \tag{3.3.40}$$

$$\beta_A\frac{\partial w}{\partial t}+\gamma_A w = v-p_A, \tag{3.3.41}$$

$$\beta_B\frac{\partial z}{\partial t}+\gamma_B z = u-p_B, \tag{3.3.42}$$

where

$$\left.\begin{array}{lll} \nu_A = \dfrac{\hat{R}^2 C_A}{\hat{L}}, & w = \dfrac{\hat{R}}{\hat{W}}\, i, & g_A(v) = -\dfrac{\hat{R}}{\hat{W}} F_A(\hat{W}v), \\ G_{BA} = \hat{R}\overline{G}_{BA}, & D_A = \hat{R} G_A, & D_{ABA} = \dfrac{\hat{R}\rho^2}{\varsigma^2}, \\ \beta_A = \dfrac{L_A}{\hat{L}}, & \gamma_A = \dfrac{R_A}{\hat{R}}, & p_A = \dfrac{E_A}{\hat{W}}, \quad I = \dfrac{\hat{R}}{\hat{W}} I^a \end{array}\right\} \tag{3.3.43}$$

and

$$\left.\begin{array}{lll} \nu_B = \dfrac{\hat{R}^2 C_B}{\hat{L}}, & z = \dfrac{\hat{R}}{\hat{W}} j, & g_B(u) = -\dfrac{\hat{R}}{\hat{W}} F_B(\hat{W}u), \\ J = \dfrac{\hat{R}}{\hat{W}} J^a, & D_B = \hat{R} G_B, & D_{ABB} = \dfrac{\hat{R}\xi^2}{\delta^2}, \\ \beta_B = \dfrac{L_B}{\hat{L}}, & \gamma_B = \dfrac{R_B}{\hat{R}}, & p_B = \dfrac{E_B}{\hat{W}}. \end{array}\right\} \tag{3.3.44}$$

Parameters D_{ABA} and D_{ABB} in Equations (3.3.43) and (3.3.44) can be shown dimensionless using Equations (3.3.9) and (3.3.13), as follows:

$$\begin{aligned} D_{ABA} &= \frac{\hat{R}\rho^2}{\varsigma^2} = \frac{\wp(\wp^2-1)}{24}\hat{R}\overline{G}_{BA} = \frac{\wp(\wp^2-1)}{24}\, G_{BA}, \\ D_{ABB} &= \frac{\hat{R}\xi^2}{\delta^2} = \frac{\ell(\ell^2-1)}{24}\hat{R}\overline{G}_{BA} = \frac{\ell(\ell^2-1)}{24}\, G_{BA}. \end{aligned} \tag{3.3.45}$$

Equations (3.3.39)-(3.3.42) are the dimensionless form of 2-dimensional models for heterocellular communication between type A and type B cells. Dimensional form of variables and parameters are defined by equations (3.3.34) and (3.3.43)-(3.3.45). These models can be deduced to the ones derived for homocellular communication, as stated in the following remark.

Remark 2.3.4 Let us set $D_{ABA} = D_{ABB} = 0$ and $\hat{L} = L_A = L_B$. Then we have $\beta_A = \beta_B = 1$ and Equations (3.3.39) and (3.3.41) can be deduced to homocellular models of type A cells of Equations (3.2.17) and (3.2.18). Similarly, models for the homocellular communication between type B cells can be deduced from Equations (3.3.40) and (3.3.42) under the above assumption.

3.4 Summary

In this chapter we developed a system of two-dimensional lattice models for cellular membrane potential, describing both homocellular and heterocellular communication between type A and type B cells. These models were derived in the respective cellular domain and then transformed to a domain of unique length-scale. A detail derivation of non-dimensional models for both cellular communication was also provided. A suitable choice of parameters during non-dimensionalisation made the system with a unique time-scale. As described previously, derivation of lattice models reduced the complexity (in terms of number of variables) of the one-dimensional homocellular and heterocellular models derived in Chapter 2.

In the following chapter, we will analyse multiple-scale structure (micro and macro) of the arterial domain by applying mathematical homogenisation theory on the one- and two-dimensional models derived in Chapters 2 and in this chapter, respectively.

Chapter 4

Multiscale Analysis and Homogenisation of Models

4.1 Introduction

In this chapter, we study a multiple scale phenomena of an arterial segment using one- and two-dimensional homocellular coupled systems developed in Chapters 2 and 3, respectively. For this, we carry out multiple scale analysis and apply the theory of mathematical homogenisation. For a detail advanced theory of homogenisation using asymptotic expansion and other methods the reader can refer [13], [45], [60], [94], [95].

In the method of homogenisation we will have two scales; microscopic and macroscopic scales. An arterial segment is assumed to be in the macroscopic-scale while the microscopic-scale is assigned to an individual cell domain. Further, we assume the microscopic dimension to be smaller than that of the characteristic dimension of the arterial segment and cells are period. In addition, the microscopic-scale is distinguished by a small parameter ε. The parameter ε refers the cell size such as width or length of the cell. In Chapter 2, we have used the parameters δ and η as the type A cell width and cell length, respectively. However, in this chapter we will use a formal asymptotic expansion for homogenisation and the parameters δ and η are replaced by the parameter ε in an appropriate way for a conventional writing of the asymptotic expansion. Figure 4.1 (a) shows a two-dimensional regular arrangement of square

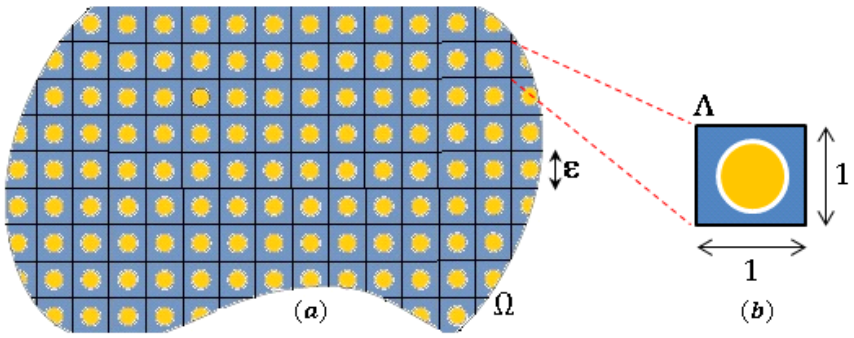

Figure 4.1: Schematic shows (a) periodic structure of a heterogenous medium in two-dimensional macroscopic domain, Ω, consisting number of regular square cells and (b) a single cell, which interprets the microscopic domain, Λ, after scaling by $1/\varepsilon$. The scaled single cell sketched in (b) is now regarded to be the unit-cell in two-dimension.

cells in the macroscopic domain, Ω. The domain of a single cell in Ω is regarded as a microscopic domain, Λ, and is scaled by $1/\varepsilon$ (see Figure 4.1 (b)). Hence, Λ interprets the unit-cell problem, which will lead to study the effects on Ω.

In the microscopic structure (based on our models derived in Chapter 2) each cell is connected via gap junction, which allows signals to transmit to the neighbouring cells due to a kind of physiological process (see Remark 2.1). Thus, it is physiologically relevant to assume that diffusion-type phenomena to be high in the cytosol of a human cell compared to that of the same phenomena in the cellular membrane. However, models incorporating cellular pumps may modify this based on the geometry of the cellular domain. Therefore, we are motivated to assume a suitable diffusion-type patterns for cellular communication so that they approximate a general diffusing pattern. Figure 4.2(a) shows an appropriate variations of diffusion-type functions. Figure 4.2(b) shows a possible approximations for the variation of general diffusion shown in Figure 4.2(a). We will explain these models (based on the cellular geometry) later in this chapter and use them to derive an effective potential variation coefficient (PVC) and a solution for the unit-cell problem.

The mathematical theory of homogenisation has been applied to a heterogeneous medium and hence the process of homogenisation develops macroscopic equations from the microscopic equations. In particular, for a reaction-diffusion type equation

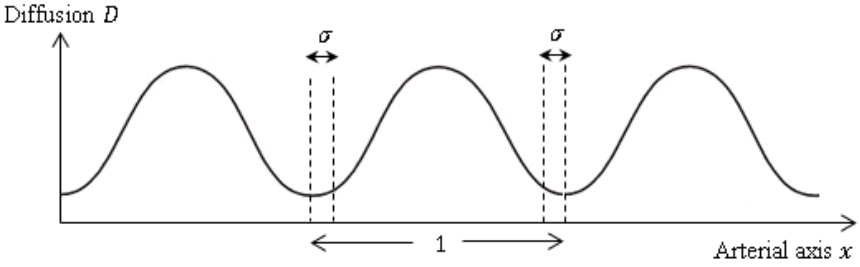

(a) A general diffusing-type pattern in Ω

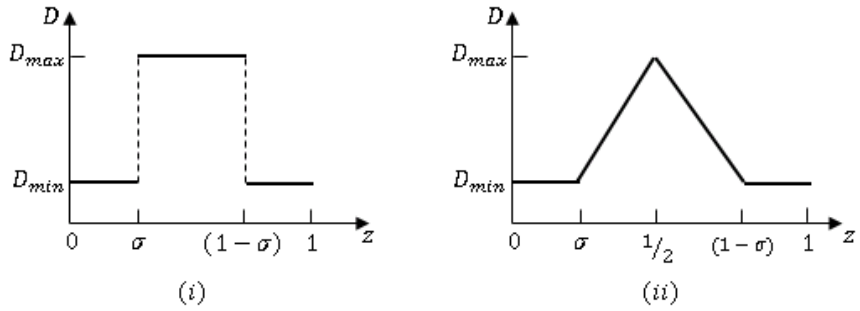

(b) Approximated versions of the general diffusion-type pattern in the unit cell as the (i) zeroth- and (ii) first-order spline, where z denotes the spatial direction in Λ

Figure 4.2: Schematic of (a) an axial diffusion in Ω where σ denotes the half-membrane width as the other half is shared with the neighbouring cell, (b) possible approximated versions of diffusing-type pattern (plotted in Figure 4.2(a)) in Λ. A relevant description of Figures 4.2(b)(i) and 4.2(b) (ii) is given in Sections 4.2.1 and 4.3.2.2, respectively.

in one-dimension, the macroscopic-diffusion, $D(x)$, is derived from the microscopic-diffusion, $D(z)$, by applying the homogenisation theory, where x and z are the macro (slow-scale) and micro (fast-scale) variables, respectively. However, in our modelling, we begin with PVC of both fast- and slow-scales rather than assigning only in the fast-scale and obtain PVC in the slow-scale. This assumption allows to incorporate

a neighbouring coupling effect of microscopic variation as a small fraction of the macroscopic variation.

4.2 Homogenisation of 1-D models

In this section we consider partially homogenised one-dimensional models of cellular communication under the assumptions and justifications described in Section 2.2.

For simplicity, we re-write models of a single cell (the n^{th} cell of m's around the circumference of the artery) of Equations (2.2.33) and (2.2.34), then we have

$$\nu\frac{\partial v_n}{\partial t} - g(v_n) + G(-v_{n-1} + 2v_n - v_{n+1}) + w_n - I_n = \frac{\partial}{\partial x}\left(D_n(x)\frac{\partial v_n}{\partial x}\right), \tag{4.2.1}$$

$$\frac{\partial w_n}{\partial t} + \gamma w_n - v_n = p, \tag{4.2.2}$$

where $g(v_n) = v_n(1 - v_n)(v_n - \alpha), 0 < \alpha < 1$, and other parameters are defined in Chapter 2. Furthermore, we apply periodic boundary conditions: $v_0 = v_m$ and $v_{m+1} = v_1$, respectively for the first $(n = 1)$ and the last $(n = m)$ cells.

Let us define the microscopic variable (fast-scale variable), $z \in \Lambda$, in terms of macroscopic variable (slow-scale variable), $x \in \Omega$ (see Figure 4.1 for the domains definition) such that $z = x/\varepsilon, \varepsilon \ll 1$. Note that we treat the domains Ω and Λ to be one-dimensional.

Let us assume that the membrane potential varies in different length-scales. Then, we use the formal asymptotic expansion in ε for v_n and w_n and hence we have:

$$v_n(x, z, t) = v_{n,0}(x, z, t) + \varepsilon v_{n,1}(x, z, t) + \varepsilon^2 v_{n,2}(x, z, t) + \cdots, \tag{4.2.3}$$

$$w_n(x, z, t) = w_{n,0}(x, z, t) + \varepsilon w_{n,1}(x, z, t) + \varepsilon^2 w_{n,2}(x, z, t) + \cdots, \tag{4.2.4}$$

where $(.)_{n,i}, i = 1, 2, \ldots$, is the i^{th}-order component of the membrane potential of the n^{th}-cell and ε is assumed to be the same for all ns. As stated in Section 4.1,

$D = D(x, z)$.

By substituting Equations (4.2.3) and (4.2.4) into Equations (4.2.1) and (4.2.2), and by grouping the powers of $\varepsilon^{-2}, \varepsilon^{-1}$ and $O(1)$, respectively, we obtain

$$\frac{\partial}{\partial z}\left(D_n \frac{\partial v_{n,0}}{\partial z}\right) = 0, \tag{4.2.5}$$

$$\frac{\partial}{\partial x}\left(D_n \frac{\partial v_{n,0}}{\partial z}\right) + \frac{\partial}{\partial z}\left[D_n\left(\frac{\partial v_{n,0}}{\partial x} + \frac{\partial v_{n,1}}{\partial z}\right)\right] = 0, \tag{4.2.6}$$

$$\begin{aligned}\frac{\partial}{\partial x}\left[D_n\left(\frac{\partial v_{n,0}}{\partial x} + \frac{\partial v_{n,1}}{\partial z}\right)\right] + \frac{\partial}{\partial z}\left[D_n\left(\frac{\partial v_{n,1}}{\partial x} + \frac{\partial v_{n,2}}{\partial z}\right)\right] = \\ \nu \frac{\partial v_{n,0}}{\partial t} - g(v_{n,0}) + w_{n,0} - I_n - G(v_{n-1,0} - 2v_{n,0} + v_{n+1,0}),\end{aligned} \tag{4.2.7}$$

and for $O(\varepsilon^{-2})$ we have an equation for the recovery variable $\omega_{n,0}$:

$$\frac{\partial w_{n,0}}{\partial t} = v_{n,0} - \gamma w_{n,0} - p. \tag{4.2.8}$$

By multiplying Equation (4.2.5) by $v_{n,0}$ and by setting an integral over the domain Λ gives

$$\int_\Lambda v_{n,0} \frac{\partial}{\partial z}\left(D_n \frac{\partial v_{n,0}}{\partial z}\right) dz = 0. \tag{4.2.9}$$

By integration by parts the Equation (4.2.9) we get

$$D_n v_{n,0} \frac{\partial v_{n,0}}{\partial z}\bigg|_\Lambda - \int_\Lambda D_n \left(\frac{\partial v_{n,0}}{\partial z}\right)^2 dz = 0. \tag{4.2.10}$$

Since the first term in the Equation (4.2.10) vanishes by periodicity, we have

$$\int_\Lambda D_n \left(\frac{\partial v_{n,0}}{\partial z}\right)^2 dz = 0, \tag{4.2.11}$$

Now, by positivity of integral we deduce from equation (4.2.11)

$$v_{n,0} = v_{n,0}(x, t). \tag{4.2.12}$$

We observe from Equation (4.2.12) that the zero$^{\text{th}}$-order component of the membrane potential, $v_{n,0}$, of the n^{th} cell to be only a possible function of macroscopic variable x, but not a function of microscopic variable z. Therefore, we see $v_{n,0}$ to be a homogenised model, as it is independent of $z = x/\varepsilon$.

Let us define the unit-cell problem,

$$\frac{\partial D_n}{\partial z} = -\frac{\partial}{\partial z}\left(D_n \frac{\partial \chi_n}{\partial z}\right), \tag{4.2.13}$$

where $\chi_n(x; z)$ is the solution of the unit-cell problem defined by D_n and it is a 1-periodic in z. Definition given by Equation (4.2.13) is valid under the application of Fredholm Alternative Lemma, as follows: suppose that

$$\begin{aligned} L^2_*(\Lambda) &= \left\{\phi(z)\ \Lambda - \text{periodic}, \int_\Lambda \phi(z)^2 dz < +\infty\right\}, \\ H^1_*(\Lambda) &= \left\{\phi \in L^2_*(\Lambda), \nabla\phi \in L^2_*(\Lambda)^N\right\}. \end{aligned}$$

Let $f(z) \in L^2_*(\Lambda)$ be a periodic function. There exists a solution in H^1_* (unique up to an additive constant) of

$$\begin{cases} -\text{div}(D(z)\nabla\chi(z)) = f, & \text{in } \Lambda, \\ z \to \chi(z), & \Lambda\text{-periodic}, \end{cases}$$

if and only if $\displaystyle\int_\Lambda f(z)dz = 0$.

By choosing $f(z) = \frac{\partial D}{\partial z}$ we show $\displaystyle\int_0^1 f(z)dz = 0$ by 1-periodicity. Hence, the conventional definition given by Equation (4.2.13) becomes possible.

From Equations (4.2.6) and (4.2.12) we have

$$\frac{\partial}{\partial z}\left(D_n \frac{\partial v_{n,1}}{\partial z}\right) = -\frac{\partial D_n}{\partial z}\frac{\partial v_{n,0}}{\partial x}. \tag{4.2.14}$$

By substituting Equation (4.2.13) into Equation (4.2.14) we have

$$\frac{\partial}{\partial z}\left(D_n \frac{\partial}{\partial z}\left(v_{n,1} - \chi_n \frac{\partial v_{n,0}}{\partial x}\right)\right) = 0. \tag{4.2.15}$$

By integrating Equation (4.2.15) twice over the domain Λ we have

$$v_{n,1}(x,z) = \chi_n \frac{\partial v_{n,0}}{\partial x} + f(x)\int_\Lambda \frac{1}{D_n}\, dz + g(x), \tag{4.2.16}$$

where $f(x)$ and $g(x)$ are arbitrary functions generated by z.

By applying the 1-periodic boundary condition on $\chi_n(x;z)$:

$$\chi_n(x;0) = \chi_n(x;1), \tag{4.2.17}$$

we show $f(x) = 0$. Hence, from Equation (4.2.16) we have

$$v_{n,1}(x,z) = \chi_n \frac{\partial v_{n,0}}{\partial x} + g(x). \tag{4.2.18}$$

One can observe that the first-order term $v_{n,1}$ of the membrane potential to ba a function of both macroscopic and microscopic scales.

Now by substituting equation (4.2.18) into equation (4.2.7) and by integrating over the domain Λ we have

$$\int_\Lambda \frac{\partial}{\partial x}\left[D_n\left(\frac{\partial v_{n,0}}{\partial x} + \frac{\partial \chi_n}{\partial z}\frac{\partial v_{n,0}}{\partial x}\right)\right] dz + \int_\Lambda \frac{\partial}{\partial z}\left[D_n\left(\frac{\partial v_{n,1}}{\partial x} + \frac{\partial v_{n,2}}{\partial z}\right)\right] dz =$$

$$\nu\frac{\partial v_{n,0}}{\partial t} - g(v_{n,0}) + w_{n,0} - I_n - G(v_{n-1,0} - 2v_{n,0} + v_{n+1,0}). \tag{4.2.19}$$

From Equation (4.2.19) and by using the fundamental theorem of calculus in one-dimension we have

$$\int_\Lambda \frac{\partial}{\partial x}\left[D_n\left(1 + \frac{\partial \chi_n}{\partial z}\right)\frac{\partial v_{n,0}}{\partial x}\right] dz + D_n\left(\frac{\partial v_{n,1}}{\partial x} + \frac{\partial v_{n,2}}{\partial z}\right) =$$

$$\nu\frac{\partial v_{n,0}}{\partial t} - g(v_{n,0}) + w_{n,0} - I_n - G(v_{n-1,0} - 2v_{n,0} + v_{n+1,0}), \tag{4.2.20}$$

where $w_{n,0} = w_{n,0}(x,t)$.

We note that the second term on the left-hand side of the Equation (4.2.20) vanishes as $v_{n,1}$ and $v_{n,2}$ are 1-periodic in z. Hence, we have

$$\nu\frac{\partial v_{n,0}}{\partial t} - g(v_{n,0}) + G(-v_{n-1,0} + 2v_{n,0} - v_{n+1,0}) + w_{n,0} - I_n = \frac{\partial}{\partial x}\left(\widetilde{D}_n \frac{\partial v_{n,0}}{\partial x}\right), \quad (4.2.21)$$

where $\widetilde{D}_n$ is given by

$$\widetilde{D}_n = \int_\Lambda D_n \left(1 + \frac{\partial \chi_n}{\partial z}\right) dz, \quad (4.2.22)$$

and is the effective PVC of the homogenised problem.

The effective PVC can be given by a diagonal tensor matrix for a system of m cells around the circumference of the artery as

$$\widetilde{D} = \begin{pmatrix} \widetilde{D}_1 & \dots & 0 & \dots & 0 \\ \vdots & \ddots & \vdots & \ddots & \vdots \\ 0 & \dots & \widetilde{D}_n & \dots & 0 \\ \vdots & \ddots & \vdots & \ddots & \vdots \\ 0 & \dots & 0 & \dots & \widetilde{D}_m \end{pmatrix}_{m\times m},$$

and this diagonal tensor matrix is only due to two scales, x and z. If different microscopic scales between cells are allowed it would then get more non-diagonal general matrix.

Equation (4.2.21) along with Equation (4.2.8) is the homogenised FHN equation derived from the non-homogenised FHN models given by Equations (4.2.1) and (4.2.2), where the homogenised or effective PVC is given by Equation (4.2.22).

Now, integration of Equation (4.2.13) over the domain Λ gives

$$D_n\left(1 + \frac{\partial \chi}{\partial z}\right) = f(x), \quad (4.2.23)$$

where $f(x)$ is an arbitrary function of integration.

By comparing Equations (4.2.22) and (4.2.23) we have

$$\widetilde{D}_n = f(x). \tag{4.2.24}$$

Hence, the effective diffusion coefficient is only a possible function of macroscopic variable and we are now required to find $f(x)$ such that $\chi_n(x;z)$ is 1-periodic in z.

We can write from Equation (4.2.23),

$$\frac{\partial \chi}{\partial z} = \frac{f(x)}{D_n} - 1. \tag{4.2.25}$$

By integrating Equation (4.2.25) with respect to z we get

$$\chi(x;z) = f(x) \int_0^z \frac{1}{D_n(z')}\, dz' - z. \tag{4.2.26}$$

Hence, from Equation (4.2.26) we have

$$\chi(x;0) = 0, \tag{4.2.27}$$

$$\chi(x;1) = f(x) \int_0^1 \frac{1}{D_n(z')}\, dz' - 1. \tag{4.2.28}$$

By comparing Equations (4.2.17), (4.2.27) and (4.2.28) we get

$$f(x) = \frac{1}{\displaystyle\int_0^1 \frac{1}{D_n(z')}\, dz'}. \tag{4.2.29}$$

Thus, from Equations (4.2.24), (4.2.26) and (4.2.29) we have

$$\widetilde{D}_n = \frac{1}{\displaystyle\int_0^1 \frac{1}{D_n(z')}\, dz'}, \tag{4.2.30}$$

$$\chi_n(x;z) = \widetilde{D}_n \int_0^z \frac{1}{D_n(z')}\, dz' - z. \tag{4.2.31}$$

Hence, the above results express the macroscopic behavior of the effective PVC whereas the solution of the unit-cell problem incorporates microscopic characterization in association with the effective PVC.

4.2.1 Example

In this section we use the homogenised models given by Equations (4.2.30) and (4.2.31) to find the effective PVC, $\widetilde{D}$, and to construct a 1-periodic solution, χ, for the unit-cell problem.

Let us assume the general PVC to be a function of both microscopic and macroscopic scales (see Figure 4.2(a)), which takes a variable separable form defined by

$$D(x;z) = \lambda(x)\mu(z). \tag{4.2.32}$$

The function $\lambda(x)$ can be chosen in a suitable form (sin function), however for the time being, we write the Equation (4.2.32) for simplicity, as

$$D(x;z) = \mu(z). \tag{4.2.33}$$

The Equation (4.2.33) defines a microscopic PVC and we will now seek a suitable form for $\mu(z)$ to interpret PVC for the unit cell.

Suppose we assume that the membrane potential varies from the cytosol to the neighbouring cell through the cellular membrane. Hence we make the following assumptions:

> (**A1**) diffusion in the cell membranes, at the microscopic level, can be modeled as low in magnitude and high in the cytosol,
>
> (**A2**) diffusion in the cytosol and in the cellular membrane are piecewise constants,
>
> (**A3**) the width of the membrane is small enough in size compared to the width of the unit cell.

Now, by the assumptions (**A1**) and (**A2**) we propose a piecewise linear model given in Figure 4.2(b)(i), where D_{max} and D_{min} are respectively taken to be the PVC in

the cytosol and the PVC through the cellular membranes to the neighbouring cells from the cytosol.

Again, by assumption (**A1**) we have

$$D_{min} = kD_{max}, 0 < k << 1. \tag{4.2.34}$$

Moreover, we assume that the PVC through the cellular membrane in the neighbouring cells is taken to be the same, as the cells are assumed as periodic. Therefore, from equations (4.2.33) and (4.2.34), we define a piecewise constant function given by,

$$\mu(z) = \begin{cases} kD_{max}, & 0 \leq z \leq \sigma; \\ D_{max}, & \sigma \leq z \leq 1-\sigma; \\ kD_{max}, & 1-\sigma \leq z \leq 1, \end{cases} \tag{4.2.35}$$

where 2σ is the membrane width of the cell and is illustrated in Figure 4.2(b)(i).

Further, by assumption (**A3**), the width of the membrane, 2σ, is much less than the width of the unit-cell (by definition width of the unit-cell is 1). Hence, we have

$$\sigma << \frac{1}{2}. \tag{4.2.36}$$

Now, by using Equation (4.2.35) we have

$$\begin{aligned} \int_0^1 \frac{1}{\mu(z)}\, dz &= \frac{1}{kD_{max}} \int_0^\sigma dz + \frac{1}{D_{max}} \int_\sigma^{1-\sigma} dz + \frac{1}{kD_{max}} \int_{1-\sigma}^1 dz, \\ &= \frac{2(1-k)\sigma + k}{kD_{max}}. \end{aligned} \tag{4.2.37}$$

Use of this result in Equations (4.2.30) and (4.2.37) shows

$$\widetilde{D} = \frac{kD_{max}}{2(1-k)\sigma + k}. \tag{4.2.38}$$

This is the effective PVC based on the microscopic PVC of Equation (4.2.35).

Now, we find

$$\int_0^z \frac{1}{\mu(z)}\,dz = \begin{cases} \dfrac{1}{kD_{max}}z, & 0 \le z \le \sigma; \\ \dfrac{(1-k)\sigma + kz}{kD_{max}}, & \sigma \le z \le 1-\sigma; \\ \dfrac{z-(1-k)(1-2\sigma)}{kD_{max}}, & 1-\sigma \le z \le 1. \end{cases} \tag{4.2.39}$$

By substituting Equations (4.2.38) and (4.2.39) into Equation (4.2.31), we have a 1-periodic solution for the unit-cell problem given by

$$\chi(x,z) = \begin{cases} az, & 0 \le z \le \sigma; \\ b\sigma(1-2z), & \sigma \le z \le 1-\sigma; \\ az - b(1-2\sigma), & 1-\sigma \le z \le 1, \end{cases} \tag{4.2.40}$$

where

$$a = \frac{1}{2(1-k)\sigma + k} - 1 \quad \text{and} \quad b = (1-k)(1+a) \tag{4.2.41}$$

(see Figure 4.3(c) for the 1-periodic solution of Equation (4.2.13)).

Now, by using Equations (4.2.34), (4.2.36) and (4.2.38), we have

$$\frac{\widetilde{D}}{D_{min}} = \frac{1}{2(1-k)\sigma + k} > 1, \tag{4.2.42}$$

That is, we get

$$D_{min} < \widetilde{D}. \tag{4.2.43}$$

Moreover, from Equations (4.2.13) and (4.2.24), we have

$$\frac{\widetilde{D}}{D} = 1 + \frac{\partial \chi}{\partial z}. \tag{4.2.44}$$

Now, in the cytosol ($\sigma \le z \le 1-\sigma$), by comparing Equations (4.2.35), (4.2.40) and (4.2.44) we have

$$\frac{\widetilde{D}}{D_{max}} = 1 - \frac{2\sigma(1-k)}{2(1-k)\sigma + k}. \tag{4.2.45}$$

From Equations (4.2.34), (4.2.36) and (4.2.45) we reduce to

$$\widetilde{D} < D_{max}. \tag{4.2.46}$$

Hence, from Equations (4.2.43) and (4.2.46) we have

$$D_{min} < \widetilde{D} < D_{max}. \tag{4.2.47}$$

As we expected at the initial stage of developing the example, one can observe from the Equation (4.2.47) that the effective PVC to be within the range of PVCs in the cytosol and cellular membrane.

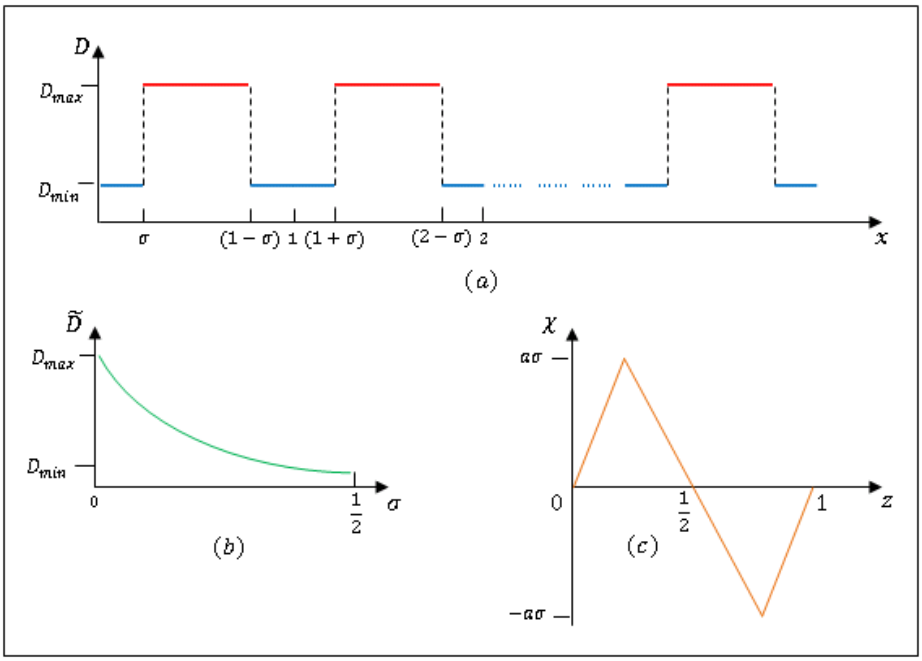

Figure 4.3: Schematic of (a) PVC in the macroscopic domain via the pattern of PVC in the unit-cell (zero$^{\text{th}}$-order spline, see Figure 4.2(b)(i)), (b) the variation of the effective PVC as a function of different cellular membrane width (see Equation (4.2.38)) and (c) the solution, χ, for the unit-cell problem.

Moreover, from Equation (4.2.38), we conclude that $\widetilde{D} \to D_{max}$ as $\sigma \to 0$ (see Figure 4.3(b)). This result shows us, for a cell with a very thin membrane layer,

the effective PVC via the membrane to the neighbouring cells is high in magnitude and is almost everywhere the same as in the cytosol. Similarly, for a cell with a thick membrane, the effective PVC is low in magnitude as in the membrane, because $\widetilde{D} \to D_{min}$ as $2\sigma \to 1$ (i.e, the membrane width $\to$ the width of the unit cell) (see Figure 4.3(b)). We note that Figure 4.3(b) interprets variation of effective PVC with respect to different membrane width and hence this variation cannot be confused with the constant effective PVC of a particular cell. That is, a cell with thick and thin cellular membrane experiences low and high effective PVC, respectively. Further, in Equation (4.2.45), $\widetilde{D} \to D_{max}$ as $k \to 1$ and is true by our definition given by Equation (4.2.34). In addition, from Equations (4.2.34) and (4.2.38), $\widetilde{D} \to 0$ as $D_{min} \to 0$. That is, the macro-domain cannot be predicted with PVC and hence no further communication between cells along the arterial axis. This result can be verified by Equation (4.2.21) as the system becomes decoupled in the axial direction as the effective PVC approaches zero. Therefore, the PVC model of the microscopic domain may be considered as a relevant model, as it provided appropriate results based on the effective PVC.

4.3 Homogenisation of 2-D Lattice Models

In this section we derive a homogenised version of models of Equations (3.2.17) and (3.2.17) in $\mathbb{R}^2$. These equations are given by

$$\nu\frac{\partial v}{\partial t} - g(v) + w - I = \frac{\partial}{\partial x}\left(D(x,y)\frac{\partial v}{\partial x}\right) + \frac{\partial}{\partial y}\left(D(x,y)\frac{\partial v}{\partial y}\right), \tag{4.3.1}$$

$$\frac{\partial w}{\partial t} = v - \gamma w - p. \tag{4.3.2}$$

For the derivation of homogenised models, we consider two different scenarios based on different assumptions. We show a full derivation of homogenised models for both scenarios. For this, each cell is considered as a two-dimensional geometry so that the length, η, and the width, δ, of the cell to be in the direction of s and z-axes, respectively, of the two-dimensional microscopic domain. Figure 4.4 shows the two-dimensional geometry of macro-micro domain, before scaling the macro-domain. As

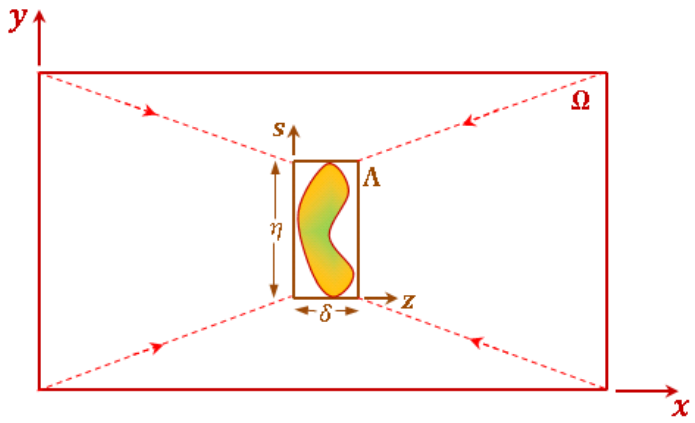

Figure 4.4: Schematic shows microscopic, Λ, and macroscopic, Ω, domains with respective axis system (z, s) and (x, y).

mentioned previously, in the macroscopic domain, the x-axis represents the arterial axis and the y-axis is set up by lifting the circumference of the artery onto $\mathbb{R}$ with 2π periodicity (see Figure 4.4).

4.3.1 Scenario 1: Homogenisation with a Unique Microscopic Scale

For a multiple scale analysis of the system of Equations (4.3.1) and (4.3.2), we make here a specific assumption based on the macroscopic domain Ω. That is, we assume that the characteristic length of the lifted circumference, y-direction, is very small compared to that of the very long characteristic length of the arterial segment, x-axis, unless both of them are chosen to be the same in lengths. Therefore, for this scenario, we consider only the fast-scale variable z by scaling x such that $z = x/\delta$, and y is not regarded for a long time changes. Hence, we do not define another fast-scale variable s in the direction of y. Therefore, the microscopic domain Λ is $(1, \eta)$-periodic. This scenario can be further explained with a help of an example as described below.

Let us assume a smooth muscle cell of width $\delta = 5$ and of length $\eta = 50$. Assume the arterial diameter and characteristic length to be 50μm and 1cm. Then, using the definition of s and z, one can find that: $s = \frac{\pi\times 50\times 10^{-6}}{50\times 10^{-6}} \approx 3$ and $z = \frac{1\times 10^{-2}}{5\times 10^{-6}} = 2000$. Thus, z is about 667 times greater than s. This means the x-direction undergoes for the changes of long-lasting period than the y-direction. Hence, we treat the system with a unique fast-scale variable z corresponding to a long arterial segment, and the tiniest lifted circumference is regarded only for a very short time changes. Thus, the microscopic domain Λ is $(1,\eta)$-periodic since it is scaled up by $1/\delta$ in the x-direction only. Therefore, this scenario becomes possible, as stated earlier.

According to the above assumptions we define

$$z = \frac{x}{\varepsilon}, \quad \varepsilon = \delta \ll 1, \quad x \in \Omega, \quad z \in \Lambda, \tag{4.3.3}$$

Hence, the spatial operators in the Equations (4.3.1) and (4.3.2) can be transformed as follows:

$$\frac{\partial}{\partial x} \longrightarrow \frac{\partial}{\partial x} + \frac{1}{\varepsilon}\frac{\partial}{\partial z}, \quad \frac{\partial}{\partial y} \to \frac{\partial}{\partial y}. \tag{4.3.4}$$

By applying formal asymptotic expansion in ε we have for v and w the following:

$$v(x,y,z,t) = v_0(x,y,z,t) + \varepsilon v_1(x,y,z,t) + \varepsilon^2 v_2(x,y,z,t) + \cdots, \tag{4.3.5}$$

$$w(x,y,z,t) = w_0(x,y,z,t) + \varepsilon w_1(x,y,z,t) + \varepsilon^2 w_2(x,y,z,t) + \cdots. \tag{4.3.6}$$

By substituting Equations (4.3.4), (4.3.5) and (4.3.6) into Equations (4.3.1) and (4.3.2), and by equating the terms of $O(\varepsilon^{-2})$, $O(\varepsilon^{-1})$ and $O(1)$ we respectively have

$$\frac{\partial}{\partial z}\left(D\frac{\partial v_0}{\partial z}\right) = 0, \tag{4.3.7}$$

$$\frac{\partial}{\partial x}\left(D\frac{\partial v_0}{\partial z}\right) + \frac{\partial}{\partial z}\left(D\frac{\partial v_0}{\partial x} + D\frac{\partial v_1}{\partial z}\right) = 0, \tag{4.3.8}$$

$$\frac{\partial}{\partial x}\left(D\frac{\partial v_0}{\partial x} + D\frac{\partial v_1}{\partial z}\right) + \frac{\partial}{\partial z}\left(D\frac{\partial v_1}{\partial x} + D\frac{\partial v_2}{\partial z}\right) + \frac{\partial}{\partial y}\left(D\frac{\partial v_0}{\partial y}\right) = \nu\frac{\partial v_0}{\partial t} - g(v_0) + w_0 - I. \tag{4.3.9}$$

Further, for $O(\varepsilon^{-2})$, the recovery variable w_0 satisfies

$$\frac{\partial w_0}{\partial t} + \gamma w_0 - v_0 + p = 0. \tag{4.3.10}$$

By multiplying Equation (4.3.7) by v_0 and by setting an integral over the domain Λ gives

$$\int_\Lambda v_0 \frac{\partial}{\partial z}\left(D\frac{\partial v_0}{\partial z}\right) dz = 0. \tag{4.3.11}$$

By integrating by parts of Equation (4.3.11) we get

$$Dv_0\frac{\partial v_0}{\partial z}\bigg|_\Lambda - \int_\Lambda D\left(\frac{\partial v_0}{\partial z}\right)^2 dz = 0. \tag{4.3.12}$$

Since the first term in the Equation (4.3.12) vanishes by periodicity, we have

$$\int_\Lambda D\left(\frac{\partial v_0}{\partial z}\right)^2 dz = 0. \tag{4.3.13}$$

By positivity of integral we deduce from Equation (4.3.13)

$$v_0 = v_0(x, y, t). \tag{4.3.14}$$

Therefore, from Equation (4.3.14), we have a homogenised solution as the zero$^{\text{th}}$-order component, v_0, of the membrane potential is only a possible function of macroscopic variables, x and y, and it does not dependent on the fast-scale variable $z = x/\varepsilon$.

Let us define the single-cell problem (here we call 'single-cell' instead of 'unit-cell' as the micro domain is (1,η)-periodic),

$$\frac{\partial D}{\partial z} = -\frac{\partial}{\partial z}\left(D\frac{\partial \chi}{\partial z}\right), \tag{4.3.15}$$

where $\chi(x, y; z)$ is the solution of the above single-cell problem and is (1,η)-periodic.

Now, Equations (4.3.8) and (4.3.15) gives

$$\frac{\partial}{\partial z}\left(D\frac{\partial v_1}{\partial z}\right) = -\frac{\partial D}{\partial z}\,\frac{\partial v_0}{\partial x}. \tag{4.3.16}$$

By substituting Equation (4.3.15) into Equation (4.3.16) we have

$$\frac{\partial}{\partial z}\left(D\frac{\partial}{\partial z}\left(v_1-\chi\frac{\partial v_0}{\partial x}\right)\right)=0. \tag{4.3.17}$$

By integrating Equation (4.3.17) twice over the domain Λ, we have

$$v_1(x,y;z)=\chi\frac{\partial v_0}{\partial x}+f(x,y)\int_\Lambda\frac{1}{D}dz+g(x,y), \tag{4.3.18}$$

where $f(x,y)$ and $g(x,y)$ are arbitrary functions of integration generated by z.

By applying a 1-periodic boundary condition on χ we have

$$\chi(x,y;0)=\chi(x,y;1), \tag{4.3.19}$$

we show $f(x,y)=0$. Hence, from Equation (4.3.18) we have

$$v_1(x,y;z)=\chi\frac{\partial v_0}{\partial x}+g(x,y). \tag{4.3.20}$$

Thus, the first-order term v_1 of the membrane potential is a function of both macroscopic and microscopic variables.

Now, by comparing Equations (4.3.9) and (4.3.20) and by setting an integral over the domain Λ we have

$$\begin{aligned}\int_\Lambda\frac{\partial}{\partial x}\left(D\left(1+\frac{\partial\chi}{\partial z}\right)\frac{\partial v_0}{\partial x}\right)dz+\int_\Lambda\frac{\partial}{\partial z}\left(D\left(\frac{\partial v_1}{\partial x}+\frac{\partial v_2}{\partial z}\right)\right)dz\\ +\int_\Lambda\frac{\partial}{\partial y}\left(D\frac{\partial v_0}{\partial y}\right)dz=\nu\frac{\partial v_0}{\partial t}-g(v_0)+w_0-I.\end{aligned} \tag{4.3.21}$$

By applying the fundamental theorem of calculus and by comparing Equations (4.3.14) and (4.3.21) we obtain

$$\frac{\partial}{\partial x}\left(\widetilde{D}_x\frac{\partial v_0}{\partial x}\right)+D\left(\frac{\partial v_1}{\partial x}+\frac{\partial v_2}{\partial z}\right)+\frac{\partial}{\partial y}\left(\widetilde{D}_y\frac{\partial v_0}{\partial y}\right)=\nu\frac{\partial v_0}{\partial t}-g(v_0)+w_0-I, \tag{4.3.22}$$

where $\widetilde{D}_x$ and $\widetilde{D}_y$ are given by

$$\widetilde{D}_x = \int_\Lambda D\left(1+\frac{\partial\chi}{\partial z}\right)dz, \tag{4.3.23}$$

$$\widetilde{D}_y = \int_\Lambda D\,dz, \tag{4.3.24}$$

and $w_0 = w_0(x,y,t)$.

The coefficients $\widetilde{D}_x$ and $\widetilde{D}_y$ are the homogenised PVCs in the x and y directions, respectively. Since the effective PVCs in the x and y directions are different, the medium is globally anisotropic.

By applying the periodic boundary condition to the second term on the left hand side of the Equation (4.3.22) for v_1 and v_2 we have

$$\nu\frac{\partial v_0}{\partial t} - g(v_0) + w_0 - I = \frac{\partial}{\partial x}\left(\widetilde{D}_x\frac{\partial v_0}{\partial x}\right) + \frac{\partial}{\partial y}\left(\widetilde{D}_y\frac{\partial v_0}{\partial y}\right). \tag{4.3.25}$$

Equation (4.3.25) along with Equations (4.3.10), (4.3.23) and (4.3.24) are the homogenised version of the FHN models of Equations (4.3.1) and (4.3.2), in two-dimension under the assumption made.

Now, integration of Equation (4.3.15) over the domain Λ gives

$$D\left(1+\frac{\partial\chi}{\partial z}\right) = f(x,y), \tag{4.3.26}$$

where $f(x,y)$ is an arbitrary function of integration.

By comparing Equations (4.3.23) and (4.3.26) we have

$$\widetilde{D}_x = f(x,y). \tag{4.3.27}$$

Hence, the effective PVC is only a possible function of slow-scale variables.

Now, we will find $f(x,y)$ such that $\chi(x,y;z)$ is 1-periodic in z.

We write from Equation (4.3.26),

$$\frac{\partial \chi}{\partial z} = \frac{f(x,y)}{D} - 1. \tag{4.3.28}$$

By integrating Equation (4.3.28) with respect to z we get

$$\chi(x,y;z) = f(x,y)\int_0^z \frac{1}{D(z')}\,dz' - z. \tag{4.3.29}$$

Hence, from Equation (4.3.29) we have

$$\chi(x,y;0) = 0, \tag{4.3.30}$$

$$\chi(x,y;1) = f(x,y)\int_0^1 \frac{1}{D}\,dz - 1. \tag{4.3.31}$$

By comparing Equations (4.3.19), (4.3.30) and (4.3.31) we get

$$f(x,y) = \frac{1}{\displaystyle\int_0^1 \frac{1}{D}\,dz}. \tag{4.3.32}$$

Thus, from Equations (4.3.24), (4.3.27) and (4.3.32) we have

$$\widetilde{D}_x = \frac{1}{\displaystyle\int_0^1 \frac{1}{D(x,y;z)}\,dz}, \tag{4.3.33}$$

$$\widetilde{D}_y = \int_0^1 D(x,y;z)\,dz, \tag{4.3.34}$$

$$\chi(z) = \widetilde{D}_x \int_0^z \frac{1}{D(x,y;z)}\,dz - z. \tag{4.3.35}$$

Thus, the effective PVCs in the x and y directions are given by a harmonic and arithmetic mean, respectively. Hence, the homogenised two-dimensional models are given by

$$\nu\frac{\partial v_0}{\partial t} - g(v_0) + w_0 - I = \frac{\partial}{\partial x}\left(\widetilde{D}_x\frac{\partial v_0}{\partial x}\right) + \frac{\partial}{\partial y}\left(\widetilde{D}_y\frac{\partial v_0}{\partial y}\right), \tag{4.3.36}$$

$$\frac{\partial w_0}{\partial t} = v_0 - \gamma w_0 - p, \tag{4.3.37}$$

where $\widetilde{D}_x$ and $\widetilde{D}_y$ are given by Equations (4.3.33) and (4.3.34), respectively.

4.3.1.1 Example

In this section, we apply models of Equations (4.3.33) and (4.3.34) to find the effective PVC, $\widetilde{D} = (\tilde{D}_x, \tilde{D}_y)$, and use Equation (4.3.35) to construct a solution χ of 1-periodicity.

We re-state the example provided for the one-dimensional case in Section 4.2.1, because it uses only one fast-scale variable, z, same as the problem concerned in scenario 1. Therefore, with the same assumptions stated in the example in Section 4.2.1, we recall the microscopic PVC defined by Equation (4.2.35). Hence, we have

$$D(z) = \begin{cases} D_{min}, & 0 \leq z \leq \sigma; \\ D_{max}, & \sigma \leq z \leq 1-\sigma; \\ D_{min}, & 1-\sigma \leq z \leq 1, \end{cases} \tag{4.3.38}$$

where $0 < \sigma < \frac{1}{2}$, and σ is the half membrane width.

As we defined in Section 4.2.1, let us take $D_{min} = kD_{max}$, where $0 < k < 1$. Hence, the Equation (4.3.38) can be written as

$$D(z) = \begin{cases} kD_{max}, & 0 \leq z \leq \sigma; \\ D_{max}, & \sigma \leq z \leq 1-\sigma; \\ kD_{max}, & 1-\sigma \leq z \leq 1. \end{cases} \tag{4.3.39}$$

Now, by using Equation (4.3.39) we find

$$\begin{aligned} \int_0^1 D(z)\, dz &= kD_{max} \int_0^\sigma dz + D_{max} \int_\sigma^{1-\sigma} dz + kD_{max} \int_{1-\sigma}^1 dz, \\ &= [1 - 2(1-k)\sigma] D_{max}, \end{aligned} \tag{4.3.40}$$

and

$$\begin{aligned} \int_0^1 \frac{1}{D(z)}\, dz &= \frac{1}{kD_{max}} \int_0^\sigma dz + \frac{1}{D_{max}} \int_\sigma^{1-\sigma} dz + \frac{1}{kD_{max}} \int_{1-\sigma}^1 dz, \\ &= \frac{2(1-k)\sigma + k}{kD_{max}}. \end{aligned} \tag{4.3.41}$$

By comparing Equations (4.3.33), (4.3.34), (4.3.40) and (4.3.41) we have

$$\widetilde{D}_x = \frac{kD_{max}}{2(1-k)\sigma + k}, \quad \widetilde{D}_y = [1 - 2(1-k)\sigma]D_{max}. \tag{4.3.42}$$

Further, by following Equations (4.2.39) and (4.2.40) we have

$$\chi(z) = \begin{cases} az, & 0 \le z \le \sigma; \\ b\sigma(1-2z), & \sigma \le z \le 1-\sigma; \\ az - b(1-2\sigma), & 1-\sigma \le z \le 1, \end{cases} \tag{4.3.43}$$

where

$$a = \frac{1}{2(1-k)\sigma + k} - 1 \quad \text{and} \quad b = (1-k)(1+a). \tag{4.3.44}$$

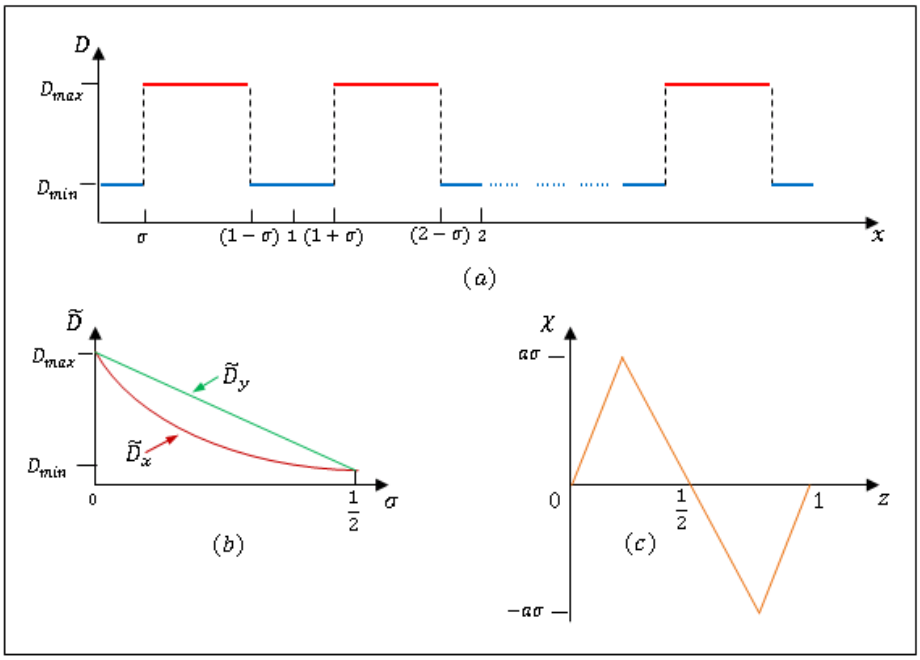

Figure 4.5: Schematic of (a) pattern of PVC in the macroscopic domain by the microscopic domain, (b) the variation of the effective PVCs, $\tilde{D} = (\tilde{D}_x$ and $\tilde{D}_y)$, with respect to different membrane width and (c) the solution, χ, for the unit-cell problem.

For a cell of very thin membrane layer (or a membrane width of negligible size compare to the cell size), effective PVC is everywhere the same and it is equivalent to the

potential variation in the cytosol because, from Equation (4.3.42), $\widetilde{D}_x, \widetilde{D}_y \to D_{max}$ as $\sigma \to 0$. This result can be considered as appropriate, as it accepts the definition of PVC defined by Equation (4.3.38).

The Figure 4.5(a) shows the pattern of macroscopic PVC via a construction of the microscopic PVC of Equation (4.3.38). As stated earlier, the variation of the effective PVC components, $\widetilde{D}_x$ and $\widetilde{D}_y$, with respect to different cellular membrane width is shown in Figure 4.5(b). Both x- and y-directional PVCs are high for a cell of thin membrane width and are low for a cell of thick membrane width. In addition, we note that the effective PVC in the y-direction always greater (rapid variation) than that of the effective PVC (slow variation) in the x-direction. This result accepts the assumption made for scenario 1. The 1-periodic solution χ for the unit cell problem is shown in Figure 4.5(c).

4.3.2 Scenario 2: Homogenisation with Different Microscopic Scales

In this case we consider slow changes of membrane potential in both x and y-spatial directions under the assumption that both the lifted circumference and the characteristic length of the arterial segment are modelled by the equal characteristic lengths. Therefore, in this case we will have two variables in both macroscopic and microscopic domains.

We define fast-scale variables z and s by the following relations:

$$z = \frac{x}{\delta}, \quad s = \frac{y}{\eta}, \quad \delta, \eta << 1, \quad x, y \in \Omega, \quad z, s \in \Lambda. \tag{4.3.45}$$

Let us take $\eta = \kappa\delta,\ \kappa \in \mathbb{R}^+$. To define a limitation on κ we consider the dimension of a single smooth muscle cell (SMC) since the type A cell resembles the SMC. The width, δ, and length, η, of an SMC belong to the intervals [3μm-10μm] and [30μm-200μm], respectively [100]. Therefore, κ can be constrained as $\frac{30}{10} \leq \kappa \leq \frac{200}{3}$. Thus,

$3 \leq \kappa \leq 66$. Moreover, let us take $\delta = \varepsilon$ for the formal asymptotic expansion and hence we have $\eta = \kappa\varepsilon$. Thus, from Equation (4.3.45) we have

$$z = \frac{x}{\varepsilon}, \quad s = \frac{1}{\varepsilon}\left(\frac{y}{\kappa}\right), \quad \varepsilon << 1, \quad 3 \leq \kappa \leq 66, \quad x, y \in \Omega, \quad z, s \in \Lambda. \tag{4.3.46}$$

Therefore, by using Equation (4.3.46), the macro-differential operators, $\frac{\partial}{\partial x}$ and $\frac{\partial}{\partial y}$, can be transformed as follows:

$$\frac{\partial}{\partial x} \longrightarrow \frac{\partial}{\partial x} + \varepsilon^{-1}\frac{\partial}{\partial z}, \quad \frac{\partial}{\partial y} \longrightarrow \frac{\partial}{\partial y} + \frac{\varepsilon^{-1}}{\kappa}\frac{\partial}{\partial s}. \tag{4.3.47}$$

The Equation (4.3.47) can then be written in the vector form:

$$\left(\frac{\partial}{\partial x}, \frac{\partial}{\partial y}\right) \longrightarrow \left(\frac{\partial}{\partial x}, \frac{\partial}{\partial y}\right) + \varepsilon^{-1}\left(\frac{\partial}{\partial z}, \frac{1}{\kappa}\frac{\partial}{\partial s}\right). \tag{4.3.48}$$

For our convenience we define the vector operators ∇_M and ∇_m such that

$$\nabla_M = \left(\frac{\partial}{\partial x}, \frac{\partial}{\partial y}\right) \text{ and } \nabla_m = \left(\frac{\partial}{\partial z}, \frac{1}{\kappa}\frac{\partial}{\partial s}\right), \tag{4.3.49}$$

where M and m denote the macroscopic and microscopic-domain, respectively, and hence the Equation (4.3.48) can be written as

$$\nabla_M \longrightarrow \nabla_M + \varepsilon^{-1}\nabla_m. \tag{4.3.50}$$

By applying on Equations (4.3.1) and (4.3.2) the operator transformations given by Equation (4.3.47) and by ordering the powers of ε, we have for $O(\varepsilon^{-2})$, $O(\varepsilon^{-1})$ and $O(1)$, respectively, the following system of equations:

$$\nabla_m \cdot (D\nabla_m v_0) = 0, \tag{4.3.51}$$

$$\nabla_M \cdot (D\nabla_m v_0) + \nabla_m \cdot (D\nabla_m v_1) + \nabla_m \cdot (D\nabla_M v_0) = 0, \tag{4.3.52}$$

$$\nabla_M \cdot (D(\nabla_M v_0 + \nabla_m v_1)) + \nabla_m \cdot (D(\nabla_M v_1 + \nabla_m v_2)) = \nu\nabla_t v_0 - g(v_0) + w_0 - I \tag{4.3.53}$$

and for $O(\varepsilon^{-2})$, we have for the recovery variable a relation:

$$\frac{\partial w_0}{\partial t} = -v_0 - \gamma w_0 - p. \tag{4.3.54}$$

We note that the Equation (4.3.51) is independent of ∇_M and therefore, by integrating that equation over the micro-domain Λ and by applying periodicity we have

$$v_0 = v_0(x, y). \tag{4.3.55}$$

Thus, the zero$^{\text{th}}$-order term of the membrane potential has been predicted in the macroscopic domain. Therefore, we have a homogenised term, as it is independent of z and s.

Now, by substituting Equation (4.3.55) into Equation (4.3.52) we get

$$\nabla_m \cdot (D\nabla_m v_1) = -\nabla_m D \cdot \nabla_M v_0, \tag{4.3.56}$$

as v_0 is independent of z and s.

Let us define the unit-cell problem in two-dimension:

$$\nabla_m D \cdot \mathbb{I} = -\nabla_m \cdot (D\,\nabla_m \chi), \tag{4.3.57}$$

where $\mathbb{I}$ is a unitary operator and $\chi(x, y; z, s)$ is 1-periodic in z and s. Moreover χ is the solution of the problem given by Equation (4.3.57), which can be re-arranged as

$$\nabla_m \cdot D(\mathbb{I} + \nabla_m \chi) = 0. \tag{4.3.58}$$

By substituting Equation (4.3.57) into (4.3.56) and then by integrating over the domain Λ we have

$$\nabla_m \cdot v_1 \mathbb{I} = \nabla_m \chi \cdot \nabla_M v_0 + \frac{g(x, y)}{D} \cdot \mathbb{I}, \tag{4.3.59}$$

where $g(x, y) = (g_1(x, y), g_2(x, y))$ are functions of integration defined on Ω.

Again by integrating over the domain Λ the Equation (4.3.59) we have a componentwise equation:

$$v_1 \mathbb{I} = \chi \nabla_M v_0 + g(x, y) \int_\Lambda \frac{1}{D}\, d\phi + h(x, y) \tag{4.3.60}$$

where $\phi = z$ or s and $h(x, y) = (h_1(x, y), h_2(x, y))$ is a function of integration defined on Ω.

Since v_1 and χ are 1-periodic in z and s, applying these periodic boundary conditions result as $(g(x, y) = 0)$

$$v_1\mathbb{I} = \chi\nabla_M v_0 + h(x, y) \tag{4.3.61}$$

Now, by comparing Equations (4.3.53) and (4.3.61) we have

$$\nu\nabla_t v_0 - g(v_0) + w_0 - I = \nabla_M.(D(\mathbb{I} + \nabla_m\chi)\nabla_M v_0) + \nabla_m.(D(\nabla_M v_1 + \nabla_m v_2)) \tag{4.3.62}$$

We note that the left-hand side of the Equation (4.3.62) is independent of (z, s). Hence by integrating the Equation (4.3.62) over the domain Λ, and then applying the fundamental theorem of calculus in two-dimension and periodic boundary conditions we have

$$\nu\nabla_t v_0 - g(v_0) + w_0 - I = \nabla_M.\left(\int_\Lambda D(\mathbb{I} + \nabla_m\chi)d\phi\,\nabla_M v_0\right) + D(\nabla_M v_1 + \nabla_m v_2). \tag{4.3.63}$$

Since the first and second-order terms, v_1 and v_2, of membrane potential are 1-periodic in z and s and by applying the periodic boundary conditions to the Equation (4.3.63) we obtain

$$\nu\nabla_t v_0 - g(v_0) + w_0 - I = \nabla_M \cdot \left(\widetilde{D}\nabla_M v_0\right), \tag{4.3.64}$$

where the effective PVC is defined by the componentwise equation:

$$\widetilde{D} = \int_\Lambda D(\mathbb{I} + \nabla_m\chi)d\phi, \tag{4.3.65}$$

where $\widetilde{D} = (\widetilde{D}_x, \widetilde{D}_y)$.

We note that Equations (4.3.64) and (4.3.65) to be the homogenised models as they are independent of z and s .

By integrating Equation (4.3.58) over the domain Λ we have

$$D(\mathbb{I} + \nabla_m \chi) = f(x, y). \tag{4.3.66}$$

where $f(x, y) = (f_1(x, y), f_2(x, y))$ is a constant vector.

Now, by substituting Equation (4.3.66) into Equation (4.3.65) we get

$$\widetilde{D} = f(x, y). \tag{4.3.67}$$

That is, from Equations (4.3.65) and (4.3.67), we have a componentwise equation:

$$\widetilde{D}_x = f_1(x, y), \quad \widetilde{D}_y = f_2(x, y). \tag{4.3.68}$$

Hence, the effective PVC are a constant in the macroscopic domain.

Now, we will find f_1 and f_2 such that $\chi(x, y; z, s)$ be a 1-periodic solution in the microscopic domain. From Equation (4.3.66) we have

$$1 + \frac{\partial \chi}{\partial z} = \frac{f_1}{D}, \tag{4.3.69}$$

$$1 + \frac{1}{\kappa}\frac{\partial \chi}{\partial s} = \frac{f_2}{D}. \tag{4.3.70}$$

By integrating Equation (4.3.69) with respect to z we have

$$\chi(x, y; z, s) = f_1 \int_0^z \frac{1}{D(x, y; z', s)}\, dz' - z + g_1(x, y; s). \tag{4.3.71}$$

where $g_1(x, y; s)$ is a function of integration in the microscopic domain.

Now, by differentiating Equation (4.3.71) with respect to s we get

$$\frac{\partial \chi}{\partial s} = f_1 \frac{\partial}{\partial s}\left(\int_0^z \frac{1}{D(x, y; z', s)}\, dz'\right) + \frac{dg_1}{ds}. \tag{4.3.72}$$

By comparing Equations (4.3.70) and (4.3.72) we have

$$\frac{dg_1}{ds} = \kappa\left(\frac{f_2}{D} - 1\right) - f_1 \frac{\partial}{\partial s}\left(\int_0^z \frac{1}{D(x, y; z', s)}\, dz'\right). \tag{4.3.73}$$

Now, by integrating Equation (4.3.73) with respect to s we have

$$g_1 = \kappa f_2 \int_0^s \frac{1}{D(x,y;z,s')}\,ds' - \kappa s - f_1 \int_0^z \frac{1}{D(x,y;z',s)}\,dz' + a, \tag{4.3.74}$$

where a is a constant of integration.

By substituting Equation (4.3.74) into Equation (4.3.71) we obtain

$$\chi(x,y;z,s) = \kappa f_2 \int_0^s \frac{1}{D(x,y;z,s')}\,ds' - z - \kappa s + a. \tag{4.3.75}$$

By starting from Equation (4.3.70) and by following the similar approach used earlier we have another form for χ given by

$$\chi(x,y;z,s) = f_1 \int_0^z \frac{1}{D(x,y;z',s)}\,dz' - z - \kappa s + b, \tag{4.3.76}$$

where b is a constant of integration.

Relations given by Equations (4.3.75) and (4.3.76) should be consistent for a unique determination of χ.

Hence, by finding $\chi(x,y;0,0)$ using Equations (4.3.75) and (4.3.76) and by equating them we have

$$a = b. \tag{4.3.77}$$

The Equation (4.3.77) along with Equations (4.3.75) and (4.3.76) shows that the last three terms on the right hand side of Equations (4.3.75) and (4.3.76) are identical. Therefore, for consistency of χ, the first term on the right hand side of the Equations (4.3.75) and (4.3.76) must be identical for any value of $z = \hat{z}$ and $s = \hat{s}$, where $0 \le \hat{z} \le 1$, and $0 \le \hat{s} \le 1$.

Hence, we have

$$f_1 \int_0^{\hat{z}} \frac{1}{D(x,y;z,\hat{s})}\,dz = \kappa f_2 \int_0^{\hat{s}} \frac{1}{D(x,y;\hat{z},s)}\,ds. \tag{4.3.78}$$

Now, we will use an appropriate boundary condition to find f_1 and f_2 separately so that the solution, χ, of the unit cell problem to be 1-periodic.

Since the integral in Equation (4.3.75) varies in the direction of s we will fix $z = \hat{z} \in [0,1]$ and use the 1- periodic boundary condition: $\chi(x,y;\hat{z},0) = \chi(x,y;\hat{z},1)$.

Hence, from Equation (4.3.75) we have

$$-\hat{z} + a = \kappa f_2 T_s(\hat{z}) - \hat{z} - \kappa + a, \tag{4.3.79}$$

where

$$T_s(\hat{z}) = \int_0^1 \frac{1}{D(x,y;\hat{z},s)}\, ds. \tag{4.3.80}$$

Equation (4.3.79) gives

$$f_2(x,y) = \frac{1}{T_s(\hat{z})}. \tag{4.3.81}$$

By similar argument we find f_1 using Equation (4.3.76) and the periodic boundary condition: $\chi(x,y;0,\hat{s}) = \chi(x,y;1,\hat{s})$, where $s = \hat{s} \in [0,1]$. Hence, we have

$$f_1(x,y) = \frac{1}{T_z(\hat{s})}, \tag{4.3.82}$$

where

$$T_z(\hat{s}) = \int_0^1 \frac{1}{D(x,y;z,\hat{s})}\, dz. \tag{4.3.83}$$

As a special case, let us assume that D to be in the variable separable form:

$$D(x,y;z,s) = \mu(z)\mu(s).$$

Then, Equations (4.3.80) and (4.3.83) can be respectively written as

$$T_s(\hat{z}) = \int_0^1 \frac{1}{D(x,y;\hat{z},s)}\, ds = \frac{1}{\mu(\hat{z})} \int_0^1 \frac{1}{\mu(s)}\, ds, \tag{4.3.84}$$

$$T_z(\hat{s}) = \int_0^1 \frac{1}{D(x,y;z,\hat{s})}\, dz = \frac{1}{\mu(\hat{s})} \int_0^1 \frac{1}{\mu(z)}\, dz. \tag{4.3.85}$$

By comparing Equations (4.3.81), (4.3.82), (4.3.84) and (4.3.85), and substituting the resultant equation into Equation (4.3.68) we have the effective PVC components:

$$\widetilde{D}_x = \mu(\hat{s})\frac{1}{\displaystyle\int_0^1 \frac{1}{\mu(z)}\,dz} \tag{4.3.86}$$

$$\widetilde{D}_y = \mu(\hat{z})\frac{1}{\displaystyle\int_0^1 \frac{1}{\mu(s)}\,ds}. \tag{4.3.87}$$

We observe, from Equations (4.3.86) and (4.3.87), that the effective PVC components to be a multiple of two terms where the one-dimensional harmonic mean has been scaled by a constant.

Reduction 4.3.2.1: For $\mu(\hat{s}) = \mu(\hat{z}) = 1$, we deduce the effective PVC to the one in the one-dimensional problem given by Equation (4.2.30), where $\widetilde{D}_x$ and $\widetilde{D}_y$ can be separately treated as one-dimensional models. Thus, two-dimensional effective PVC components are the scaled one-dimensional effective PVCs (see equation (4.2.30)).

Reduction 4.3.2.2: For $\mu(\hat{z}), \mu(\hat{s}) > 1$, the two-dimensional PVC is greater than that of the corresponding one-dimensional PVC, and we call it as 'accelerated 1D-PVC'. Similarly, a 'decelerated 1D-PVC' can be defined for the two-dimensional diffusion for $\mu(\hat{z}), \mu(\hat{s}) < 1$.

Reduction 4.3.2.3: From Equations (4.3.78) and (4.3.80)-(4.3.83) we have

$$\frac{\displaystyle\int_0^{\hat{z}} \frac{1}{D(x,y;z,\hat{s})}\,dz}{\displaystyle\int_0^1 \frac{1}{D(x,y;z,\hat{s})}\,dz} = \kappa\frac{\displaystyle\int_0^{\hat{s}} \frac{1}{D(x,y;\hat{z},s)}\,ds}{\displaystyle\int_0^1 \frac{1}{D(x,y;\hat{z},s)}\,ds} \tag{4.3.88}$$

Hence, Equation (4.3.88) can be written as

$$\frac{1}{\int_0^1 \frac{1}{D}\,dz} \times \frac{1}{\frac{1}{\int_0^{\hat{z}} \frac{1}{D}\,dz}} = \kappa \frac{1}{\int_0^1 \frac{1}{D}\,ds} \times \frac{1}{\frac{1}{\int_0^{\hat{s}} \frac{1}{D}\,ds}}. \tag{4.3.89}$$

Therefore, Equation (4.3.89) gives

$$\widetilde{D}_y^R = \kappa \widetilde{D}_x^R, \tag{4.3.90}$$

where $\widetilde{D}_x^R$ and $\widetilde{D}_y^R$ are defined to be the x- and y-directional "relative effective PVC", respectively, corresponding to the point $(\hat{z}, \hat{s})$, which are given by

$$\widetilde{D}_x^R = \frac{1}{\int_0^{\hat{z}} \frac{1}{D}\,dz} \times \frac{1}{\frac{1}{\int_0^1 \frac{1}{D}\,dz}} = \frac{1}{\int_0^{\hat{z}} \frac{1}{D}\,dz} \times \frac{1}{\widetilde{D}_x}, \tag{4.3.91}$$

$$\widetilde{D}_y^R = \frac{1}{\int_0^{\hat{s}} \frac{1}{D}\,ds} \times \frac{1}{\frac{1}{\int_0^1 \frac{1}{D}\,ds}} = \frac{1}{\int_0^{\hat{s}} \frac{1}{D}\,ds} \times \frac{1}{\widetilde{D}_y}. \tag{4.3.92}$$

From Equation (4.3.90), we proved for an arbitrary point $(\hat{z}, \hat{s}) \in [0,1] \times [0,1]$ the y-directional relative effective PVC to be the κ multiple of the x-directional relative PVC. Since $(\hat{z}, \hat{s})$ is arbitrary, the result is true for all point in the two-dimensional domain. Therefore, dimension of a single cell play a role in determining the effective PVC along the axes of the macroscopic system. We will take this result for numerical simulations in the next chapter.

Reduction 4.3.2.4: We have physiologically restricted κ in the interval [3, 66]. However, if we allow (mathematically) κ to vary from 0 to ∞, then we can summarize the following results;

i. As $\kappa \to 1$, from Equations (4.3.90), $\widetilde{D}_y^R \to \widetilde{D}_x^R$. That is, our models can be deduced to homogenised models of a square cell (see the intersection of two curves in Figure 4.6).

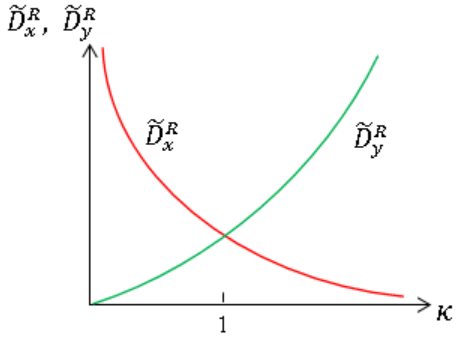

Figure 4.6: Schematic shows the variation of effective, relative PVCs for various cell dimension in terms of κ, not to scale.

ii. From Equations (4.3.90), (4.3.91) and (4.3.92), $\widetilde{D}_y^R \to \infty$ and $\widetilde{D}_x^R \to 0$ as $\kappa \to \infty$ (see Figure 4.6). Similarly, $\widetilde{D}_y^R \to 0$ and $\widetilde{D}_x^R \to \infty$ as $\kappa \to 0$. That is, as mentioned earlier, $\widetilde{D}_y$ need to be high for a cell of $\eta >> \delta$ to carry the potential effects along the y-direction and this result is logically true.

4.3.2.1 Example 1

As used in the previous sections, we construct similar examples for illustrating the effective PVC components, $\widetilde{D}_x$ and $\widetilde{D}_y$, for the system considered in scenario 2. For this, we apply the homogenised models given by Equations (4.3.80)-(4.3.83) to derive the effective PVCs.

Based on similar assumptions stated earlier, for simplicity, we assume the microscopic PVC D to be in the variable separable form:

$$D(x, y; z, s) = D(x, y)D(z, s). \tag{4.3.93}$$

In the interest of studying the macroscopic variation via the periodicity of the microscopic PVC, we only concentrate on $D(z, s)$ rather than on diffusion $D(x, y)$. Therefore, as one of the forms of the microscopic PVC we choose $D(z, s)$ to be in the

variable separable form:

$$D(z,s) = \mu(z)\mu(s). \tag{4.3.94}$$

As stated in Section 4.2.1, we model this problem under the following assumptions:

(**A1**) PVC in the cytosol is higher than the diffusion in the cellular membrane,

(**A2**) PVC in the cytosol and membrane in the z- and s-direction are different,

(**A3**) pattern of PVC in the z- and s-direction respectively obeys the form of first-order spline as shown in Figure 4.2(b)(i),

(**A4**) the width of the membrane, 2σ, is small enough in size compared to the size of the unit-cell.

Hence, by assumptions (**A1**)-(**A3**) we have

$$\mu(z) = \begin{cases} D_{minz}, & 0 \le z \le \sigma; \\ D_{maxz}, & \sigma \le z < \frac{1}{2}; \\ D_{max}, & z = \frac{1}{2}; \\ D_{maxz}, & \frac{1}{2} < z \le 1-\sigma; \\ D_{minz}, & 1-\sigma \le z \le 1, \end{cases} \tag{4.3.95}$$

and

$$\mu(s) = \begin{cases} D_{mins}, & 0 \le s \le \sigma; \\ D_{maxs}, & \sigma \le s < \frac{1}{2}; \\ D_{max}, & s = \frac{1}{2}; \\ D_{maxs}, & \frac{1}{2} < s \le 1-\sigma; \\ D_{mins}, & 1-\sigma \le s \le 1, \end{cases} \tag{4.3.96}$$

where D_{max} is a superposition of D_{maxz} and D_{maxs} in the centre of the cytosol, and $D_{minz} < D_{maxz}$ and $D_{mins} < D_{maxs}$. Further, by assumption (**A1**), we have $D_{minz} = k_z D_{maxz}$, and $D_{mins} = k_s D_{maxs}$, where $0 < k_z < 1$ and $0 < k_s < 1$. Moreover, σ is the half membrane width which satisfies $0 < \sigma < \frac{1}{2}$ due to the assumption (**A4**).

Thus, Equation (4.3.95) and (4.3.96) can be respectively written as

$$\mu(z) = \begin{cases} k_z D_{maxz}, & 0 \leq z \leq \sigma; \\ D_{maxz}, & \sigma \leq z < \frac{1}{2}; \\ D_{max}, & z = \frac{1}{2}; \\ D_{maxz}, & \frac{1}{2} < z \leq 1 - \sigma; \\ k_z D_{maxz}, & 1 - \sigma \leq z \leq 1, \end{cases} \tag{4.3.97}$$

and

$$\mu(s) = \begin{cases} k_s D_{maxs}, & 0 \leq s \leq \sigma; \\ D_{maxs}, & \sigma \leq s < \frac{1}{2}; \\ D_{max}, & s = \frac{1}{2}; \\ D_{maxs}, & \frac{1}{2} < s \leq 1 - \sigma; \\ k_s D_{maxs}, & 1 - \sigma \leq s \leq 1, \end{cases} \tag{4.3.98}$$

Now, by using Equation (4.3.97) we find

$$\begin{aligned} \int_0^1 \frac{1}{\mu(z)}\, dz &= \frac{1}{k_z D_{maxz}} \left(\int_0^{\sigma} dz + k_z \int_{\sigma}^{1-\sigma} dz + \int_{1-\sigma}^{1} dz \right), \\ &= \frac{2(1-k_z)\sigma + k_z}{k_z D_{maxz}}. \end{aligned} \tag{4.3.99}$$

Similarly, by applying Equation (4.3.96), we have

$$\int_0^1 \frac{1}{D(s)}\, ds = \frac{2(1-k_s)\sigma + k_s}{k_s D_{maxs}}. \tag{4.3.100}$$

By substituting Equations (4.3.99) and (4.3.100) into Equations (4.3.86) and (4.3.87) we have the effective PVC components, $\widetilde{D}_x$ and $\widetilde{D}_y$ as follows:

$$\widetilde{D}_x = \frac{k_z D_{maxz} \mu(\hat{s})}{2(1-k_z)\sigma + k_z}, \quad \widetilde{D}_y = \frac{k_s D_{maxs} \mu(\hat{z})}{2(1-k_s)\sigma + k_s}. \tag{4.3.101}$$

where $0 \leq \hat{z}, \hat{s} \leq 1$. Hence, Equation (4.3.101) can be written as

$$\widetilde{D}_x = \mu(\hat{s}) \mathfrak{D}_x, \quad \widetilde{D}_y = \mu(\hat{z}) \mathfrak{D}_y, \tag{4.3.102}$$

where $\mathfrak{D}_x$ and $\mathfrak{D}_y$ are given by

$$\mathfrak{D}_x = \frac{k_z D_{maxz}}{2(1-k_z)\sigma + k_z}, \quad \mathfrak{D}_y = \frac{k_s D_{maxs}}{2(1-k_s)\sigma + k_s}. \tag{4.3.103}$$

Hence, from Equations (4.3.102) and (4.3.103), we observe that $\widetilde{D}_x$ and $\widetilde{D}_y$ have been obtained by scaling the one-dimensional effective PVCs; $\mathfrak{D}_x$ and $\mathfrak{D}_y$ (see equations (4.2.38)) by $\mu(\hat{s})$ and $\mu(\hat{z})$, respectively. Since $\mu(\hat{z})$ and $\mu(\hat{s})$ are defined on the interval [0,1], $\widetilde{D}_x$ and $\widetilde{D}_y$ can be differently defined on [0,1]×[0,1] based on values taken by $\hat{z}$ and $\hat{s}$. In other words, as stated earlier, $\widetilde{D}_x$ and $\widetilde{D}_y$ are the accelerated or decelerated $\mathfrak{D}_x$ and $\mathfrak{D}_y$ corresponding to $\mu(\hat{s}) \gtrless 1$ and $\mu(\hat{z}) \gtrless 1$, respectively. As a simplest case, for $\mu(\hat{z}) = \mu(\hat{s}) = 1$, one can see that $\widetilde{D}_x$ and $\widetilde{D}_y$ are deduced to $\mathfrak{D}_x$ and $\mathfrak{D}_y$, respectively.

As discussed in the earlier examples, for a thin and thick cellular membrane layers, we analyse the problem in the σ-limit of 0 and 1/2, respectively. From Equations (4.3.102) and (4.3.103), we have

$$\begin{aligned} &\widetilde{D}_x \longrightarrow \mu(\hat{s}) D_{maxz}, \quad \widetilde{D}_y \longrightarrow \mu(\hat{z}) D_{maxs}, \quad \text{as} \quad \sigma \longrightarrow 0, \\ &\widetilde{D}_x \longrightarrow \mu(\hat{s}) D_{minz}, \quad \widetilde{D}_y \longrightarrow \mu(\hat{z}) D_{mins}, \quad \text{as} \quad \sigma \longrightarrow 1/2. \end{aligned} \tag{4.3.104}$$

Further, for $\hat{z}, \hat{s} \in [0, \sigma]$ (the case of cellular membrane), from Equations (4.3.95), (4.3.96) and (4.3.104), we have

$$\begin{aligned} &\widetilde{D}_x \longrightarrow D_{mins} D_{maxz}, \quad \widetilde{D}_y \longrightarrow D_{minz} D_{maxs}, \quad \text{as} \quad \sigma \longrightarrow 0, \\ &\widetilde{D}_x \longrightarrow D_{mins} D_{minz}, \quad \widetilde{D}_y \longrightarrow D_{minz} D_{mins}, \quad \text{as} \quad \sigma \longrightarrow 1/2. \end{aligned} \tag{4.3.105}$$

Results in Equation (4.3.105) are shown in Figure 4.7. The red curve in the middle illustrates that how does the effective PVC changes for cells of different membrane width, in one-dimension (for which $D_{minz}, D_{mins} = 1$). The green and blue curves illustrate the scaled $D_{minz}, D_{mins} > 1$ and $0 < D_{minz}, D_{mins} < 1$, respectively, variation of the effective PVC against cells of different membrane width, in two-dimension.

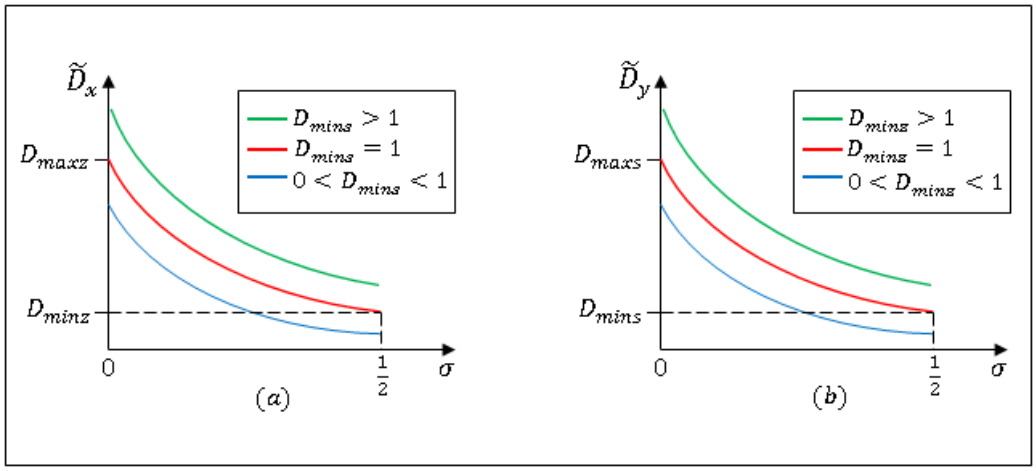

Figure 4.7: Schematic shows (a) $\widetilde{D}_x$ and (b) $\widetilde{D}_y$, against cells of different membrane width. Curves in red indicate the effective PVCs along the x- and y-directions in one-dimension, while the effective PVCs along the x- and y-directions in two-dimension are shown by curves of green and blue. The green and blue curves illustrate an accelerated and decelerated effective PVCs, respectively, of the effective PVC shown by the red curves.

Now, we calculate the integral:

$$\int_0^s \frac{1}{\mu(s)}\,ds = \begin{cases} \dfrac{s}{k_s D_{maxs}}, & 0 \le s \le \sigma; \\ \dfrac{(1-k_s)\sigma + k_s s}{k_s D_{maxs}}, & \sigma \le s \le 1-\sigma; \\ \dfrac{s-(1-k_s)(1-2\sigma)}{k_s D_{maxs}}, & 1-\sigma \le s \le 1. \end{cases} \tag{4.3.106}$$

By substituting Equations (4.3.102) and (4.3.106) into Equation (4.3.75), we have a 1-periodic solution for the unit-cell problem as:

$$\chi(z,s) = \begin{cases} as - z, & 0 \le s \le \sigma; \\ bs - z + c, & \sigma \le s \le 1-\sigma; \\ as - z - d, & 1-\sigma \le s \le 1, \end{cases} \tag{4.3.107}$$

where

$$a = \left(\frac{1}{2(1-k_s)\sigma + k_s} - 1\right)\kappa, \quad b = (a+\kappa)k_s - \kappa,$$
$$c = \sigma(a-b), \qquad\qquad d = (1-2\sigma)(a-b), \tag{4.3.108}$$

and $a, c, d > 0$ and $b < 0$ since $\sigma < \frac{1}{2}, k_s < 1$ and $\kappa > 1$.

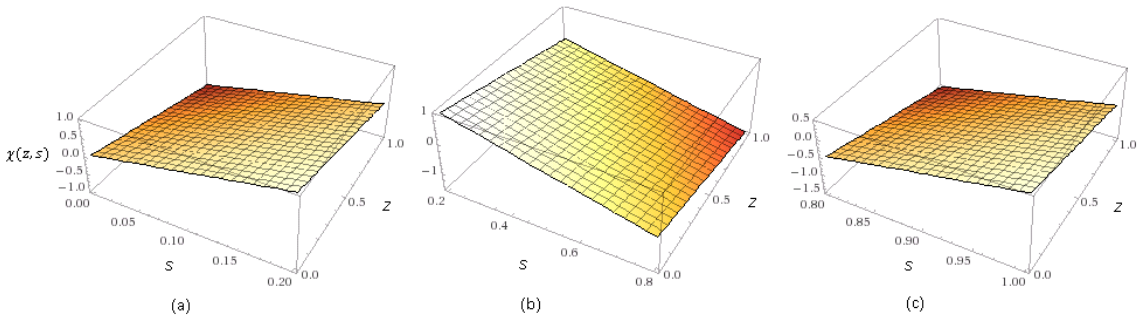

Figure 4.8: Schematic shows a 1-periodic solution, $\chi(z,s)$, for the unit cell problem for a set of dimensionless parameter values: σ=0.2, k_s=0.5 and κ=10, using Equations (4.3.107) and (4.3.108). Subplots (a), (b) and (c) together show the 1-periodicity of $\chi(z,s)$ modelled by piece-wise function in the intervals [0, 0.2], [0.2, 0.8], and [0.8, 1] in Equations (4.3.107) and (4.3.108).

Similarly, using Equation (4.3.76), a consistent relation for $\chi(z,s)$ can be found as follows:

$$\chi(z,s) = \begin{cases} \xi z - \kappa s, & 0 \le z \le \sigma; \\ \zeta z - \kappa s + \vartheta, & \sigma \le z \le 1-\sigma; \\ \xi z - \kappa s - \rho, & 1-\sigma \le z \le 1, \end{cases} \tag{4.3.109}$$

where

$$\xi = \frac{1}{2(1-k_z)\sigma + k_z} - 1, \quad \zeta = (\xi+1)k_z - 1,$$
$$\vartheta = \sigma(\xi - \zeta), \qquad\qquad \rho = (1-2\sigma)(\xi - \zeta). \tag{4.3.110}$$

The Figure 4.8 shows a 1-periodic solution of $\chi(z,s)$. The 1-periodicity is divided in the sub-intervals (a)$[0,\sigma]$, (b)$[\sigma, 1-\sigma]$ and (c)$[1-\sigma, 1]$, as $\chi(z,s)$ is modelled by piece-wise functions in the respective sub-intervals. For this, we used a set of non-dimensional parameter values; σ=0.2, k_s=0.5 and κ=10, where the half membrane

width, σ, was set to 0.2. Further, by using k_s=0.5, we assumed the microscopic PVC for the cellular membrane to be a half of the microscopic PVC for the cellular cytosol, along the s-axis. In addition, the length of the cell was assumed to be 10 times grater than the width of the cell and hence κ=10. Similar schematic of Figure 4.8 can also be illustrated for the unit-cell problem using Equations (4.3.109) and (4.3.110).

4.3.2.2 Example 2

In this example we derive an effective PVC in two-dimension using a combination of zeroth- and first-order splines as shown in Figures 4.2(b)(i) and 4.2(b)(ii), respectively. We assume the PVC to be different along the length-wise direction (s-direction) in the cytosol, which periodically reduces from the peak value at the centre of the cytosol to a law value in the cellular membrane. This assumption replaces the assumption (A3) stated in the Example in Section 4.3.2.1 and hence we use the model in Figure 4.2(b)(ii) for the PVC along the s-direction. Moreover, we apply the model in Figure 4.2(b)(i) for the microscopic PVC along the z-axis. These two forms are chosen due to the fact that the variation in s-direction is slower than the z-directional variation based on the dimension of the single cell. We will otherwise follow all other assumptions stated in the Example in Section 4.3.2.1.

We use the same definition for $D(z,s) = \mu(z)\mu(s)$ (see Figure 4.9(a)) and from Equation (4.3.95) we have

$$\mu(z) = \begin{cases} D_{minz}, & 0 \leq z < \sigma; \\ D_{max}, & \sigma \leq z \leq 1-\sigma; \\ D_{minz}, & 1-\sigma < z \leq 1. \end{cases} \tag{4.3.111}$$

In addition, we re-define the microscopic PVC along the s-direction (see Figure 4.9(b) based on the above assumptions as;

$$\mu(s) = \begin{cases} D_{mins}, & 0 \le s \le \sigma; \\ as + b, & \sigma \le s < \frac{1}{2}; \\ D_{max}, & \sigma = \frac{1}{2}; \\ -as + c, & \frac{1}{2} < s \le 1 - \sigma; \\ D_{mins}, & 1 - \sigma \le s \le 1, \end{cases} \tag{4.3.112}$$

where σ is the half membrane width and

$$\begin{aligned} a = \frac{D_{max} - D^\star}{\varsigma}, \qquad b = \frac{(2\varsigma - 1)D_{max} + D^\star}{2\varsigma}, \quad c = a + b, \\ D_{minz} = k_z D_{max}, \qquad D_{mins} = a\sigma + b, \quad k_z < 1, \end{aligned} \tag{4.3.113}$$

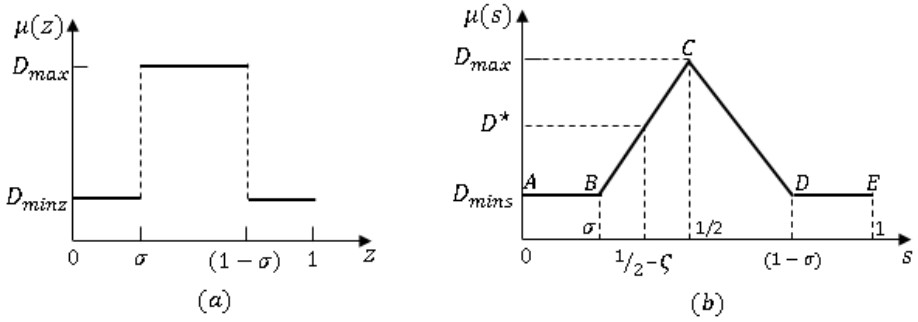

Figure 4.9: Schematic shows the microscopic variation of diffusion along (a) z- and (b) s-direction. Maximum value at the center of the cytosol is set up as D_{max} in both cases.

and ς is an arbitrary point in the interval $[\sigma, \frac{1}{2}]$ satisfying $0 < \varsigma + \sigma < \frac{1}{2}$. Note that the maximum value of $\mu(z)$ and $\mu(s)$ is taken as D_{max}, which is the value at the centre of the cytosol.

As derived in the previous example, from Equation (4.3.101), we have the effective PVC in the x-direction as

$$\widetilde{D}_x = \frac{k_z D_{max} \mu(\hat{s})}{2(1 - k_z)\sigma + k_z}, \tag{4.3.114}$$

where $\mu(\hat{s})$ is defined by Equation (4.3.112). Now, we find

$$\begin{aligned}\int_0^1 \frac{1}{D(s)}\,ds &= \int_0^{\sigma} \frac{1}{D_{mins}}\,ds + \int_{\sigma}^{\frac{1}{2}} \frac{1}{as+b}\,ds + \int_{\frac{1}{2}}^{1-\sigma} \frac{1}{-as+c}\,ds + \int_{1-\sigma}^{1} \frac{1}{D_{mins}}\,ds \\ &= \frac{\sigma}{a\sigma+b} + \frac{1}{a}\ln\left|\frac{\frac{a}{2}+b}{a\sigma+b}\right| - \frac{1}{a}\ln\left|\frac{-a(1-\sigma)+c}{-\frac{a}{2}+c}\right| + \frac{\sigma}{a\sigma+b} \\ &= \frac{2\sigma}{a\sigma+b} + \frac{1}{a}\ln\left|\left(\frac{\frac{a}{2}+b}{a\sigma+b}\right)^2\right|. \end{aligned} \tag{4.3.115}$$

As derived earlier, from Equation (4.3.87), the effective PVC in the y-direction is given by

$$\widetilde{D}_y = \mu(\hat{z})\frac{1}{\int_0^1 \frac{1}{D(s)}\,ds}, \tag{4.3.116}$$

where $\mu(\hat{z})$ is given by equation (4.3.111).

Therefore, by comparing Equations (4.3.115) and (4.3.116) we have

$$\widetilde{D}_y = \frac{a(a\sigma+b)\mu(\hat{z})}{2a\sigma + (a\sigma+b)\ln|c^{\star}|}, \tag{4.3.117}$$

where $c^{\star} = \left(\frac{\frac{a}{2}+b}{a\sigma+b}\right)^2$.

As predicted earlier, from Equations (4.3.114) and (4.3.117), the effective PVCs in the x- and y-directions are high or low based on $\mu(\hat{s}) \gtrless 1$ and $\mu(\hat{z}) \gtrless 1$, respectively.

Now, by using Equations (4.3.113) and (4.3.117) we have

$$\begin{aligned}\widetilde{D}_y &\longrightarrow \frac{a\mu(\hat{z})}{\ln|(c^{\star})_{\sigma=0}|} = \frac{(D_{max}-D^{\star})\mu(\hat{z})}{\varsigma\ln\left|\left(\frac{2\varsigma D_{max}}{(2\varsigma-1)D_{max}+D^{\star}}\right)^2\right|} \quad as \quad \sigma \longrightarrow 0, \\ \widetilde{D}_y &\longrightarrow \left(\frac{a}{2}+b\right)\mu(\hat{z}) = \mu(\hat{z})D_{max} \quad as \quad \sigma \longrightarrow \frac{1}{2}. \end{aligned} \tag{4.3.118}$$

Further, from Equation (4.3.114) we note

$$\begin{aligned} \widetilde{D}_x &\longrightarrow \mu(\hat{s})D_{max} \quad as \quad \sigma \longrightarrow 0, \\ \widetilde{D}_x &\longrightarrow \mu(\hat{s})D_{minz} \quad as \quad \sigma \longrightarrow \frac{1}{2}. \end{aligned} \tag{4.3.119}$$

For example, consider a simplest case: $\mu(\hat{z}) = \mu(\hat{s}) = 1$. Then, for a cell of thick membrane layer we have $\widetilde{D}_x \longrightarrow D_{minz}$ and $\widetilde{D}_y \longrightarrow D_{max}$ as $\sigma \longrightarrow \frac{1}{2}$. Hence, $\widetilde{D}_x < \widetilde{D}_y$. However, the result may vary based on definition of $\mu(z)$ and $\mu(s)$ as well as the specific values of $\mu(\hat{z})$ and $\mu(\hat{s})$. In addition, a simplest form of the unit cell solution $\chi(z, s)$ can be found as stated in the previous example.

4.4 Summary

In this chapter, we have derived one- and two-dimensional homogenised models for the reaction diffusion-type equations developed in Chapters 2 and 3. These homogenised models were derived based on different length scales; macroscopic and microscopic scales, using formal asymptotic analysis. The potential variation coefficient (PVC) at the microscopic level was allowed in both fast and slow-scales. Importantly, we derived the homogenised models based on the dimension of the microscopic (cellular-level) and macroscopic (arterial-level) domains. Therefore, our models discovered more comprehensive and cohesive communication protocols between homocellular cells rather than the homogenised models derived so far. Hence, the method and the results showed in this chapter can be applied to study the multiple scale structure of a system with more complexity, such as heterocellular communication. As an application of the one- and 2-dimensional homogenised models, we constructed some number numerical examples under different scenarios and showed some relevant results that may be considered in relation to cellular physiology. In addition, 1-periodic solution for the unit cell problem was also illustrated for the numerical examples.

In the following chapter we will numerically solve the one- and two-dimensional homogenised models derived in this chapter and study for the system dynamics.

Chapter 5

Numerical Simulations, Results and Discussion

In this chapter we will firstly consider the membrane potential models of a ring of discrete coupled cells derived in Chapter 2 and study the dynamical properties of that system under a bifurcation parameter. As the second and third cases, we undertake a numerical simulation study for describing in detail the dynamics of the cellular membrane potential variation of type A cells, using the one- and two-dimensional homogenised partial differential equations (HPDEs) derived in Chapter 4.

5.1 Parameter Determination

This section discusses the possibility of assigning values for the parameters in our discrete models, given by Equations (5.2.1) and (5.3.1) and in the one- and two-dimensional HPDEs derived in Chapter 4. Most of the literature on the dynamical system based on one-dimensional FHN models deal with a single FHN system, in the absence of the parameter p and in some cases, in the absence of external stimulus I or with a constant I-value. Moreover, a literature search for two-dimensional FHN models show a lack of work, to the best of our knowledge, that has used the parameters p and I together in an FHN system. However, in our coupled system of cells these parameters have a great importance, as p models the Nernst potential of the cell and I is used as the bifurcation parameter for the excitement of cells that varies

in time and space. Therefore, we set up the values of all parameters in our models in the presence of p and I. Further, the values of all parameters are dimensionless, as we have modelled the system with dimension-free equations.

Firstly, we determine the parameter values during the dynamical study of the coupled discrete models given by Equation (5.2.1) in MATCONT. For this, we tune the values of the parameters until a converging orbit is numerically constructed for the existence of solution of the discrete system of cells. Based on these numerical experiments, we fixed the parameter values as: $\nu = 0.01, \alpha = 0.95, \gamma = 0.12, G = 0.1$, $\boldsymbol{p} = 0.3$ and initially, $\boldsymbol{I} = 0$. We also found a small neighbourhood of these parameter values in predicting possible converging orbits. However, a search for a parameter space of p and the controlling parameter γ of the recovery variable w during the numerical simulations of the one- and two-dimensional models again showed a very small neighbourhood of $p = 0.3$ and $\gamma = 0.12$, which varies through an order of 10^{-3}. Therefore, for the rest of the simulations these values are fixed as the standard values of p and γ. Secondly, the values of ν and most of the values of α less than the values mentioned above were found as cost in computational time during the simulation of 1-dimensional models, as the system became more stiff due to the nonlinear nature of our coupled FHN system. Therefore, for better results we fixed ν and α as 0.01 and 0.95, respectively. However, different values for α are used for the 2-dimensional models as they are fully continuous. Finally, we allow the coupling coefficient G in the discrete system of equations to vary and hence, we studied the corresponding dynamics of the system under the variation of G. However, for the rest of the simulations, we choose $G = 0.1$ for better and more precise results.

5.2 Bifurcation in a Ring of Coupled cells

The possible pattern of oscillation for a ring of coupled cells, can be classified by means of its symmetry groups [14, 46, 83, 88]. However, the existence of periodic solution of a system of cells may not be proven since in general the system of cells is

not an equivariant system (in some cases the system may be equivariant under the action of a suitable group)[83, 88] and by an assertion that "nearest neighbour coupling" (that is, the effect of the n^{th} cell on the m cell does not depend on the k^{th} cell) [46], [83] and [88]. In certain cases, existence of such solution can be guaranteed by bifurcation techniques [83]. Therefore, since our system (given by Equation (5.2.1)) is a $2m$-dimensional nonlinear system and cannot be solved analytically for simplicity we have studied a ring of three-cells coupled around the circumference of the arterial ring and examine the existence of solution by studying the system bifurcation. See Section 4 of Chapter XVIII in [46] for a discussion about the patterns of oscillation that generally occur in a ring of three coupled cells.

Our mathematical models for a ring of m coupled cells are given by Equations (2.2.13) and (2.2.14):

$$\begin{aligned} \nu\frac{d\boldsymbol{v}}{dt} &= \boldsymbol{g}(\boldsymbol{v}) + GA\boldsymbol{v} - \boldsymbol{w} + \boldsymbol{I}, \\ \frac{d\boldsymbol{w}}{dt} &= \boldsymbol{v} - \gamma\boldsymbol{w} - \boldsymbol{p}, \end{aligned} \tag{5.2.1}$$

where all terms are defined earlier.

As mentioned above, for simplicity we consider three cells (m=3) coupled around the ring and the terms in (5.2.1) are redefined by

$$\boldsymbol{v} = \begin{pmatrix} v_1 & v_2 & v_3 \end{pmatrix}^T, \quad \boldsymbol{w} = \begin{pmatrix} w_1 & w_2 & w_3 \end{pmatrix}^T, \quad \boldsymbol{I} = \begin{pmatrix} I_1 & I_2 & I_3 \end{pmatrix}^T,$$

$\boldsymbol{g}(\boldsymbol{v}) = \begin{pmatrix} g(v_1) & g(v_2) & g(v_3) \end{pmatrix}^T, g(v) = v(v-\alpha)(1-v), 0 < \alpha < 1$, and

$$A = \begin{pmatrix} -2 & 1 & 1 \\ 1 & -2 & 1 \\ 1 & 1 & -2 \end{pmatrix}.$$

We numerically solve the above 6-variable system using the MATCONT continuation

toolbox in Matlab. Detailed MATCONT continuation techniques with illustrated examples are discussed in [22], [48], [61], [77] and [85].

For a time integration, we set up the initial condition as: $\boldsymbol{v}(0) = \mathbf{0}$ and $\boldsymbol{w}(0) = \mathbf{0}$. As mentioned in Section 5.1, the initial value of parameters in Equation (5.2.1) was tuned until the system was predicted with a converging orbit. Figure 5.1 shows a spirally converging orbit in the fast-slow plane of the membrane potential of the cell 1. Similar convergence was observed for the other two cells. Therefore, the values of the parameters were set as: $\nu = 0.01, \alpha = 0.95, \gamma = 0.12, G = 0.1$ and $\boldsymbol{p} = 0.3$ and $\boldsymbol{I} = 0$.

To study the effect on the stability of the equilibrium, we initiate integration from the equilibria by allowing the external stimulus $\boldsymbol{I}$ to vary in its parameter space.

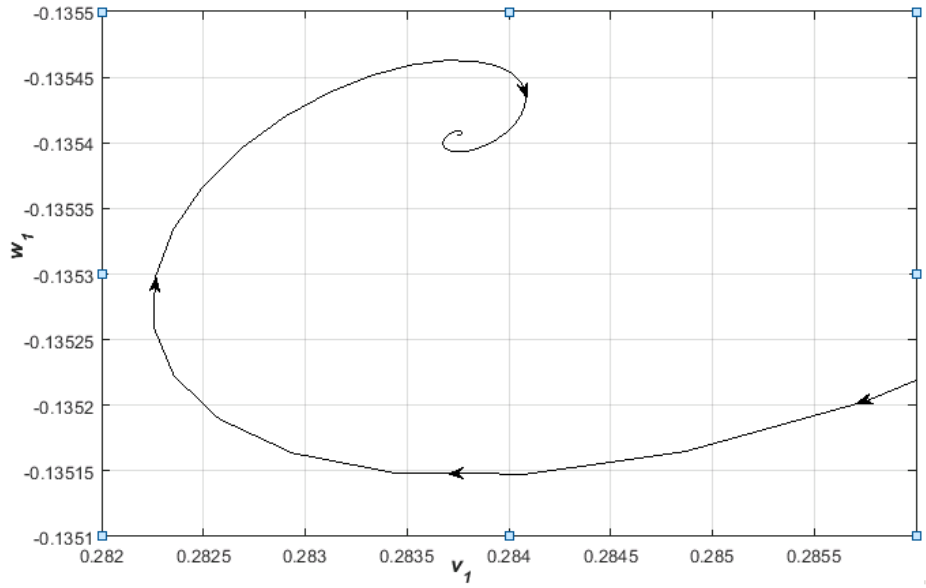

Figure 5.1: Schematic shows a spiral orbit of the cellular membrane potential of cell one converging to $(0.2837512738, -0.1354060515)$ during the initial time integration.

Results revealed the existence of a pair of "Hopf" bifurcation points, H_1 and H_2,

denoted by the red star in the bifurcation diagram in Figure 5.2. At these Hopf bifurcation points the system loses its stability and a periodic solution (orbit) can emerge [51, 107]. The same Hopf bifurcation points were obtained for the other two cells as they produced a symmetry solution. Moreover, the limit cycles born from H_1 and H_2 are stable, corresponding to negative first Lyapunov coefficients. However, in our case, studying the stability of the Hopfs with respect to a parameter regime is complicated as our FHN system is six-dimensional. Therefore, the simple Hopf theorem cannot be applied. This led us to bring the notion of the equivariant Hopf theorem under a possible group of symmetries (refer to Section 4 of Chapters VII and VIII in [46]). Furthermore, the application of the Center Manifold Theorem may

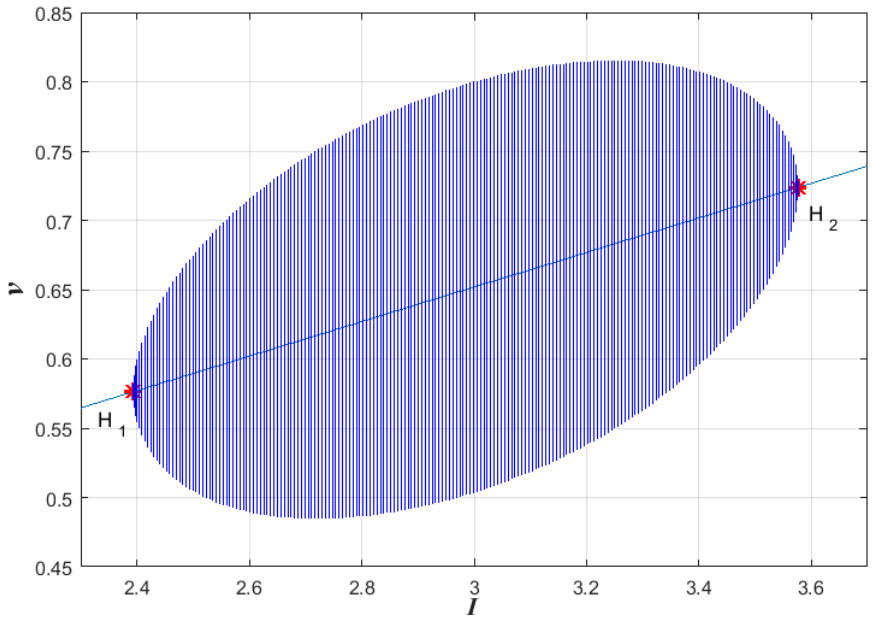

Figure 5.2: Schematic shows an existence of Hopf bifurcation for the cellular membrane potential. Hopf points: $H_1 \equiv (2.393663, 0.576289)$ and $H_2 \equiv (3.576200, 0.723714)$ are denoted by red stars. Oscillations of the membrane potential are predicted between the Hopf points.

also be needed to reduce the higher dimensional system to a two-dimensional system and to study the stability in the reduced manifold. As this is not an easy task to

accomplish, we do not deal with in this thesis.

To study the dynamics of the system between the two Hopf points, we start continuation from the first Hopf point H_1 with the intention of plotting a branch of limit cycles and finding the period of each limit cycle when the bifurcation parameter I varies. We have found that birth of limit cycles as oscillations between H_1 and H_2. That is, the membrane potential loses its stability at H_1 and oscillates between H_1 and H_2 as I increases from 2.393663 to 3.576200. In Figure 5.2, the oscillatory domain of the membrane potential is shown by the blue envelope. The two linear segments plotted outside the oscillatory domain indicate the stable steady states of the membrane potential. As described in Section 1.2, an oscillatory domain of different envelope shapes along with stable steady states were predicted for the cytosolic $[Ca^{2+}]$ in the smooth muscle cells (SMCs) in [74], [75], [105] and [106]. Therefore, these references justify our result for type A cells - the SMCs.

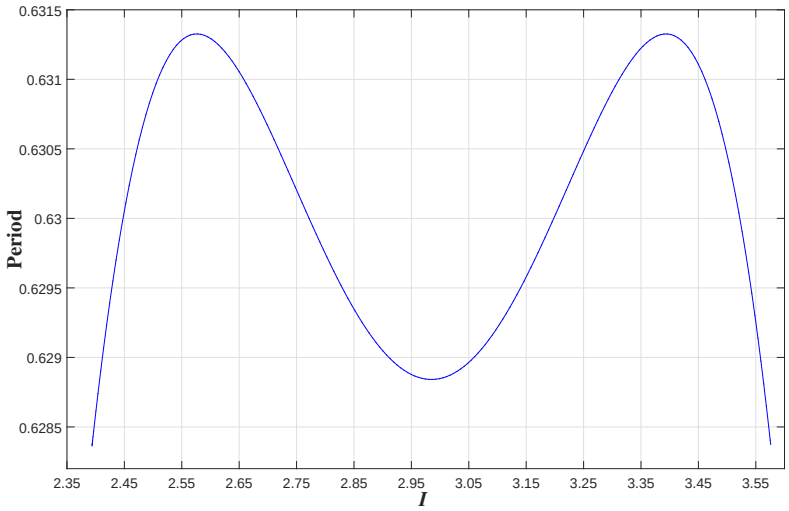

Figure 5.3: Period of oscillations as I varies.

The '$\mathcal{M}$'-shaped curve in Figure 5.3 shows the monotonically increasing and decreasing pattern of the period of oscillations as the external stimulus increases during the

oscillatory period. One can see from the first quarter of the phase of oscillations that the period of oscillation is prolonged and then shortened in the second quarter of the oscillatory phase. Similar results are observed in the second half of the oscillatory phase. A curve of '$\mathcal{W}$'-shaped can be predicted for the variation of the frequency of oscillations as I grows. Thus, frequency of oscillations increases close to the bifurcation points. This coincides with the theory of bifurcation. In addition, variation of the period of oscillations can be studied by plotting a phase response curve (PRC), which demonstrates the effect on the oncoming oscillations of the cell when a small input pulse is applied to the cell (refer to [22] and [49] for PRC analysis).

5.2.1 Effect of Coupling Coefficient

In the previous section we fixed the value of the coupling coefficient G to 0.1 and showed that our FHN system is predicted with oscillations between two Hopf bifurcation points. However, to study the effect of G on the dynamics of the ring of three discrete cells, we carried out numerical experiments for a set of values of G. Results revealed a depletion of the oscillatory domain as the Hopf points move towards each other along the line of the unstable steady state (the linear line segment with in the oscillatory domain in Figure 5.2) of the membrane potential when G varies in an interval [0.020, 0.105] (see Figure 5.4(a)).

For $G = 0.110\,(> 0.105)$ and greater, no bifurcation is observed and hence the system returns to the steady state. In addition, a single Hopf bifurcation is observed for $G = 0.010, 0.015\,(< 0.020)$. The oscillatory domain in each case is predicted between the Hopf point on the H_1-line and its corresponding Hopf point on the H_2-line. Therefore, from Figure 5.4(b), one can see that the oscillatory domain is depleted as the first and second Hopf points move towards each other along H_1-line and H_2-line, respectively for every G-value increased by 0.005. A similar notion of moving Hopfs was illustrated in [75]. As described in Section 1.2, for $G = 0$ (a single FHN oscillator) we find both Hopf points: $H_1 \equiv (0.325295, 0.347904)$ and $H_2 \equiv (5.621941, 0.974706)$

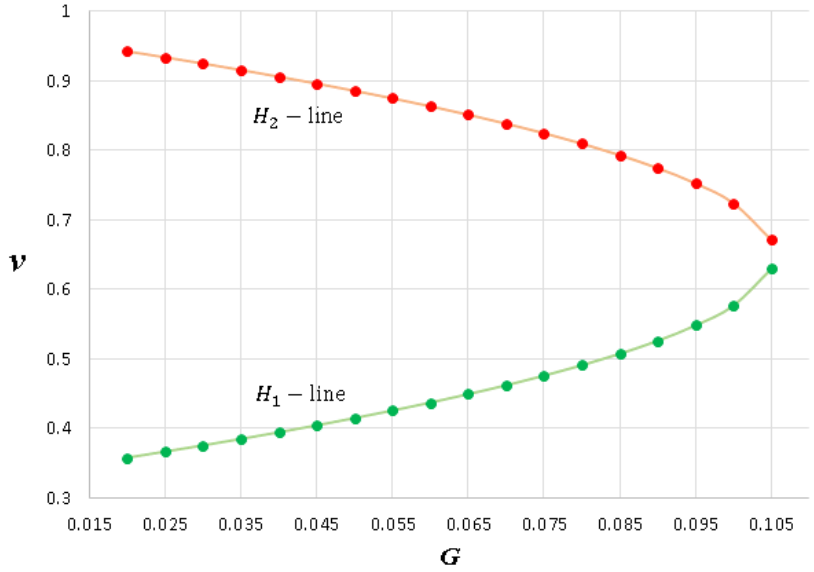

(a)

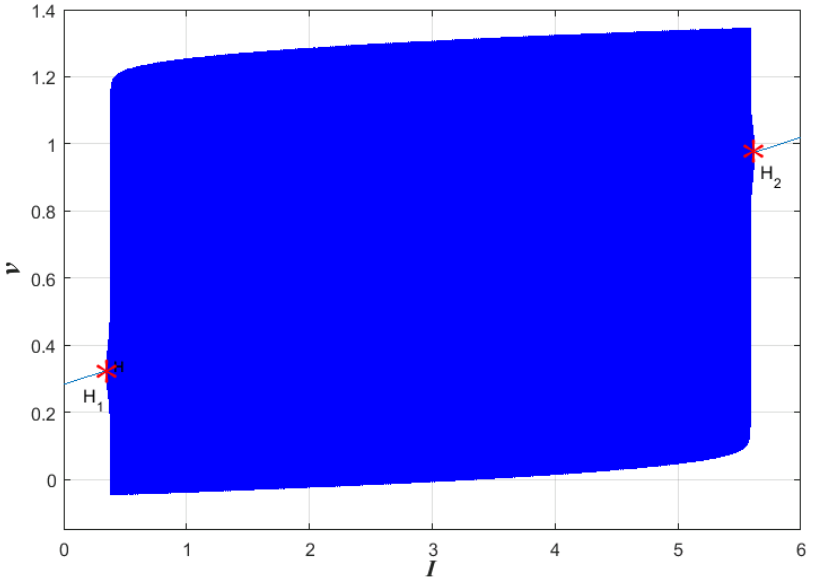

(b)

Figure 5.4: Schematic shows (a) moving Hopf points of v as G increases in the interval [0.020, 0.105], with the first and seconf Hopf points shown respectively along the H_1-line and H_2-line and (b) a parallelogram-type oscillatory envelope for the single ($G = 0$) type A cell.

to be supercritical and the shape of the oscillatory domain is predicted as shown in Figure 5.4(b). Similarly, the existence of Hopf points for a single system of FHN models was discussed in [52].

In the following section we will study the macro-spatial variation of the ring of three discrete cells in one-dimension using the homogenized models derived in Chapter 4.

5.3 Wave Dynamics of 1-D Cellular Network

In this section we apply the HPDEs given by Equations (4.2.8) and (4.2.21) to study numerically the spatial variation of the cellular membrane potential of the arterial ring of three discrete type A cells studied in the previous section. By writing a set of similar equations (4.2.8) and (4.2.21) for the three discrete cells, we have:

$$\nu\frac{\partial \boldsymbol{v}}{\partial t} - \boldsymbol{g}(\boldsymbol{v}) + GA\boldsymbol{v} + \boldsymbol{w} - \boldsymbol{I} = \widetilde{D}\frac{\partial^2 \boldsymbol{v}}{\partial x^2}, \tag{5.3.1}$$

$$\frac{\partial \boldsymbol{w}}{\partial t} + \gamma\boldsymbol{w} - \boldsymbol{v} + \boldsymbol{p} = \boldsymbol{0}, \tag{5.3.2}$$

where the macroscopic term (zero$^{\text{th}}$-order component) of the excitation and recovery variables of the three cells are given by $\boldsymbol{v}$ and $\boldsymbol{w}$ respectively. Note that $\widetilde{D}$ in equation (4.2.24) is taken as a constant for numerical simulations.

Let us approximate the second derivative modelled by Equation (5.3.1) by a three-point finite difference approximation given by:

$$\left.\frac{\partial^2 \boldsymbol{v}}{\partial x^2}\right|_i \approx \frac{\boldsymbol{v}_{i-1} - 2\boldsymbol{v}_i + \boldsymbol{v}_{i+1}}{\delta^2}, \tag{5.3.3}$$

where the spatial point and the mesh size are denoted by i and δ (the width of the type A cell) respectively. For our study we undertook simulations on a one-dimensional torus, $\mathfrak{T}$, by allowing periodic boundary conditions at the ends of the arterial segment. In addition, we applied periodic boundary conditions between the first and the last cells of each ring along the arterial axis, which conceptually create a cylindrical shape

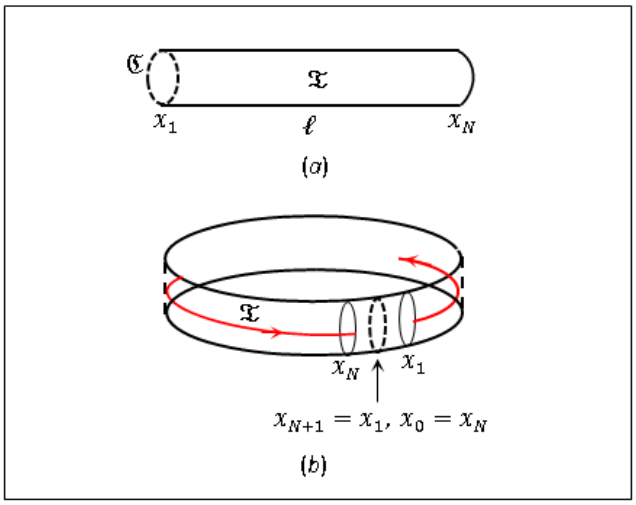

Figure 5.5: Schematic (b) shows a conceptually constructed one-dimensional torus, $\mathfrak{T}$, from the cylindrical shape arterial segment $\mathfrak{T}$, shown in (a), by applying period boundary conditions along the edges of the arterial segment, where ℓ is the characteristic length of the artery.

of the artery in one-dimension as described in Chapter 1. A corresponding geometrical interpretation of these boundary conditions is shown in Figure 5.5. Furthermore, we set up zero-initial conditions to bring the same conditions for the ring of the three cells studied in Section 5.2. Therefore, we have:

$$\boldsymbol{v}(x,0) = \mathbf{0},\ \ \boldsymbol{w}(x,0) = \mathbf{0}, \tag{5.3.4}$$

$$\boldsymbol{v}(x_0,t) = \boldsymbol{v}(x_N,t),\ \ \boldsymbol{v}(x_{N+1},t) = \boldsymbol{v}(x_1,t), \tag{5.3.5}$$

$$v_0(x_i,t) = v_3(x_i,t),\ \ v_4(x_i,t) = v_1(x_i,t),\ \ \forall\ i = 1,\ldots,N, \tag{5.3.6}$$

where the subscript of v denotes the cell number around the circumference of the arterial ring and N denotes the total number of spatial points along the arterial axis.

We discretized the dimensionless space and time into 250 and 3000 mesh points respectively. Further, we use the same parameter values as used in Section 5.2, that is: $\nu = 0.01, \alpha = 0.95, \gamma = 0.12, G = 0.1$ and $p = 0.3$. Moreover, the macroscopic

PVC $\widetilde{D}$ was tuned during the numerical experiments so that the dynamics are clearly predictable. Hence, it was finally fixed as $\widetilde{D} = 0.001$.

As found in Section 5.2, in the absence of spatial diffusion there is an oscillatory domain predicted by two Hopf bifurcation points, $\mathrm{H}_1 : (I, v) \equiv (2.393663, 0.576289)$ and $\mathrm{H}_2 : (I, v) \equiv (3.576200, 0.723714)$ for the ring of three discrete cells. To form such an oscillatory domain, we applied an external stimulus in the form of a second-order spline (see Figure 5.6) to create the existing oscillatory state of the ring, using the specified Hopf values of I while I varies spatially. The spatially varying first-order spline form of I assigned with the low value 0 (<2.393662) and high value 4 (>3.576186) allows the system to have an oscillatory domain in space. This oscillatory domain is assigned in the regions of $R2$ ($50 < i \leq 125$, the region of positive gradient) and $R3$ ($125 \leq i < 200$, the region of negative gradient) (see Figure 5.6). Other regions $R1$ ($1 < i \leq 50$) and $R4$ ($200 \leq i \leq 250$) are kept with zero-stimulus; that is, these regions are non-stimulated. In addition, the assumption of I in the form of the above second-order spline allows the cells in space to experience the external stimulus as a periodical application with respect to a reference point. This reference point is assumed to be the middle cell, $x = 125$ along the arterial axis (see Figure 5.6) where the peak value 4 of I is applied at $x = 125$. We studied the effect on the system by applying a periodic stimulus. Using this stimulus, we stimulated only cells 1 and 3 and leave the cell 2 non-stimulated to study the connection effects on the non-stimulated cell by the neighbouring stimulated cells.

We solve the system given by Equations (5.3.1) and (5.3.2) for the membrane potential $\boldsymbol{v}$ using Equations (5.3.3)-(5.3.6). Results revealed a similar pattern of oscillations in all cells and a subsequent propagation of forward and backward plane waves from stimulated regions to non-stimulated regions in all cells. Figures 5.7(a) and 5.7(e) respectively show wave cycles of discrete cells 1, 2 and 3 in the non-stimulated regions R1 (at i=25) and R4 (at i=225), while Figure 5.7(c) shows wave cycles of

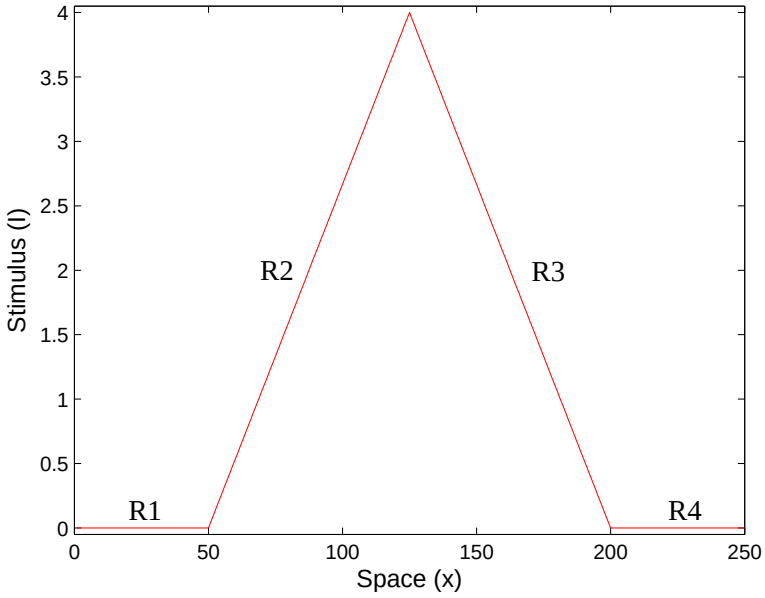

Figure 5.6: Schematic shows a periodically setup external stimulus of the form of a first-order spline applied to the system. Segments R_1 and R_4 indicate non-stimulated regions. Other regions are stimulated with the spatial gradient 4/75.

highly stimulated first and third cells located in the centre (i=125) of the spatial domain. From Figures 5.7(a) and 5.7(c) we observe that the number of wave cycles in all cells has been developed from non-stimulated regions to stimulated regions due to the influence of stimulus of the first-order spline. Figure 5.8 also shows the variation of number of wave cycles with respect to spatial points, in the non-stimulated and stimulated regions R1 and R2. Cells in the non-stimulated regions produce a low number of wave cycles compared to the cells in the stimulated regions, as they are excited only by propagating waves from the stimulated regions. We also note that due to the nearby coupling effect, the spatial domain of cell 2 has the same dynamical effect as of cells 1 and 3, even though it is not stimulated.

From Figure 5.7, we see the propagation of forward waves (waves move in the positive

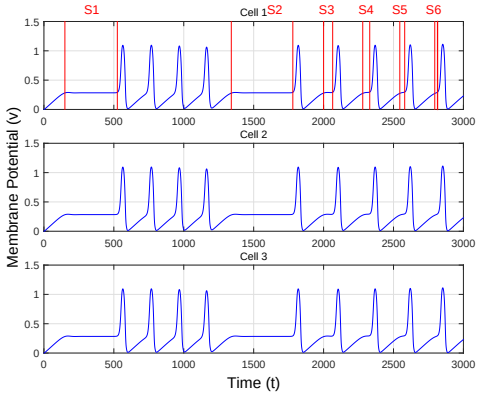

(a) at i=25

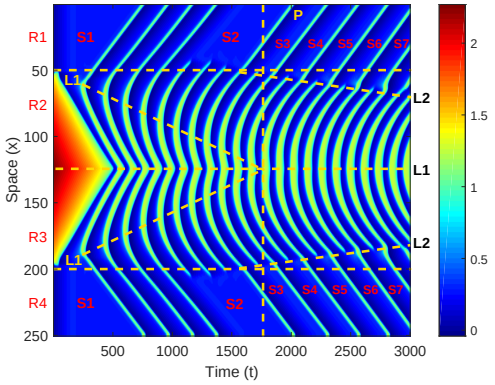

(b) cell-1

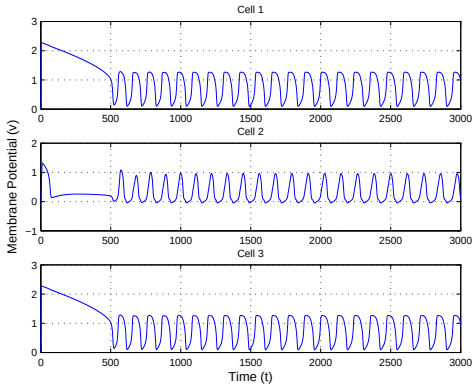

(c) at i=125

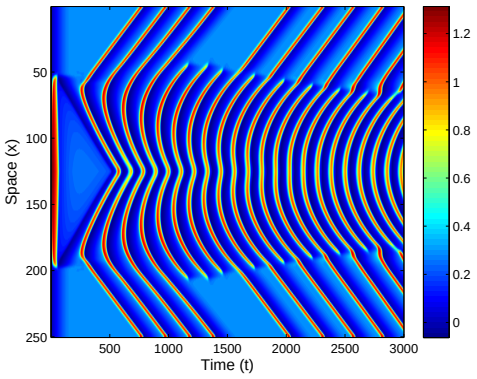

(d) cell-2

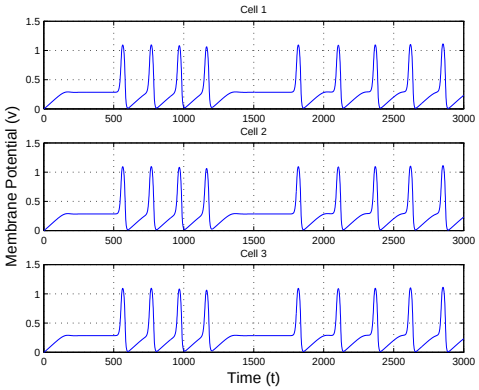

(e) at i=225

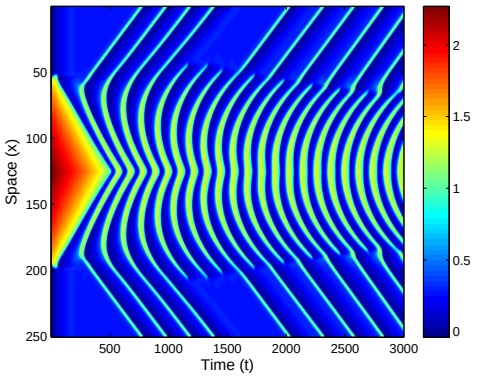

(f) cell-3

Figure 5.7: Schematic shows oscillations in all three cells at (a), (e) non-stimulated and (c) highly stimulated spatial points along the arterial axis and propagation of forward and backward waves along arterial axis in (b), (f) stimulated cells 1 and 3 and (d) non-stimulated cell 2. R1, R4-nonstimulated regions, R2, R3-stimulated regions and S-steady states.

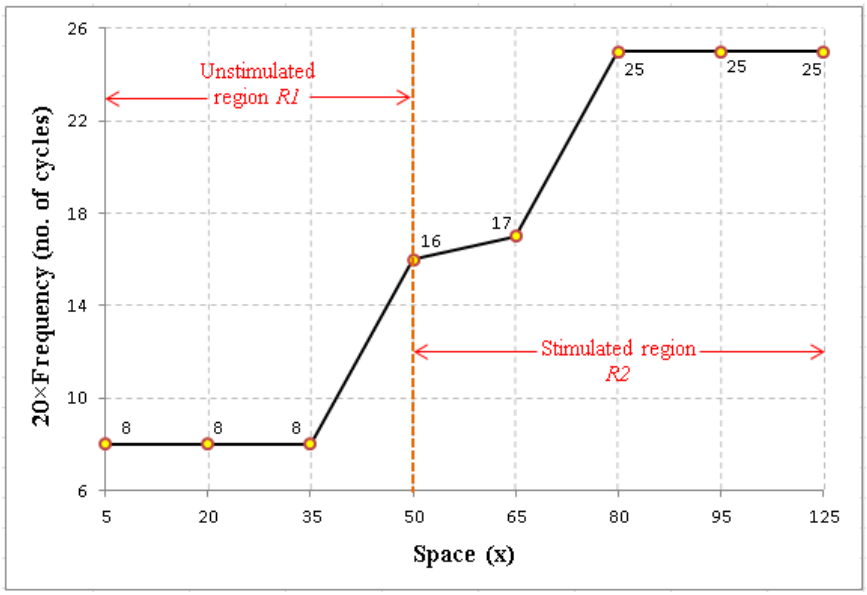

Figure 5.8: Schematic shows the variation of frequency in the non-stimulated and stimulated regions R1 and R2. A symmetrical trend can be predicted for R3 and R4.

x-direction, that have patterns formed by fringes of negative gradients) and backward waves (waves move in the negative x-direction, that have patterns formed by fringes of positive gradients) in cells. In particular, the non-stimulated region R1 receives only backward waves transmitted from the region R2 (see Figure 5.7(b)), stimulated by I of positive gradient (see segment R2 in Figure 5.6). Similarly, the non-stimulated region R4 only receives forward waves sent out from the region R3 (see Figure 5.7(b)), stimulated by I of negative gradient (see segment R3 in Figure 5.6). However, stimulated regions R2 and R3 are found with both forward and backward waves. From this result we understand that there should be a specific spatial location in the stimulated region from which both forward and backward waves are initially created. We call this initial point the "point of initiation of waves" (**PIW**).

We observed the PIW of the first backward wave in R2 region as the first endpoint of the uppermost inclined broken yellow line (L1) in Figure 5.7(b), which is calculated

at approximately $x = 61$. Similarly, a symmetrical point $x = 189$, the first endpoint of the lowermost inclined broken yellow line (L1) in Figure 5.7(b)) is the PIW of the first forward wave in the R3 region. At these points the system is stimulated with an I-value: $(61 - 50) \times 4/75 = 0.587$, where $4/75$ is the spatial gradient of I (see Figure 5.6). Therefore, 0.587 is the required threshold value of I for the initiation of wave propagation under the conditions applied. It is noted that the regions stimulated with stimulus value greater than 0.587 did not initially produce any visible wave fringes as they experienced high frequency excitation. However, the possibility of producing waves in the highly stimulated regions becomes viable when the initial high excitation is distributed to the surrounding region. This is why we later found that the PIW moves along the line L1 towards the centre region, finally settling at $x = 125$. This important wave dynamics has not been reported in any previous research and helps us to further understand the dynamics of waves in the non-stimulated region with multiple steady states.

Initially, the forward and backward waves created at $x = 61$ at time $t = 250$, respectively move toward the highly stimulated region of R2 and non-stimulated region R1. At the same time, symmetrically created forward and backward waves at $x = 189$, respectively penetrate the non-stimulated R4 region and highly stimulated region of R3. This dynamics is clearly pictured in Figure 5.7(b). As time progresses, moving forward and backward waves towards the centre from $x = 61$ and $x = 189$, respectively shrinks the high excitations, while both PIW move along the inclined broken yellow lines towards the centre from $x = 61$ and $x = 189$. These same amplitude waves moving towards each other cease in the centre until both PIW reach the middle of the domain at time $t = 1763$ (a dimensionless time $\simeq$11.75). This cessation of waves in the centre is shown along the horizontal broken line passing through $x = 125$ in Figure 5.7(b). After $t = 1763$, the R2 and R3 regions are found with only backward and forward waves, respectively as the PIW is now settled at the centre (see 5.7(b)), where the fringes beyond the vertical line and above and below the horizontal line

passing through the centre are captured with a unique spatial gradient: the upper fringes with a positive gradient and the lower fringes with a negative gradient.

To further understand this, the dynamics described above are shown in Figure 5.9 as a time series of snap shots of excitation and moving waves obtained from a movie file. The horizontal and vertical axes respectively denote the spatial points along the

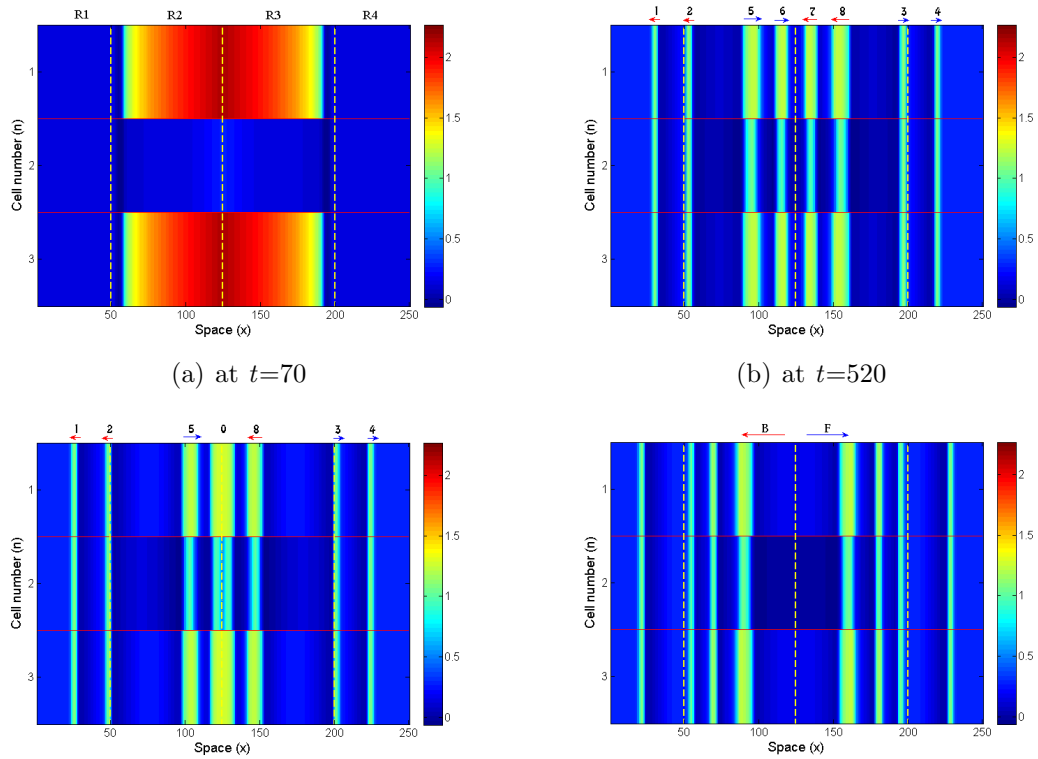

(a) at t=70

(b) at t=520

(c) at t=560

(d) at t=1850

Figure 5.9: Schematic shows in cells 1, 2 and 3 the (a) excitation and (b), (c) and (d) moving forward and backward travelling waves at various time points, obtained from the movie file. R1 and R4 - non-stimulated regions. R2 and R3 - stimulated regions. Waves are identified by numbers 0 to 8. B - forward waves. F - backward waves. Horizontal thin red lines separate each of the cells around the circumference. Regions are separated by vertical yellow dotted lines. The centre vertical yellow dotted line separates the region R2 from R3 stimulated by I of the positive and negative gradient respectively.

arterial axis and the three discrete cells around the arterial circumference. The cells are separated by horizontal red lines (other notations used in Figure 5.9 are given in the figure description). Figure 5.9(a) shows excited cellular regions, $R2$ and $R3$, of cells 1 and 3. Other regions, $R1$ and $R4$ of cells 1 and 3 and the cell 2 do not show excitation as they are not stimulated.

At the later stage propagation of backward wave into the non-stimulated R1 region and forward waves into R4 region is shown by numbers 1, 2 and 3, 4 respectively (see Figure 5.9(b)). In addition, waves indicated by numbers 2 and 5, 6 respectively represent the backward and forward waves in the stimulated R2 region. Similarly, numbers 7, 8 and 3 respectively show the propagation of the backward and forward wave in the stimulated R3 region. The same amplitude waves indicated by numbers 6 and 7 and another pair of same amplitude waves 5 and 8 are moving towards the centre. These same amplitude forward and backward waves are in a state of superposing and are about to cease each other. This is shown by number 0 in Figure 5.9(c).

In addition, the existence of only the forward (F) and backward (B) wave in the regions of R3 and R2, respectively at time $t = 1850$ (> 1763) is presented in Figure 5.9(d). These observations clearly support the dynamics described based on Figure 5.9. In the following subsection, we will describe the existence of multiple steady states as an important dynamics of the cellular membrane potential of type A cells.

5.3.1 Multiple Steady States

The existence of 2^{N^2} multiple steady states of a discrete 2-dimensional FHN equation, where N is the number of spatial points in the x- and y-direction in the absence of slow variable w and the external stimulus I was proven mathematically for an isotropic medium in [91]. Further, propagation of waves and the stability of the FHN-related discrete bistable system has been discussed in [32], [118], [123] and [124]. References [2], [69] and [81] have also discussed the notion of wave propagation and its failure

in relation to multi-stability. In particular, in [81] a method of determining critical coupling coefficients for a general system and the appearance of multistability below the critical value are provided. In our research, we estimate a critical value for the distance between the moving PIW and the boundary separating the stimulated and non-stimulated regions, above that the existence of multiple steady states can be found. We also use interference of waves to describe multiple steady states.

We will discuss the dynamics of waves in the non-stimulated regions of R1 and R4 in all cells. From Figures 5.7(a) and 5.7(b), one can observe that there are a number of steady states in the non-stimulated regions R1 and R4 in all cells. These multiple steady states are denoted by S1, S2,$\cdots$, S7. The first two steady states are predicted with long lasting time (**LT**): S1 with a dimensionless time 2.500 and S2 with 2.733, compared to other steady states for which LTs shrink as time progresses (see Figure 5.7(a)). Steady states S1s appear until the non-stimulated regions R1 and R4 receive backward and forward waves transmitted from the stimulated regions R2 and R3, respectively. In other words, R1 and R4 first lose their stability when they receive nearby coupling effects from R2 and R3. However, the velocity of each wave in R2 and R3 decreases when it travels towards the non-stimulated region from the corresponding PIW, since the gradient of each wave fringe in Figure 5.7(b) reduces in space. Note that the gradient of fringes directly measures the velocity of the corresponding wave, since the schematic is plotted as distance against time.

In addition to the velocity, the distance between each PIW along the inclined broken line L1 (top and bottom) with respect to each wave and the boundary separating the stimulated and non-stimulated region ($x = 50$ and $x = 200$) increases as time progresses. These two crucial factors prevent the R1 and R4 regions from receiving propagating waves after a time of approximately $t = 913$ (a dimensionless time $\simeq$6.08). Therefore, R1 and R4 attain the second steady state S2. As one of the conditions, one can conclude that there is a critical value for the distance between PIW

and the boundary separating the stimulated and non-stimulated regions, below which the non-stimulated region cannot be found with a steady state under the application of the stimulus used in the form of the second-order spline. This critical value is known as the "distance to the steady state" (**DSS**). By taking the fourth wave as the wave for the DSS, we approximately calculate the distance between the PIW (on line L1) of the fouth wave and the boundary passing through $x = 50$. For this, we map a vertical line on Figure 5.7(b) for the tangent at the PIW of the fourth wave and a line parallel to the time axis so that the intersection of these two lines at the PIW gives a required point for determining the DSS. Hence, we find this point of intersection at (913, 82). Thus, at time t=913, the dimensionless DSS can be calculated as (82-50)×20/249=2.57, where 20/249 is the size of the spatial mesh.

Aside from the role of DSS, interference of waves due to the excitation of the medium plays a major role in the attainment of multiple steady states. This notion can be explained using simulation results, as follows. In Figure 5.7(b), after $t = 627$, at a low stimulated region $x = 51$ and its nearby neighbourhood, the system starts to reinforce by excitation, as discussed previously for $x = 61$. In the subsequent motion, when a wave 'P', created at the earliest time step from PIW, passes the above region, that interferes with another wave, 'Q', during its creation in the same region due to the reinforcement. The relative phase (phase difference) between 'P' and 'Q' pushes 'P' with greater amplitude and sudden increased velocity immediately after the interference (see the connecting points along line L2 in the Figure 5.7(b)). Figure 5.10 shows a phase difference and a small change in amplitude between waves moving through three successive spatial points. This dynamics was observed through increasing interference visibility and speed of the wave 'P' after the interference of 'P' and 'Q' in a movie file. As a result, the reinforced wave 'P' (see Figure 5.7(b)) penetrates into non-stimulated regions and hence non-stimulated regions lose their steady state S2. However, since there is a time lag between two successive interference, the non-stimulated regions again undergo the next steady state S3 as the

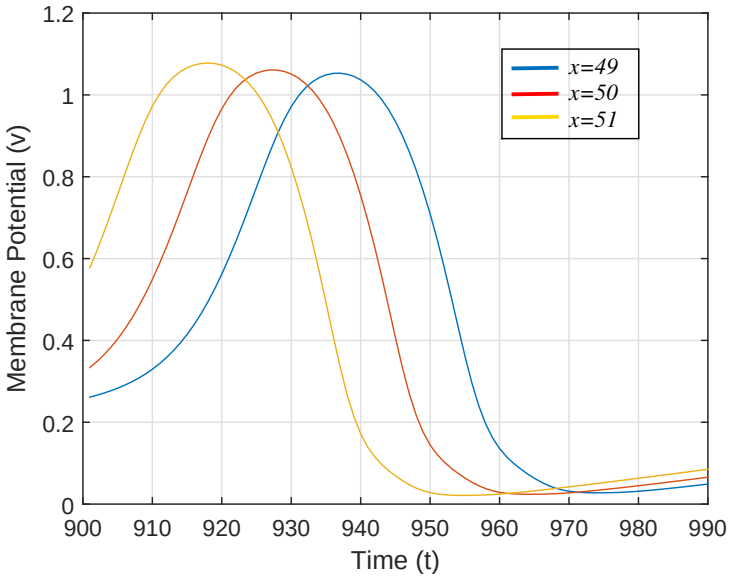

Figure 5.10: Schematic shows phase difference between and a small change in amplitude of waves moving through successive spatial points in a particular time interval (900,990).

upcoming wave from PIW has no ability to penetrate the non-stimulated region in the absence of interference and because the distance between PIW and the boundary separating the stimulated and non-stimulated regions is 4.34, which is greater than DSS=2.57. This dynamics continues and leads the system for every other annihilation of backward waves in R1 and forward waves in R4. Thus, the non-stimulated regions are predicted with subsequent steady states: S3, S4, and so on, while a new set of PIW follows the line L2. These new PIWs are the 'points of interference of waves' (**NPIW**) created in the region of law stimulation. Hence, a new DSS corresponding to NPIW can also be defined, called **NDSS**, since NPIW moves towards the centre region along line L2. When NDSS≥DSS, the non-stimulated region can be predicted with other steady state of long LT, like as S2 in spite of interference.

Figure 5.11 shows a linear variation of the LT of steady states $S3,\cdots, S7$ in the simulation time $t = 3,000$ (dimensionless time=20). The shrinkage of the LT of

steady states (see Figure 5.7(a)) indicates the existence of further wave propagation in the non-stimulated region in the subsequent time period. To see this dynamics, we carry out simulation for extended time periods, each of at 3,000 units (see Figure 5.12). Following a sudden drop in the membrane potential at approximately time about $t = 4,250$ (a dimensional time $\simeq 28.33$) (see Figure 5.12(a)), and a consequent sudden rise and drop within the next time interval 550, non-stimulated regions attain consecutive steady states Sn, Sn+1 and Sn+2. The reason for this sudden change

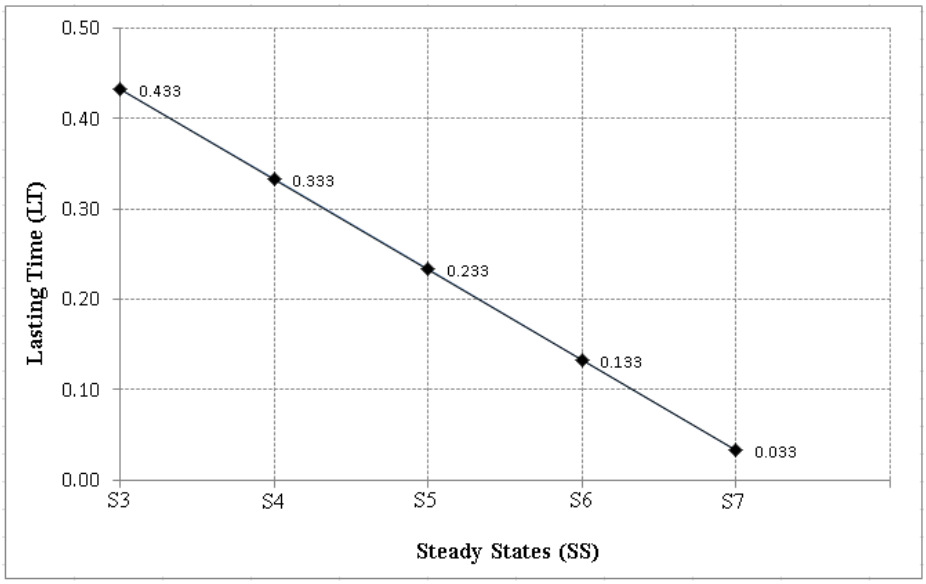

Figure 5.11: Schematic shows shrinkage of the LT of steady states (SS) S3, S4 and so on. Numbers denoted at each point indicate the LT of corresponding SS. The SS and its LT for the dimensional time period 20 can be modelled by a relation $LT = -0.1SS + 0.533$.

in the membrane potential is not clear. Following this sudden change, the system is set to a transient pattern with multiple steady states, during $t = 6000 : 9000$ (see Figures 5.12(b) and 5.12(d)). These steady states are observed in both stimulated ($50 < x < 75$) and non-stimulated ($x < 50$) regions. The LT of steady states in the non-stimulated regions is twice that of the LT of steady states observed in the stimulated regions, as the non-stimulated regions receive only a single wave for every two waves propagating in the stimulated regions (see Figure 5.12(d)). The reason for

this dynamics can be explained by three waves, as follows.

First, consider two successive waves, P1 and P2, initiated from PIW along line L1 and moving towards the non-stimulated region. Then, P1 interferes with a hidden wave, Q1, created at the corresponding NPIW on line L2 by excitation (see Figures 5.12(c) and 5.12(d)). As described earlier, the interference reinforces Q1 and

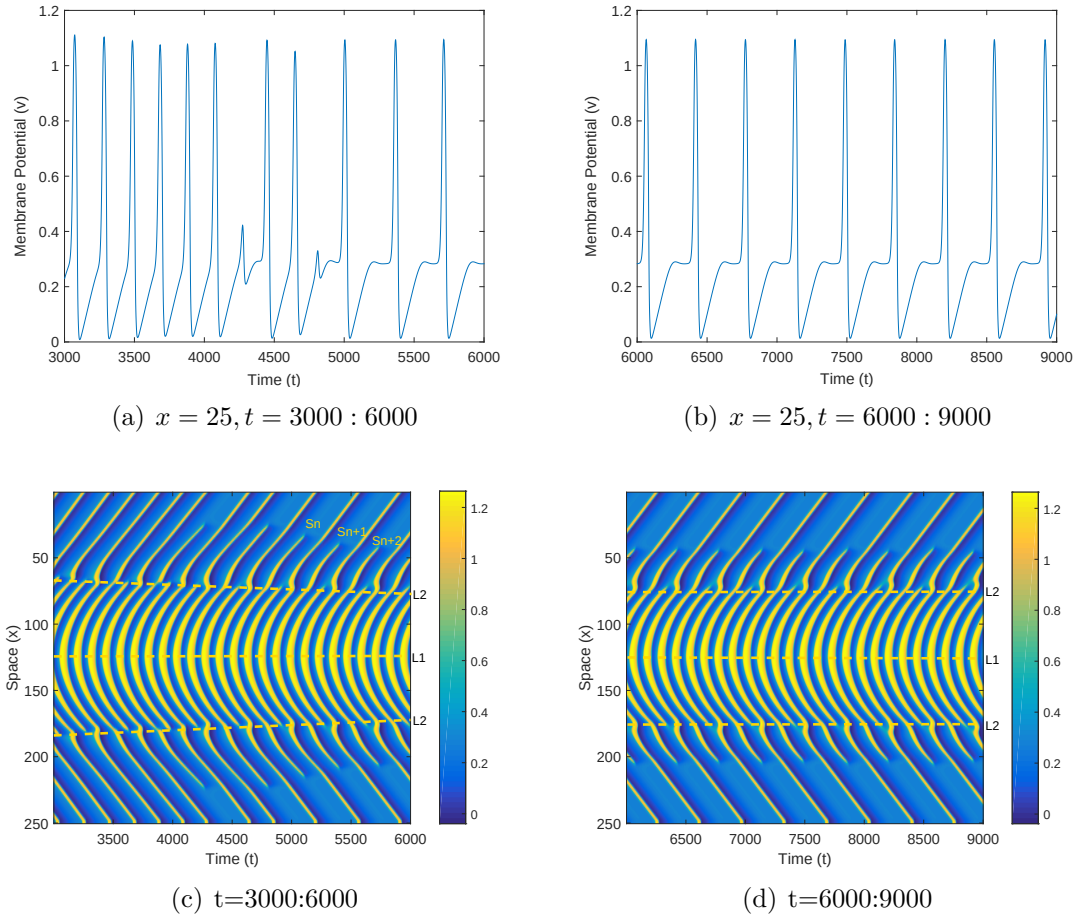

(a) $x = 25, t = 3000 : 6000$

(b) $x = 25, t = 6000 : 9000$

(c) t=3000:6000

(d) t=6000:9000

Figure 5.12: Schematic shows (a), (c) the state of dynamics changes to transient pattern and (b), (d) a full transient pattern with multiple steady states.

simultaneously weakens P1. Therefore, the weak P1 vanishes immediately while the

interference pushes Q1 from the NPIW. However, when P2 reaches NPIW the reinforcement is weak compared to when P1 is reached. This reinforces wave P2 without producing another hidden wave Q2 for interference and P2 starts to travel with a low amplitude compared to the amplitude of the reinforced Q1. The strongly reinforced Q1 then penetrates and travels through the non-stimulated region while the weak P2 stops just beyond the boundary separating the stimulated and non-stimulated regions. This dynamics is repetitive and the system attains multiple steady states at two different spatial locations: first, in the stimulated region spanned by $50 < x < 75$ and second in the non-stimulated region spanned by $x < 50$ (see Figure 5.12(d)) then at two more locations by symmetry. As described above, the period of steady states

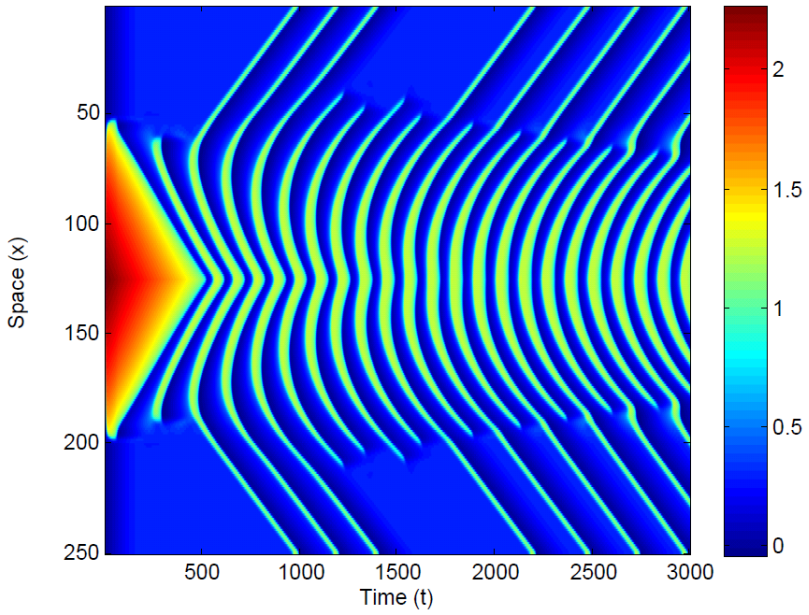

Figure 5.13: Schematic shows the wave dynamics in the first cell of 5 circumferentially coupled cells.

in the first region is observed as of time between P2 and Q1, while the time between two successive Q1s is observed to be the period of steady states in the second region. Hence, the LT of steady states in the non-stimulated regions is twice that of the LT

of the steady states in the stimulated regions.

To study the dynamics of increased number of cells around the circumference we carry out simulation on 5 circumferentially couple cells. Result revealed similar dynamical behavior of 3 circumferentially coupled cells, but an increment in the lasting time of steady states is observed compared to that in case of 3 circumferentially coupled cells. These results are shown in Figure 5.13.

In the following section we will explore the dynamics of a population of cells in two-dimension.

5.4 Wave Dynamics of 2-D Cellular Network

In this section, we study the dynamics of the 2-dimensional cellular system modelled by HPDEs given by Equations (4.3.25) and (4.3.64) derived in Chapter 4. For convenience, we rewrite those equations in a unique form:

$$\nu\frac{\partial v}{\partial t} - g(v) + w - I = \frac{\partial}{\partial x}\left(\widetilde{D}_x\frac{\partial v}{\partial x}\right) + \frac{\partial}{\partial y}\left(\widetilde{D}_y\frac{\partial v}{\partial y}\right), \tag{5.4.1}$$

$$\frac{\partial w}{\partial t} = v - \gamma w - p, \tag{5.4.2}$$

where $v = v(x, y, t), w = w(x, y, t)$, $I = I(x, y, t)$ and $g(v) = v(v - \alpha)(1 - v)$, $0 < \alpha < 1$.

Since the HPDEs treat the effective PVCs, $\widetilde{D}_x$ and $\widetilde{D}_y$, as different, the macro-domain is an anisotropic medium. Furthermore, for numerical simulations, let us assume $\widetilde{D}_x$ and $\widetilde{D}_y$ are constants, then Equations (5.4.1) and (5.4.2) can be given by:

$$\nu\frac{\partial v}{\partial t} - g(v) + w - I = \widetilde{D}_x\frac{\partial^2 v}{\partial x^2} + \widetilde{D}_y\frac{\partial^2 v}{\partial y^2}, \tag{5.4.3}$$

$$\frac{\partial w}{\partial t} = v - \gamma w - p. \tag{5.4.4}$$

We solve the problem of Equations (5.4.3) and (5.4.4) in a rectangular domain, as the

characteristic length of the artery along the x-axis is different from the characteristic length of the lifted arterial circumference along the y-axis. For this, we use the Matlab built-in differential equation solver ode45.

We use a five-point finite difference approximation scheme for the modelling of the second derivatives in Equations (5.4.3) and (5.4.4), which are given by;

$$\begin{aligned} \left.\frac{\partial^2 \boldsymbol{v}}{\partial x^2}\right|_{(i,j)} &\approx \frac{\boldsymbol{v}_{i-1,j} - 2\boldsymbol{v}_{i,j} + \boldsymbol{v}_{i+1,j}}{\delta^2}, \\ \left.\frac{\partial^2 \boldsymbol{v}}{\partial y^2}\right|_{(i,j)} &\approx \frac{\boldsymbol{v}_{i,j-1} - 2\boldsymbol{v}_{i,j} + \boldsymbol{v}_{i,j+1}}{\eta^2}, \end{aligned} \tag{5.4.5}$$

where i and j respectively denotes the spatial points along the x- and y-axes. The grid size along the x- and y-axes is defined by the width of the cell δ and by the length of the cell η, respectively such that $\eta = 10\delta$ (as described in Equation (4.3.46) in Chapter 4, $\kappa = 10$).

We initially assign the excitation and recovery variables a zero value and cells are assumed to be periodic in both x and y directions. Hence, the initial conditions and periodic boundary conditions are respectively set as follows:

$$v(x, y, 0) = w(x, y, 0) = 0; \tag{5.4.6}$$

$$\left.\begin{aligned} v(x_0, y_j, t) &= v(x_N, y_j, t), \\ v(x_{N+1}, y_j, t) &= v(x_1, y_j, t), \end{aligned}\right\} \forall\ j = 1, \ldots, M, \tag{5.4.7}$$

$$\left.\begin{aligned} v(x_i, y_0, t) &= v(x_i, y_M, t), \\ v(x_i, y_{M+1}, t) &= v(x_i, y_1, t), \end{aligned}\right\} \forall\ i = 1, \ldots, N, \tag{5.4.8}$$

where $M, N \in \mathbb{Z}^+$ denote the total number of spatial points along the x- and y-axis, respectively. For a reasonable computational time, we used: $M = 80$ and $N = 54$. Based on the values of M and N above, our rectangular spatial geometry consists of 80×54=4,320 cells, among which only 240 cells (five bands, each of which have

48 cells) along the x-direction and 216 cells (six bands, each of which have 36 cells) along the y-direction at the centre of the domain are stimulated. We stimulated 456 cells in total, around 10.56% of the total number of cells. We applied a weakly time-dependent spatially-varying bi-directional stimulus, $I(x, y, t)$, defined by:

$$I(x, y, t) = \begin{cases} (I_x, I_y), & 0 \leq t \leq t_a; \\ 0, & t_a < t \leq t_T, \end{cases} \tag{5.4.9}$$

where t_a and t_T are an arbitrary and total time of simulation, respectively.

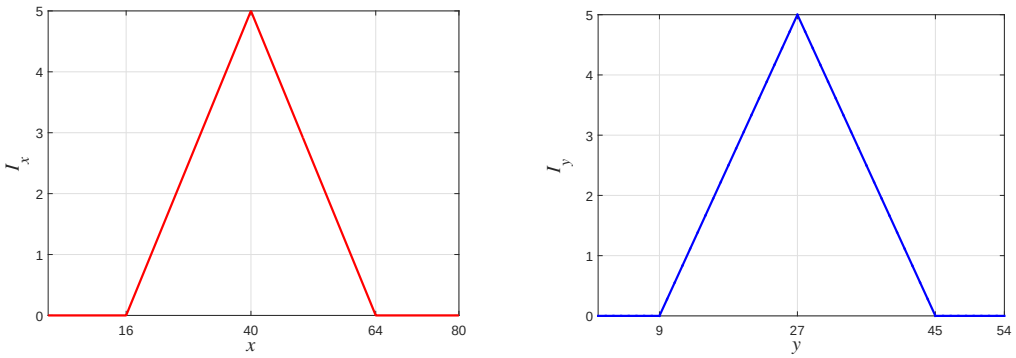

(a) I_x vs x (b) I_y vs y

Figure 5.14: Schematic of the bi-directional spatially varying stimulus $I = (I_x, I_y)$, defined by Equation (5.4.10) where (a) I_x is applied in the x-direction and (b) I_y is applied in the y-direction.

As proposed for the one-dimensional case, I_x and I_y are assumed to be in the form of the second-order spline (one of the forms of periodicity), defined as:

$$I_x = \begin{cases} 0, & 0 \leq x \leq 16, \\ (5/24)\, x, & 17 \leq x \leq 40, \\ 5 - (5/24)\, x, & 41 \leq x \leq 64, \\ 0, & 65 \leq x \leq 80, \end{cases} \quad , \quad I_y = \begin{cases} 0, & 0 \leq y \leq 9, \\ (5/18)\, y, & 10 \leq y \leq 27, \\ 5 - (5/18)\, y, & 28 \leq y \leq 45, \\ 0, & 46 \leq y \leq 54. \end{cases} \tag{5.4.10}$$

Note that from Equation (5.4.10), the strength of the stimulus in the x and y direction is set up as different by assigning them with a different spatial gradient (see Figure

5.14 for a geometrical interpretation of I_x and I_y).

In the following subsections we will show the existence of curved wave-fronts, curved wave-backs, nearly circular waves (target pattern), rigidly rotating spirals with drifts and meanders and static spirals with continuous drift. In general, most of these pattern formations were previously discussed in [35], [36], [66], [86], [87], [97], [110], [113] and [125]. Some were only studied for a few models (for example, Belousov-Zhabotinsky reaction model in [86], the Berkley model in [93] and a synaptic depression model in [71]). We show for first time the possibility of a FHN displaying all of the above spatial patterning together and we describe the corresponding dynamics based on different parameter values and space-time dependent stimuli.

5.4.1 Curved Wave-Fronts and Nearly Circular Waves

Consider the discretized domain described in the preceding section and solve the system using the initial and boundary conditions given by Equations (5.4.6)-(5.4.8). Under the parameters values explained in Section 5.1, we set the parameters of Equations (5.4.3)-(5.4.5) as follows:

$$\widetilde{D}_x = 0.001, \widetilde{D}_y = 0.1, a = 0.95, \nu = 0.01, \gamma = 0.12, p = 0.3, \delta = 0.1, \eta = 1,$$

where $\widetilde{D}_x$ and $\widetilde{D}_y$ are initially assigned with the above values.

Using these parameter values and Equations (5.4.3)-(5.4.10) with $t_a = t_T$ we solve the problem in the rectangular domain. Results from the simulation showed an excited cellular region activated by the spatially varying bi-directional stimulus (see Figure 5.15(a)), where the excited cells are shown by a region of '+' sign. In subsequent time, initial spatial variation of the membrane potential appears as curved traveling waves in both the x- and y-directions (see Figure 5.15(a)). These curved traveling waves are wave-fronts, since the direction of their movement is the same as the normal outward unit, and they propagate to the surrounding region of zero stimulus. These traveling wave-fronts convert most of the regions of the cellular network into an excited state.

Full domain excitation depends on the threshold value of the stimulus applied in each direction and how far the curved wave-fronts travel from the stimulated region. The latter depends on the relationship between the curvature and speed of the wave-front.

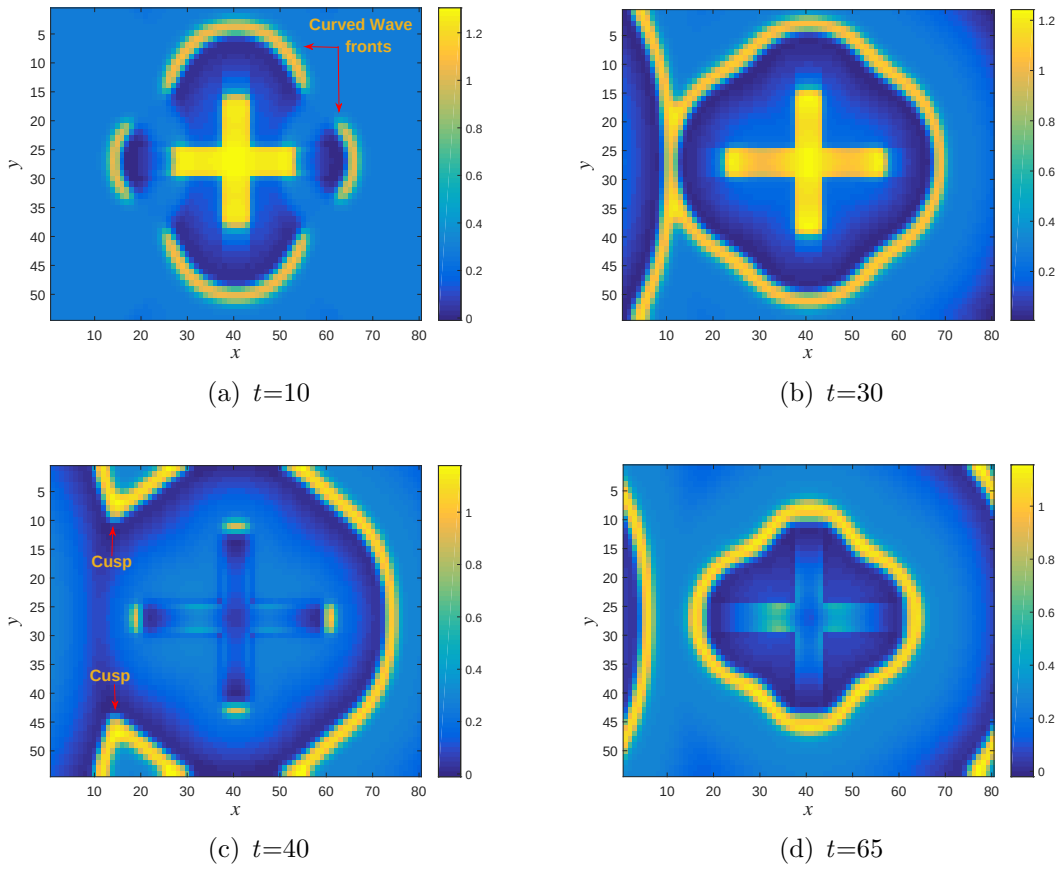

(a) t=10 (b) t=30

(c) t=40 (d) t=65

Figure 5.15: Schematic shows (a) an application of bi-directional stimulus at the centre of the domain and moving curved fronts towards the boundaries, (b) successive circular wave-fronts collide each other, (c) moving cusps away from each other in the up and down direction, after the collision and (d) waves spreading with reduced curvature.

The curvature-speed relationship can be given by the 'eikonal' equation: $c_f = c_p - \kappa D$, where c_f, c_p, D and κ the speed of the wave-front or back, speed of the plane wave, the transport coefficient and the curvature of the wave, respectively [86, 113]. For

a wave-front, $c > 0$ and $\kappa < 0$ and for a wave-back, $c < 0$ and $\kappa > 0$ (see [86] and [113]). From the eikonal equation, one can observe that an increment in the positive curvature decreases the speed of wave propagation. In addition to the curvature effect on the wave-front, in our simulation we identified the role of a properly-assigned spatially-varying bi-directional stimulus in reducing the time lag between bi-directional wave-fronts. This reduced time lag increases the possibility of forming a closed loop by connecting the bi-directional wave-fronts. To explain this result, we carried out numerical experiments for the same region of excitation as pictured in Figure 5.15, based on the peak value of I_x and I_y (see Figure 5.14 where the peak value of $I_x = I_y = 5$).

First, at a peak value of $I_x = 4$ and $I_y = 6$, cells are stimulated respectively with the stimulus of the spatial gradient, approximately 0.17 (=4/(40-16)) and 0.33 (=6/(27-9)) in the x- and y-direction (see Figure 5.14). In another case, at a peak of $I_x = 4$ and $I_y = 5$, the stimulus in the x- and y-direction gradually changes by a spatial gradient of 0.17 and 0.28 (=5/(27-9)), respectively. In both cases, I_y has a high gradient strength compared to the gradient of I_x and hence simulation results showed the rapid movement of the wave-front in the y-direction rather than the wave-front moving in the x-direction. Thus, the time lag between the bi-directional wave-front is greater in magnitude as the y-directional wave-front moves faster. However, in the actual case, with a peak value of $I_x = I_y = 5$, the stimulus gradually changes through increments, approximately 0.21 (=5/(40-16)) and 0.28 (=5/(27-9)), respectively in the x- and y-direction. In the first two scenarios the difference between the spatial gradient of I_x and I_y is 0.33-0.17=0.16 and 0.28-0.17=0.11, respectively. However, in the latter case the difference is 0.28-0.21=0.07, which intuitively indicates the strength of the stimulus in each direction is notably distributed compared to the first two cases, as $0.07 < 0.11 < 0.16$. In the latter case, the time lag between bi-directional wave-fronts is small compared to the first two cases. Therefore, the time lag between the x- and y-directional wave- fronts close to the stimulated region is controlled by the difference

between the spatial gradient of the stimulus applied along the x and y-direction. At the peak value of $I_x = I_y = 5$, as a result of both minimized time lag and high curvature (at a later stage of the simulation), the bi-directional wave-fronts superimpose at their ends through a chain-wise connection immediately after they created. This dynamics results at the formation of a closed loop, which turns into a propagation of a nearly circular wave (target pattern) (see Figure 5.15(b) and Figure 5.15(d)). Therefore, a bi-directional, spatially-distributed stimulus with a pair of threshold gradients could have the ability to produce circular waves. For the stimulated region in Equation (5.4.10), the threshold value of the spatial gradients of the stimulus in the x- and y-direction is found as 0.21 and 0.28, respectively at two-decimal places.

In the subsequent motion the collision of moving circular periodical waves in the up and down y direction creates upward and downward moving cusps (see Figure 5.15(c)), respectively in the regions of high curvature. Since these cusps are moving away from each other, they round off and spread widely and quickly so that the curvature of the wave-front becomes reduced (similar dynamics can be seen in [113]). The resultant dynamics in our problem makes the system free from the target pattern and hence is prevented from having other two-dimensional wave patterns, such as closed loop and spiral patterns, as the curvature becomes reduced or vanishes. By allowing the system to keep producing target pattern through a connection of cusp points, the dynamics of the system can be further studied. In this case we hope to form continuous wave-backs (moving opposite to the outward normal) instead of wave-fronts. We will achieve this in the following section.

5.4.2 Curved Wave-Backs and Nearly Circular Waves

As discussed in the previous section, we show the existence of curved wave-backs and nearly circular wave-backs (target patterns) by changing the value of the parameters a and $\widetilde{D}_y$, for which we set dimensionless values: $a = 0.25$ and $\widetilde{D}_y = 0.05$. Other parameters are set as defined in Section 5.4.1. The initial and boundary conditions

used are defined by Equations (5.4.6)-(5.4.8). The external stimulus is defined by Equation (5.4.10) and is applied for the full simulation period, that is, $t_a = t_T$.

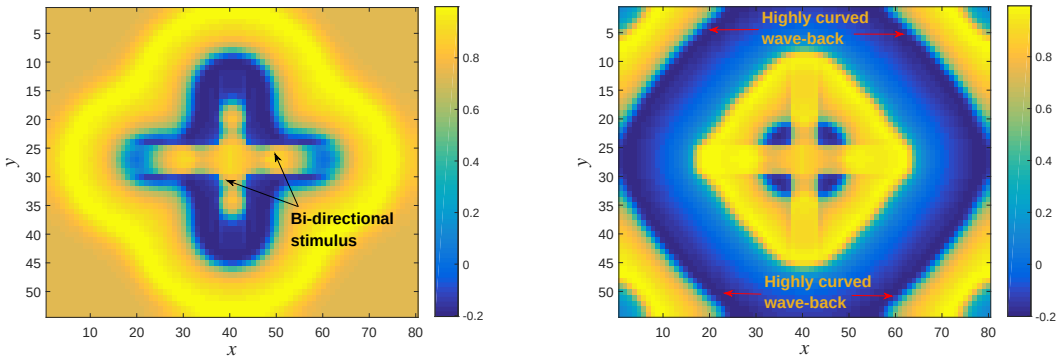

(a) t=5

(b) t=55

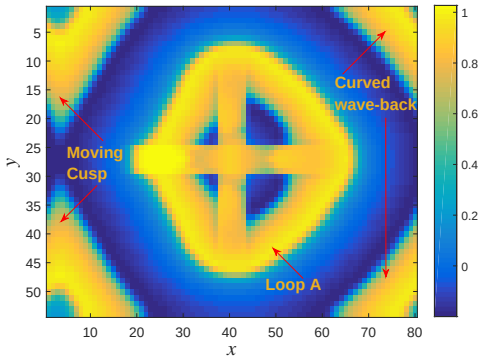

(c) t=305

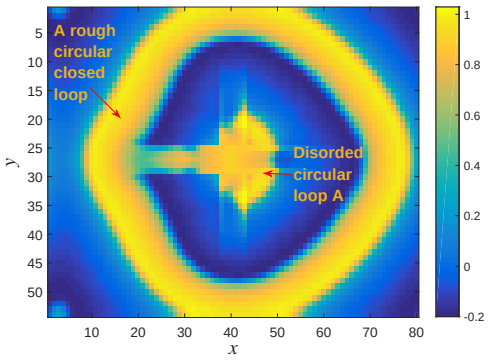

(d) t=330

Figure 5.16: Schematic shows (a) excitation of cells due to the application of bi-directional stimulus at the centre of the domain, (b) highly curved wave-backs at the top and bottom of the domain, (c) face-to-face moving cusps in the up and down direction, and (d) a moving, nearly circular wave-back created by collision of cusps shown in Figure (c). Loop A in Figure (c) dissipates in the region of the stimulated cells.

Results reveled the existence of curved wave-backs as the waves moved towards the stimulated region of cells instead of carrying the activated signals away from the stimulated region. In other words, the direction of movement of the curved waves

is opposite to the normal outward unit, and in this case, the excited region of cells behaves like a sink. Figure 5.16(a) shows excitation of cells around the stimulated region and in their neighbourhood. Since the periodic wave-backs are moving towards the region of excitation, the collision of moving curved wave-backs in the up and down y-spatial direction (see Figure 5.16(b)) creates face-to-face moving cusps in the regions of high curvature (see Figure 5.16(c)). These moving cusps superimpose each other and hence round off their edges to form a closed loop around the region of excited cells. The resultant pattern of the loop is a nearly circular wave-back (see loop A in Figure 5.16(d)). The circular wave-back propagates very rapidly towards the region of stimulated cells and the resultant shape becomes a disordered pattern, as long as, the pattern dissipates due to excitation in the middle of the domain (see the centre of the circular loop in Figure 5.16(d)). This dynamics was found to be repetitive over the simulation time.

This raises two questions: first, in general, under what circumstances can the symmetry of a target pattern be broken? Second, if a symmetry breaking of rapidly moving wave-backs is possible, then what are the underlying dynamics of the cellular system? The first question has been answered by previous research. For example, in [97], the insertion of a blast of air into a small portion of the circular wave-front was used to mechanically brake the symmetry of the system. In [110], wave-fronts exposed to ultra-violet light caused the partial cessation of the front, resulting in a free spiral end. Further, a notion of properly assigned initial conditions, and an application of concentric stimulus at the neighbourhood of the wave-fronts were proposed in [115], [116] and [117]. These notions were well-tested for the formation of spiral waves in [15], [16], [44], [96] and [109]. The importance of these spiral waves was then studied in relation to inducing tachycardia (high frequency-induced heartbeat) and subsequent physical condition, the uncoordinated contraction of the cardiac muscle of the ventricles in the heart ("ventricular fibrillation") [1, 17, 25, 34, 67, 86, 92, 96, 102, 121].

As we are modelling communication (in terms of the cellular membrane potential) between a population of type A cells in the interest of studying its biology-related dynamics, we conducted a literature search to find a biological process to make our modelling more meaningful. In references [7], [10], [28] and [98], we noted the importance of the cellular membrane potential depolarization in relation to some pathological states (mentioned in the following section) of the human body. Therefore, we will model a specific state of the cellular membrane potential depolarization for which the symmetry of the target pattern will be broken.

5.4.3 A Physiological or Pathophysiological Scenario

There are some physiological or pathophysiological situations that can make certain parts of the cellular system to behave with sudden distinct characteristics [100] that can be considered deterministic. First, we consider a dramatic electrical change experienced by a cell. In most cells, the membrane potential is known by the difference

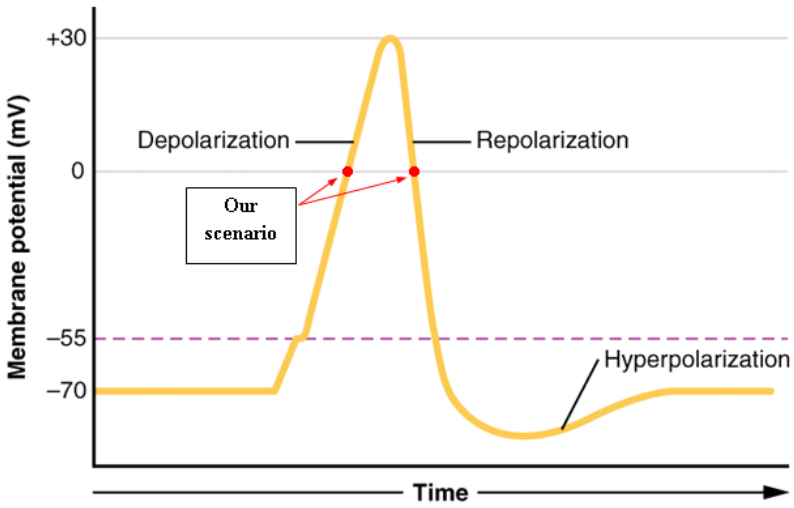

Figure 5.17: Schematic of changes in cellular membrane potential from steady state to hyperpolarization via depolarization and repolarization. Figure reproduced with free accessing license from Wikipedia.

between the potential of negatively-charged cytosol and the surrounding environment

of the cell [100]. However, in the process of depolarization the negatively-charged rapidly becomes positive for a very short time (see Figure 5.17). This change in physiology allows for the spread of electrical impulses as a propagation of waves, both within a cell and on specific occasions, between cells [100]. Membrane potential depolarization has been proposed as an important factor in the initiation of muscle fatigue [98], the silencing of brain electrical activity (spreading depression) [28] and is associated with a decrease in the stiffness of the endothelial cells [7]. In [10], the membrane potential depolarization (not due to the increment of intracellular Na^+ concentration) has been found to play a role in epithelial wound healing by gradually extending its spread towards the neighbouring cells from the leading edge of wounds. The notion of depolarization is therefore essential in the study of cellular activity, transmission between cells and the function of an organism [100].

Second, we may consider a pathological situation: patches of damaged cells (for example, cancer cells), which can be considered an appearance of spatial inhomogeneity in a homogeneous cellular medium. In both situations the change in membrane potential from negative to positive (or vice versa) could be possible, where the sudden attainment of zero potential (see red dots in Figure 5.17) and its consequences in a population of cells are paramount. In the following section we introduce depolarization- or spatial heterogeneity-related "zero-state intermediate condition" at a particular point in the simulation, for which the membrane potential of a patch of cells in the domain becomes zero. We call this the "domain of depolarization".

5.4.3.1 Symmetry Breaking: Rigidly Rotating Spiral Waves

A reaction-diffusion system on a plane is found to be invariant under the Euclidean group [5] and hence a spiral wave is a symmetry-breaking solution of that system [5, 86, 113]. The tip of the spiral can be created for slowly moving, highly curved wave-fronts [113] and wave-backs. In our simulations, we show the existence of spiral waves by breaking the target pattern (circular waves) obtained through wave-backs

in Section 5.4.2 (see Figure 5.16(d)). This section is a repetition of the simulation described in Section 5.4.2, but we introduce the scenario that membrane potential begins to depolarize in a patch of cells due to the opening and closing of ion channels or other means. We apply the "zero-state intermediate condition" at an arbitrary time ($t = t_{dp}$) at which the "domain of depolarization" attains the zero potential. For this, we setup the left half of the spatial domain as the domain of depolarization and one-third of the total simulation time as the time point, t_{dp}, of the zero-state intermediate condition. The domain of depolarization is defined by $0 < x \leq 40$ and $0 < y \leq 54$ and $t_{dp} = \frac{t_T}{3} = \frac{2000}{3} \approx 667$.

For simulations, the bi-directional stimulus defined by Equations (5.4.9) and (5.4.10) is applied until time t_a, and was thereafter switched. The time point t_a defined in Equation (5.4.9) was set to be exactly t_{dp}, as we wanted to analyse the long-term behaviour of the system under the zero-state intermediate condition in the absence of stimulus. Hence, $t_a \approx 667$. Further, the values of the parameters are kept the same as defined in Section 5.4.2:

$$\widetilde{D}_x = 0.001, \widetilde{D}_y = 0.05, a = 0.25, \nu = 0.01, \gamma = 0.12, p = 0.3, \delta = 0.1, \eta = 1.$$

From the simulation, at time $t = 666$ we see the same circular wave-back as predicted in Figure 5.16(d), since all the conditions applied to the system are the same until the zero-state intermediate condition is applied at $t = 667$. That is, the pattern is repetitive until the breaking time $t = 667$. Since the domain of depolarization reaches the zero membrane potential at time $t = 667$, the first half of the propagating circular wave-back shown in Figure 5.16(d) is broken up. This break-up causes the ends of the other half of the circular wave-back to curl around a pair of points (spatial singularities) and thus produces symmetrical free ends in the upper and lower regions of the domain (see Figure 5.18(a)). These free ends then become the tips for the formation of rotating spirals (see Figure 5.18(b)). A qualitative analysis in relation to change of sign of the normal velocity at a point along the interface separating the excited and recovery regions can be seen in [35] and [86] for the formation of free spiral ends.

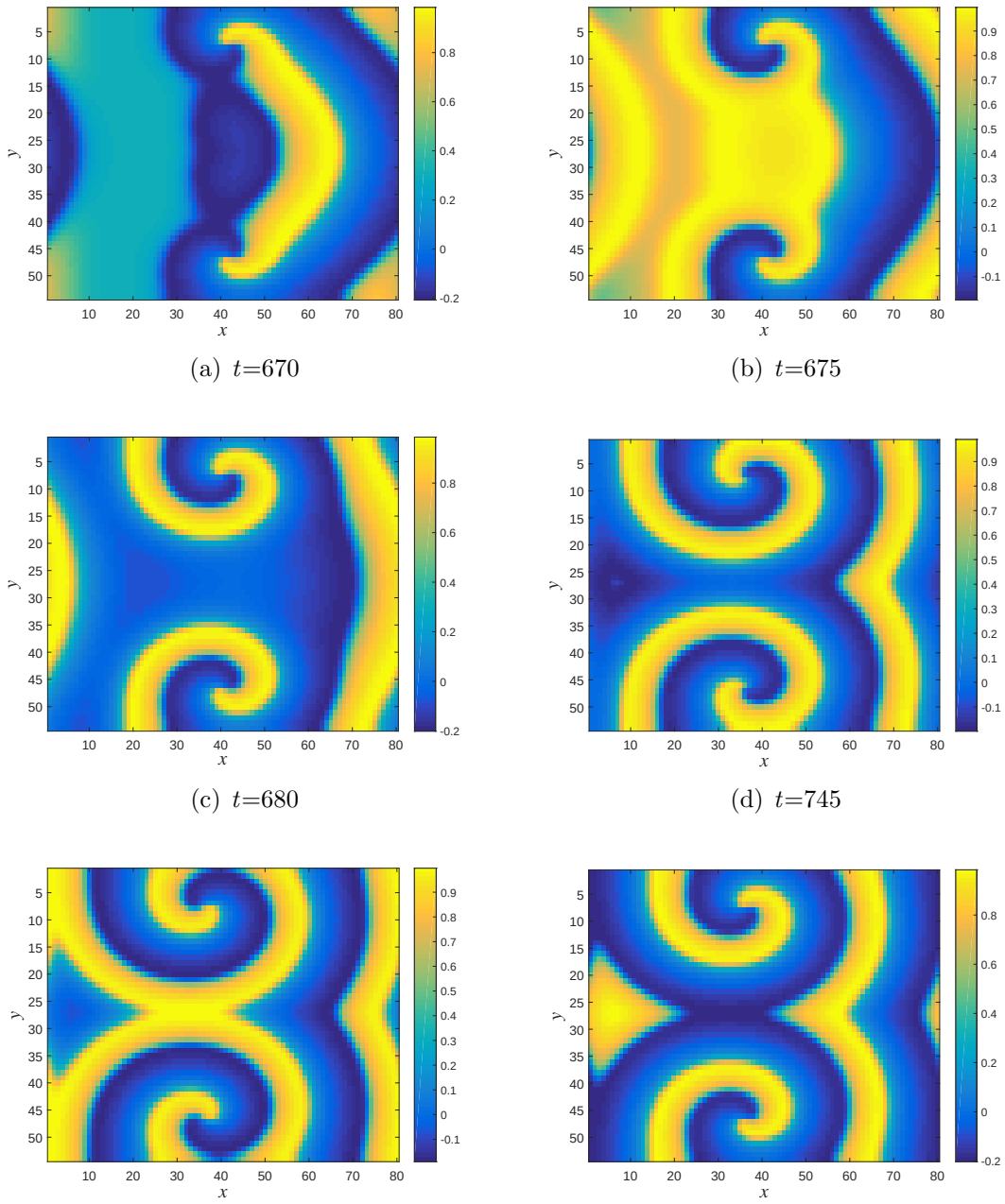

(a) t=670 (b) t=675

(c) t=680 (d) t=745

(e) t=795 (f) t=920

Figure 5.18: Schematic shows (a) the formation of free ends, (b) evolution of rotating spiral arms, (c) and (d) evolution of common tail and birth of the "twin-spirals", (e) collision of curved arm portion of the spirals and (f) repetitive formation of common tail.

In the subsequent simulation, the right half of the next available circular wave-back evolves toward a connecting tail for both spiral arms appearing in the upper and lower regions. This dynamics is shown in Figures 5.18(a)-Figure 5.18(d) as a continuous time series. A completed birth of rigidly and steadily rotating spiral waves are shown in 5.18(d), where the top and bottom spirals rotate in counter-clockwise and clockwise directions, respectively. We name these "twin-spirals" as the tails of the two spirals are connected. This common tail does not disappear as it is periodically repetitive in time. The repetition is caused by the collision of the curved portion (see Figure 5.18(e)) of the spiral arms, which creates a new common tail and supports the spirals to rotate in the directions mentioned above. Furthermore, since the spirals rotate steadily and rigidly, under the notion that steadily rotating spirals trace out a circular path [3, 43], we approximately calculate the angular speed of the spiral tip from the simulation results and by applying the relation $T = 2\pi/\omega$. We found a full rotation of the spiral tip is completed over a dimensionless time 260. This gives a dimensionless angular speed, $\omega = 0.02418$, to five-decimal places.

In the following section we will study the effect of the x-directional macroscopic PVC, $\widetilde{D}_x$, on the pattern formation, while the y-directional macroscopic PVC, $\widetilde{D}_y$, remains unchanged.

5.4.3.1.1 Effect of PVC: slow rotation, drift and meander: To study the effect of PVC, we first reduce $\widetilde{D}_x = 0.001$ by half, while the other conditions and parameters are kept the same as in Section 5.4.3.1. Hence, $\widetilde{D}_x = 0.0005$. Results reveal that the system is being self-excited (oscillations grow in amplitude) at specific spatial locations (indicated by green circles in Figures 5.19(a) and 5.19(b)) and regions other than the self-excitation are exposed with a pair of rigidly rotating twin-spirals. This is because the slow variation of potential coefficient allows two successive wave-backs to break up at a time, hence producing an additional twin-spirals not seen in the case of $\widetilde{D} = 0.001$. Moreover, the self-excitations circled in Figure 5.19 play a major role

in determining the direction of the rotation of the spirals. This can be described as follows.

The growing amplitude of the self-excitation of cells in the middle of the four spirals (see large green circles in Figures 5.19(a) and 5.19(b)) pulls the twin-arms of the spirals towards the region of self-excitation. This dynamics forces the twin-arms to turn

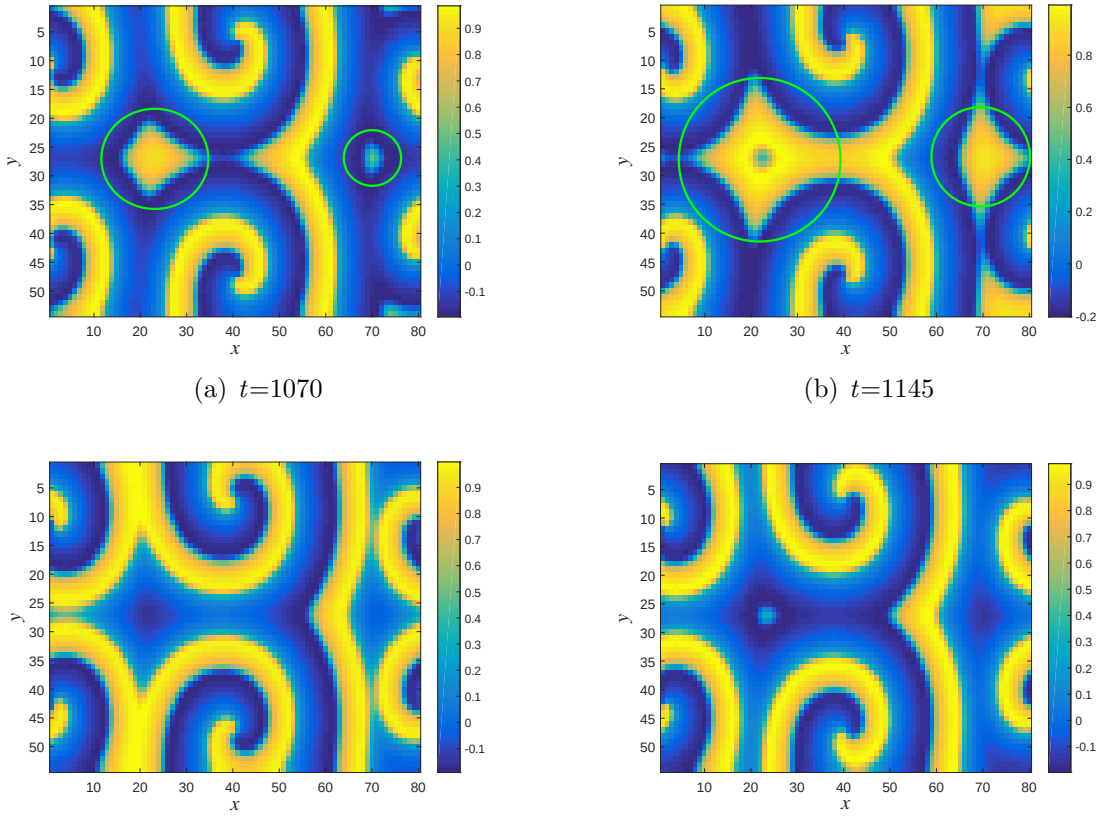

(a) t=1070 (b) t=1145

(c) t=1295 (d) t=1370

Figure 5.19: Schematic shows (a) pairs of twin-spirals with some cells becoming self-excited, (b) the development of self-excitation (denoted by green circles), (c) creation of highly curved portion of spiral arms through self-excitation and (d) diverging spirals rotating clockwise and anti-clockwise. See Figure 5.20 for the direction of rotations of diverging spirals.

towards the region of self-excitation, hence leading the left and right spirals located in the upper region to rotate counter-clockwise and clockwise, respectively. This dynamics can also be seen in Figures 5.19(a) and 5.19(b), as the length of the highly curved section of arms from the tip of the spirals decreases as the self-excitation grows. That is, the length of the spiral arm is greater in the absence of self-excitation. Similar dynamics are described for the left and right spirals appearing in the lower region, rotating in clockwise and counter-clockwise directions, respectively. From Figures 5.19(b) and 5.19(c) we see that the spirals rotate through approximately 180 degrees in the outward direction over the time period 150 (=1295-1145) due to the maximum self-excitation (larger green circle in Figure 5.19(c)). Therefore, the spirals are divergent as each of them rotates outwards from its core (see Figure 5.20 for the direction of rotation of each spiral, observed in a movie file). Such outward rotating spirals were observed in some systems [90, 119], including calcium wave activities in cortical tissue culture [114] and a fertilized Xenopus oocyte [79] and in pathological states, such as heart ventricular fibrillation [17] and retinal spreading depression [47].

In the continuous time series, since the direction of rotation of spirals (in any order other than the diagonal) is contrary to each other, the interaction between spirals pushes the arms away from each other. The shape of the spirals is then determined by the interaction induced by self-excitation. In addition, we observed a formation of thinner spiral waves in contrast to the thicker one seen in the case of $\widetilde{D}_x = 0.001$. That is, low-valued $\widetilde{D}_x$ splits thicker spiral waves into a number of thinner ones. This is why, together with the outward rotation of spirals, we later we found for $\widetilde{D}_x < 0.0005$, the conversion of spirals waves into forward and backward plane waves due to more splits of spirals. Moreover, the tip of the twin-spirals rotates slowly with the same constant angular speed. As found before, the dimensionless angular speed of the tip of the spirals in this case is calculated to be approximately 0.01676, since a full circular path the tip of the spirals is completed over a dimensionless time approximately 375. Note that the angular speed of each spiral tip in $\widetilde{D}_x = 0.001$ was found earlier

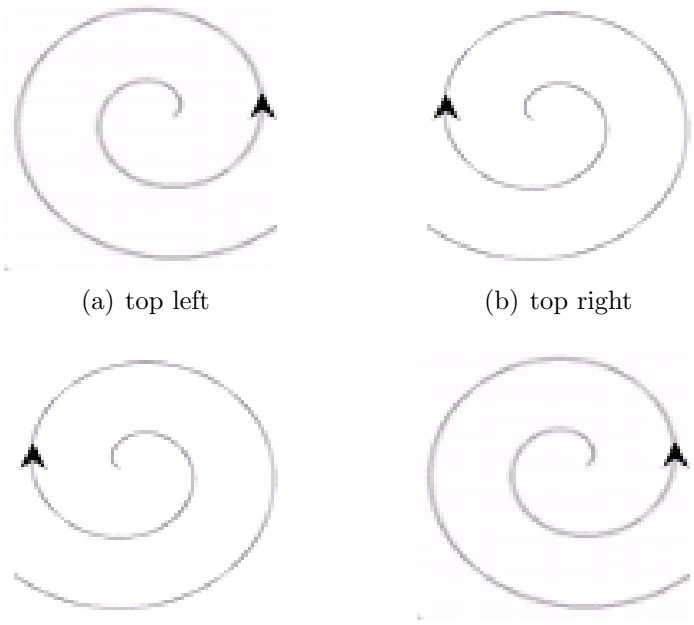

(a) top left (b) top right

(c) bottom left (d) bottom right

Figure 5.20: Schematic shows the direction of rotation of each diverging spiral appearing at the (a) top left, (b) top right, (c) bottom left and (d) bottom right, of the sub figures of Figure 5.19. Here (a) and (c) and (b) and (d) are pair of twin-spirals.

to be $\omega = 0.02418$. Therefore, the slow macroscopic variation of PVC decreases the angular speed of the spiral tip. However, to prove this result we carried out more experiments to provide a better understanding of the system dynamics. We concluded that 0.0005 was the critical value of $\widetilde{D}_x$ below which the system can be observed with a family of forward and backward plane waves as seen in the one-dimensional problem.

To further study the effect, $\widetilde{D}_x$ was increased by half of its earlier value 0.001. Hence, we set $\widetilde{D}_x = 0.0015$. As in case of $\widetilde{D}_x = 0.001$, the system produced a single twin-spirals. In addition, these spirals are identified with drifting dynamics. The drift of a spiral wave can be defined by its translocation, with time as a rigidly rotating spiral only holds one symmetry [5] and therefore it is possible that the location and phase of

a spiral wave is likely to experience changes when stability of such symmetry is broken [5]. Therefore, for the increased $\widetilde{D}_x$ value, we found this kind of translocation of the twin-spirals, as shown in Figure 5.21. Initially, at $t = 670$, the tip of the twin-spirals

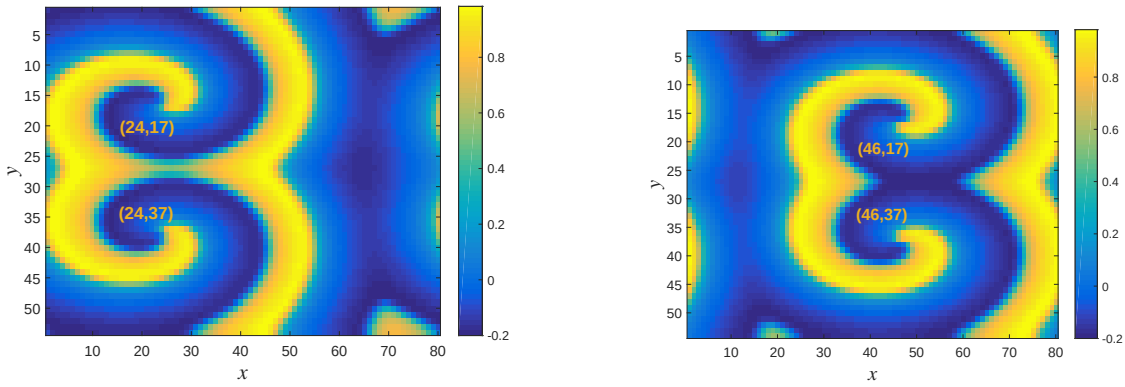

(a) t=720 (b) t=1070

Figure 5.21: Schematic shows for $\widetilde{D}_x = 0.0015$ the location of the twin-spirals at (a) $t = 720$ and (b) $t = 1070$. Drift is induced through 22 spatial points, over a time 350, along the x-axis. Rotation of top and bottom spirals are the clockwise and anti-clockwise, respectively.

was found near the spatial coordinates (5,17) and (5,37) (not shown in Figure 5.21). In the subsequent time, spirals were drifted to the spatial coordinates; (24,17) and (24,37), respectively (see Figure 5.21(a)) at time $t = 720$ and to (46,17) and (46,37) (see Figure 5.21(b)) at time $t = 1070$. Therefore, we identify "PVC induced drifts" for $\widetilde{D}_x = 0.0015$, that were not seen in the previous cases ($\widetilde{D}_x = 0.0005, 0.001 < 0.0015$). Refer to [5] and [43] for other kinds of drifts such as resonant drift, inhomogeneity induced drift, anisotropy induced drift, boundary induced drift and drift due to interaction of spirals. In the next section we report another kind of drift: the stimulus induced drift. In addition to $\widetilde{D}_x = 0.0015$, we also identified for $\widetilde{D}_x = 0.0020, 0.0025$ a number of drifts along the x-direction. We concluded that there is a threshold value for $\widetilde{D}_x$ above which drifts can be induced for rigidly rotating spiral waves. In our modelling, we found the threshold value of $\widetilde{D}_x$ to be 0.0015. Hence, from the

above results and discussion, one can be defined an interval $0.0005 \leq \widetilde{D}_x \leq 0.0025$ for which the system possesses rigidly rotating twin-spirals. As spirals rotate steadily and rigidly soon after drifts are accomplished, we find the angular speed of the tip of spirals to be 0.03810, 0.04657 and 0.04836, corresponding to $\widetilde{D}_x$ values 0.0015, 0.0020 and 0.0025.

$\widetilde{D}_x$	ω
0.0005	0.01678
0.0010	0.02418
0.0015	0.03810
0.0020	0.04657
0.0025	0.04836

Table 5.1: $\widetilde{D}_x$-related angular speed

The time taken by the tip of spirals to complete a full rotation in each case is 165, 135 and 130, respectively. With the angular speed of the tip found earlier for $\widetilde{D}_x = 0.0005$ and 0.001, the Table 5.1 summarizes the results of $\widetilde{D}_x$-related angular speed. Now, we seek to discover the dynamics of the system if $\widetilde{D}_x > 0.0025$. For $\widetilde{D}_x > 0.0025$,

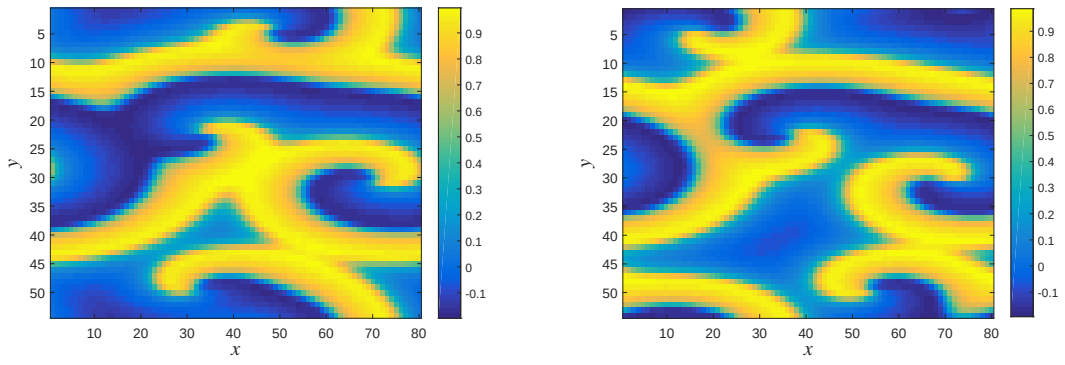

(a) t=1095 (b) t=1195

Figure 5.22: Schematic shows for $\widetilde{D}_x = 0.003$ a nonsymmetric pattern of interacting pair of twin-spirals due to meandering.

we report the dynamics as a transition from rigidly rotating spirals to meandering spirals (path of the spiral tip is not a closed curve, and can form different patterns such as flower petals), hence forming a non-periodic pattern in the domain. Figure

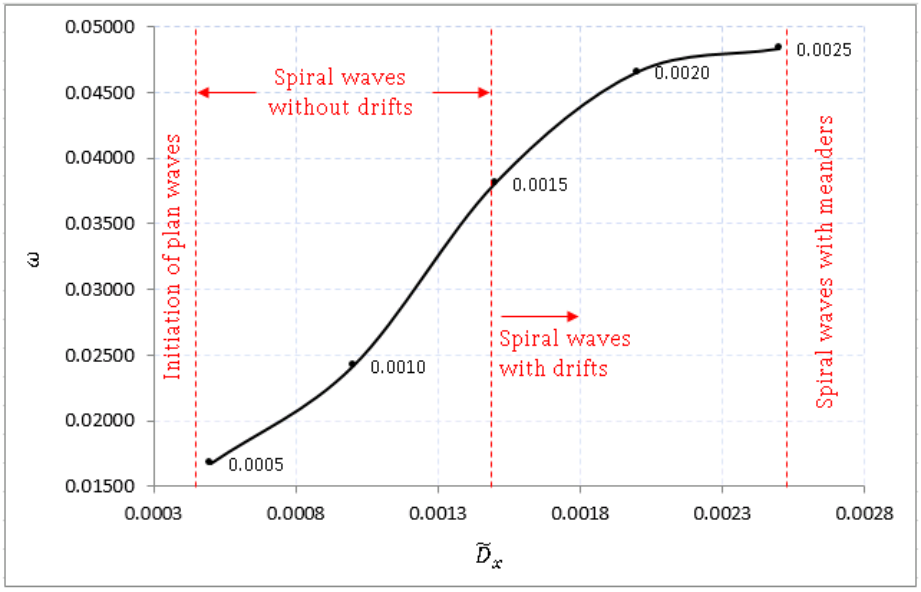

Figure 5.23: Schematic shows a trend of the angular speed of the spiral tip with PVC in the interval $0.0005 \leq \widetilde{D}_x \leq 0.0025$. The critical and threshold values of diffusion below and above which the initiation of plane waves and meandering spirals are shown by the first and second red dotted red vertical lines. Labels on the graph denote the PVC values used for plotting.

5.22 shows a meandering spiral pattern for $\widetilde{D}_x = 0.003$. The dynamics of spirals moving near the top and bottom boundaries of the domain are observed with a complex nature, as they seem to interact with other spirals, creating a kind of rolling motion with drifts. This rolling motion and the continuous interactions between spirals due to the increased $\widetilde{D}_x$ causes the system to create meandering spirals. In addition, the top and bottom spirals rotate in clockwise and anti-clockwise directions, respectively. The middle twin-spirals are initially created near the right boundary and this pair is directed towards the centre region, as shown in Figure 5.22(b). Rotations of these spirals are observed in clockwise and anti-clockwise directions. In an other case,

$\widetilde{D}_x = 0.004$, we noticed similar dynamics with meanders and drifts and the direction of the rotation of each spiral was observed to be contrary to the direction of rotations observed for $\widetilde{D}_x = 0.003$. Therefore, the direction of the rotation of spirals was determined by both interactions between spirals and the membrane potential coefficient.

The complete dynamics of spiral waves based on $\widetilde{D}_x$ are illustrated in Figure 5.23. It shows a monotonically increasing variation of angular speed with $\widetilde{D}_x$ in the interval $0.0005 \leq \widetilde{D}_x \leq 0.0025$ (in which steadily and rigidly rotating spirals were observed), as summarized in Table 5.1. Other intervals $\widetilde{D}_x > 0.0025$ and $0 < \widetilde{D}_x < 0.0005$ separated by dotted red vertical lines indicating the existence of meandering spirals and the initiation of forward and backward plane waves. We did not find the angular speed of the tip of meandering spirals, as they are not stationary and the path of the spiral tip, in general, does not follow a closed curve.

5.4.3.1.2 Effect of stimulus: wave-break and drifts In the preceding subsection we studied various membrane potential coefficients for the dynamics of the system under the influence of a weakly time-dependent, spatially-varying bi-directional stimulus. In this section we report other possible dynamics of the same cellular system, not only under the influence of the continuous action of bi-directional stimulus defined by Equations (5.4.9) and (5.4.10), where $t_a = t_T$, but we also study the dynamics induced by a uni-directional stimulus.

For the first case, the parameters are set as defined in Section 5.4.3.1, with $\widetilde{D}_x = 0.001$. As explained in Sections 5.4.2 and 5.4.3.1, results reveal the existence of twin-spirals through the initiation of curved wave-backs followed by nearly circular waves. The continuous action of the bi-directional stimulus and its high excitation of cells near the stimulus creates unstable twin-spirals. Thus, the twin-spiral undergoes a "wave-break", separating the tails of the spiral from its arms. This dynamics is shown in Figures 5.24(a) and Figure 5.24(b). Consequently, broken spiral sections experience drifts towards a region of low excitation where they reform stable spiral shapes (the

tip of the up and down spirals was in this case found to move approximate spatial points (5, 9) and (5, 45)), respectively) and start to rotate rigidly and steadily. Similar kinds of dynamics can been in [5], [17], [43], [92] and [121]. Therefore, wave-break

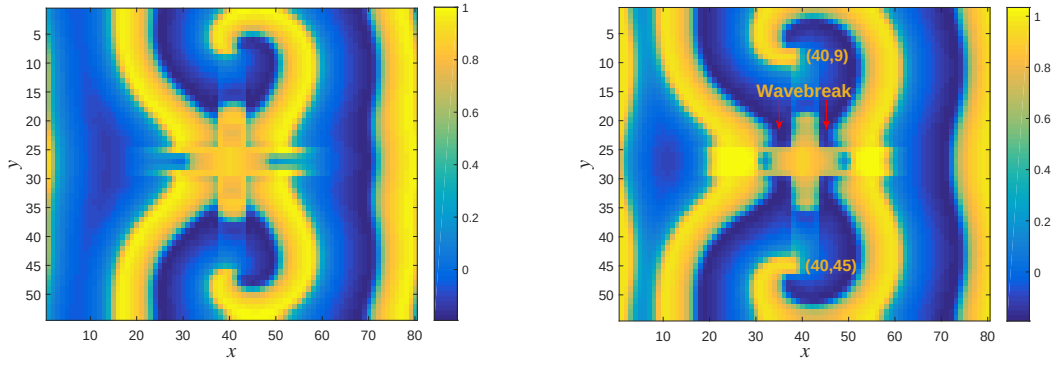

(a) t=695 (b) t=720

(c) t=1245 (d) t=1995

Figure 5.24: Schematic shows (a) a systematically created spiral wave, (b) wave break, (c) stimulus induced drift and (d) drift induced by the interaction of spirals.

and drift are induced by stimulus, but are not due to PVC since this dynamics was not predicted for $\widetilde{D}_x = 0.001$ in the previous section. In the subsequent motion, spirals located in the upper and lower regions experience further drifts respectively from spatial points near (5,9) and (5,45) to (20,9) and (20,45) (see Figure 5.24(c)) and then to (30,9) and (30,45) (see Figure 5.24(d)). Latter drifts were induced due

to the interactions between the arms of spirals (see Figures 5.24(c) and 5.24(d) for their interactions), which drew the spirals to move forward as they rotated contrary to each other.

Secondly, as an effect of stimulus on the system, we report another dynamics not previously been observed in any earlier literature. We categorize this as static twin-spirals (non-rotating spiral form) with continuous drift. For studying this dynamics, we allowed a uni-directional stimulus only (instead of bi-directional stimulus). We applied in the y-direction stimulus I defined by Equation (5.4.9) where $I_x = 0$ and I_y is taken with a peak value 4.9 (see Figure 5.25). For simulation we considered five

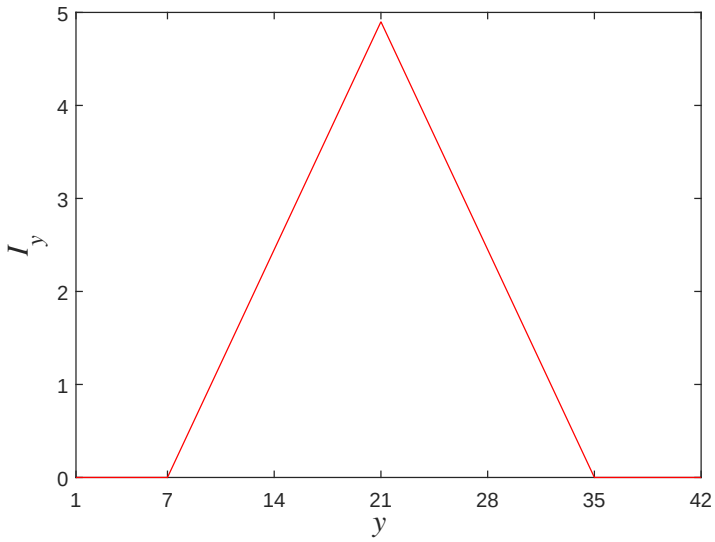

Figure 5.25: Schematic shows the uni-directional stimulus applied in the y-direction. Peak value of the stimulus is taken as 4.9 with a spatial gradient of 0.35.

bands of cells in the centre in the y-direction and stimulated each of them using the same stimulus, I_y. The domain is setup with spatial points in dimensions of 60×42. With this domain dimension, the spatial gradient of I_y is now 4.9/(21-7)=0.35 (see

Figure 5.25). This value is greater than that used in previous scenarios (approximately 0.28) in order to model the stimulus I_y. Importantly, I_y was switched off at $t_a = 850$ in Equation (5.4.9) and the simulation was carried out for a dimensionless time period of 2,500. We used the same parameter values as in the previous section, but $\widetilde{D}_x$ was taken as 0.0005, the critical value for the nonexistence of spiral waves predicted earlier. Results revealed the existence of "static twin-spiral" (spiral wave

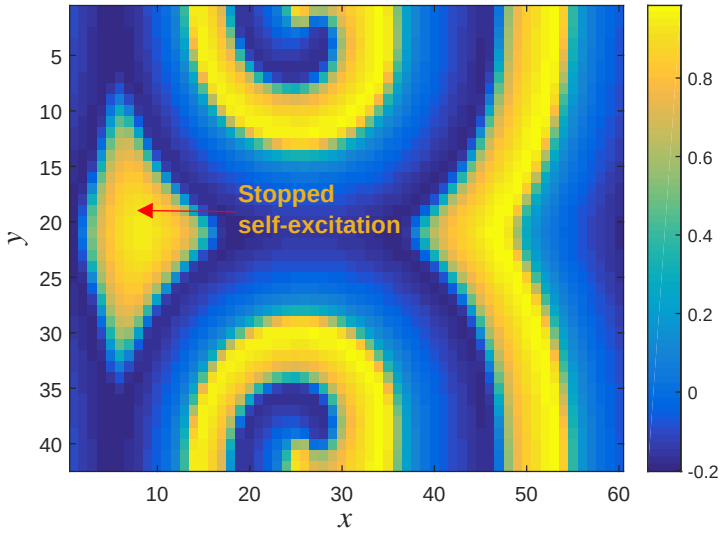

Figure 5.26: Schematic shows a "static twin-spiral" under the application of uni-directional stimulus shown in Figure 5.25 with $D_x = 0.0005$.

forming with non-rotating dynamics) that undergoes continuous drift along the x-direction. That is, the fixed form of spiral pattern shown in Figure 5.26 was observed to move continuously from the left boundary to the right throughout the simulation time.

To explain the dynamics of the static twin-spirals pattern formation, we recall the dynamics explained in section 5.4.3.1 for $D_x = 0.0005$. In that case, we showed that twin-spirals appeared with slow rotations, as D_x was small and the direction

of the spiral tips rotation was determined by the self-excitation of cells caused by bi-directional stimulus $I = (I_x, I_y)$. However, in this case, since the cells were not stimulated in the x-direction, the self-excitation of cells was limited to a particular level and stopped when the oscillating circular wave-back was broken. Therefore, slow rotations of spiral tips ceased in the presence of law D_x as well as in the absence of self-excitation. This cessation of slow rotation of spirals led the system towards the formation of static spirals. In addition, these spirals experience a continuous drift throughout the simulation time, as 0.0005 is considered the critical value for the formation of moving plane waves. This dynamics was noted only for the spatial gradient of 0.35 (or the peak value 4.9) of the time-dependent, spatially-varying stimulus I applied to the domain as mentioned previously. The system was not exposed to spiral waves for any value less than or greater than 0.35. The formation of static twin-spiral with continuous drift may be considered a long-term pathological state of cells, as it does not vanish in a long-run and the spiral patterning has been considered to be one of the pathological indications of some human diseases as described before.

5.5 Summary

In this chapter we have numerically solved the one- and two-dimensional homogenised partial differential equations of membrane potential. In both cases, we used a spatially-varying stimulus defined in the form of a second-order spline. This form of stimulus is introduced based on the Hopf bifurcation points identified for a ring of three coupled, discrete cells in the absence of potential variation coefficient (PVC). The one-dimensional numerical experiments revealed the existence of forward and backward plane waves along the arterial axis. This one-dimensional study is also showed the existence of multiple steady states of the cellular membrane potential in the macroscopic arterial domain. The existence of multiple steady states were explained in relation to a critical value of the distance between moving point of initiation of waves and the boundary separating the stimulated and non-stimulated regions. In addition, the notion of interference via system reinforcement was also used to describe the multiple

steady states of the system.

Based on numerical experiments of two-dimensional lattice models, we showed the existence of curved wave-fronts and -backs, nearly circular wave-fronts and -backs, and finally, the existence of spiral waves. In the case of spiral waves, we identified an interval for which the system is predicted with rigidly and steadily rotating twin-spirals with increasing angular speed of the tip of the spirals with respect to an increasing effective PVC. Dynamics of the spirals were explained in terms of drifts, meanders wave-break, interpreting the role of PVC and types of stimulus. In addition, we also reported the existence of moving static twin-spiral (non-rotating spirals). Most of the dynamics explained in this chapter have not been reported for a multi-dimensional, discrete as well as continuous FHN system.

Chapter 6

Homoclinic Orbits, Results and Discussion

In Chapter 4 we showed by numerical simulations the existence of plane waves for the one- and two-dimensional homogenised partial differential equations (HPDEs) derived in chapter 4. This result has been justified in this chapter by constructing homoclinic orbits corresponding to a critical wave speed.

A homoclinic orbit at some parameter values of a dynamical system is a loop which leaves from the equilibrium as a branch of the unstable manifold and reaches again the same equilibrium. Thus, any traveling impulse can be defined by a homoclinic orbit and the type of the equilibrium determines the shape of the impulse (impulse with monotone tail or oscillating tail is corresponding to a saddle or saddle-focus equilibrium) [20]. Mathematically speaking, a solution $u(t)$ of the dynamical system is interpreted by an orbit which is homoclinic to the equilibrium point u_0 and $u(t) \to u_0$ as $t \to \pm\infty$. Therefore, a study of the equilibrium's stability and the construction of homoclinic orbit in the travelling wave coordinate system justifies the existence of wave solution we have shown numerically in chapter 5.

For constructing homoclinic orbits we apply the method of homotopy in MATCONT.

In particular, we follow [20] in which a full detail theoretical description of the homotopy method with illustrative examples can be found. Other work can be found in [20], [22], [23] and [77]. However, here we briefly explain the necessary step by step process of the Homotophy method in developing homoclinic orbit for the one-dimensional problem and follow the same procedure for the two-dimensional problem.

6.1 Homoclinic Orbits of 1-D Homogenised Models

Let us consider the one-dimensional HPDEs for the system of coupled 3 cells the Equations (5.3.1) and (5.3.2), then we have

$$\nu\frac{\partial \boldsymbol{v}}{\partial t} - \boldsymbol{g}(\boldsymbol{v}) + GA\boldsymbol{v} + \boldsymbol{w} - \boldsymbol{I} = \widetilde{D}\frac{\partial^2 \boldsymbol{v}}{\partial x^2}, \tag{6.1.1}$$

$$\frac{\partial \boldsymbol{w}}{\partial t} + \gamma\boldsymbol{w} - \boldsymbol{v} + \boldsymbol{p} = \boldsymbol{0}, \tag{6.1.2}$$

where all notations in Equations (6.1.1) and (6.1.2) are given in Chapter 2 and $\boldsymbol{v} = (v_1 \;\; v_2 \;\; v_3)^{\mathrm{T}}$ and $\boldsymbol{w} = (w_1 \;\; w_2 \;\; w_3)^{\mathrm{T}}$.

First, we will analyze the stability of the equilibria of the system given by Equations (6.1.1) and (6.1.2) as it is important to initiate the method of homotopy for homoclinic orbits.

6.1.1 Stability of the Equilibrium

Let us define the traveling wave coordinate:

$$z = x + ct, \tag{6.1.3}$$

where $c > 0$ denotes the dimensionless wave speed.

By substituting Equation (6.1.3) into Equations (6.1.1) and (6.1.2) we have a system

of ordinary differential equations (ODEs):

$$\begin{aligned} c\nu \boldsymbol{v}' &= \widetilde{D}\boldsymbol{v}'' + \widetilde{D}'\boldsymbol{v}' + \boldsymbol{g}(\boldsymbol{v}) - GA\boldsymbol{v} - \boldsymbol{w} + \boldsymbol{I}, \\ c\boldsymbol{w}' &= \boldsymbol{v} - \gamma\boldsymbol{w} - \boldsymbol{p}, \end{aligned} \tag{6.1.4}$$

where $' = \frac{d}{dz}$.

Let us define $\boldsymbol{v}' = \frac{d\boldsymbol{v}}{dz} = \boldsymbol{u}$, where $\boldsymbol{u} = (u_1 \;\; u_2 \;\; u_3)^{\mathrm{T}}$.

The system in Equation (6.1.4) can be written as a system of first-order ODEs:

$$\begin{aligned} \boldsymbol{v}' &= \boldsymbol{u}, \\ \boldsymbol{u}' &= \frac{(c\nu - \widetilde{D}')\boldsymbol{u} - \boldsymbol{g}(\boldsymbol{v}) + GA\boldsymbol{v} + \boldsymbol{w} - \boldsymbol{I}}{\widetilde{D}}, \\ \boldsymbol{w}' &= \frac{\boldsymbol{v} - \gamma\boldsymbol{w} - \boldsymbol{p}}{c}. \end{aligned} \tag{6.1.5}$$

Most of the work in relation to homoclinic orbits of FHN have been studied for a single FHN system (that is, G=0) and in the absence of the parameters p and I. These literature are not limited to [38], [39], [40], [42], [52], [56], [70], [73], [99]. In the absence of the parameters p and I, previous work considered a trivial unique steady state (0,0,0) which arose in the absence of G, I and p. However, these parameters are crucial in our models for the cellular communication, which respectively model the conductance of gap junctions between cells, excitable behavior of cells and the Nernst potential.

Now, let us take $\widetilde{D} = D$, a constant. Then the system given by Equation (6.1.5) can be written as:

$$\boldsymbol{v}' = \boldsymbol{u}, \tag{6.1.6}$$

$$\boldsymbol{u}' = \frac{c\nu\boldsymbol{u} - \boldsymbol{g}(\boldsymbol{v}) + GA\boldsymbol{v} + \boldsymbol{w} - \boldsymbol{I}}{D}, \tag{6.1.7}$$

$$\boldsymbol{w}' = \frac{\boldsymbol{v} - \gamma\boldsymbol{w} - \boldsymbol{p}}{c}. \tag{6.1.8}$$

For equilibria, we have $\boldsymbol{v}' = \boldsymbol{u}' = \boldsymbol{w}' = \mathbf{0}$ and hence the steady states of the system of equations given by Equations (6.1.6)-(6.1.8) can be found by solving the system of vector algebraic equations:

$$\begin{aligned} \boldsymbol{u} &= \mathbf{0}, && (6.1.9)\\ \boldsymbol{w} &= \boldsymbol{g}(\boldsymbol{v}) - GA\boldsymbol{v} + \boldsymbol{I}, && (6.1.10)\\ \boldsymbol{v} &= \gamma\boldsymbol{w} + \boldsymbol{p}. && (6.1.11) \end{aligned}$$

By substituting Equation (6.1.11) in the Equation (6.1.10) we have a cubic vector polynomial:

$$\begin{aligned} \gamma^3\boldsymbol{w}^3 - (1+\alpha-3p)\gamma^2\boldsymbol{w}^2 &+ \left(3p^2 - 2(1+\alpha)p + \alpha + \frac{1}{\gamma}\right)\gamma\boldsymbol{w} \\ &+ \gamma GA\boldsymbol{w} - \boldsymbol{g}(p) - \boldsymbol{I} = \mathbf{0}, \end{aligned} \tag{6.1.12}$$

where the powers in the polynomial are raised to the components of the vector $\boldsymbol{w}$ and $\boldsymbol{g}(p) = (\ g(p) \quad g(p) \quad g(p)\ )^{\mathrm{T}}$ with

$$g(p) = g(v|_p) = p(1-p)(p-\alpha). \tag{6.1.13}$$

Now, we choose the steady state stimulus to be

$$\boldsymbol{I} = -\boldsymbol{g}(p). \tag{6.1.14}$$

By substituting Equation (6.1.14) into Equation (6.1.12) we have an obvious real unique solution $\boldsymbol{w} = \mathbf{0}$.

By substituting $\boldsymbol{w} = \mathbf{0}$ in the Equation (6.1.11) the system of three-cells can be found with a unique steady state:

$$(\boldsymbol{v}, \boldsymbol{u}, \boldsymbol{w}) = (\boldsymbol{p}, \mathbf{0}, \mathbf{0}). \tag{6.1.15}$$

That is, the unique steady state given by Equation (6.1.15) can be written in the form:

$$(v_1, u_1, w_1; v_2, u_2, w_2; v_3, u_3, w_3) = (p, 0, 0; p, 0, 0; p, 0, 0). \tag{6.1.16}$$

We observe, from Equation (6.1.16), that the steady state of the coupled three-cells system to be depend on the parameter p. In other words, the membrane potential becomes Nernst potential in the equilibrium state. Hence, this result coincide with the Nernst equation, as the Nernst equation predicts the membrane potential to be equal to the Nernst potential when the cellular membrane is in the dynamical equilibrium with respect to one type of ion (see [72]).

We linearize the three-cells coupled system about the steady state of Equation (6.1.15). For this, we find the Jacobian (as the circulant matrix) of the 9-dimensional system of Equations (6.1.6)-(6.1.8) with respect to the steady state (p, 0, 0):

$$J = \begin{pmatrix} P & Q & Q \\ Q & P & Q \\ Q & Q & P \end{pmatrix}, \tag{6.1.17}$$

where

$$P = \begin{pmatrix} 0 & 1 & 0 \\ \frac{3p^2-2(1+\alpha)p+\alpha+2G}{D} & \frac{c\nu}{D} & \frac{1}{D} \\ \frac{1}{c} & 0 & -\frac{\gamma}{c} \end{pmatrix}, \quad Q = \begin{pmatrix} 0 & 0 & 0 \\ -\frac{G}{D} & 0 & 0 \\ 0 & 0 & 0 \end{pmatrix}. \tag{6.1.18}$$

Here we do not derive analytically any constraints for the wave speed c in terms of other parameters appeared in the Jacobian, as our system of coupled three-cells modelled by a characteristic polynomial of order 9, which is not easily solve (or impossible) for eigen-values. Therefore, we are only interested in determining numerically the approximate eigen-values, which will categorize the type of the equilibrium. For this, we use the same parameter values, as used in the chapter 5 since the set of values emerged propagation of plan waves in one-dimension. Thus, let us take

$$\alpha = 0.95,\ \nu = 0.01,\ D = 0.001,\ G = 0.1,\ \gamma = 0.12,\ p = 0.3,\ c = 1.7. \tag{6.1.19}$$

By substituting these values into the Equation (6.1.18) we find a set of approximated eigen-values of the Jacobian as 3 reals and 3-pairs of complex conjugates with negative

real part. Note that we have chosen an initial value 1.7 for c. However, numerical experiments for other various range of c values also showed the same result (3 reals and 3-pairs of complex conjugates eigen-values with negative real part). Hence, the equilibrium point can be categorized as a *hyperbolic saddle focus* and is unstable. Therefore, the dimension of the stable and unstable manifolds are found as 6 and 3, respectively, and this result will be used for the construction of homoclinic orbits in the following section by defining the initial unstable connection parameters in relation to the dimension of the stable and unstable manifold.

6.1.2 Existence of Homoclinic Orbits

As mentioned before, we use the method of homotopy in MATCONT for constructing homoclinic orbits and briefly explain the necessary steps for the time integration and continuation.

We consider the problem in traveling wave coordinates, for which we use the system given by Equations (6.1.6)-(6.1.8). The Matlab solver *Ode45* is used for numerical integration. Moreover, we start with the steady state given by Equation (6.1.16), as an initial point, and 'connection saddle' as a curve type for the method of Homotopy. The initial value of parameters is taken as in Equation (6.1.19). Since we use the steady state to be the initial point of time integration, we take the initial value of the stimulus to be its value at the steady state. Hence, by comparing Equations (6.1.13), (6.1.14) and (6.1.19) we set

$$I = p(1-p)(\alpha - p) = 0.1365, \tag{6.1.20}$$

for all cells.

As stated before, since the dimension of the stable manifold is greater than the dimension of the unstable manifold we chose the first unstable parameter, $UParam1$, to be -1, and we leave the second unstable parameter, $UParam2$, as 0 (by default). $UParam2$ can be set to one of the directional values, -1 and 1, if the dimension of

the unstable manifold of the cell system is 6 (see [20] for similar argument). The unstable parameters $UParam1$ and $UParam2$ determine the initial direction of integration; whether in the direction of departing or approaching the equilibrium point [20]. Hence, we start integration in the direction of leaving the steady state and expect to approach the same steady state when a homoclinic orbit converges.

The initial time integration produced an orbit of a parabolic-shape curve ABC (see Figure 6.1), which is denoted by inner and outer green arrows. That is, the curve

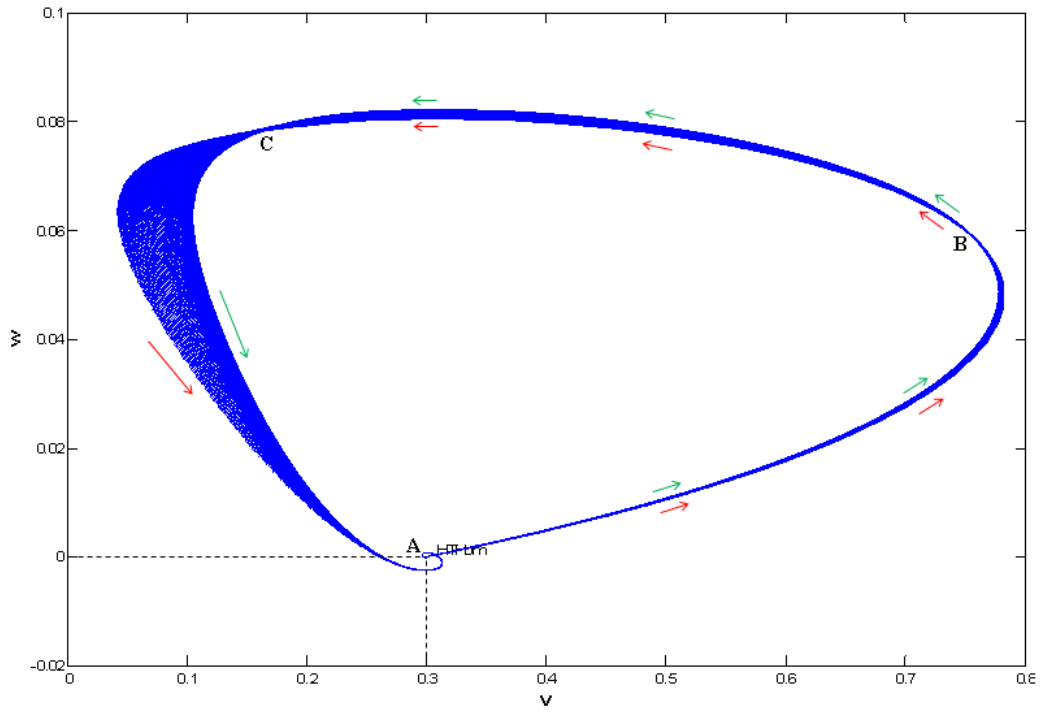

Figure 6.1: A completed orbit $ABCA$ denoted by green arrows shows the existence of homoclinic orbit for the first cell in the ring of three-coupled cells. Homoclinic orbit is labeled by 'HTHom'. Same orbit was obtained for other two cells in the coupled three-cells system

initiated at the steady state A and followed the path of the inner-line AB denoted by the green arrows. It crossed at B and reached the point C by following the

path of the outer-line BC denoted by green arrows. Obviously, this curve is good enough to proceed with the homotopy method. After the initial integration we found that one of the three stable connection parameters, $SParam1$, to be non-zero and other stable connection parameters, $SParam2$ and $Sparam3$, to be zero. This result showed that the end point of the plane tangent to the stable invariant manifold at the saddle focus was not obtained. Note that, all zero-valued stable connection parameters confirm the end-point of the plane tangent to the stable invariant manifold at the saddle focus is obtained (see [20]). Therefore, we carried out continuation by choosing BVP-discretization of 50 mesh intervals and 4 collocation points. We allowed the wave speed c, the non-zero stable parameter $SParam1$ and the distance to the saddle focus from the last point of the orbit (the homoclinic parameter) to be free.

After the discretization process continuation of integration produced (for finding a best fit) a family of curves denoted by dark blue thinner region and ended up with the inner curve CB, connecting the outer curve BA denoted by inner and outer red arrows, respectively (see Figure 6.1). For this curve, we obtained all of the stable parameters zero. Therefore, this curve lies in the unstable manifold with the end-point in the stable eigen-space of the equilibrium (see [20]). That is, this curve may be considered to be the boundary between the stable and unstable manifold.

We start continuation from the point C and, during the integration, we obtained another family of curves CA (wider dark blue region from the outer line indicated by the red arrow to the inner line denoted by the green arrow) spiraling towards the saddle-focus A. Finally, we found a best fit to be the inner curve CA denoted by the green arrow. We noted that each curve CA in the wider dark blue region has been connected to a corresponding curve CB and then to a corresponding curve BA in the thinner blue regions. Therefore, we found a homoclinic orbit $ABCA$ (indicated by green arrows) which finally set back to the saddle-focus A (see Figure 6.1). For this homoclinic orbit, the wave speed c was found to be 1.2328888, which is the critical

value for the existence of homoclinic orbits of the coupled three cells system of Equations (6.1.1) and (6.1.2), in the traveling wave coordinate system. As equilibrium be a saddle focus, we conclude that traveling wave is initiated as a traveling impulse of oscillating tails and propagation of wave is confirmed through construction of homoclinic orbit.

In the following section we will show for 2-dimensional models the existence of homoclinic orbits.

6.2 Homoclinic Orbits of 2-D Homogenised Models

As state before, in this section we study (without considering the symmetry breaking condition introduced in chapter 5) the existence of homoclinic orbits for the two-dimensional homogenised models of Equations (5.4.1) and (5.4.2).

6.2.1 Stability of the Equilibrium

The homogenised models for the two-dimensional problem are given by Equations (5.4.1) and (5.4.2):

$$\nu\frac{\partial v}{\partial t} - g(v) + w - I = \frac{\partial}{\partial x}\left(\widetilde{D}_x\frac{\partial v}{\partial x}\right) + \frac{\partial}{\partial y}\left(\widetilde{D}_y\frac{\partial v}{\partial y}\right), \tag{6.2.1}$$

$$\frac{\partial w}{\partial t} = v - \gamma w - p, \tag{6.2.2}$$

where $v = v(x, y, t), w = w(x, y, t)$, $I = I(x, y, t)$ and $g(v) = v(v - \alpha)(1 - v)$, $0 < \alpha < 1$. Further, $\widetilde{D}_x$ and $\widetilde{D}_y$ are homogenised potential variation coefficients (PVCs), which are taken as constants, defining $\widetilde{D}_x = D_1$ and $\widetilde{D}_y = D_2$ for numerical integration.

Let us define a traveling wave coordinate (see Figure 6.2):

$$z = \sqrt{x^2 + y^2} + ct, \tag{6.2.3}$$

where $c = \sqrt{c_1^2 + c_2^2}$ which makes an wave angle θ with the positive x-axis in the two-dimensional domain so that

$$v(x, y, t) = v(z), \quad w(x, y, t) = w(z). \tag{6.2.4}$$

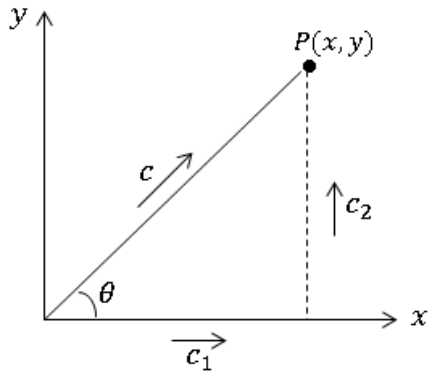

Figure 6.2: Schematic shows a method of conversion of two-dimensional domain into the traveling wave coordinate. P is an arbitrary point, c is the resultant velocity of the two-dimensional wave and θ is the wave angle.

By using Equations (6.2.3) and (6.2.4) we find

$$\frac{\partial v}{\partial t} = \frac{\partial z}{\partial t}\frac{dv}{dz} = c\,\frac{dv}{dz}, \tag{6.2.5}$$

$$\frac{\partial v}{\partial x} = \frac{\partial z}{\partial x}\frac{dv}{dz} = \frac{x}{\sqrt{x^2+y^2}}\,\frac{dv}{dz} = \cos\theta\,\frac{dv}{dz}, \tag{6.2.6}$$

$$\frac{\partial v}{\partial y} = \frac{\partial z}{\partial y}\frac{dv}{dz} = \frac{y}{\sqrt{x^2+y^2}}\,\frac{dv}{dz} = \sin\theta\,\frac{dv}{dz}, \tag{6.2.7}$$

$$\frac{\partial w}{\partial t} = \frac{\partial z}{\partial t}\frac{dw}{dz} = c\,\frac{dw}{dz}. \tag{6.2.8}$$

By substituting Equations (6.2.5)-(6.2.8) into Equations (6.2.1) and (6.2.2) we have

$$c\nu\frac{dv}{dz} - g(v) + w - I = D\frac{d^2v}{dz^2}, \tag{6.2.9}$$

$$c\frac{dw}{dz} + \gamma w = v - p, \tag{6.2.10}$$

where $D = D_1 \cos^2\theta + D_2 \sin^2\theta$.

The above models can be deduced to the one-dimensional single cell model of Equation (6.1.4), for which $G = 0$, $D_1 = \widetilde{D}, D_2 = 0$ and $\theta = 0$.

Let us take $\boldsymbol{v}' = \frac{d\boldsymbol{v}}{dz} = \boldsymbol{u}$ then we have

$$v' = u, \tag{6.2.11}$$

$$u' = \frac{c\nu u - g(v) + w - I}{D}, \tag{6.2.12}$$

$$w' = \frac{v - \gamma w - p}{c}. \tag{6.2.13}$$

Hence, steady states of the system of Equations (6.2.11)-(6.2.13) are given by

$$u = 0, \tag{6.2.14}$$

$$v = \gamma w + p, \tag{6.2.15}$$

$$w = g(v) + I. \tag{6.2.16}$$

By substituting Equations (6.2.15) into Equation (6.2.16) we have a cubic polynomial,

$$\gamma^3 w^3 - (1 + \alpha - 3p)\gamma^2 w^2 + \left(3p^2 - 2(1+\alpha)p + \alpha + \frac{1}{\gamma}\right)\gamma w - g(p) - I = 0, \tag{6.2.17}$$

where $g(p) = g(v|_p) = p(1-p)(p-\alpha)$.

Equation (6.2.17) is similar to the cubic polynomial of Equation (6.1.12) with $G = 0$. Therefore, as explained in the one-dimensional case, the unique steady state (under the steady state stimulus $I = -g(p)$) of the system of Equations (6.2.11)-(6.2.13) is given by (v, u, w)=$(p, 0, 0)$.

To study the stability we linearize the system of Equations (6.2.11)-(6.2.13) about the steady state (v, u, w)=$(p, 0, 0)$. For this, we find the Jacobian of the system of Equations (6.2.11)-(6.2.13) at the steady state as:

$$J = \begin{pmatrix} 0 & 1 & 0 \\ \frac{3p^2-2(1+\alpha)p+\alpha}{D} & \frac{c\nu}{D} & \frac{1}{D} \\ \frac{1}{c} & 0 & -\frac{\gamma}{c} \end{pmatrix}, \tag{6.2.18}$$

where $D = D_1 \cos^2\theta + D_2 \sin^2\theta$.

We define the parameters (other than c and θ) with the same values as in the one-dimensional case, to compare with the critical value of the one-dimensional wave speed 1.2328888. Hence, we have

$$\alpha = 0.95,\ \nu = 0.01,\ D_1 = 0.001,\ D_2 = 0.1,\ \gamma = 0.12,\ p = 0.3. \tag{6.2.19}$$

Note that PVCs: D_1 and D_2 has been taken to be the one-dimensional PVC, D, and the circumferential coupling coefficient, G.

By substituting Equation (6.2.19) in the Equation (6.2.18) of Jacobian and by numerically experimenting a set of different values for c and θ (see columns 1 and 2 in Table 6.1), we find again the steady state (p, 0, 0) to be a saddle focus, as the eigen-values of the Jacobian with respect to the steady state are one positive real and a pair of complex conjugates with negative real parts. Therefore, the dimension of the stable and unstable manifold is 2 and 1,respectively. As discussed in the previous section, we will assign the first unstable parameter $UParam1$ by the directional value -1 and the second unstable parameter $UParam2$ by its default value 0 for the initiation of homotopy method.

6.2.2 Existence of Homoclinic Orbits

To construct homoclinic orbits for the models of Equations (6.2.1) and (6.2.2), we apply the method of homotopy in the traveling wave coordinate system given by Equations (6.2.11)-(6.2.13). We followed time integration and continuation as described in the previous section. Further, we use the same parameter values as given in the equation (6.2.19). We set the initial value of c corresponding to θ, as given in

Wave angle θ	Initial c-values	Determined critical c-values
0	1	1.2328888
$\pi/12$	2.8	3.4062167
$\pi/6$	5.9	6.2562515
$\pi/4$	8.2	8.7613609
$\pi/3$	9.5	10.694955
$5\pi/12$	11.3	11.913108
$\pi/2$	11.8	12.328927

Table 6.1: Initial and critical values of wave speed corresponding to $\theta, 0 \leq \theta \leq \pi/2$, for which homoclinic orbits were obtained.

Table 6.1 and hence continue the integration process for every pair of (θ, c). We show the existence of homoclinic orbit for every pair of (θ, c). The Figure 6.3 shows a homoclinic orbit for $\theta = \pi/2$. The critical wave speed was calculated as c=12.328927.

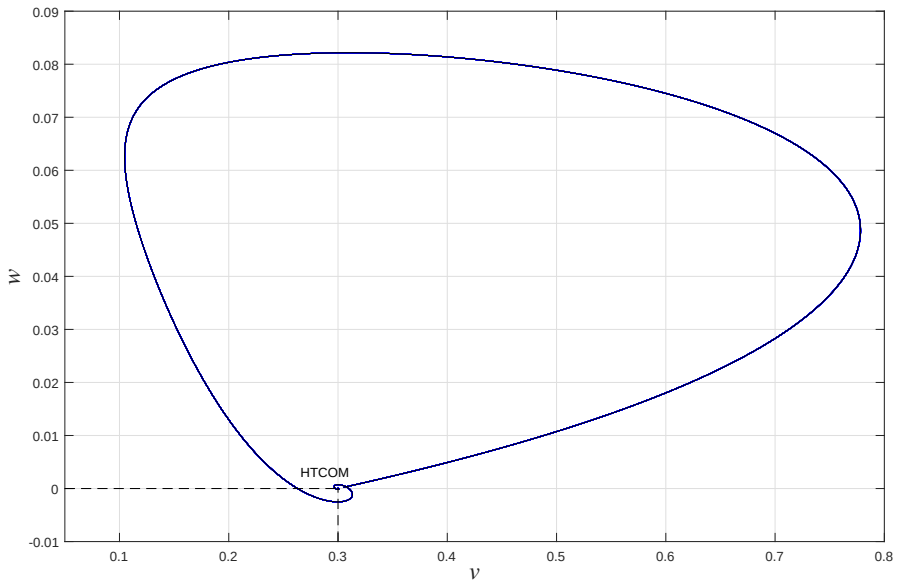

Figure 6.3: Existence of homoclinic orbit at a critical wave speed c=12.328927 and $\theta = \pi/2$

We obtained similar homoclinic orbits (not shown here) and their corresponding wave

speed for other θ-values, $0 < \theta < \pi/2$, as shown in Table 6.1. We noted the one-dimensional wave speed 1.2328888 has been obtained for $\theta = 0$ due to the fact that the two-dimensional models are deducible to the models of one-dimension for $\theta = 0$. In addition, the wave speed increases as the wave angle θ increases from 0 to $\pi/2$. Therefore, waves move faster along the lifted circumferential direction of the artery rather than moving along the arterial axis. The Figure 6.4 shows a monotonically

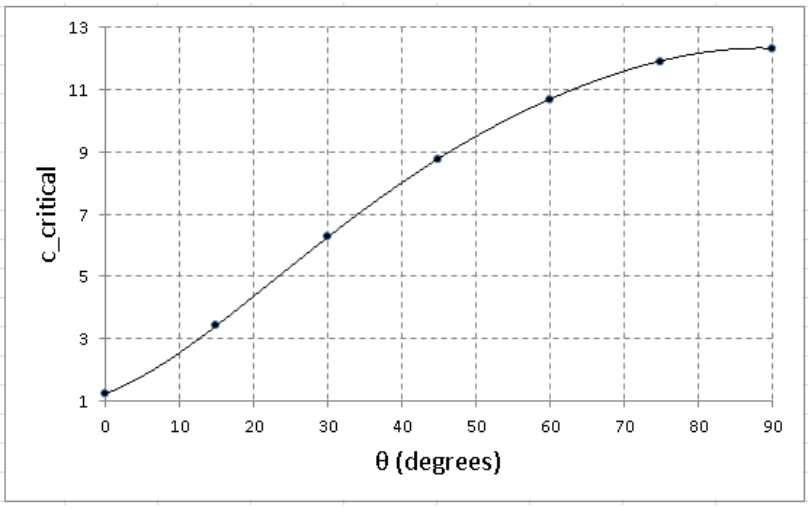

Figure 6.4: Variation of critical 2-dimensional wave speed with angle, for which homoclinic orbits exist

increasing trend of the wave speed, c_{critical}, as wave angle θ increases. The relationship between c_{critical} and θ can be modelled by a fifth-order polynomial with $R^2 = 1$ (a measure of 100% goodness of the fit) and is given by

$$c_{\text{critical}} = -4 \times 10^{-9}\theta^5 + 1 \times 10^{-6}\theta^4 - 1 \times 10^{-4}\theta^3 + 5.6 \times 10^{-3}\theta^2 + 8.65 \times 10^{-2}\theta + 1.2321. \tag{6.2.20}$$

Therefore, the polynomial given by Equation (6.2.20) can be used to determine the critical wave speed at any angle in the first quadrant, for which homoclinic orbit exists under the parameter values assumed.

6.3 Continuation of Homoclinic Orbits

To identify the co-dimension of bifurcation, we proceed with a continuation of homoclinic orbit of one-dimensional plan waves using two-parameter analysis (see [20]). For this, we allow the parameters α and c to vary along the homoclinic curve. We identified points for *double real stable leading eigenvalues* (DRS) in the (α, c)-plane. That is, while two parameters are varied along the homoclinic orbit, bifurcation occurs corresponding to DRS point which is classified as one of the bifurcation points for the co-dimension two bifurcation with respect to the equilibrium, see [20]. Similarly, continuation of homoclinic orbit in the (α, I) parameter space also identified DRS points for the two-dimensional plane waves. Hence, the two-dimensional macroscopic system undergoes a codimension two bifurcation.

We compare this results with the results of a number of previous work: [8], [9], [52], [57] and [76], even though these references dealt with a single FHN system in the absence of the parameter p. In [52], it has been proved that the existence of part of a homoclinic orbit as a 'C'-shape curve as we have shown as the curve CA denoted by green arrows in Subsections 6.1.2 and 6.2.2. In addition, this kind of C-shape curve was also reported in [9]. Moreover, we have shown that the existence of homoclinic orbit for the wave speed 1.2328888 which interprets the existence of slow waves. Similarly, existence of slow waves has been proved in [42] and discussed in [52]. Further, the existence of homoclinic orbits have been proved in [8] and [57]. In [76], an application of the exchange lemma has been discussed in proving the existence of a codimension two bifurcation between waves in (c, ν, α)-parameter space. Therefore, the existence of codimension two bifurcation we have shown here for homoclinic orbit by continuation technique has been confirmed according to [76]. Hence, our results are comparable with the results of the above mentioned literature.

6.4 Summary

In this chapter, we studied the existence of membrane potential plane waves of the one- and two-dimensional HPDEs derived in chapter 4, by constructing homoclinic orbits using the method of homotopy in MATCONT. This study is therefore a justification for the existence of plane waves shown by numerical experiments in chapter 5. Existence of the waves was shown by three main phenomena; type of the equilibrium, existence of homoclinic orbit with critical wave speed and co-dimension of bifurcation. For both one- and two-dimensional HPDEs we identified a unique steady state which was categorized as a hyperbolic saddle-focus. This result confirmed an initiation of traveling impulse of oscillating tails. Moreover, we confirmed a periodic wave solution through the construction of homoclinic orbits with a corresponding critical wave speed. In addition, we noted the speed of the wave has been monotonically increased in the direction of wave angle increased. Finally, continuation of homoclinic orbits in a two-parameter space identified a co-dimension two bifurcation for both one- and two-dimensional HPDEs in the traveling wave coordinate system.

Conclusion

In this research, an attempt has been made to mathematically model human arterial cellular signalling between a population of cells. This research showed a method of modelling the dynamics of a biological process and in particular, the dynamics of the cellular membrane potential. Thus, the method we followed in this research can be applied in modelling any physiological phenomena of a complex system at different length scales. In the interest of modelling cellular signalling, we considered the cellular membrane potential of a population of human arterial smooth muscle cells (SMCs) and endothelial cells (ECs). Signalling among and between these two cells types was considered as homocellular and heterocellular communication, respectively. Cells were then treated as the electrical equivalents of FitzHuge-Nagumo (FHN) nonlinear models and hence we were able to derive models for both homocellular and heterocellular communication. However, we only studied the dynamics of homocellular communication between SMCs; the dynamical study of heterocellular communication between SMCs and ECs has been left for future work.

In Chapter 1, the possibility of modelling both SMCs and ECs using FHN models was described in terms of local dynamical similarities between our FHN models and the models of Koenigsberger et al., since the Koenigsberger et al. models were validated by published in vitro experiments results obtained on rat mesenteric arterial segments. In addition, a notion of using different values for the same parameters in our FHN models with respect to each cell type was also described.

As the first goal of our research, we developed a system of discrete autonomous ordinary differential equations (ODEs) for a population of cells around the circumference of an arterial-ring. For simplicity, this system was studied for three coupled SMCs using a standard continuation technique in MATCONT. Results revealed the existence of Hopf bifurcation followed by a transition from steady state into an oscillatory state (and vice versa) in all cells. The oscillatory state of the membrane potential was predicted between two stable Hopf points under the application of an external stimulus that acted as a bifurcation parameter. Moreover, an M-shape curve for the period of oscillations of the cellular membrane potential was also predicted.

Secondly, we have considered continuous rings of discrete cells along the arterial axis and derived one-dimensional reaction-diffusion type of equations for both homocellular and heterocellular communication among and between SMCs and ECs, by homogenising the rings along the arterial axis, x. The resultant models were constructed so that they were discrete around the circumference of the artery as well as continuous along the arterial axis. Similarly, a two-dimensional reaction-diffusion type system was also derived by lifting the arterial circumference in the second Cartesian direction y for both homocellular and heterocellular communication among and between SMCs and ECs. A method of deriving these models was illustrated in Chapters 2 and 3.

We then studied the micro-macro phenomena of the homocellular communication between SMCs. For this, we applied the theory of mathematical homogenisation with formal asymptotic expansion to the one- and two-dimensional reaction-diffusion type equations and derived homogenised partial differential equations (HPDEs), macroscopic equations. During the homogenisation process, the one- and two-dimensional effective potential variation coefficients (PVC) were also derived. These homogenised models can be regarded as more comprehensive and cohesive versions of the homogenised models derived so far, as our HPDEs were derived based on the dimension

of the macroscopic arterial segment and microscopic cellular domain of SMCs. In particular, the microscopic PVC was considered in both fast and slow scales rather than defining them in fast-scale only. This assumption allowed us to incorporate a neighbouring coupling effect of microscopic variation as a small fraction of the macroscopic variation. Therefore, our HPDEs can be applied to more complicated system. As an application of the macroscopic PVC in one and two dimensions, we constructed numerical examples as a possible form of PVC in the microscopic domain and applied them to the macroscopic models to illustrate a possible cellular physiology. A solution to the unit-cell problem in one and two dimensions was also provided.

As the next goal of this study, one-dimensional HPDEs were numerically simulated using a three-point finite difference method, zero-initial and periodic boundary conditions and by applying a stimulus in the form of a first-order spline. The first-order spline form was selected based on the Hopf bifurcation points identified for the ring of three discrete cells and the periodicity of cells. Results revealed the existence of membrane potential forward and backward plane waves along the arterial axis. The dynamics of these waves were then studied using spatial patterning of the membrane potential and a movie file created for the wave propagation. Frequency of wave cycles was observed developing from the non-stimulated to stimulated region. The threshold value of the stimulus for the initiation of waves was found. In addition, non-stimulated regions and a particular region of the stimulated region were predicted with multiple steady states. In particular, we discussed the occurrence of multiple steady states in terms of a new physical parameter not previously reported: the distance between the point of initiation of waves (PIW) in the stimulated region and the boundary separating the stimulated and non-stimulated regions and system reinforcement. The critical value of that distance, 'distance to steady state' (DSS), was found. Furthermore, we found that DSS and the time lag between two successive reinforcements led the system to attain every other annihilation of waves in the non-stimulated region and hence the cessation of waves then became steady states of the system. A line

of negative-gradient was also predicted for the lasting period of the steady-states, in the one-third of the total simulation time. Due to a sudden drop and rise in the membrane potential, we showed the existence of multiple steady states and a corresponding transient spatial patterning in a particular region of the stimulated domain under a new PIW. However, the reason for the sudden drop in membrane potential is unclear. Following the attainment of the transient pattern, a period of steady states in the non-stimulated region was found to be double that of the period of steady states in the stimulated region.

Finally, we investigated the dynamics of the cellular membrane potential using two-dimensional HPDEs. For this, the system was simulated using five-point finite difference method, zero-initial conditions, periodic boundary conditions and by applying stimulus in the same form of the first-order spline used previously in both x and y directions. Initial results revealed the propagation of membrane potential as curved wave-fronts, curved wave-backs, circular wave-fronts and circular waves-backs. We examined the role of the properly-assigned, spatially-varying bi-directional stimulus in producing circular loops and found the relative spatial gradient of the x- and y-directional stimulus was small enough to create circular loops. Detailed results and discussion on the dynamics of these waves was given in Chapter 5.

To further study the dynamics of the cellular membrane potential, we considered the physiological process 'potential depolarization', and showed breaking of the symmetry of circular wave-backs when the zero-potential state of the depolarization process was attained. As a result, the membrane potential was found as waves of rigidly rotating twin-spirals. In the following study, we investigated in detail the dynamics of the twin-spirals based on the effect of the x-directional effective PVC. For an increased PVC, spirals waves were predicted with drifting dynamics and subsequently these waves experienced meanders as PVC was further increased. In addition, slowly rotating diverging twin-spirals were observed for low-value PVCs. In the case of

low-value PVCs, a number of twin-spirals were increased due to the self-excitation of the system and hence this growing number of diverging spirals with considerably reduced curvature were then converted to forward and backward plane waves. We found a critical value of PVC for the existence of plane waves and rotating spirals with drifts and meanders. The intermediate interval between these critical values showed the existence of rigidly and steadily rotating twin-spirals. In this case, the angular speed of the spiral tip was found to follow a monotonically-increasing curve as PVC increases. Drifts of spirals in this study were categorized as PVC-induced drift, stimulus-induced drift and interaction-induced drift. Furthermore, as an effect of the stimulus we reported wave break under the action of weakly time-dependent bi-directional stimulus and a new spiral dynamics defined as 'static twin-spirals' with continuous drift (a non-rotating continuously moving spiral) under the action of uni-directional stimulus. Alternatively, the zero-potential intermediate condition can be also considered a spatial heterogeneity of a patch of damaged cells, such as cancer cells of the smooth muscle or plaque formation of damaged cells. That is, initiation and re-entrance of spiral waves may be regarded as an indication of a sudden change in the cellular physiology or as a pathological stage of a disease, such as tachycardia or ventricular fibrillation as stated in the literature. Interestingly, the static twin-spirals we have predicted in our modelling may also be considered to be a long-term pathological state.

As a final goal of this study, we proved the existence of plane waves in one- and two-dimensions (without considering the symmetry breaking condition in two-dimension) by constructing homoclinic orbits in a traveling wave coordinate system. Construction of homoclinic orbits for a system of 5 circumferentially coupled cells (a case of extended number of cells) in one-dimension showed a computational complexity as the system became more stiff due to the increased number of nonlinear differential equations in the travelling wave coordinate system. Therefore, computational time

increases drastically. For the two-dimensional cellular system, the speed of the membrane potential plane waves was found as a monotonically-increasing function of wave angle. This result revealed that waves move fast around the circumferential direction than that along the axial direction. Moreover, the one-dimensional partially homogenised cellular system can be regarded as a particular case of the two-dimensional fully homogenised system since the two-dimensional critical speed of the plane waves is being deduced to the one-dimensional wave speed for the zero wave-angle. In addition, as said above, we found a critical value of the x-directional macroscopic PVC below which spiral waves can be turned to forward and backward plane waves in the one-dimensional case. Therefore, some of the dynamics of the partially homogenised system can be derived from the fully homogenised system. Moreover, in both systems, we showed a co-dimension two bifurcation via continuation of homoclinic orbit, which proved an earlier result for a single unit FHN system.

Future Direction of the Research

This section briefly describes a 3 possible future direction of research with novel ideas, as an extension of this research. In this thesis, we have well developed for heterocellular communication between type A and type B cells a system of reaction-diffusion equations which are both discrete and continuous in one-dimension, and are a full continuous lattice models in two-dimension. The dimensionless form of these models in one- and two-dimension are respectively given by

$$\begin{aligned} \nu_A \frac{\partial \boldsymbol{v}}{\partial t} + \boldsymbol{w} - \boldsymbol{g}_A(\boldsymbol{v}) + G_A[A_m]\boldsymbol{v} &+ G_{BA}(\wp \boldsymbol{v} - [L]\boldsymbol{u}) \\ &= \frac{\partial}{\partial x}\left(D_A(x) \frac{\partial \boldsymbol{v}}{\partial x} \right) + \boldsymbol{I}, \end{aligned} \tag{6.4.1}$$

$$\beta_A \frac{\partial \boldsymbol{w}}{\partial t} + \gamma_A \boldsymbol{w} = \boldsymbol{v} - \boldsymbol{p}_A, \tag{6.4.2}$$

$$\begin{aligned} \nu_B \frac{\partial \boldsymbol{u}}{\partial t} + \boldsymbol{z} - \boldsymbol{g}_B(\boldsymbol{u}) + G_B[A_{m\wp}]\boldsymbol{u} &+ \ell G_{BA}(\boldsymbol{u} - [1]\boldsymbol{v}) \\ &= D_{AB}[1] \frac{\partial^2 \boldsymbol{v}}{\partial x^2} + \frac{\partial}{\partial x}\left(D_B(x) \frac{\partial \boldsymbol{u}}{\partial x} \right), \end{aligned} \tag{6.4.3}$$

$$\beta_B \frac{\partial \boldsymbol{z}}{\partial t} + \gamma_B \boldsymbol{z} = \boldsymbol{u} - \boldsymbol{p}_B, \tag{6.4.4}$$

and

$$\begin{aligned} \nu_A \frac{\partial v}{\partial t} + w &- g_A(v) + \wp\, G_{BA}(v-u) - I \\ &= \frac{\partial}{\partial x}\left(D_A \frac{\partial v}{\partial x}\right) + \frac{\partial}{\partial y}\left(D_A \frac{\partial v}{\partial y}\right) + D_{ABA}\frac{\partial^2 u}{\partial y^2}, \end{aligned} \tag{6.4.5}$$

$$\begin{aligned} \nu_B \frac{\partial u}{\partial t} + z &- g_B(u) + \ell G_{BA}(u-v) \\ &= \frac{\partial}{\partial x}\left(D_B \frac{\partial u}{\partial x}\right) + \frac{\partial}{\partial y}\left(D_B \frac{\partial u}{\partial y}\right) + D_{ABB}\frac{\partial^2 v}{\partial x^2}, \end{aligned} \tag{6.4.6}$$

$$\beta_A \frac{\partial w}{\partial t} + \gamma_A w = v - p_A, \tag{6.4.7}$$

$$\beta_B \frac{\partial z}{\partial t} + \gamma_B z = u - p_B, \tag{6.4.8}$$

where v and u are respectively the cellular membrane potential of type A and type B cells. Other notations are respectively described in chapter 2 and chapter 3.

Firstly, as a future, work a multiscale analysis and homogenisation of the 1-dimensional heterocellular models given by equations (6.4.1)-(6.4.4) can be studied. As a result, a newly developed system of HPDEs can then be numerically simulated for an arterial macro-domain, for studying the spatial pattern formation and their related dynamics of the heterocellular cellular system, by assigning different parameter values for type A and type B cells. This work will include enough results for a paper publication.

Secondly, in the similar way explained above, a system of 2-dimensional HPDEs can be derived from models given by equations (6.4.5)-(6.4.8), which can then be used to study a spatial patterning and their dynamics in a 2-dimensional macro arterial domain. It can also be regarded as a standard work for another research paper.

Finally, as an application of the method of study carried out and proposed above in this thesis, similar kind of spatial models will be developed in the field of Pharmacokinetics. Up to now, an ADME (absorbtion-distribution-metabolism-excretion)

process of a specific drug in the human body has been mainly studied as a physiological compartmental study, where human organs are treated as compartments. For this, a system of ordinary differential equations have been used to model the dynamics of the drug. However, a cellular level study of a particular human organ has a vital importance based on a specific disease. For example, specific spatial heterogeneities of cancer cells need to be identified for a chemotherapeutic treatment, and the most common way of this treatment has been via intravenous injection. In addition, during this treatment it is common that the neighboring cells get affected. Therefore, as a cellular communication, spatial models in terms of a drug concentration need to be developed and studied via their multiscale structure, to treat the system at the cellular level. Hence, as a future direction of a new research, instead of using existing coupled ordinary differential equations to model the kinetics of a drug, a system of spatial models need to be developed to understand cellular level pharmacokinetics of the drug. It will give rise to a new discovery related to new therapeutic strategies, and we hope to develop such a new area of research and to work on it.

Bibliography

[1] Maurits A Allessie, Felix IM Bonke, and Francien JG Schopman, *Circus movement in rabbit atrial muscle as a mechanism of tachycardia*, Circulation research **33** (1973), no. 1, 54–62.

[2] ARA Anderson and BD Sleeman, *Wave front propagation and its failure in coupled systems of discrete bistable cells modelled by FitzHugh-Nagumo dynamics*, International Journal of Bifurcation and Chaos **5** (1995), no. 01, 63–74.

[3] Peter Ashwin, Ian Melbourne, and Matthew Nicol, *Hypermeander of spirals: local bifurcations and statistical properties*, Physica D: Nonlinear Phenomena **156** (2001), no. 3, 364–382.

[4] C Atkinson, GEH Reuter, and CJ Ridler-Rowe, *Traveling wave solution for some nonlinear diffusion equations*, SIAM Journal on Mathematical Analysis **12** (1981), no. 6, 880–892.

[5] V. N. Biktashev, *Drift of spiral waves*, **2** (2007), no. 4, 1836, revision 138403.

[6] Georg Breier, Ursula Albrecht, Sylvia Sterrer, and Werner Risau, *Expression of vascular endothelial growth factor during embryonic angiogenesis and endothelial cell differentiation*, Development **114** (1992), no. 2, 521–532.

[7] Chiara Callies, Johannes Fels, Ivan Liashkovich, Katrin Kliche, Pia Jeggle, Kristina Kusche-Vihrog, and Hans Oberleithner, *Membrane potential depolarization decreases the stiffness of vascular endothelial cells*, Journal of cell science **124** (2011), no. 11, 1936–1942.

[8] Gail A Carpenter, *A geometric approach to singular perturbation problems with applications to nerve impulse equations*, Journal of Differential Equations **23** (1977), no. 3, 335–367.

[9] Alan R Champneys, Vivien Kirk, Edgar Knobloch, Bart E Oldeman, and James Sneyd, *When Shilnikov meets Hopf in excitable systems*, SIAM Journal on Applied Dynamical Systems **6** (2007), no. 4, 663–693.

[10] Silvia Chifflet, Julio A Hernández, and Silvina Grasso, *A possible role for membrane depolarization in epithelial wound healing*, American Journal of Physiology-Cell Physiology **288** (2005), no. 6, C1420–C1430.

[11] Jeng-Jiann Chiu, Li-Jing Chen, Cheng-Nan Chen, Pei-Ling Lee, and Chih-I Lee, *A model for studying the effect of shear stress on interactions between vascular endothelial cells and smooth muscle cells*, Journal of Biomechanics **37** (2004), no. 4, 531–539.

[12] Jonathan C Choy, David J Granville, David WC Hunt, and Bruce M McManus, *Endothelial cell apoptosis: biochemical characteristics and potential implications for atherosclerosis*, Journal of molecular and cellular cardiology **33** (2001), no. 9, 1673–1690.

[13] Doina Cioranescu and Patrizia Donato, *An introduction to homogenization, volume 17 of Oxford Lecture Series in Mathematics and its Applications*, The Clarendon Press Oxford University Press, New York **4** (1999), 118.

[14] Debapriya Das, Dhruba Banerjee, and Jayanta K Bhattacharjee, *Super-critical and sub-critical Hopf bifurcations in two and three dimensions*, Nonlinear Dynamics **77** (2014), no. 1-2, 169–184.

[15] Jorge M Davidenko, Paul Kent, and José Jalife, *Spiral waves in normal isolated ventricular muscle*, Physica D: Nonlinear Phenomena **49** (1991), no. 1, 182–197.

[16] Jorge M Davidenko, Paul F Kent, Dante R Chialvo, Donald C Michaels, and Jose Jalife, *Sustained vortex-like waves in normal isolated ventricular muscle.*, Proceedings of the National Academy of Sciences **87** (1990), no. 22, 8785–8789.

[17] Jorge M Davidenko, Arcady V Pertsov, Remy Salomonsz, William Baxter, and José Jalife, *Stationary and drifting spiral waves of excitation in isolated cardiac muscle*, (1992).

[18] Cor de Wit, Markus Boettcher, and Volker J Schmidt, *Signaling across myoendothelial gap junctions-fact or fiction?*, Cell Communication and Adhesion **15** (2008), no. 3, 231–245.

[19] Cor de Wit and Tudor M Griffith, *Connexins and gap junctions in the EDHF phenomenon and conducted vasomotor responses*, Pflügers Archiv-European Journal of Physiology **459** (2010), no. 6, 897–914.

[20] Virginie De Witte, Willy Govaerts, Yuri A Kuznetsov, and Mark Friedman, *Interactive initialization and continuation of homoclinic and heteroclinic orbits in MATLAB*, ACM Transactions on Mathematical Software (TOMS) **38** (2012), no. 3, 18.

[21] Christian Derst, Jürgen Daut, Regina Preisig-Müller, et al., *ATP-sensitive potassium channels in capillaries isolated from guinea-pig heart*, The Journal of Physiology **525** (2000), no. 2, 307–317.

[22] A Dhooge, W Govaerts, Yu A Kuznetsov, W Mestrom, AM Riet, and B Sautois, *MATCONT and CL MATCONT: Continuation toolboxes in matlab*, Universiteit Gent, Belgium and Utrecht University, The Netherlands (2006).

[23] Annick Dhooge, Willy Govaerts, and Yu A Kuznetsov, *MATCONT: a MATLAB package for numerical bifurcation analysis of ODEs*, ACM Transactions on Mathematical Software (TOMS) **29** (2003), no. 2, 141–164.

[24] Hai K Diep, Edward J Vigmond, Steven S Segal, and Donald G Welsh, *Defining electrical communication in skeletal muscle resistance arteries: a computational approach*, The Journal of Physiology **568** (2005), no. 1, 267–281.

[25] Stephen M Dillon, Maurits A Allessie, Philip C Ursell, and Andrew L Wit, *Influences of anisotropic tissue structure on reentrant circuits in the epicardial border zone of subacute canine infarcts.*, Circulation research **63** (1988), no. 1, 182–206.

[26] Hong Ding, Paul Kubes, and Chris Triggle, *Potassium-and acetylcholine-induced vasorelaxation in mice lacking endothelial nitric oxide synthase*, British Journal of Pharmacology **129** (2000), no. 6, 1194–1200.

[27] Kim A Dora, *Cell-cell communication in the vessel wall*, Vascular Medicine **6** (2001), no. 1, 43–50.

[28] Jens P Dreier, *The role of spreading depression, spreading depolarization and spreading ischemia in neurological disease*, Nature medicine **17** (2011), no. 4, 439–447.

[29] G Edwards, KA Dora, MJ Gardener, CJ Garland, and AH Weston, *K-plus; is an endothelium-derived hyperpolarizing factor in rat arteries*, Nature **396** (1998), no. 6708, 269–272.

[30] GR Egoire Allaire, Alain Damlamian, and Ulrich Horunung, *Two-scale convergence on periodic surfaces and applications*.

[31] Geoffrey G Emerson and Steven S Segal, *Electrical coupling between endothelial cells and smooth muscle cells in hamster feed arteries role in vasomotor control*, Circulation Research **87** (2000), no. 6, 474–479.

[32] Thomas Erneux and Grégoire Nicolis, *Propagating waves in discrete bistable reaction-diffusion systems*, Physica D: Nonlinear Phenomena **67** (1993), no. 1, 237–244.

[33] Michel Félétou and Paul M Vanhoutte, *The alternative: EDHF*, Journal of Molecular and Cellular Cardiology **31** (1999), no. 1, 15–22.

[34] Xia Feng, Xiang Gao, De-Bei Pan, Bing-Wei Li, and Hong Zhang, *Unpinning of rotating spiral waves in cardiac tissues by circularly polarized electric fields*, Scientific reports **4** (2014).

[35] Paul C Fife, *Understanding the patterns in the bz reagent*, Journal of Statistical Physics **39** (1985), no. 5-6, 687–703.

[36] ———, *Dynamics of internal layers and diffusive interfaces*, vol. 53, SIAM, 1988.

[37] Xavier F Figueroa, Brant E Isakson, and Brian R Duling, *Connexins: gaps in our knowledge of vascular function*, Physiology **19** (2004), no. 5, 277–284.

[38] Richard FitzHugh, *Mathematical models of threshold phenomena in the nerve membrane*, The Bulletin of Mathematical Biophysics **17** (1955), no. 4, 257–278.

[39] ———, *Impulses and physiological states in theoretical models of nerve membrane*, Biophysical Journal **1** (1961), no. 6, 445–466.

[40] ———, *Mathematical models of excitation and propagation in nerve. Chapter 1 in h. p. schwan*, McGraw-Hill Book Co., N.Y., 1966.

[41] Ingrid Fleming and Rudi Busse, *Signal transduction of enos activation*, Cardiovascular Research **43** (1999), no. 3, 532–541.

[42] Gilberto Flores, *Stability analysis for the slow traveling pulse of the FitzHugh-Nagumo system*, SIAM J. Math. Anal. **22** (1991), no. 2, 392–399.

[43] Andrew J Foulkes, *Drift and meander of spiral waves*, arXiv preprint arXiv:0912.4247 (2009).

[44] David W Frazier, Patrick D Wolf, J Marcus Wharton, AS Tang, William M Smith, and Raymond E Ideker, *Stimulus-induced critical point. Mechanism for electrical initiation of reentry in normal canine myocardium.*, Journal of Clinical Investigation **83** (1989), no. 3, 1039.

[45] Pranay Goel, James Sneyd, and Avner Friedman, *Homogenization of the cell cytoplasm: the calcium bidomain equations*, Multiscale Modeling & Simulation **5** (2006), no. 4, 1045–1062.

[46] Martin Golubitsky, Ian Stewart, et al., *Singularities and groups in bifurcation theory*, vol. 2, Springer Science & Business Media, 2012.

[47] NA Gorelova and J Bureš, *Spiral waves of spreading depression in the isolated chicken retina*, Journal of neurobiology **14** (1983), no. 5, 353–363.

[48] Willy Govaerts, Yuri A Kuznetsov, and Annick Dhooge, *Numerical continuation of bifurcations of limit cycles in MATLAB*, SIAM journal on scientific computing **27** (2005), no. 1, 231–252.

[49] Willy Govaerts and Bart Sautois, *Phase response curves, delays and synchronization in MATLAB*, Computational Science–ICCS 2006, Springer, 2006, pp. 391–398.

[50] RJ Gryglewski, S Moncada, and RMJ Palmer, *Bioassay of prostacyclin and endothelium-derived relaxing factor (EDRF) from porcine aortic endothelial cells*, British Journal of Pharmacology **87** (1986), no. 4, 685–694.

[51] John Guckenheimer, *Singular Hopf bifurcation in systems with two slow variables*, SIAM Journal on Applied Dynamical Systems **7** (2008), no. 4, 1355–1377.

[52] John Guckenheimer and Christian Kuehn, *Homoclinic orbits of the FitzHugh-Nagumo equation: The singular-limit*, Discrete and Continuous Dynamical Systems¿ Series S **2** (2009), no. 4, 851.

[53] Tara L Haas and Brian R Duling, *Morphology favors an endothelial cell pathway for longitudinal conduction within arterioles*, Microvascular research **53** (1997), no. 2, 113–120.

[54] Cornelia Hahn and Martin A Schwartz, *The role of cellular adaptation to mechanical forces in atherosclerosis*, Arteriosclerosis, thrombosis, and vascular biology **28** (2008), no. 12, 2101–2107.

[55] Nicole E Hastings, Michael B Simmers, Oliver G McDonald, Brian R Wamhoff, and Brett R Blackman, *Atherosclerosis-prone hemodynamics differentially regulates endothelial and smooth muscle cell phenotypes and promotes pro-inflammatory priming*, American Journal of Physiology-Cell Physiology **293** (2007), no. 6, C1824–C1833.

[56] S. P. Hastings, *Some mathematical problems from neurobiology*, The American Mathematical Monthly **82** (1975), no. 9, pp. 881–895.

[57] SP Hastings, *On the existence of homoclinic and periodic orbits for the FitzHugh-Nagumo equations*, The Quarterly Journal of Mathematics **27** (1976), no. 1, 123–134.

[58] David Heeger, *The membrane equation*, Lecture series (2000), 1–13.

[59] Anders Holmbom, Nils Svanstedt, and Niklas Wellander, *Multiscale convergence and reiterated homogenization of parabolic problems*, Applications of Mathematics **50** (2005), no. 2, 131–151.

[60] Mark H Holmes, *Introduction to perturbation methods*, vol. 20, Springer Science & Business Media, 2012.

[61] William R Holmes, May Anne Mata, and Leah Edelstein-Keshet, *Local perturbation analysis in MATCONT*, (2014).

[62] Tzung K Hsiai, *Mechanosignal transduction coupling between endothelial and smooth muscle cells: role of hemodynamic forces*, American Journal of Physiology-Cell Physiology **294** (2008), no. 3, C659–C661.

[63] I Hüttner, O Kocher, and G Gabbiani, *Endothelial and smooth-muscle cells*, Diseases of the arterial wall, Springer, 1989, pp. 3–41.

[64] E. M. Izhikevich and R. FitzHugh, *FitzHugh-Nagumo model*, Scholarpedia **1** (2006), no. 9, 1349–.

[65] William F Jackson, James M Huebner, and Nancy J Rusch, *Enzymatic isolation and characterization of single vascular smooth muscle cells from cremasteric arterioles*, Microcirculation **3** (1996), no. 3, 313–328.

[66] Wolfgang Jahnke and Arthur T Winfree, *A survey of spiral-wave behaviors in the Oregonator model*, International Journal of Bifurcation and Chaos **1** (1991), no. 02, 445–466.

[67] Jose Jalife, *Mathematical approaches to cardiac arrhythmias*, New York Academy Sciences, 1990.

[68] Adam Kapela, Sridevi Nagaraja, and Nikolaos M Tsoukias, *A mathematical model of vasoreactivity in rat mesenteric arterioles. ii. Conducted vasoreactivity*,

American Journal of Physiology-Heart and Circulatory Physiology **298** (2010), no. 1, H52–H65.

[69] James P Keener, *Propagation and its failure in coupled systems of discrete excitable cells*, SIAM Journal on Applied Mathematics **47** (1987), no. 3, 556–572.

[70] James P Keener and James Sneyd, *Mathematical Physiology: I: Cellular Physiology*, vol. 1, Springer, 2009.

[71] Zachary P Kilpatrick and Paul C Bressloff, *Spatially structured oscillations in a two-dimensional excitatory neuronal network with synaptic depression*, Journal of computational neuroscience **28** (2010), no. 2, 193–209.

[72] Richard Klabunde, *Cardiovascular physiology concepts*, Lippincott Williams & Wilkins, 2011.

[73] Eckehard; Dahlem Markus A. Kneer, Frederike; Schll, *Nucleation of reaction-diffusion waves on curved surfaces*, New Journal of Physics **16** (2014), no. 5, 1824–1833.

[74] Michèle Koenigsberger, Roger Sauser, Jean-Louis Bény, and Jean-Jacques Meister, *Role of the endothelium on arterial vasomotion*, Biophysical journal **88** (2005), no. 6, 3845–3854.

[75] Michèle Koenigsberger, Roger Sauser, Mathieu Lamboley, Jean-Louis Bény, and Jean-Jacques Meister, *Ca 2+ dynamics in a population of smooth muscle cells: modeling the recruitment and synchronization*, Biophysical journal **87** (2004), no. 1, 92–104.

[76] Martin Krupa, Björn Sandstede, and Peter Szmolyan, *Fast and slow waves in the FitzHugh–Nagumo equation*, Journal of Differential Equations **133** (1997), no. 1, 49–97.

[77] Yu A Kuznetsov, *Tutorial ii: One-parameter bifurcation analysis of equilibria with MATCONT*, Diakses di http://www. staff. science. uu. nl/˜ kouzn101/NBA/L AB2. pdf.[Diakses: 22 Oktober 2012] (2009).

[78] Mathieu Lamboley, Philippe Pittet, Michèle Koenigsberger, Roger Sauser, Jean-Louis Bény, and Jean-Jacques Meister, *Evidence for signaling via gap junctions from smooth muscle to endothelial cells in rat mesenteric arteries: possible implication of a second messenger*, Cell calcium **37** (2005), no. 4, 311–320.

[79] James Lechleiter, Steven Girard, Ernest Peralta, and David Clapham, *Spiral calcium wave propagation and annihilation in Xenopus laevis oocytes*, Science **252** (1991), no. 5002, 123–126.

[80] Darcy Lidington, Yves Ouellette, and Karel Tyml, *Endotoxin increases intercellular resistance in microvascular endothelial cells by a tyrosine kinase pathway*, Journal of cellular physiology **185** (2000), no. 1, 117–125.

[81] RS MacKay and J-A Sepulchre, *Multistability in networks of weakly coupled bistable units*, Physica D: Nonlinear Phenomena **82** (1995), no. 3, 243–254.

[82] Mahmoud Bakheet Ali Mansour, *Travelling wave solutions for doubly degenerate reaction-diffusion equations*, ANZIAM J **52** (2010), 101–109.

[83] Ian Stewart Martin Golubitsky, *Hopf Bifurcation with Dihedral Group Symmetry: Coupled Nonlinear Oscillators*, Contemporary Mathematics **56** (1986), 131–173.

[84] Colin D Mathers, Doris Ma Fat, and JT Boerma, *The global burden of disease: 2004 update*, World Health Organization, 2008.

[85] Hil Meijer, *Matcont Tutorial: ODE GUI version.*

[86] Ehud Meron, *Pattern formation in excitable media*, Physics reports **217** (1992), no. 1, 1–66.

[87] Ehud Meron and Pierre Pelcé, *Model for spiral wave formation in excitable media*, Physical review letters **60** (1988), no. 18, 1880.

[88] J. Moehlis and E. Knobloch, *Equivariant dynamical systems*, **2** (2007), no. 10, 2510.

[89] Alexander Mülsch, Eberhard Bassenge, and Rudi Busse, *Nitric oxide synthesis in endothelial cytosol: evidence for a calcium-dependent and a calcium-independent mechanism*, Naunyn-Schmiedeberg's archives of pharmacology **340** (1989), no. 6, 767–770.

[90] JD Murray, *Chapter 4. mathematical biology ii: spatial models and biomedical applications*, 2003.

[91] VI Nekorkin, VA Makarov, VB Kazantsev, and Manuel G Velarde, *Spatial disorder and pattern formation in lattices of coupled bistable elements*, Physica D: Nonlinear Phenomena **100** (1997), no. 3, 330–342.

[92] Niels F Otani, *A primary mechanism for spiral wave meandering*, Chaos: An Interdisciplinary Journal of Nonlinear Science **12** (2002), no. 3, 829–842.

[93] Ulrich Parlitz, Alexander Schlemmer, and Stefan Luther, *Synchronization patterns in transient spiral wave dynamics*, Physical Review E **83** (2011), no. 5, 057201.

[94] GA Pavliotis, *Homogenization theory for partial differential equations*, Lecture Notes, Department of Mathematics, South Kensington Campus, Imperial College, London (2004).

[95] Jens Persson, *Selected Topics in Homogenization*, Ph.D. thesis, Mid Sweden University, 2012.

[96] Arkady M Pertsov, Jorge M Davidenko, Remy Salomonsz, William T Baxter, and Jose Jalife, *Spiral waves of excitation underlie reentrant activity in isolated cardiac muscle.*, Circulation research **72** (1993), no. 3, 631–650.

[97] Theo Plesser, Stefan C Mueller, and Benno Hess, *Spiral wave dynamics as a function of proton concentration in the ferroin-catalyzed Belousov-Zhabotinskii reaction*, Journal of Physical Chemistry **94** (1990), no. 19, 7501–7507.

[98] Marbella Quiñonez, Fernando González, Consuelo Morgado-Valle, and Marino DiFranco, *Effects of membrane depolarization and changes in extracellular [K+] on the ca2+ transients of fast skeletal muscle fibers. Implications for muscle fatigue*, Journal of muscle research and cell motility **31** (2010), no. 1, 13–33.

[99] John Rinzel and Joseph B. Keller., *Traveling wave solutions of a nerve conduction equation*, Biophysical Journal **13** (1973), no. 12, 1313–1337.

[100] Stanley Leonard Robbins, Vinay Kumar, et al., *Robbins and cotran pathologic basis of disease*, Saunders/Elsevier Philadelphia, 2010.

[101] Una S. Ryan, *Endothelial cells*, vol. 3, CRC Press Inc, 1988.

[102] Faramarz H Samie, Omer Berenfeld, Justus Anumonwo, Sergey F Mironov, Sharda Udassi, Jacques Beaumont, Steven Taffet, Arkady M Pertsov, and José Jalife, *Rectification of the background potassium current a determinant of rotor dynamics in ventricular fibrillation*, Circulation research **89** (2001), no. 12, 1216–1223.

[103] Faustino Sánchez-Garduño, Philip K Maini, and E Kappos, *A review on travelling wave solutions of one-dimensional reaction diffusion equations with nonlinear diffusion term*, Forma **11** (1996), no. 1, 45–59.

[104] Shaun L Sandow, Robin Looft-Wilson, Beth Doran, T Hilton Grayson, Steven S Segal, and Caryl E Hill, *Expression of homocellular and heterocellular gap junctions in hamster arterioles and feed arteries*, Cardiovascular research **60** (2003), no. 3, 643–653.

[105] MA Shaikh, T David, and DJN Wall, *Effects of spatially varying agonist concentration on calcium signalling in coupled vascular endothelial and smooth muscle cells.*

[106] Mohsin Ahmed Shaikh, David JN Wall, and Tim David, *Macro-scale phenomena of arterial coupled cells: a massively parallel simulation*, Journal of The Royal Society Interface **9** (2012), no. 70, 972–987.

[107] Sanjiv Sharma, Etienne B Coetzee, Mark H Lowenberg, Simon A Neild, and Bernd Krauskopf, *Numerical continuation and bifurcation analysis in aircraft design: an industrial perspective*, (2014).

[108] JA Sherratt, *On the form of smooth-front travelling waves in a reaction-diffusion equation with degenerate nonlinear diffusion*, Math. Model. Nat. Phenom **5** (2010), no. 5, 64–79.

[109] Nitaro Shibata, Peng-Sheng Chen, Ellen G Dixon, Patrick D Wolf, ND Danieley, William M Smith, and Raymond E Ideker, *Influence of shock strength and timing on induction of ventricular arrhythmias in dogs*, American Journal of Physiology-Heart and Circulatory Physiology **255** (1988), no. 4, H891–H901.

[110] Gordon S Skinner and Harry L Swinney, *Periodic to quasiperiodic transition of chemical spiral rotation*, Physica D: Nonlinear Phenomena **48** (1991), no. 1, 1–16.

[111] Bauer E Sumpio, J Timothy Riley, and Alan Dardik, *Cells in focus: endothelial cell*, The international journal of biochemistry & cell biology **34** (2002), no. 12, 1508–1512.

[112] Cam Ha T Tran, Edward J Vigmond, Frances Plane, and Donald G Welsh, *Mechanistic basis of differential conduction in skeletal muscle arteries*, The Journal of Physiology **587** (2009), no. 6, 1301–1318.

[113] John J Tyson and James P Keener, *Singular perturbation theory of traveling waves in excitable media (a review)*, Physica D: Nonlinear Phenomena **32** (1988), no. 3, 327–361.

[114] Alexej Verkhratsky, Richard K Orkand, and Helmut Kettenmann, *Glial calcium: homeostasis and signaling function*, Physiological reviews **78** (1998), no. 1, 99–141.

[115] Arthur T Winfree, *Rotating chemical reactions*, Scientific American (1974), no. 230, 82–95.

[116] ———, *When time breaks down: the three-dimensional dynamics of electrochemical waves and cardiac arrhythmias*, Princeton University Press Princeton, 1987.

[117] ———, *Electrical instability in cardiac muscle: phase singularities and rotors*, Journal of theoretical Biology **138** (1989), no. 3, 353–405.

[118] ———, *Varieties of spiral wave behavior: An experimentalists approach to the theory of excitable media*, Chaos: An Interdisciplinary Journal of Nonlinear Science **1** (1991), no. 3, 303–334.

[119] ———, *The geometry of biological time*, vol. 12, Springer Science & Business Media, 2001.

[120] Yoshimichi Yamamoto, Megan F Klemm, Frank R Edwards, and Hikaru Suzuki, *Intercellular electrical communication among smooth muscle and endothelial cells in guinea-pig mesenteric arterioles*, The Journal of Physiology **535** (2001), no. 1, 181–195.

[121] H Zhang and AV Holden, *Chaotic meander of spiral waves in the FitzHugh-Nagumo system*, Chaos, Solitons & Fractals **5** (1995), no. 3, 661–670.

[122] Gong Zhao, Xiaobin Xu, Manuel Ochoa, Weiqun Shen, and Thomas H Hintze, *Interaction between prostacyclin and nitric oxide in the reflex control of the coronary circulation in conscious dogs*, Cardiovascular Research **32** (1996), no. 5, 940–948.

[123] BERTRAM Zinner, *Stability of traveling wavefronts for the discrete Nagumo equation*, SIAM journal on mathematical analysis **22** (1991), no. 4, 1016–1020.

[124] Bertram Zinner, *Existence of traveling wavefront solutions for the discrete nagumo equation*, Journal of differential equations **96** (1992), no. 1, 1–27.

[125] Vladimir Sergeevich Zykov, *Simulation of wave processes in excitable media*, Manchester University Press, 1987.